TECHNISCHE UNIVERSITÄT MÜNCHEN

TUM School of Natural Sciences

Charge carrier properties and electronic correlations in the organic metals κ-(BEDT-TTF)$_2$X near the Mott metal-insulator transition

Shamil Erkenov

Vollständiger Abdruck der von der TUM School of Natural Sciences der Technischen Universität München zur Erlangung des akademischen Grades eines

Doktors der Naturwissenschaften (Dr. rer. nat.)

genehmigten Dissertation.

Vorsitz:

Prüfende der Dissertation:
1. Prof. Dr. R. Gross
2.

Die Dissertation wurde am bei der Technischen Universität München eingereicht und durch die TUM School of Natural Sciences am angenommen.

Abstract

The Mott metal-insulator transition is one of the most fundamental correlation-driven instabilities in normal metals. A well-established model system for studying the bandwidth-controlled quasi-two-dimensional Mott instability is provided by the organic κ-(BEDT-TTF)$_2X$ salts, where X denotes a monovalent anion. These salts can exhibit metallic/superconducting or Mott antiferromagnetic/nonmagnetic insulating ground states, depending on external parameters such as pressure or anion substitution. In this study, we systematically investigate the influence of these modifications near the Mott transition on the key internal parameters of the electronic system: electronic correlation strength, spin frustration, and disorder, which ultimately determine the electronic ground state. We successfully employed high magnetic field techniques to investigate quantum and semiclassical oscillations of magnetoresistance, which turn out to be powerful tools not only for mapping the Fermi surface geometry but also for probing these internal parameters.

Our results reveal that the analogy often-drawn between external pressure and so-called *chemical pressure* - arising from subtle isoelectronic chemical substitutions - is not straightforward. The application of external pressure reduces the electronic correlation strength and drives the system away from the Mott transition. Furthermore, we have found that pressure increases the geometrical frustration ratio. In contrast, anion substitution in some salts modifies both the frustration ratio and correlation strength, while in others it primarily alters the electronic ground state through changes in the frustration ratio, with the correlation strength remaining nearly unchanged. We further found that magnetic instabilities in these systems are closely tied to frustration: salts with higher frustration remain non-magnetic, while less frustrated compounds tend to exhibit antiferromagnetic order, in agreement with theoretical predictions. In addition, we investigated the influence of the thermal history on the electronic properties. For certain salts, variations in thermal treatment induce structural modifications, which serve as additional sources of disorder and can drive the system into a Mott-Anderson insulating state. Overall, the quantum oscillations, in combination with the anisotropic semiclassical magnetoresistance, allow us to disentangle the roles of different mechanisms, such as external pressure, chemical substitution, and disorder, in shaping the electronic ground state both near and away from the Mott metal-insulator transition. Furthermore, these experiments provide a critical quantitative test for theoretical predictions concerning the evolution of the conduction system near the bandwidth-controlled MIT.

Contents

1 Introduction

Es irrt der Mensch so lang er strebt.

Faust. J.W.Goethe

The physical properties of materials, including their electronic structure and transport properties, such as electrical conductivity, have long been of great interest to researchers. The first theoretical model describing interacting electrons in a material was developed by L. Landau in the 1950s and is known as the Fermi liquid theory [1]. In this model, strongly interacting electrons near the Fermi surface (FS) can be treated as non-interacting quasiparticles with renormalized parameters.

Several experimental techniques are used to study the FS, including scanning tunneling microscopy, angle-resolved photoemission spectroscopy, cyclotron resonance, and others. One of the most powerful methods for investigating the FS is based on magnetic quantum oscillations (MQO). Two types of such oscillations, associated with magnetization and electrical resistance, were discovered in the 1930s and are known as the de Haas-van Alphen [2] and Shubnikov-de Haas [3] effects, respectively. The theoretical foundation for these oscillations was laid by Landau, who predicted the orbital quantization of electron motion in a magnetic field. However, a comprehensive theory linking quantum oscillations with the geometry of the FS was developed later, in the 1950s, by Onsager, Lifshitz, and Kosevich [4, 5]. Since then, MQO measurements have become a powerful and indispensable tool for probing the FS of a wide range of materials, including strongly correlated electron systems such as organic metals [6, 7], as well as other correlated-electron materials of topical interest. These include cuprate [8–10] and iron-based [11–13] superconductors, topological conductors [14–16], and heavy-fermion compounds [17–19].

The aforementioned Fermi liquid theory predicts a metallic behavior for interacting electron systems. However, systems with a half-filled band and strong electronic correlations can exhibit an insulating ground state, which contradicts the predictions of the Fermi liquid model. The first theory to describe this metal-insulator transition (MIT) in strongly correlated systems was proposed by N. Mott in the 1930s [20]. Mott considered a system in which electrons experience on-site Coulomb repulsion in competition with hopping-driven kinetic energy. The strength of the Coulomb repulsion is governed by on-site electron interactions, while the hopping energy depends on the inter-site distance. As this distance increases, the hopping energy decreases. At a critical separation, the Coulomb repulsion dominates over hopping, leading to electron localization, the opening of a gap at the Fermi energy, and the onset of the Mott transition. In this model, half-filling of the band is a crucial condition, as it prevents electrons from bypassing the repulsion by hopping to unoccupied sites.

Further significant progress in understanding the Mott transition was achieved with

developing the Dynamical Mean-Field Theory (DMFT) approaches [21, 22]. These approaches also identify two key parameters that determine the ground-state properties of the system: the strength of electronic correlations and the amount of spin frustration. The correlation strength is believed to control the mobility of charge carriers, while the spin frustration ratio influences the magnetic ordering of the system.

However, the ideal Mott scenario is not fully realizable in real crystals. Charge-carrying quasiparticles, upon scattering on structural disorder, lose coherence and decay. In simple terms, when the scattering rate becomes sufficiently high, such that the mean free path of the electrons becomes comparable to the lattice spacing, the electrons become localized at their respective sites. This localization leads to the formation of an insulating state, a phenomenon first described by P. Anderson [23], and subsequently referred to as Anderson localization. Modern theoretical approaches based on DMFT [24] predict a transition into an insulating state, characterized by a fragmentation or 'clusterization' of the crystal into electronically disconnected regions as a result of disorder-induced scattering.

Despite extensive theoretical and experimental research on the physics of correlated electrons and the observation of Mott and Anderson instabilities in many materials, our understanding of the system's evolution near the MIT remains incomplete. Several open questions persist, including: How do conductive quasiparticles evolve near the MIT? What is the critical strength of electronic correlations? What roles do magnetic interactions and disorder play in the MIT? To address these fundamental questions, it is essential to study high-quality, easily tunable materials where the effects of electronic correlations, magnetic frustration, and disorder can be systematically controlled.

One of the most promising material classes for studying strongly correlated electron systems and MIT is organic charge-transfer salts. These materials initially attracted considerable attention after W. Little proposed them in 1964 as potential candidates for room-temperature superconductivity [25]. In the 1980s, superconductivity was first experimentally observed in this class of materials [26], which significantly intensified interest in them, particularly due to the presumed unconventional pairing mechanisms. However, despite the early optimism, the highest superconducting transition temperature (T_c) achieved in these materials remains around 14 K [27], far below room temperature. As a result, expectations for realizing high-T_c superconductivity in organic salts have gradually waned.

Nevertheless, a new perspective emerged when it was discovered that these materials provide an ideal platform for investigating strongly correlated electron systems, Mott physics, field-induced density wave transitions, and many other novel phenomena. In general, the properties of organic salts are similar to those of other anisotropic layered materials, including high-T_c cuprates, iron pnictides and chalcogenides, nickelates, and graphene-based systems [9, 13, 16, 19]. The phase diagrams of organic salts exhibit a rich variety of ground states, including Fermi liquid, Mott insulating, superconducting, spin-density wave, charge-density wave, and other exotic phases [28–30].

The key advantages of organic charge-transfer salts are their small energy scales and high tunability, making them ideal for tuning via moderate physical pressure or chemical substitution. Additionally, these compounds are typically very clean and feature simple quasi-one-dimensional (q1D) or quasi-two-dimensional (q2D) electronic structures. Therefore, they can be studied under relatively moderate magnetic fields

and temperatures using techniques such as magnetic quantum oscillations and angle-dependent magnetoresistance oscillations (AMRO) [7]. These methods provide direct access to the Fermi surface topology and charge carrier properties.

This work focuses on the so-called κ-(BEDT-TTF)$_2X$ salts, where BEDT-TTF denotes an organic donor molecule, X represents the anion, and κ refers to the molecular packing structure within the organic layers. These compounds consist of alternating insulating anion layers and conducting organic layers. Within the organic layers, pairs of BEDT-TTF molecules form dimers, which are arranged in an anisotropic triangular lattice. Each dimer donates one electron to the anion layer, resulting in an effectively half-filled conduction band. Due to differences in the conduction bandwidth and lattice anisotropy among various κ-salts, a wide range of ground states can be realized even at ambient pressure. Some compounds exhibit superconductivity, while others display antiferromagnetic or non-magnetic Mott insulating behavior.

This work is dedicated to the investigation of four organic salts, abbreviated as κ-NCS, κ-Br, κ-Cl, and κ-CN (the full chemical names will be provided in the following chapters). At ambient pressure, κ-NCS and κ-Br exhibit metallic or superconducting ground states, with superconducting transition temperatures $T_c > 10\,\mathrm{K}$. In contrast, κ-Cl and κ-CN display Mott insulating ground states, characterized by antiferromagnetic and non-magnetic ordering, respectively. Upon the application of pressure, both κ-Cl and κ-CN can be driven into metallic or superconducting states.

This gives rise to several fundamental questions: What determines the differences in ground states at ambient pressure? Which parameters does the anion substitution change? How do these parameters of the electronic system evolve during the application of pressure? Although there have been some theoretical suggestions on this matter, no explicit systematic investigation aimed at a critical experimental verification of the suggestions has been done. The aim of this work is to address these central and the outlined above questions and disentangle the roles of various parameters (correlation strength, frustration, and disorder) that govern the formation of the electronic ground state and Mott and Anderson instabilities. The thesis is structured as follows:

Chapter 2 (*Theoretical background*) provides a basic introduction to magneto-quantum oscillations, with a focus on Shubnikov-de Haas oscillations and general magnetoresistive transport, as these constitute our primary experimental methods. The chapter explains the origins of these phenomena and outlines the key parameters that govern both the quantum oscillations and the classical magnetoresistance. In addition, it offers an overview of the Mott and Anderson transitions, as well as the mechanisms responsible for the formation of different electronic ground states.

Chapter 3 (*Organic κ-salts*) introduces the main properties of the κ-salts studied in this work, including their crystal structures and phase diagrams. We present a concise overview of the investigated κ-salts, highlighting the key observed phenomena and differences between them. The chapter discusses the current understanding of Mott physics in κ-salts and examines the influence of physical pressure and anion substitution on MIT key electronic parameters, such as correlation strength and frustration. The impact of thermal history and disorder on the ground state and superconductivity is also addressed. In addition to reviewing the established knowledge in the field, this chapter highlights open questions and unresolved issues relevant to the ongoing research.

Chapter 4 (*Experimental setup*) describes in detail the experimental techniques and setups used in this research. This includes a discussion of controlling the main tuning parameters - pressure, magnetic field, and temperature - as well as the facilities used to apply magnetic fields and their respective limits.
Chapter 5 (*Antiferromagnetic Mott insulator κ-Cl*) is one of the central chapters of this thesis, where we present an extensive investigation of κ-Cl and compare the results with those previously reported for κ-NCS. We determine the Fermi surface of κ-Cl and its evolution under pressure. Additionally, we study the electronic correlation strength and spin frustration in this material over a broad pressure range, including both the purely metallic/superconducting state and the metal/insulator phase coexistence region. The obtained parameters are then compared with those of κ-NCS to identify key differences between the salts and their roles in the ground state formation. This chapter includes a detailed description of the analytical methods used and is frequently referenced in later chapters that apply similar methodologies.
Chapter 6 (*Influence of thermal history on κ-salts*) is dedicated to investigating the impact of thermal history on κ-Br and κ-Cl salts. We demonstrate how subtle structural changes, induced by varying the cooling rate through a glass-like transition around 80 K, can significantly influence disorder, electronic correlations, and eventually the electronic ground state in these compounds.
Chapter 7 (*Anion substitution effect in κ-Br and κ-Cl*) provides a comparative analysis of κ-Cl and κ-Br, where the anion substitution is isoelectronic and, therefore, preserves structural similarity. We present measurements across a broad pressure range, focusing on the evolution of electronic correlation strength. This analysis contributes to a deeper understanding of the mechanisms underlying chemical substitution effects and their influence on ground-state formation.
Chapter 8 (*Non-magnetic Mott insulator κ-CN*) presents a comprehensive study of the spin-liquid candidate κ-CN and compares its properties with the three previously discussed salts. We then attempt to construct a generalized phase diagram that captures the ground states of these compounds across different pressures. Based on our findings, we draw conclusions regarding the roles of correlation strength and frustration in the ground state formation, and discuss the evolution of quasiparticle properties across the metal-insulator transition.
Chapter 9 (*Summary*) is the final chapter, which summarizes the most important results of the thesis. Here, we revisit the main objectives and challenges of the research, address them using our findings, and propose new perspectives for future studies and further development of the field.

2 Theoretical background

A comprehensive explanation of the fundamental aspects of electronic transport in solid-state physics is provided in many standard textbooks, such as [31–33]. Additionally, an extensive overview of organic salts is given in [6, 7, 34, 35]. Therefore, in this chapter, I aim to summarize the key concepts relevant to the research topic of this thesis. The section will be structured to construct a self-contained explanation of the underlying physics while avoiding excessive detail on less relevant aspects.

2.1 Magnetic quantum oscillations

The primary experimental methods used in this work are based on magnetic quantum oscillations (MQO) and angle-dependent magnetoresistance oscillations (AMRO). The origin of MQO lies in the quantization of electron orbits in a magnetic field $\boldsymbol{B}$ due to the Lorentz force acting on the electrons in a free electron gas

$$\frac{d\boldsymbol{p}}{dt} = \boldsymbol{F}_L = -e(\boldsymbol{v} \times \boldsymbol{B}). \tag{2.1}$$

In a semi-classical picture, the electrons perform an orbital motion within the plane perpendicular to the magnetic field at the cyclotron frequency $\omega_c = eB/m_0$ with the electron mass m_0 and elementary charge e. In the $k_x k_y$-plane, perpendicular to the magnetic field along the z-direction ($\boldsymbol{B}||z$), the electron's energy spectrum becomes quantized according to the Bohr-Sommerfeld quantization condition and can be expressed as:

$$E = \left(n + \frac{1}{2}\right)\hbar\omega_c + \frac{\hbar^2 k_z^2}{2m_0}. \tag{2.2}$$

These quantized energy levels due to the motion within the plane perpendicular to the field can be visualized as concentric isoenergetic circles in $\boldsymbol{k}$-space (Fig. 2.1(a)), with an energy difference $\Delta E = \hbar\omega_c$ (which is $\sim 1.5\,\mathrm{meV}$ for a free electron in a field of 15 T). In addition, there is a free motion parallel to the field direction leading to a parabolic dispersion.

In the real crystals with a quasi-two-dimensional (quasi-2D) and three-dimensional (3D) Fermi surfaces (FS), these circles extend along the z-direction, forming coaxial cylinders known as Landau tubes (Fig. 2.1(b)). In q2D case, the Fermi energy (E_F) separates occupied tubes from unoccupied ones (Fig. 2.1(c)). Since only the electrons near the Fermi energy can move across the FS, the cyclotron frequency is modified as:

$$\omega_c = \frac{2\pi eB}{\hbar^2}\left(\frac{\partial S}{\partial E}\right)^{-1}_{k_z} = \frac{eB}{m_c}, \tag{2.3}$$

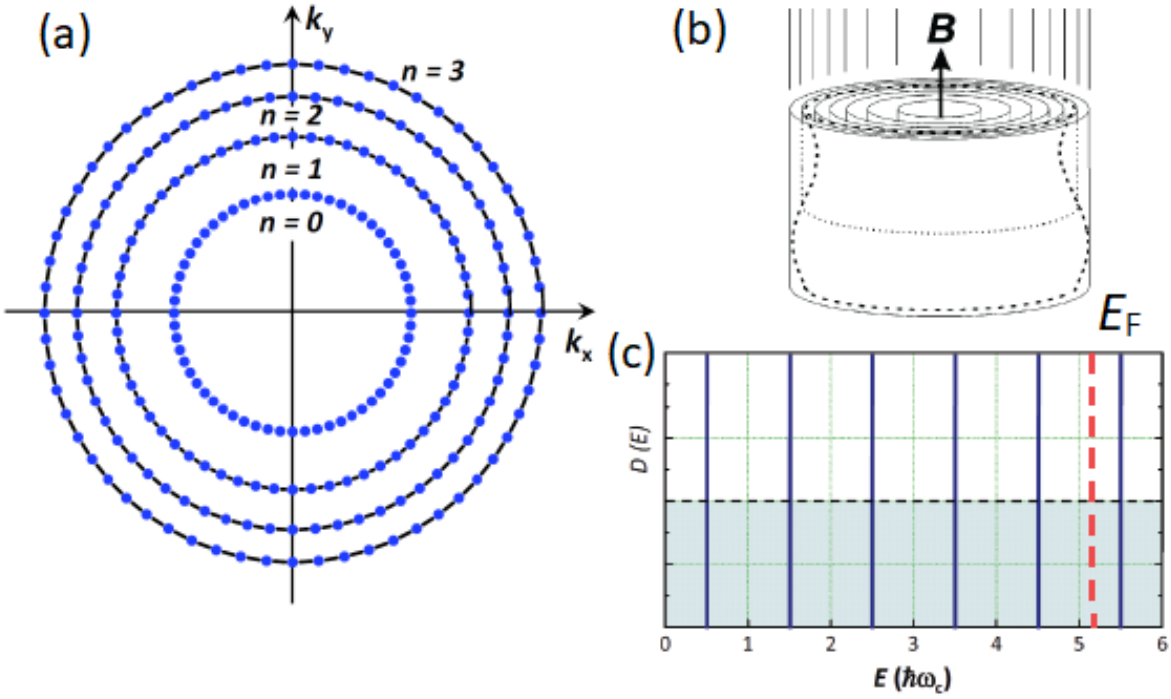

Figure 2.1: (a) Quantization of electronic states in the k_xk_y-plane for free electrons with a magnetic field applied perpendicular to the plane [31]. The number of dots on the concentric circles symbolizes the degeneracy of the quantized levels. (b) Illustration of Landau tubes in a quasi-2D FS [7]. (c) Corresponding density of states in units of $\hbar\omega_c$ for a perfect 2D system [31]. Vertical blue solid lines represent the Landau levels, while the red dashed line indicates the Fermi energy. As ω_c increases with the magnetic field, the distribution stretches along the energy (E) axis, and the Landau levels eventually cross the Fermi surface. The light blue shaded area depicts the density of states in the absence of a magnetic field.

where S is the area in k-space enclosed by an electron orbit with constant energy $E = E_F$ and fixed k_z, which is the component of $\boldsymbol{k}$ paralell to $\boldsymbol{B}$. We can introduce the cyclotron mass as:

$$m_c = \frac{\hbar^2}{2\pi}\left(\frac{\partial S}{\partial E}\right)_{k_z}. \tag{2.4}$$

The cross-sectional area of the n-th Landau tube can be expressed using the Onsager relation [5]:

$$S_n = (n+\gamma)\frac{2\pi eB}{\hbar}, \tag{2.5}$$

where $\gamma \sim 1$ is a phase constant. The quantum number n represents the tube index. In metals, we typically have $n \gg 1$ for tubes with energies close to E_F due to the large Fermi energy of metals. As the magnetic field increases, the size of the Landau tubes and their degeneracy also grow. At specific field values, the cross-sectional area of a tube can align with the FS (Fig. 2.1(c)). With further increases in field strength and tube size, this tube moves beyond the FS, leading to a redistribution of electrons into lower

energy levels [32]. This variation in the density of states at the FS influences several physical properties of the system [32], including magnetization (de Haas-van Alphen effect [2]) and electrical conductivity (Shubnikov-de Haas effect [3]).

The field value B_n, at which the cross-sectional area of the n-th Landau tube equals the extremal FS cross-sectional area S_{extr} (perpendicular to the magnetic field $\boldsymbol{B}$), can be derived from the quantization condition. This alignment of the cross-sectional areas of the Landau tubes and the FS occurs periodically in the inverse magnetic field. Therefore, we can introduce the frequency of these crossings, F, given by the expression

$$F = \left[\Delta\left(\frac{1}{B}\right)\right]^{-1} = S_{\text{extr}}\,\frac{\hbar}{2\pi e}. \tag{2.6}$$

Interestingly, the extremal cross-sectional area is obtained from the measured oscillation frequency without any adjustable parameters.

2.2 Shubnikov-de Haas effect and Lifshitz-Kosevich formula

The oscillations in magnetization were first quantitatively described for an arbitrary dispersion by I.M. Lifshitz and A.M. Kosevich [4], who formulated what has become the standard theory for describing de Haas-van Alphen oscillations (dHvA). In contrast, the theory of Shubnikov-de Haas (SdH) oscillations is more complex and remains less fully understood. This complexity arises because, in principle, it requires explicit consideration of the various scattering processes influenced by a quantizing magnetic field [32]. Nevertheless, in most cases, it suffices to follow Pippard's idea [36], which suggests that the scattering probability, and thus the resistivity, are proportional to the density of states near the Fermi level. Consequently, the oscillatory component of the conductivity can be expressed in the following form:

$$\frac{\sigma}{\sigma_0} = \sum_{r=1}^{\infty} \frac{1}{r^{1/2}} a_r \cos\left[2\pi r\left(\frac{F}{B} - \frac{1}{2}\right) \pm \frac{\pi}{4}\right], \tag{2.7}$$

$$a_r \propto \frac{m_c B^{1/2}}{(S'')^{1/2}_{\text{extr}}} R_T(r) R_{\text{D}}(r) R_S(r), \tag{2.8}$$

where σ_0 is the background conductivity, and a_r includes the damping factors R_T, R_{D}, and R_S, which are described in the following subsections.

2.2.1 Temperature damping factor R_T

When $T > 0$, the Fermi distribution of single-electron occupation probabilities becomes less sharp, causing the electron distribution at the Fermi level E_{F} to become thermally smeared out. This spread results in a range of slightly different extremal cross-section orbits around the Fermi surface, each contributing oscillations with slightly altered frequencies [32]. Consequently, the peak in the oscillation spectrum broadens, leading

to a reduction in oscillation amplitude. Lifshitz and Kosevich [4] demonstrated that the temperature dependence of this damping is governed by the normalized effective cyclotron mass, $\mu = m_c/m_0$, and can be expressed as:

$$R_T(r) = \frac{Kr\mu T/B}{\sinh(Kr\mu T/B)}, \tag{2.9}$$

where coefficient $K = 2\pi^2 k_B m_0/\hbar e \approx 14.69\,\mathrm{T/K}$. Thus, Eq. (2.9) can be used to determine the effective cyclotron mass μ by measuring the temperature dependence of the SdH oscillation amplitude.

2.2.2 Dingle damping factor R_D

In addition to the smearing of the FS, the Landau tubes are not infinitely sharp due to scattering processes. This results in a finite scattering time τ, softening the distribution on the Landau tubes from a delta function to a Lorentz distribution with a half-width $\Gamma = \hbar/2\tau$. By defining the Dingle temperature [37]

$$T_D = \hbar/(2\pi k_B \tau), \tag{2.10}$$

we can express the Dingle damping factor as follows:

$$R_D(r) = \exp\left(-K\mu T_D/B\right). \tag{2.11}$$

With μ known from the temperature damping discussed above, we can use Eq. (2.11) to determine T_D from the field dependence of the oscillation amplitude, providing insights into the scattering rate and the quality of the samples.

2.2.3 Spin-splitting damping factor R_S

The third damping factor accounts for the effect of Zeeman splitting. When an electron's spin aligns either parallel or antiparallel to the magnetic field, its energy shifts by $\Delta E = \pm g\mu_B B$, where g is the Landé factor and μ_B is the Bohr magneton. This shift causes each Landau tube to split into two subbands. For free electrons, $g = 2$, making the energy difference $\Delta E = \hbar\omega_c$, which matches the energy spacing between two neighboring Landau levels. As a result, the contributions of electrons with antiparallel spin in the n-th Landau tube align in phase with those of parallel spins in the $(n+1)$-th tube [32]. However, in real crystals, where $g \neq 2$ and $\mu \neq 1$, this phase alignment is imperfect, resulting in a damping factor given by:

$$R_S(r) = \cos(\frac{\pi}{2} r\mu g). \tag{2.12}$$

At certain values of the cyclotron mass, this damping factor equals zero and can lead to a vanishing oscillation amplitude [38–41].

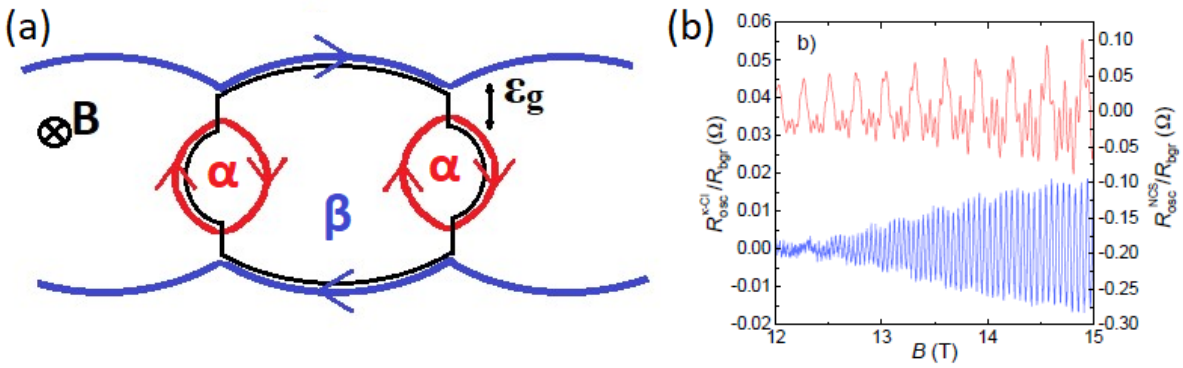

Figure 2.2: (a) Example of a 2D FS formed by two conduction bands, resulting in a closed pocket (red) and two open sheets (blue). The black line represents the magnetic breakdown orbit. (b) Oscillating part of the magnetoresistance normalized to the background resistance for κ-Cl (blue, left scale) and for κ-NCS (red, right scale) [42].

2.3 Magnetic breakdown

Until now, we have only considered electrons in a single conduction band moving along a classical orbit. However, this perspective changes when multiple conduction bands, separated by an energy gap E_g, are located near the Fermi energy. As the magnetic field increases and $\hbar\omega_c$ achieves the order of magnitude of E_g^2/E_F, the probability of tunneling between bands rises significantly [32]. This phenomenon is known as magnetic breakdown (MB).

An example similar to the behavior observed in our samples is illustrated in Fig. 2.2(a). In the semiclassical picture, electrons are confined to a single band (neglecting scattering effects), allowing only the classical α-orbit (red) as a possible closed trajectory. However, when electrons tunnel between the bands, a second trajectory - the β-orbit (black line) - becomes accessible. As a result, two frequencies appear in the SdH spectrum. Since the tunneling probability $P = \exp(-B_{MB}/B)$ increases exponentially with the magnetic field, the magnetic breakdown field B_{MB} can be defined as:

$$B_{MB} \simeq \frac{mE_g^2}{e\hbar E_F}, \tag{2.13}$$

where E_g is the interband gap at the MB junction [32]. Thus, the conditions under which MB becomes relevant are given by the criterion: $\hbar\omega_c \gtrsim E_g^2/E_F$ or $B \gtrsim B_{MB}$. Fig. 2.2(b) presents normalized SdH oscillations for the organic salts κ-Cl (blue) and κ-NCS (red) (abbreviations will be explained later in Chapter 3) from [42]. In the red curve, the dominant contribution to the oscillations comes from the α-frequency ($\sim$ 600 T), whereas in the blue curve, the dominant contribution is from the β-frequency ($\sim$ 4000 T).

2.4 Angle-dependent magnetoresistance oscillations (AMRO)

During the 1990s, extensive research on layered organic superconductors established angle-dependent magnetoresistance oscillations (AMRO) [43–47] as a powerful technique for investigating the geometry of the Fermi surface of strongly anisotropic layered metals through interlayer magnetotransport (for a review, see [7]). The conductivity

$$\sigma_{ij} = -\frac{2e^2\tau}{(2\pi)^3}\int \frac{df_0}{dE} v_i(\boldsymbol{k})\overline{v}_j(\boldsymbol{k})d\boldsymbol{k}, \tag{2.14}$$

and consequently the resistivity, in metals with a slightly warped cylindrical FS depend on the averaged electron velocity

$$\overline{v}_j(\boldsymbol{k}) = \frac{1}{\tau}\int_{-\infty}^{0} v_j(\boldsymbol{k},t))e^{t/\tau}dt, \tag{2.15}$$

where f_0 is the equilibrium Fermi distribution function and i, j are the x, y, and z components, with z-axis bound to the interlayer direction. The quantity $\overline{v}_j(\boldsymbol{k})$ represents the velocity averaged over the scattering time. Based on this relationship, significant changes in the interlayer resistivity are expected as the magnetic field is tilted from a direction perpendicular to the conducting layers to one parallel to the layers. At certain polar angles θ - defined as the angle between the magnetic field and the normal to the conducting planes - the interlayer resistivity exhibits pronounced enhancements (Fig. 2.3(b)), manifesting as angle-dependent magnetoresistance oscillations (AMRO) [7].

The first calculation of the polar angle positions where AMRO maxima should occur for a cylindrical FS was conducted by Yamaji [48]. The dispersion relation for a slightly corrugated cylindrical FS can be written in a simplified form:

$$E(k) = E_{\parallel}(k_x,k_y) + E_{\perp}(k_z) = \frac{\hbar^2}{2m}(k_x^2+k_y^2) - 2t_{\perp}\cos(k_z d), \tag{2.16}$$

where the interlayer hopping energy $t_{\perp} \ll E_{\parallel}$, and d is the interlayer spacing constant. The tilted cyclotron orbit, with its position along the k_z-direction labeled by k_z^0, lies in the plane perpendicular to the magnetic field $\boldsymbol{B}$. For a position on this orbit with azimuthal angle ϕ, the projection of the Fermi wave vector onto the z-axis can be expressed using the geometrical relation (Fig. 2.3(a))

$$k_z(\phi) = k_z^0 - k_{\mathrm{F}}(\phi)\cos(\phi)\tan(\theta). \tag{2.17}$$

In this case, the component of $\boldsymbol{k}$ perpendicular to the field can be calculated from Eq. (2.16) by setting it equal to the Fermi energy: $\frac{\hbar^2 k_{\mathrm{F}}^2}{2m} = \frac{\hbar^2}{2m}(k_{\parallel}\cos(\theta))^2 - 2t_{\perp}\cos(k_z d)$.

We can express the area of the orbit cross section using the values for $k_{\parallel}$ and k_z^0 as

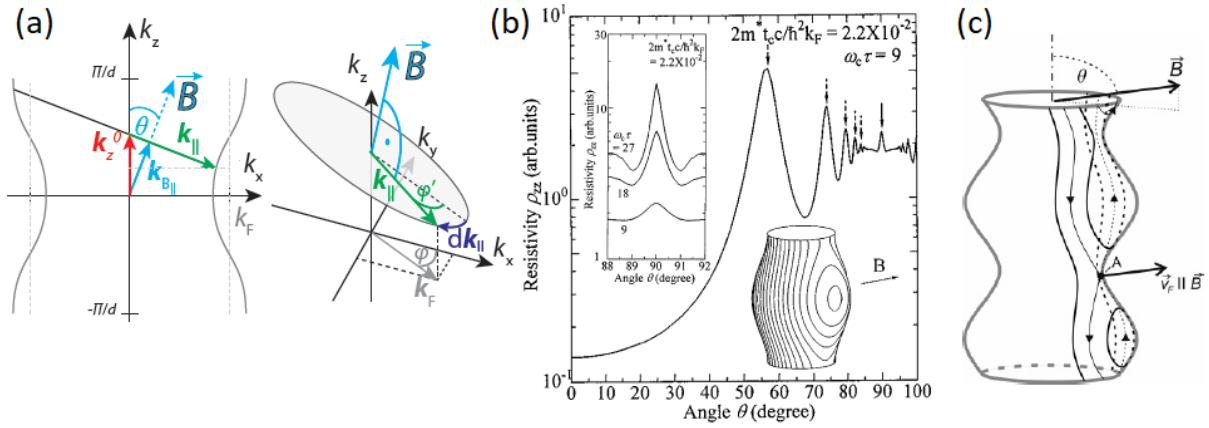

Figure 2.3: (a) A corrugated cylindrical FS, where θ represents the polar angle with respect to the direction of the magnetic field [49]. The quantity k_z^0 denotes the position of the tilted cyclotron orbit (gray ellipse) along the k_z-direction, $k_{\parallel}$ is the wave vector of this cyclotron orbit, and k_F represents the Fermi wave vector in the absence of warping. (b) Calculated AMRO from [50]. Dashed arrows indicate the AMRO maxima, while the solid arrow marks the peak feature at $\theta = 90°$. The upper left inset shows the peak feature at different values of the parameter $\omega_c\tau$ for various magnetic field strengths. The lower right inset schematically illustrates cyclotron orbits on the warped FS at θ close to 90°. (c) A schematic representation of cyclotron orbits on a warped cylindrical FS under a nearly in-plane magnetic field. The thin line (with arrows indicating electron motion direction) represents the self-crossing orbit, which separates the region of large single-connected orbits (left) from the region where each orbit splits into a large orbit and a small closed loop at the FS edge (right of the self-crossing orbit). The Fermi velocity near the crossing point A is nearly parallel to the magnetic field [7].

given by:

$$\begin{aligned} S_{\text{orb}}\cos(\theta) &= \int_0^{2\pi} dS\cos(\theta) = \int_0^{\pi} d\phi (k_{\parallel}\cos(\theta))^2 = \\ &= \int_0^{\pi} d\phi \left[k_F^2 + 4mt_{\perp}\cos(k_z d)/\hbar^2\right] = \\ &= \int_0^{\pi} d\phi \left[k_F^2 + 4mt_{\perp}\cos(k_z^0 d - k_F d\tan(\theta)\cos(\phi))/\hbar^2\right] = \\ &= \pi k_F^2 + 4\pi m t_{\perp}\cos(k_z^0 d) J_0(k_F d\tan(\theta))/\hbar^2. \end{aligned} \tag{2.18}$$

Yamaji noted [48] that this equation can be integrated using the zeroth-order Bessel function J_0. At certain polar angles, when the Bessel function $J_0 = 0$, the cross-sectional area $S_{\text{orb}}\cos(\theta)$ becomes independent of the position k_z^0. In this case, all the cyclotron orbits enclose the same area. The condition, when it happens, is called 'Yamaji condition' and can be expressed as

$$\tan(\theta_n) \approx \frac{\pi}{k_B^{\max} d}(n - \frac{1}{4}), \tag{2.19}$$

where $k_B^{\max}$ is the maximal projection of the in-plane Fermi wave vector k_F on the field rotation plane.

The physical nature of AMRO can be understood by considering that, in a strong magnetic field, the interlayer conductivity, σ_{zz}, is determined by the interlayer velocity, v_z, averaged over the period of an electron's motion along a closed orbit. The latter can be expressed as

$$\overline{v}_z = \overline{\partial E/\hbar \partial k_z} = -\frac{\partial S_{\text{orb}}(k_z^0)/\partial k_z^0}{\hbar(\partial S_{\text{orb}}/\partial E)_{k_z}} = -\frac{\hbar \partial S_{\text{orb}}(k_z^0)/\partial k_z^0}{2\pi m_c}. \tag{2.20}$$

The velocity v_z depends on the derivative of the orbit area with respect to its position in k-space and can be expressed as a function of k_z^0. In the quasi-2D case, the cyclotron mass increases proportionally to $1/\cos(\theta)$. Generally, the derivative $\partial S_{\text{orb}}(k_z^0)/\partial k_z^0$ is finite, causing σ_{zz} to saturate. However, at Yamaji's angles, $\partial S_{\text{orb}}(k_z^0)/\partial k_z^0 \approx 0$, leading to a vanishing average velocity $\overline{v}_z$ and, consequently, a vanishing σ_{zz}.

2.5 Coherence peak

When the magnetic field is nearly parallel to the conducting layers, a peak feature appears in $R(\theta)$ for certain materials [43, 51, 52], as shown in Fig. 2.3(b) inset. Experiments have demonstrated that the width of this peak remains independent of the magnetic field strength, indicating a geometrical origin for the phenomenon [7].

This peak feature can be understood by considering the warping of the cylindrical FS. For tilt angles closer to the parallel orientation than a critical angle θ_c, additional closed orbits form on the sides of the warped FS, as illustrated in Fig. 2.3(b) inset. At the same critical angle, self-crossing orbits emerge, depicted by thin lines with arrows in Fig. 2.3(c).

For a weakly warped cylinder ($t_\perp \ll E_F$), the Fermi velocity v_F of electrons near the self-crossing point A becomes nearly parallel to the magnetic field. Consequently, the Lorentz force at this point is minimal, and the electron velocity remains nearly unchanged. The interlayer projection of this velocity contributes significantly to the interlayer conductivity. This behavior results in a local minimum in the interlayer resistance at $\theta = \pi/2 - \theta_c$.

As θ approaches 90°, the interlayer velocity v_z^A decreases, reaching exactly zero at $\theta = 90°$. This leads to a sharp peak in magnetoresistance for $90° - \theta_c < \theta < 90° + \theta_c$. In organic metals, typical peak widths range from approximately 1° to 3°. The width of the coherence peak can be used to estimate the anisotropy ratio $2t_\perp/E_F$ from experimental data using the equation [50]:

$$\frac{\theta_c}{k_F d} \simeq \frac{t_\perp}{E_F}. \tag{2.21}$$

The feature described above is referred to as the 'coherence peak' because it exclusively affects coherent interlayer transport. Incoherent interlayer transport, primarily driven by impurity scattering, remains largely insensitive to magnetic fields parallel to the layers. Consequently, the presence of a coherence peak serves as strong evidence that coherent transport dominates the interlayer conductivity.

2.6 Beating phenomena in quantum oscillations

At Yamaji angles, as previously mentioned, the Fermi surface cross-section in the plane perpendicular to the magnetic field remains independent of k_z^0. However, at intermediate angles, due to the warping of the FS, the cross-sectional areas are different depending on k_z^0, leading to the minimal and maximal extremal cross-sectional areas, with slightly different oscillation frequencies ($F_{\min}$ and $F_{\max}$).

The total SdH oscillation signal is the sum of contributions from each of these areas. When the frequencies are sufficiently close to each other, their superposition results in periodic constructive and destructive interference, forming beats (Fig. 2.4(a)). Consequently, the amplitude of the oscillations is proportional to the coefficient [7, 53, 54]:

$$R_{\text{beat}} = |\cos(\pi\frac{\Delta F}{B} - \frac{\pi}{4})|, \tag{2.22}$$

where $\Delta F = F_{\max} - F_{\min}$ denotes the difference between the maximal and minimal extremal cross-sectional areas of the FS. When the coefficient $R_{\text{beat}} = 0$, we observe a node in the oscillations, with vanishing amplitude [8, 11, 43, 55–58]. The beating frequency is proportional to the difference between the maximal and minimal cross-sectional areas of the FS

$$\Delta F = F_{max} - F_{min} = \frac{\Delta S}{2\pi e\hbar} \approx \frac{8\pi m t_\perp J_0(k_F d\tan(\theta))}{2\pi e\hbar^3\cos(\theta)} = \Delta F_0 \frac{J_0(k_F d\tan(\theta))}{\cos(\theta)}, \tag{2.23}$$

where $\Delta F_0 = 4mt_\perp/e\hbar^3$ and directly depends on the strength of warping. The difference in cross-sectional areas can be calculated from Eq. (2.18). Changes in the magnetic field orientation induce variations in both the maximal and minimal extremal cross-sectional areas, thereby altering the beat frequency. The θ dependence of the beat frequency is given by Eq. (2.23). A change in the beat frequency also leads to a shift in the node position. Fig. 2.4(b) shows the node positions as a function of the tilting angle.

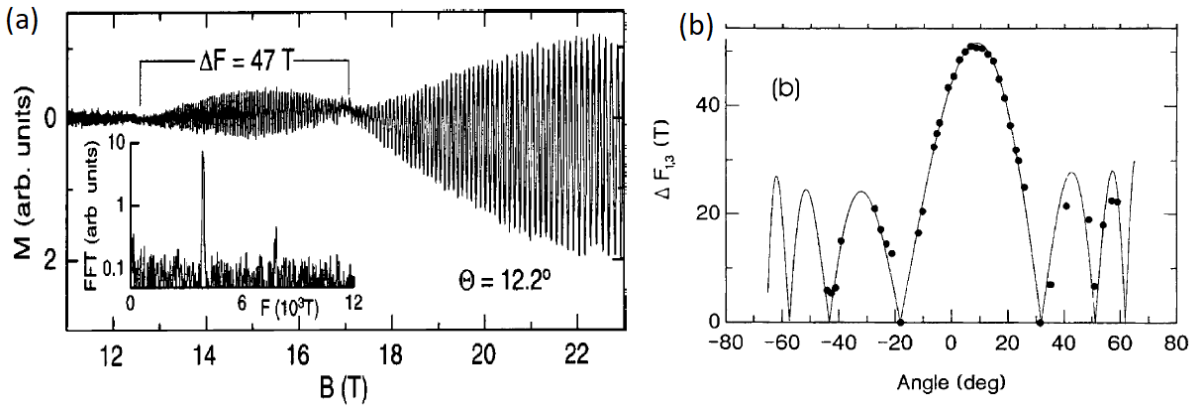

Figure 2.4: (a) dHvA oscillations in β-(BEDT-TTF)$_2$IBr$_2$ at $T \approx 0.4$ K, at the field slightly tilted from the direction normal to the layers from [7]. The inset shows the FFT of the data. (b) Angular dependence of the beat node position in dHvA oscillations from panel (a).

Taking $R_{\text{beat}} = 0$, we can calculate the node positions B_n of the beating feature as a function of frequency:

$$B_n = \frac{4\Delta F}{4n+3} = \frac{4\Delta F_0}{4n+3}\frac{J_0(k_F d\tan(\theta))}{\cos(\theta)}. \tag{2.24}$$

Furthermore, this dependence can be used to fit the θ dependence of the node positions (Fig. 2.4(b)). The fit reveals the beat frequency at perpendicular orientation, ΔF_0, and the node index n. The ratio of the beating frequency and the β-frequency can be used to estimate the FS warping using Eq. (2.25), as well as the interlayer transfer integral $t_\perp$, using the relation

$$\frac{t_\perp}{E_F} \approx \frac{\Delta k_F}{k_F} \approx \frac{\Delta F}{2F}. \tag{2.25}$$

2.7 Fermi liquid theory

In the theoretical concepts described above, charge carriers were treated as non-interacting electrons (Fermi gas). However, in real metals, electrons interact more or less strongly with each other. In such cases, the system can be effectively described within the framework of Fermi liquid (FL) theory, developed by L. Landau in the 1950s [1]. This theory employs renormalization methods and treats the low-energy excitations of the electron system as quasiparticles. These quasiparticles behave similarly to non-interacting electrons in a Fermi gas but possess renormalized properties due to electron-electron interactions.

The Hamiltonian of the system can be expressed as the sum of two terms [33, 59]: $H = H_0 + H_{\text{int}}$. Here, H_0 denotes the Hamiltonian of non-interacting fermions in the periodic lattice potential, which gives rise to a modified electronic dispersion and defines the concept of band electrons with an associated band mass. The second term, H_{int}, accounts for electron-electron interactions, which renormalize the quasiparticle properties. Correspondingly, the total energy of the system can be written as the sum of two contributions: $E(k) = E_0(k) + E_{\text{int}}(k)$, where E_{int} encapsulates interaction effects.

Within the Fermi liquid framework, the concept of the Fermi surface remains well-defined as the boundary between occupied and unoccupied states at zero temperature. However, many-body interactions can modify both the shape and properties of the FS. In particular, the quasiparticle dispersion near the FS becomes renormalized, resulting in an effective mass different from the bare band mass [33, 59, 60]. Following Landau's notation of linearized dispersion, and as a conceptual tool for illustrating renormalization effects in a Fermi liquid, the effective mass can be expressed in terms of the band mass as:

$$\begin{aligned} m^* = \frac{p_F}{v_F} = \hbar k_F \left(\frac{dE(k)}{\hbar\, dk}\Big|_{k=k_F}\right)^{-1} &= \hbar^2 k_F \left(\frac{dE_0(k)}{dk}\Big|_{k=k_F} + \frac{dE_{\text{int}}(k)}{dk}\Big|_{k=k_F}\right)^{-1} \\ &= m_{\text{band}}\left(1 + \frac{dE_{\text{int}}/dk|_{k=k_F}}{dE_0/dk|_{k=k_F}}\right)^{-1} = m_{\text{band}}(1+A_0). \end{aligned} \tag{2.26}$$

Here, the band mass m_{band} captures the interactions of non-interacting charge carriers with the periodic potential of the lattice, while Landau FL parameter A_0 captures the

finite interactions of the band electrons. The degree of similarity between quasiparticles and electrons in a non-interacting system can be quantified through the quasiparticle residue Z. This parameter represents the overlap of wave functions between non-interacting electrons and quasiparticles, indicating how closely the quasiparticle resembles the original, non-interacting particles [33, 60, 61]. The quasiparticle residue is also approximately related to the effective mass and, in our work, will be considered through the relation: $Z = m_{\text{band}}/m^*$. The value of Z ranges between 0 and 1 and can be understood as follows:

- $Z \approx 1$: The quasiparticles closely resemble free electrons, experiencing weak interactions. The system behaves similarly to a non-interacting Fermi gas.
- $Z < 1$: The quasiparticles are 'dressed' by interactions, meaning that they carry a cloud of excitations around them, which makes them "heavier". This is captures by a reduced value of Z, which indicates stronger electronic correlations.
- $Z \to 0$: The quasiparticles are no longer well-defined. This occurs near a quantum critical point, where fluctuations are so strong that the quasiparticle lifetimes vanish.

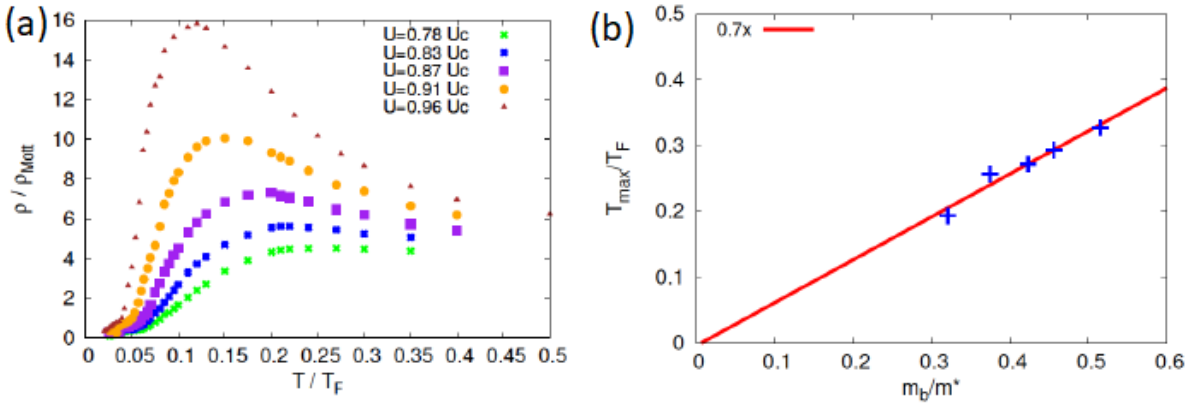

Figure 2.5: (a) Resistivity maxima in the strongly correlated metallic regime of a half-filled Hubbard model within DMFT theory [62]. The resistivity is given in units of ρ_{Mott}, maximal resistivity according to the Boltzmann quasiclassical theory of transport [63, 64]. (b) Dependence of T_{max} on m^* from DMFT theory [62, 65]. The band mass $m_{\text{b}} = m_{\text{band}}$.

As transport is carried by heavy quasiparticles, the resistivity strongly increases with temperature due to inelastic electron-electron scattering. Within the FL theory, the temperature dependence of resistivity at low temperatures is given by [60, 65]:

$$\rho(T) = \rho_0 + AT^2. \tag{2.27}$$

This relation holds over a limited low-temperature range below the coherence temperature $T^*(\sim 0.1T_{\text{F}})$. Referring to theoretical investigations [66–68], T^* might correspond to the crossover temperature between a FL and marginal FL, in which the quasiparticles are scattered by critical fluctuations of the gauge field [69]. The coefficient A is

related to the effective mass through the Kadowaki-Woods law [70–72]: $A \propto (m^*)^2$. Fig. 2.5(a) shows the temperature dependence of resistivity, calculated for different correlation strengths (which will be introduced in later sections). The maximum in resistivity corresponds to the destruction of quasiparticles at temperature $T_{\max}$. This maximum temperature has been predicted to be linearly proportional to the effective mass [65], as given by equation (see Fig. 2.5(b)):

$$\frac{T_{\max}}{T_{\mathrm{B}}} \propto \frac{m_{\mathrm{band}}}{m^*}. \tag{2.28}$$

2.8 Mott transition

The Fermi liquid model described above is valid only in the metallic state. However, when electronic correlations become strong, a system with a half-filled electronic band can transform into an insulating state. This phenomenon was first described by Mott and Peierls in [20, 73] and later termed the Mott transition. They considered a lattice of hydrogen-like atoms and predicted a metal-insulator transition (MIT) depending on the lattice period.

In real crystals, the transition is more complex. The first theory incorporating electronic interactions was developed by Hubbard, Anderson, and Kanamori [21, 74, 75]. They introduced the key concepts of the so-called Hubbard model, which describes electrons moving in a crystal lattice, hopping between adjacent lattice sites, and experiencing strong Coulomb repulsion when occupying the same site. The Hamiltonian for this model is given by

$$H = U \sum_i c^\dagger_{i,\uparrow} c_{i,\uparrow} c^\dagger_{i,\downarrow} c_{i,\downarrow} - t \sum_{\langle i,j \rangle,\sigma} \left(c^\dagger_{i,\sigma} c_{j,\sigma} + c^\dagger_{j,\sigma} c_{i,\sigma} \right). \tag{2.29}$$

Here, t represents the hopping energy, which facilitates electron movement between neighboring sites, while U denotes the on-site Coulomb repulsion, introducing an energy penalty when two electrons occupy the same lattice site, thereby leading to electron localization. The operators $c^\dagger_{i,\sigma}$ and $c_{i,\sigma}$ are the creation and annihilation operators for an electron on lattice site i with spin σ. The summations over i and $\langle i,j \rangle$ are performed over all lattice sites and all pairs of neighboring lattice sites, respectively, while σ accounts for both spin directions. The ratio U/t, known as the correlation strength ratio, determines the ground state of the system, leading to two main possible phases:

- Metallic phase for weak correlations and small U/t
- Mott insulating phase for strong correlations and large U/t

For a simple explanation [21], we consider a half-filled system with two possible electron states. The first state corresponds to the single electron occupancy of a lattice site, forming the Lower Hubbard Band (LHB). The second state corresponds to the double occupancy of a site, forming the Upper Hubbard Band (UHB). The energy difference between these two states is determined by U.

When U/t is small, electrons do not experience a significant energy penalty for double occupancy, resulting in a system that consists of a mixture of both states, with the

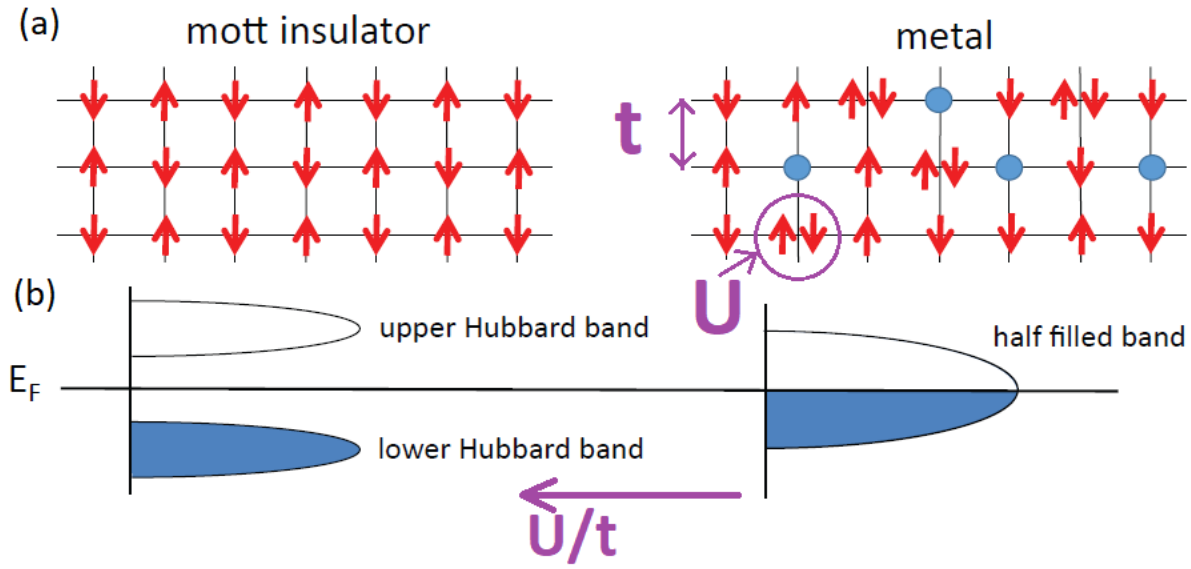

Figure 2.6: Sketch of (a) electron distribution on a 2D square latticeand (b) corresponding density of states in the Mott insulating and metallic phase at half-filling [42]. The arrows represent spin-up and spin-down electrons, while the blue circles indicate unoccupied sites.

LHB and UHB overlapping (Fig. 2.6, metallic state). As U/t increases, the energy cost of double occupancy grows, shifting the UHB to a higher energy (Fig. 2.6, insulating state). This shift creates an energy gap between the UHB and LHB, marking the onset of the Mott MIT. The critical value $(U/t)_c$ at which this gap forms corresponds to the transition point. According to nomenclature, this type of insulator is referred to as a Mott-Hubbard insulator [21, 76].

Another type of transition occurs in systems with long-range order. In the presence of strong spin interactions, neighboring electrons tend to align with specific spin orientations. In the simplest case, neighboring electrons adopt opposite spin orientations, leading to the formation of long-range antiferromagnetic order. As a result, the unit cell effectively doubles, containing electrons with both spin orientations at each site, which is equivalent to a fully occupied band. This transition into an antiferromagnetic insulating state occurs below a finite critical temperature T_c. According to nomenclature, this is known as a Mott-Heisenberg insulator [76].

The key difference between a Mott-Hubbard insulator and a Mott-Heisenberg insulator is that in the latter, the energy gap emerges only below the critical temperature T_c and vanishes above it. In contrast, a Mott-Hubbard insulator has a fixed energy gap that persists regardless of temperature, although thermal excitation can lead to partial occupation of states within the gap.

An increase in the correlation strength not only alters the ground state of the system but also affects its electronic properties. One of the pioneering studies linking the evolution of the quasiparticle residue to electronic correlations was conducted by

Brinkman and Rice in 1970 [77]. They proposed a quadratic dependence

$$\frac{m_{\text{band}}}{m^*} = Z \approx \left(1 - \left(\frac{U}{U_0}\right)^2\right) \tag{2.30}$$

of the quasiparticle residue on the correlation strength. According to their work, the quasiparticle residue Z vanishes as the system approaches the critical value U_0 for the Mott transition. This leads to a divergence in the quasiparticle effective mass, marking the transition from a Fermi liquid to a Mott insulator.

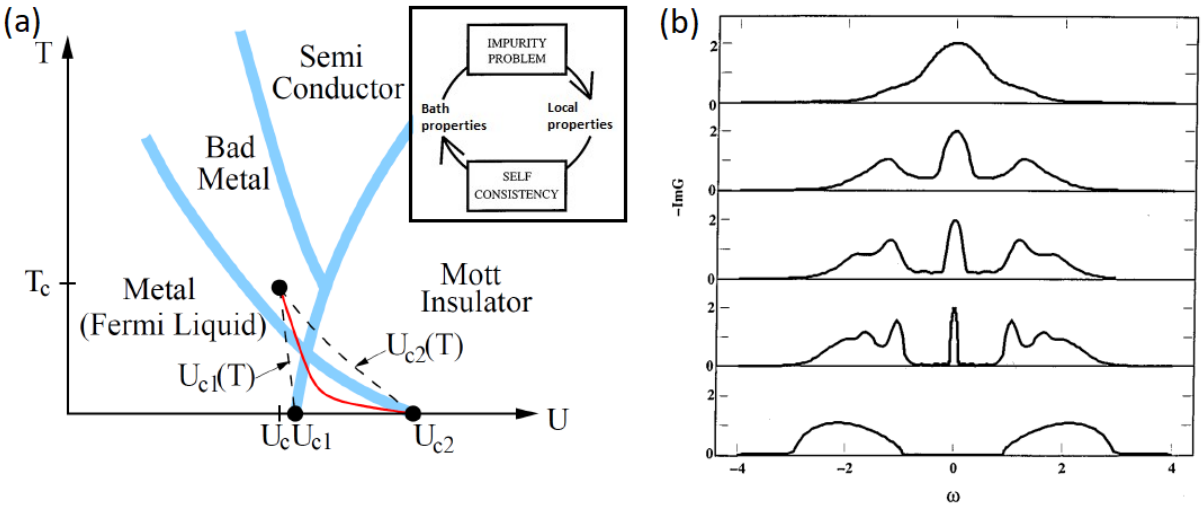

Figure 2.7: (a) Paramagnetic phases of the Hubbard model within DMFT, schematically showing the spinodal lines of the Mott insulating and metallic mean-field solutions (dashed), the first-order transition line (solid), and the critical endpoint, adapted from [78]. Inset: Steps of the DMFT calculation [22]. (b) Local spectral density of states at $T = 0$ for several values of U [22]. The first four curves (from top to bottom, $U/W = 1, 2, 2.5, 3$) correspond to an increasingly correlated metal, while the bottom one ($U/W = 4$) is an insulator. W is an effective half-bandwidth.

Further breakthrough progress in the theory of the Mott MIT was made through calculations based on Dynamical Mean-Field Theory (DMFT) [22]. This theory considers a crystal containing many strongly interacting electrons. However, it simplifies the problem by focusing on a single lattice site while representing all other electrons in the crystal as an effective, dynamical mean-field environment (often referred to as a 'bath'). This approximation transforms the original lattice problem into a single-site impurity model coupled to the bath. The impurity model is solved iteratively: at each step, the bath parameters are adjusted so that the impurity's local properties precisely match those computed from the original lattice. This procedure is repeated until self-consistency is achieved, ensuring that the properties of the impurity and the lattice remain consistent (Fig. 2.7(a), inset).

DMFT has successfully described many observed features of the Mott transition, including its first-order character and the coexistence region where both metallic and insulating phases are present. This coexistence region can be understood as follows:

DMFT provides a mean-field solution for the insulating phase when $U > U_{c1}$ and for the metallic phase when $U < U_{c2}$, with $U_{c1}(T) < U_{c2}(T)$ at a given temperature T. Consequently, there exists a range of U values in which both metallic and insulating solutions are stable.

Additionally, the density of states of the strongly correlated metal is predicted [22, 79] to display a three-peak structure, made of a quasiparticle band close to the Fermi energy surrounded by lower and upper Hubbard bands (Fig. 2.7(b)). As the correlation strength increases, the system approaches the insulating state. The quasiparticle peak of the density of states narrows and eventually collapses at the critical value U_{c2} (Fig. 2.7(b)). The quasiparticle residue Z is also predicted to vanish as the system approaches U_{c2}, as shown in Fig. 2.8(a). Consequently, the effective mass m^* is expected to diverge at U_{c2}, where the Fermi liquid solution breaks down, signaling the transition to an insulating state. However, this divergence in effective mass may not be readily observed experimentally. The first-order nature of the transition causes most of the sample to occupy the insulating phase when U lies within the coexistence region between $U_{c1}(T)$ and $U_{c2}(T)$. As a result, the sample predominantly exhibits insulating behavior, making the region near $U_{c2}(T)$ - where the effective mass would diverge - effectively inaccessible to conventional experimental probes.

2.9 Influence of magnetic ordering

Magnetic ordering can significantly impact the mass enhancement in correlated electron systems. In this section, we present a theoretical prediction on how magnetic interactions affect the Mott MIT, a factor not captured by the single-site DMFT. Cluster DMFT (CDMFT) [80, 81] addresses this limitation by extending the analysis from a single lattice site to a 2×2 cluster on a square lattice.

It is predicted that incorporating magnetic ordering does not alter the first-order nature of the Mott transition, but significantly modifies the shape of the coexistence region and lowers the critical interaction strength U_c at the transition's endpoint. Within this coexistence region, a strongly incoherent anomalous metallic state is observed, exhibiting a scattering rate that violates the expected quadratic temperature dependence. This incoherent metallic phase suggests a breakdown of conventional Fermi liquid behavior.

The incoherence of this metallic state also prevents the evaluation of the quasiparticle residue Z at low temperatures near U_{c2}. However, in the normal metallic state (outside the coexistence region), Z exhibits an almost linear dependence on U, similar to the single-site DMFT results, as shown in Fig. 2.8(b). This trend, however, is interrupted by the coexistence region, where spatial coherence is lost before the effective mass of quasiparticles can diverge, leading to a cutoff in quasiparticle renormalization.

As CDMFT predicts a shift of the critical U_c to lower values due to magnetic interactions, the Mott MIT occurs at a higher Z and a lower effective mass [80–85]. To explore systems with lower Z, it is necessary to reduce the influence of magnetic interactions. This scenario can be realized in systems with increased spin frustration. In such systems, competing spin interactions prevent the system from undergoing magnetic ordering.

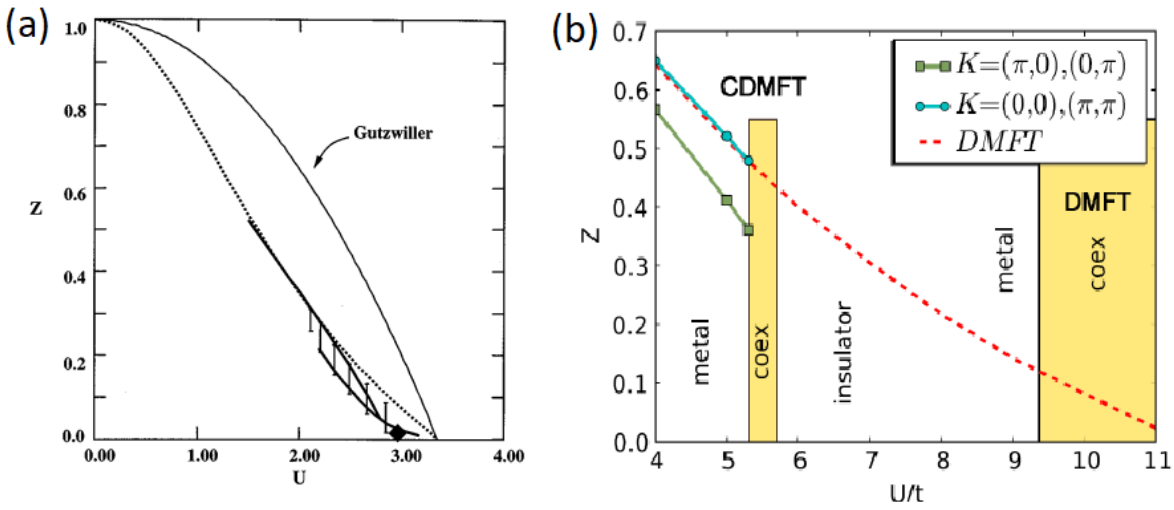

Figure 2.8: (a) The quasiparticle residue Z as a function of U, adapted from [22]. (b) The quasiparticle residue Z vs. U/t for different orbitals in CDMFT. Below the transition point, the $(0,0)$ and (π,π) orbitals exhibit a Z value nearly identical to that of single-site DMFT (dotted line), while quasiparticles in the $(\pi,0)$ orbital are more strongly renormalized, adapted from [80].

2.10 Anderson localization

The transition model described above is valid for a system with an ideal crystal lattice. However, in real crystals, impurities and lattice defects influence electronic transport, affect the scattering rate, and can also lead to localization. A model to investigate the impact of disorder on electronic correlations and the metal-insulator transition was proposed by Anderson in 1958 [23, 86]. In this model, impurities are assumed to be located at lattice sites, with each site possessing a distinct electron energy level, denoted by E_i, where i indexes individual lattice sites. This setup results in a system of periodically arranged potential wells with varying depths, as illustrated in Fig. 2.9(a). Anderson formulated the Hamiltonian for this system as a sum of two components: the hopping energy t and the sum of the energies of electrons localized at each isolated site E_i.

$$H = t \sum_{\langle i,j\rangle,\sigma} \left(c^{\dagger}_{i,\sigma} c_{j,\sigma} + c^{\dagger}_{j,\sigma} c_{i,\sigma} \right) + \sum_{i} E_i c^{\dagger}_{i,\sigma} c_{i,\sigma} \tag{2.31}$$

The effective magnitude of these site energies E_i is referred to as the disorder strength U_{dis}. In the Anderson model, the key dimensionless parameter is U_{dis}/t. Anderson's primary result, which has been extensively validated by subsequent research, can be summarized as follows:

- **Metallic phase at low disorder:** For small U_{dis}/t, the fraction of delocalized states spans nearly the entire energy band. In this regime, electrons can move freely, and the system behaves as a metal.

- **Critical disorder value:** There exists a critical value $(U_{\text{dis}}/t)_c$ at which the first localized states transition to delocalized states. At this point, these states can extend across the lattice, enabling limited conduction.

- **Anderson insulating phase at high disorder:** When U_{dis}/t is large, all electronic states become localized. Electrons are confined to specific regions in the lattice, preventing conduction, thereby resulting in an insulating behavior, known as an Anderson insulator. Unlike a Mott insulator (Fig. 2.9(b)), an Anderson insulator does not exhibit a gap (Fig. 2.9(a)). Instead, localization arises due to enhanced scattering.

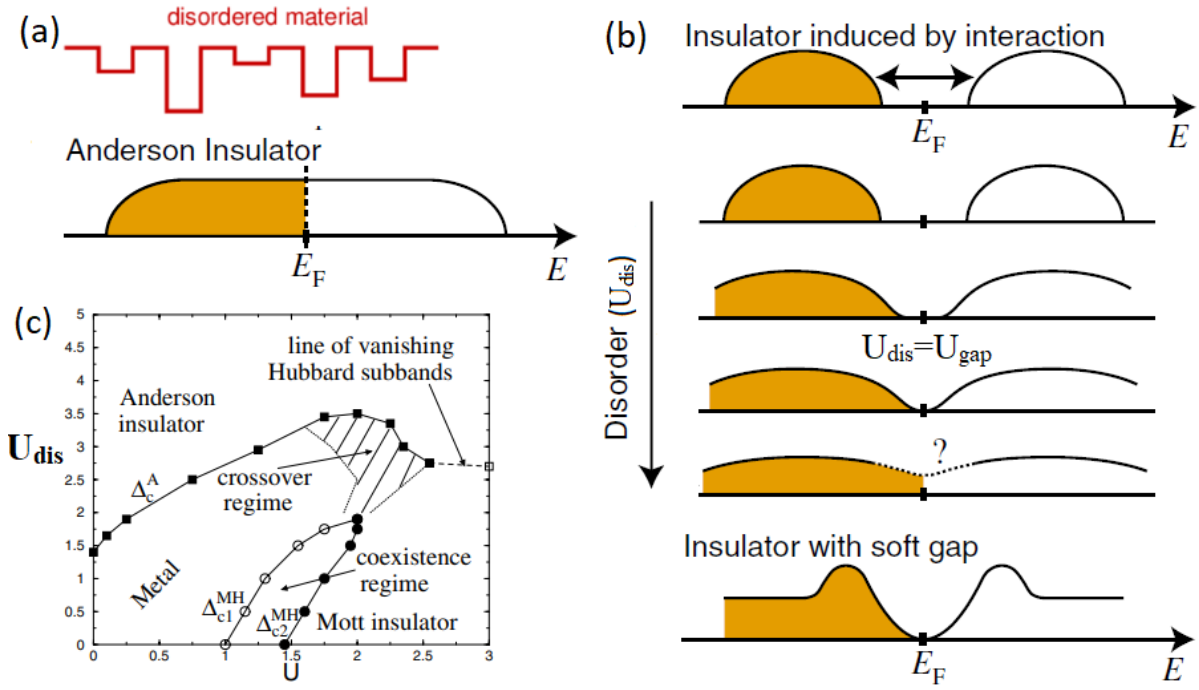

Figure 2.9: (a) Sketch of the potential landscape in the Anderson model and the schematic density of states in an Anderson insulator. (b) Schematic density of states in a Mott insulator, showing the effect of increasing disorder strength U_{dis}, which leads to an insulator with a soft gap [87]. (c) Nonmagnetic ground-state phase diagram of the Anderson-Hubbard model at half-filling, as calculated by DMFT, with the typical local density of states [88].

Further investigation using DMFT calculations [88] incorporates an additional term in the Hamiltonian related to the on-site Coulomb repulsion. As the disorder strength increases in a system with strong electronic correlations, the energy gap gradually vanishes (Fig. 2.9(b)) and eventually collapses at a critical disorder strength $U_{\text{dis}} \approx U_{\text{gap}}$. However, for disorder strengths exceeding this critical value ($U_{\text{dis}} > U_{\text{gap}}$), the density of states at the Fermi level remains zero, leading to the formation of a so-called soft Coulomb gap [87]. It is important to note that the soft Coulomb gap is not restricted to half-filling.

The phase diagram in Fig. 2.9(c) demonstrates that correlation strength and disorder can play opposing roles in determining the ground state. The Mott insulator, characterized by a correlation gap, is strictly defined only for $U_{\text{dis}} = 0$, while the gapless Anderson insulator is defined only for $U = 0$. Correlation strength can drive the system from an Anderson insulating state into a metallic state, just as disorder can drive the system from a Mott insulator to a metal. Consequently, a system exhibiting strong electronic correlations in the presence of finite disorder is referred to as a *disordered Mott insulator* [88]. In contrast, a system with moderate correlations that becomes increasingly disordered evolves into what is termed a *correlated Anderson insulator* (in this work, we will also refer to it as a *Mott-Anderson insulator*, using "Mott" to emphasize the role of electronic correlations). In the intermediate disorder and correlation crossover regime (Fig. 2.9(c), hatched area), the metallic and insulating phases cannot be rigorously distinguished. Furthermore, at high correlation and disorder strengths, the Mott and Anderson insulators are continuously connected. Thus, by varying U and U_{dis}, it is possible to transition between these two insulating phases without passing through a metallic state.

3 Organic κ-salts

In this thesis, the family of κ-type organic charge transfer salts, which are based on organic donor molecules, such as bis(ethylenedithio)tetrathiafulvalene (BEDT-TTF or ET), was investigated. The following sections provide an overview of their crystal structures, along with a detailed examination of their physical and electronic properties. Special attention is given to the distinctions between the studied materials, with an emphasis on their respective phase diagrams. Lastly, the impact of thermal history on their structural and electronic properties is analyzed and discussed. In this work we will investigate 4 salts: κ-(BEDT-TTF)$_2$Cu$_2$[N(CN)$_2$]Cl (κ-Cl), κ-(BEDT-TTF)$_2$Cu$_2$[N(CN)$_2$]Br (κ-Br), κ-(BEDT-TTF)$_2$Cu$_2$(CN)$_3$ (κ-CN), κ-(BEDT-TTF)$_2$Cu(NCS)$_2$ (κ-NCS).

3.1 Crystal structure

To understand the unique features of organic charge-transfer salts, it is essential to first examine their crystal structure. These crystals consist of alternating conducting and insulating layers (Fig. 3.1). The insulating layers are formed by a monovalent anion and do not contribute to conductivity because they lack electronic bands. However, the choice of anions significantly influences the physical properties of the resulting salts, as will be demonstrated.

Since the anion layers separate the conducting sheets, there is minimal overlap with electron orbitals perpendicular to the layers, resulting in weak interlayer conductivity. Consequently, these materials exhibit highly anisotropic electrical conductivity, classifying them as quasi-two-dimensional (q2D) conductors.

The conducting layers are composed of relatively flat organic molecules, as shown in Fig. 3.2. In the BEDT-TTF molecule, the central two carbon atoms, bonded to sulfur atoms, are connected by a double bond. Together with the sulfur atoms, these carbon atoms form rings where s- and p-orbitals hybridize to create σ- and π-molecular orbitals. The σ-orbitals, located in the molecular plane, provide structural stability, while the π-orbitals, oriented perpendicular to the plane, facilitate conductivity. The overlap of π-orbitals between neighboring molecules leads to the formation of delocalized electronic states, i.e., electronic bands, making the organic layers conductive.

The molecules in the conducting layers are oriented nearly perpendicular to the planes they form. The specific alignment of the molecules relative to one another determines their physical properties and defines distinct structural phases [35]. The most prominent of these phases are shown in Fig. 3.2(b). Among these, the κ-phase salts are the primary focus of this study.

The κ-phase is particularly noteworthy because neighboring BEDT-TTF molecules form dimers. Each dimer donates one electron to the monovalent anion, resulting in

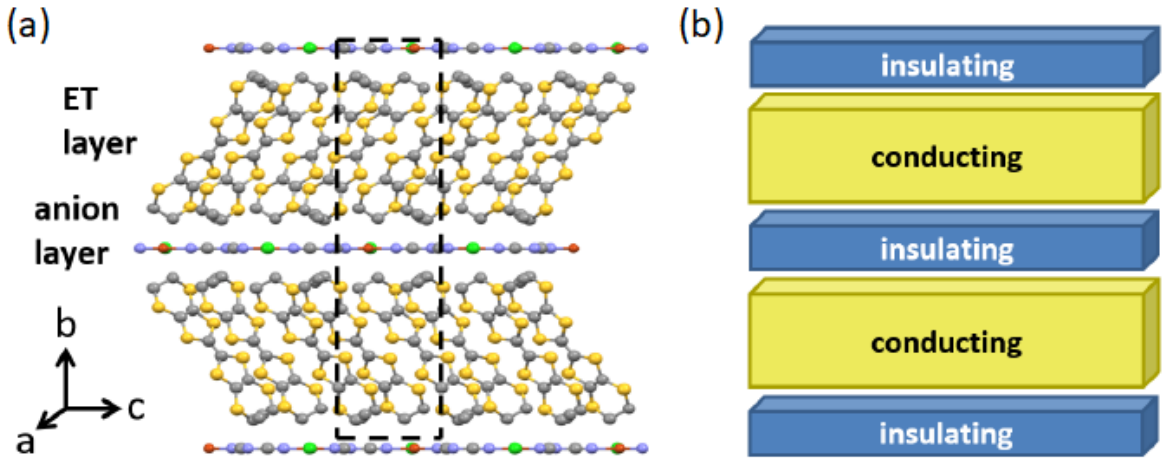

Figure 3.1: (a) Crystal structure of κ-Cl (according to the crystallographic data in [89]) with the unit cell indicated as dashed line. (b) Sketch of the general layered structure of κ-phase salts. The BEDT-TTF layers, which are parallel to the ac-plane, are highly conductive, whereas the anion layers in between are insulating [42].

the formation of a hole (charge carrier) in the conducting layer. For simplicity, we will refer to these charge carriers (holes) as electrons throughout the text. Two dimers form one unit cell, resulting in a total of two electrons per unit cell. Since there are two dimers per unit cell, there are also two molecular orbitals per unit cell - one from each dimer. These orbitals form two energy bands: a lower-energy band and a higher-energy band. Each band can accommodate two electrons per unit cell (one per spin direction), resulting in a total capacity of four electrons per unit cell. Therefore, the system is effectively half-filled with two electrons per unit cell. This half-filling condition is crucial for the emergence of the Mott insulating state [35].

The dimers form an anisotropic triangular lattice, with the unit cell parameters listed in Table 3.1 for the κ-salts discussed in this work. These parameters were measured un-

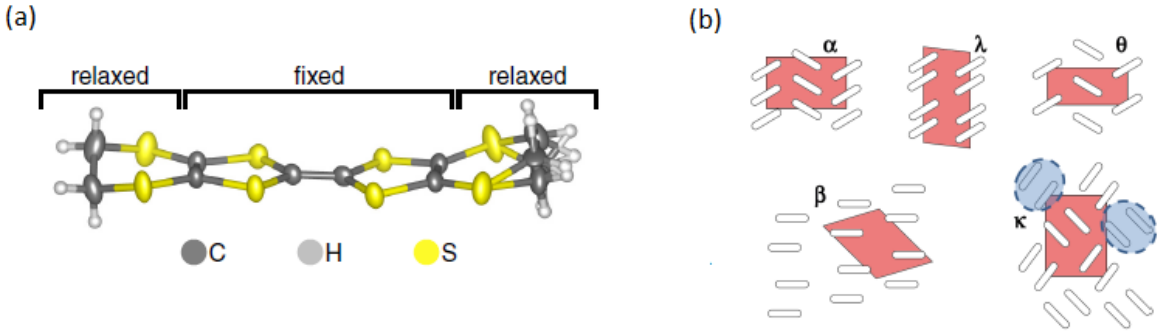

Figure 3.2: (a) Chemical structure of the BEDT-TTF molecule. (b) Schematic illustration of the molecular packing of BEDT-TTF molecules in the α-, β-, λ-, θ-, and κ-phases. The red shaded areas indicate the unit cells, while the blue ellipses highlight the dimerization of BEDT-TTF molecules in the κ-phase salts (adapted from [35]).

Salt	a [nm]	b [nm]	c [nm]	Angles	S_{BZ} [nm^{-2}]
κ-NCS	1.637	0.838	1.278	111.5°	36.82
κ-Br	1.287	2.949	0.847	90°	36.18
κ-Cl	1.287	2.943	0.838	90°	36.57
κ-CN	1.612	0.859	1.340	113.4°	34.27

Table 3.1: Unit cell parameters of κ-salts at low temperatures, compiled from [90–93]. The column labeled 'Angles' indicates the angle between the interlayer axis and the plane of the conducting layers. S_{BZ} denotes the area of the first Brillouin zone.

der ambient pressure and at low temperatures, as reported in [90–93]. For κ-Br and κ-Cl, the a and c axes correspond to the in-plane unit cell dimensions aligned with the conducting layers, while the b axis is oriented perpendicular to the layers. The crystal structure exhibits orthorhombic symmetry. This symmetry implies the presence of inversion symmetry in the lattice. The BEDT-TTF molecules are not perfectly perpendicular to the layers but are slightly tilted. This tilt alternates in opposite directions in neighboring layers (Fig. 3.1(a)). As a result, the unit cell dimension b includes the thickness of two layers. For κ-NCS and κ-CN, the b and c axes correspond to the unit cell dimensions within the conducting layers, while the a axis is oriented in the interlayer direction. In these salts, the BEDT-TTF molecules in adjacent layers are tilted in the same direction, and the unit cell contains only a single conducting layer. The crystal structure exhibits monoclinic symmetry, with the in-plane axes b and c being mutually perpendicular, while the interlayer axis a is tilted relative to the plane of the layers. The angle between the a-axis and the layers is provided in the 'Angles' column of Table 3.1.

3.2 Electronic band structure

The band structure calculations, performed using the extended Hückel method (EHC) based on a two-dimensional tight-binding approximation, predict the Fermi surface (FS) of κ-salts in the $k_x k_y$-plane to consist of two open sheets (red) and a closed pocket (blue), as shown in Fig. 3.3 [91, 94, 95]. Lately, first-principles calculations [96–99], based on density functional theory (DFT), confirmed the form of the FS. Both methods show that intradimer interaction does not significantly change with pressure or anion substitution [91, 100]. The main impact on the ground state formation is realized through changes in interdimer transfer integrals and anisotropy, as discussed in Sec. 3.5. Fig. 3.4 shows the band structure calculated by the EHC (a) and DFT (c) methods for κ-CN. The calculated FS was confirmed by quantum oscillation experiments [101–104].

The FS shape remains largely unchanged along the k_z-direction, exhibiting only a slight warping. For clarity, this warping is exaggerated in the illustration in Fig. 3.3(b). The quasi-two-dimensional nature of the FS not only simplifies the analysis compared to the often complex three-dimensional (3D) FSs but also enhances the strength of quantum oscillations. This feature enables the investigation of electronic properties,

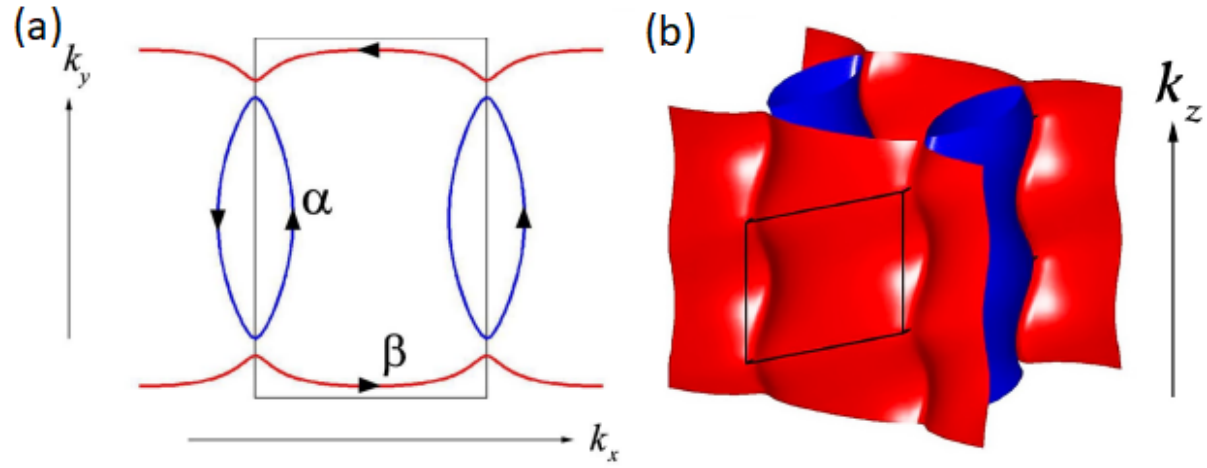

Figure 3.3: 2D (a) and 3D (b) Fermi surface of κ-NCS. The warping in k_z-direction is exaggerated for better visibility. Therefore, the FS can be considered to be quasi-two-dimensional, consisting of a closed pocket (blue) and two open sheets (red) [105].

such as the FS and the effective cyclotron mass, using moderate steady magnetic fields, although pulsed fields are required in some cases.

Quantum oscillation measurements reveal two fundamental frequencies. The first frequency is $F_\alpha \sim 500\,\mathrm{T}$ to $800\,\mathrm{T}$ [7, 106–108]. This frequency corresponds to a Fermi cylinder with a cross-sectional area of approximately 15 % to 20 % of the first Brillouin zone (BZ), attributed to the α-orbit (Fig. 3.3(a), blue lines). This result is in good agreement with theoretical calculations.

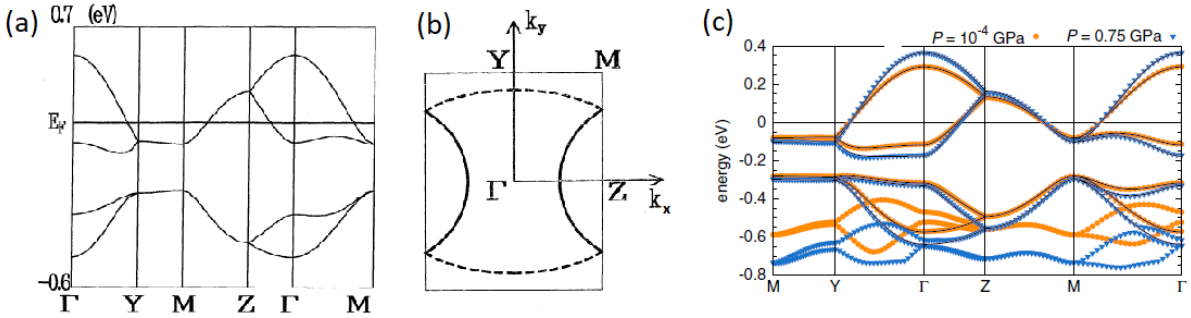

Figure 3.4: The energy dispersion (a) and the FS (b) of κ-CN from [91], calculated with EHC method. (c) DFT band structure of κ-CN at ambient pressure and at pressure 0.75 GPa from [96].

The second frequency is related with the magnetic breakdown regime (Sec. 2.3), where electrons can tunnel between different parts of the FS, leading to oscillations with a frequency of approximately $F_\beta \sim 4\,\mathrm{kT}$. This frequency corresponds to the area of the entire first Brillouin zone [90, 92] and is attributed to the β-orbit (Fig. 3.3(a), includes both blue and red lines).

The presence of inversion symmetry in κ-Cl and κ-Br, in contrast to its absence in κ-NCS and κ-CN, leads to a degeneracy of the conducting bands at the Brillouin zone boundary. As a result, the interband gap is expected to vanish. Consequently, the

quantum oscillations in these materials should correspond to the complete magnetic breakdown regime, wherein only the large β-orbit is realized. Indeed, the frequency F_β dominates the oscillation spectrum in both κ-Cl and κ-Br [102, 103]. However, the presence of the frequency F_α has also been experimentally detected in these compounds [102, 109], indicating that a finite interband gap exists ($\Delta_{MB} \approx 1.6\,\text{meV}$ [110]), although it is significantly smaller than that in the κ-NCS salt ($\Delta_{MB} \approx 4.3\,\text{meV}$ [111]).

3.3 Phase diagram

Salts with different anions exhibit various dimer sizes and arrangement within the layers. These variations in dimer positioning result in distinct ground states. The ground state can be fully metallic or superconducting (e.g., κ-NCS, κ-Br), or insulating (e.g., κ-Cl, κ-CN) [94, 112–114]. In the insulating state, depending on the spin configuration, the system may exhibit either antiferromagnetic ordering (κ-Cl) or no magnetic ordering (κ-CN). The phase diagrams for κ-Cl and κ-CN from [115] are shown in Fig. 3.5. The ground state of κ-CN is not yet fully understood, but the most likely candidates are the quantum spin liquid (QSL) and valence bond solid (VBS) states [116–122]. These states will be described in more detail in Sec. 3.6 dedicated to investigating κ-CN.

The application of pressure reduces the interdimer distances, thereby increasing the bandwidth and eventually driving the compound into a metallic state. A coexistence

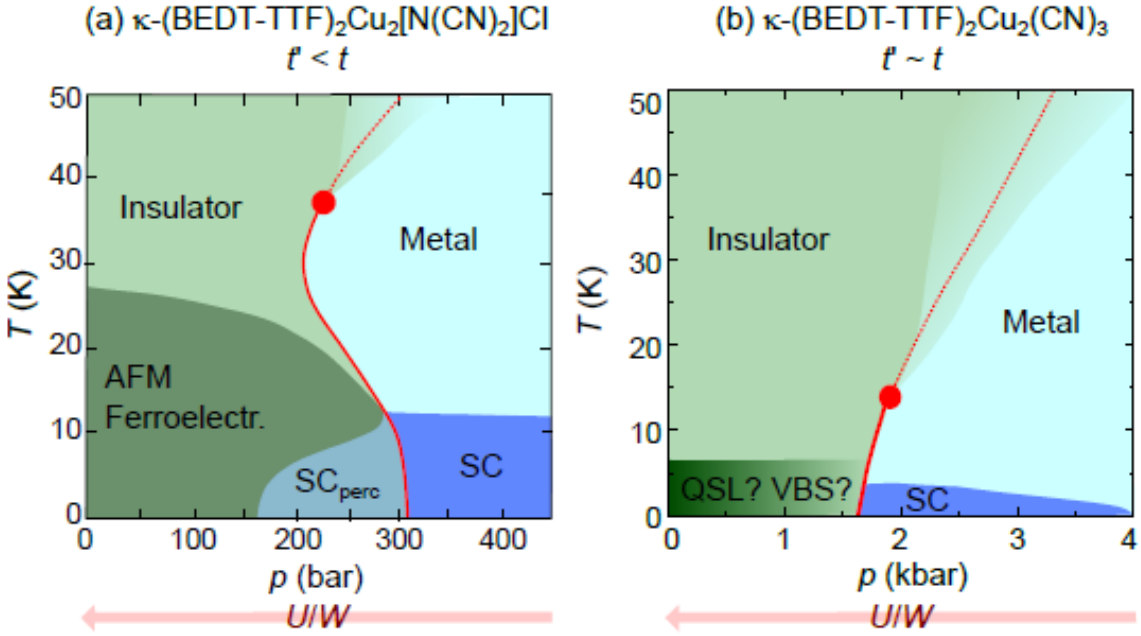

Figure 3.5: Experimental temperature-pressure phase diagrams of κ-phase charge-transfer salts: κ-Cl (a) and κ-CN (b) from [115]. At ambient pressure and low temperatures, both compounds exhibit a Mott insulating ground state. Upon applying pressure, a first-order Mott metal-insulator transition is induced. On the metallic side of the Mott transition, both compounds exhibit superconductivity.

region emerges between the metallic and insulating phases, in which the material contains spatially separated clusters of both metallic and insulating phases. Electrical conduction in this regime is facilitated by percolation through the metallic clusters, enabling the bulk sample to exhibit metallic behavior. It is worth noting that, due to their high compressibility, organic salts exhibit significantly lower critical pressures for the Mott transition (on the order of $\sim$ 0.1 GPa), compared to inorganic materials, which typically require higher pressures [123, 124].

3.4 Anion substitution effect

Changes in the anion have a pronounced impact on the unit cell parameters [125]. As a result, chemical substitution of the anion is often considered to mimic the effects of external pressure and is thus commonly referred to as a form of 'chemical pressure'. For example, κ-Cl is an insulator, whereas the isostructural κ-Br is a metal. This concept allows each anion substitution to correspond to a certain 'ambient' pressure, enabling all such compounds to be placed on a unified phase diagram (Fig. 3.6(a)). However, there is also an alternative perspective that anion substitution affects the ground state by modifying the anisotropy of the dimer triangular lattice [100]. In this case, anion substitution acts differently from pressure application, meaning that placing all salts on the same phase diagram is not always valid. In both cases, we emphasize that since these anions are monovalent, they do not dope the organic layer away from half-filling, making this an isoelectronic substitution.

Another form of 'chemical pressure' is achieved through deuteration in the organic conducting layer. Each BEDT-TTF molecule contains eight hydrogen atoms (Fig.3.2(a)), which can be substituted with deuterium atoms. This substitution can shift the compound closer to the insulating state. For example, the fully hydrogenated κ-Br has a metallic ground state at ambient pressure, while fully deuterated κ-Br is located in the coexistence region on the phase diagram (Fig.3.6(a)). By varying the concentration of deuterated atoms, it is possible to finely tune the position of the compound on the phase diagram (Fig. 3.6(b)). This variation can be achieved either by adjusting the concentration of fully deuterated BEDT-TTF molecules [126] or by selectively incorporating deuterium atoms at specific positions within the BEDT-TTF molecule [127]. Both methods influence the compound in a similar way. This shift on the phase diagram is attributed to the so-called (negative) 'chemical pressure' effect. One possible explanation is that it arises from the slight difference in C-H and C-D bond lengths [126].

3.5 Electronic ground state formation

Let's now discuss in more detail the mechanism of the ground state formation. As was discussed above, each dimer has one charge carrier (hole) which is influenced by strong on-site Coulomb repulsion U for a double occupancy. Additionally, due to the hybridization of the neighboring dimers, electrons have a non-zero transfer integral t, which allows hopping between adjacent dimers (Fig. 3.7(a)). When the on-site Coulomb repulsion is strong, electrons tend to remain on their dimers without hop-

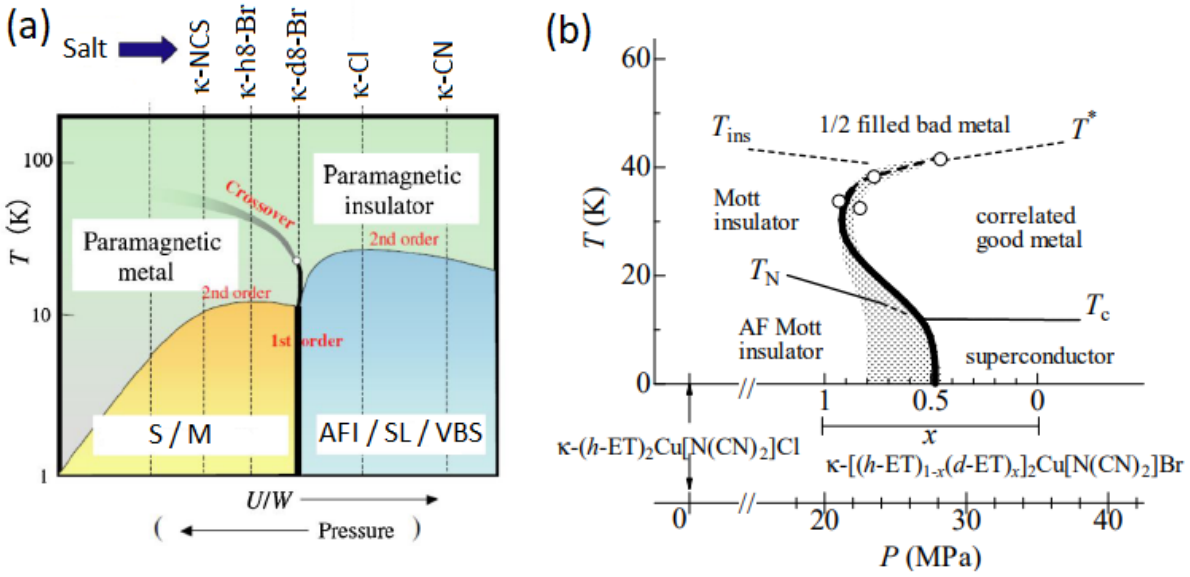

Figure 3.6: (a) Generic phase diagram of κ-salts as a function of hydrostatic pressure, with increasing pressure from right to left and correlation strength (U/t) increasing from left to right [29]. The dashed lines indicate the ambient-pressure positions for different salts. (b) Phase diagram of κ-Cl and κ-Br. Horizontal axis represents the substitution ratio x in κ-h$_x$-d$_{1-x}$-Br, and the corresponding pressure for κ-Cl in the slowly cooled condition [126].

ping, leading to the formation of an insulating state. In contrast, when the hopping integral is stronger, the particles can move between dimers, resulting in a metallic state. The ratio between the on-site Coulomb repulsion and the hopping integral, U/t, is referred to as the correlation strength ratio. This ratio is a key parameter in determining the formation of the system's ground state [35, 125, 128–130]. An increase in correlation strength pushes the system closer to an insulating state [30, 125, 131, 132].

During the formation of the insulating state, the spin ordering depends on the spin interactions between the electrons and the anisotropy of the triangular lattice. The anisotropy of the system is determined by the geometrical frustration ratio (t'/t), which compares the transfer integrals between the nearest neighbors, t, and the next-nearest neighbors, t' (Fig. 3.7(a)). If the system has an anisotropic triangular lattice, the neighboring electrons adopt opposite spin orientations, resulting in an antiferromagnetic insulating state [133–136]. However, if the system has an isotropic triangular lattice of spins with $t'/t = 1$, the spin ordering becomes more complicated, and several different spin configurations are possible. In the classical case, the most stable is the 120° Néel order configuration with non-collinear spins and long-range magnetic ordering (Fig.3.7(b)). In the quantum limit, for spin $S = 1/2$, quantum fluctuations can destabilize magnetic order, potentially leading to spin-liquid or valence bond solid states (Fig. 3.7(b)) [116, 117]. While the formation of a VBS state has been established in some materials [137], the realization of a QSL remains under debate due to the lack of definitive experimental evidence.

According to calculations [96], applying pressure compresses the compound, moving dimers closer to each other and increasing the transfer integral t, while leaving U

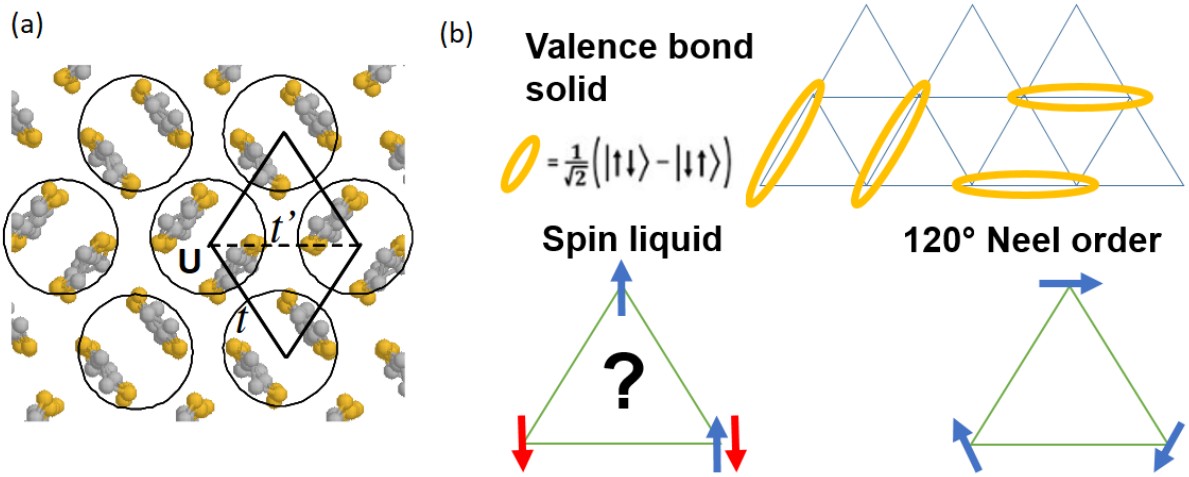

Figure 3.7: (a) Schematic representation of the dimers, correlation strength U, nearest neighbor tansfer integral t and next-nearest neighbor tansfer integral t'. (b) Schematic representation of spin configurations for the 120° Néel order, spin liquid, and valence bond solid states.

almost unchanged. This leads to a decreased correlation strength ratio U/t, shifting the compound on the phase diagram toward the metallic state. Meanwhile, the frustration ratio t'/t is believed to be largely independent of pressure [96].

Table 3.2 presents values of correlation strength and frustration ratios for different salts at ambient pressure obtained from model calculations [96]. According to these calculations, κ-Cl has a lower U/t ratio than κ-NCS, suggesting that κ-Cl should be more metallic. However, experimental measurements reveal that κ-Cl exhibits an antiferromagnetic insulating state, while κ-NCS is metallic (Fig. 3.6(a)). Moreover, κ-Br also exhibits a metallic state, despite having a smaller U/t ratio than κ-Cl. This discrepancy suggests that either the calculation methods are inaccurate or the ground state formation is governed by a more complex interplay between the correlation strength and the frustration ratio. κ-CN has the highest correlation strength, correlating with the higher critical pressure experimentally observed. Additionally, the high frustration ratio of κ-CN leads to the absence of magnetic ordering, which has also been confirmed experimentally [30, 116, 117].

To validate the calculated values, one should compare them with experimental data. S. Oberbauer conducted a comparative measurement of κ-Cl and κ-NCS near MIT during his Master's thesis [42]. The samples were measured simultaneously at low pressures (< 0.2 GPa), and the results indicate similar effective masses in the metallic state

	κ-NCS	κ-Cl	κ-Br	κ-CN
Correlation strength U/t	6.0	5.5	5.1	7.3
Frustration ratio t'/t	0.58	0.44	0.42	0.83

Table 3.2: Calculated correlation strength and frustration ratios at ambient pressure for different κ-salts from [96].

for both salts. This suggests comparable renormalization effects [110], although it does not provide unequivocal proof. This finding contradicts theoretical calculations and raises the question of why salts with comparable correlation strengths exhibit different ground states. One possible explanation involves the influence of the frustration ratio on the ground state, as was proposed in [100], that anisotropy and the degree of frustration play a significant role in determining the nature of the ground state. Furthermore, the experiment revealed that the correlation strength is an order of magnitude more sensitive to the applied pressure than predicted in [96]. Resolving these discrepancies requires a more in-depth investigation, particularly by comparing salts with different ground states and measurements in a wider pressure range. Addressing this issue is one of the objectives of this thesis.

3.6 Magnetotransport and phase diagram of κ-CN

The organic compound κ-CN is one of the earliest candidates proposed for a spin-liquid state [116, 138–140]. At the same time, most of organic Mott insulators exhibit antiferromagnetic ordering [141, 142], while κ-CN is predicted to possess a nearly ideal triangular lattice and shows no signs of antiferromagnetic transition down to temperatures as low as 32 mK [116, 143, 144]. It was widely considered to host a gapless quantum spin-liquid state for nearly two decades. However, recent electron spin resonance measurements revealed the presence of a spin gap opening at 6 K [117, 145]. In this state, neighboring spins form singlet pairs (Fig. 3.7(b)), described by the quantum-mechanical state $(|\uparrow\downarrow\rangle - |\downarrow\uparrow\rangle)/\sqrt{2}$, with a total spin $S = 0$. Despite extensive investigations, the exact nature of the ground state - whether quantum spin-liquid or valence bond liquid - remains unresolved.

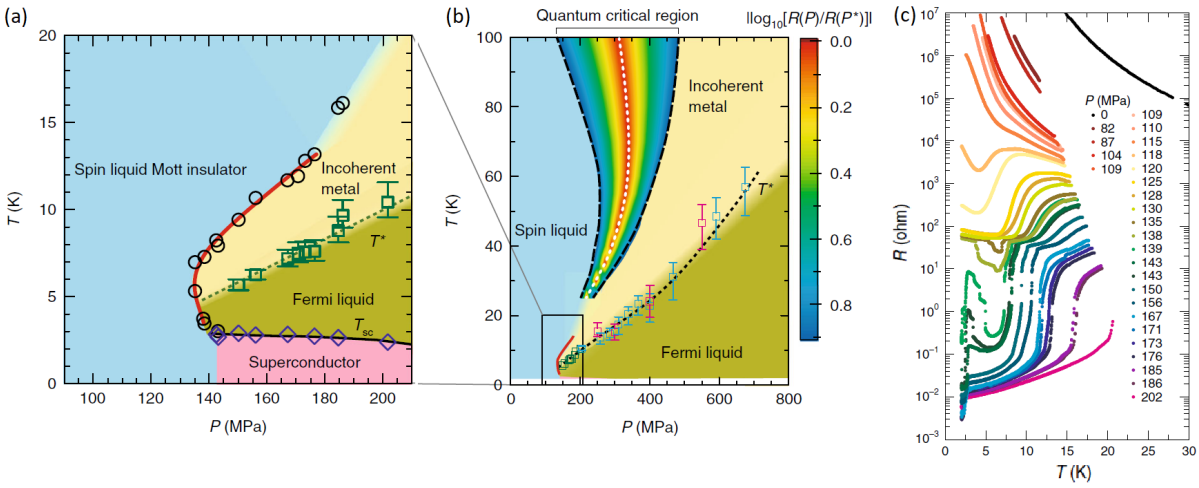

Figure 3.8: Pressure-temperature phase diagram of κ-CN at low temperatures near the Mott transition (a) and over a broader temperature-pressure range (b), adapted from [69]. (c) Temperature dependence of the resistance at various pressures, showing a pronounced upturn near the critical pressure, indicative of a first-order Mott MIT [69].

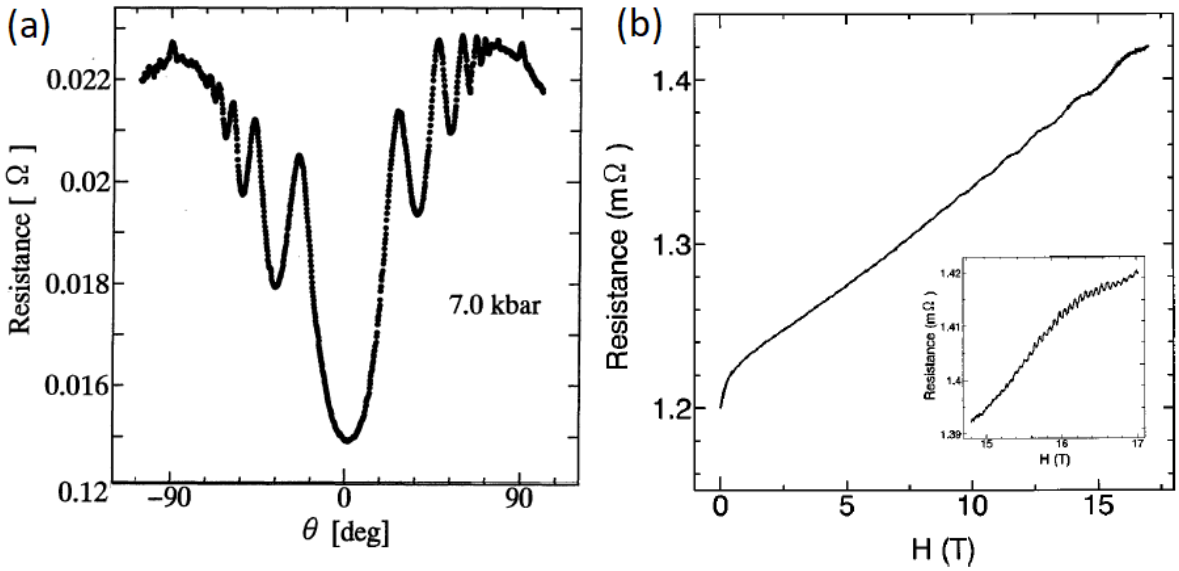

Figure 3.9: (a) Angle θ dependence of the magnetoresistance for κ-CN under pressures of 0.7 GPa and $T = 1.4$ K in a magnetic field of 15 T, adapted from [52]. (b) In-plane magnetoresistance of κ-CN at 1.5 K under 0.7 GPa. The magnetic field was applied perpendicular to the conducting plane [104].

Numerous studies have explored the behavior of κ-CN over a wide range of temperatures and pressures, contributing to the construction of its phase diagram. At ambient pressure, κ-CN resides in a Mott insulating state [69], which is suppressed under applied pressure, giving way to a metallic phase at a critical pressure $p_c \approx 0.13$ GPa (Fig. 3.8(a), (b)). In a narrow pressure window around 0.13 GPa to 0.14 GPa, close to p_c, the resistance of the compound exhibits a pronounced upturn upon cooling (Fig. 3.8(c)), indicating a metal-insulator phase coexistence within the first-order Mott metal-insulator transition.

Despite extensive transport studies of κ-CN, the investigation of its magnetoresistive properties remains challenging due to its low residual resistance, small sample size, and the low amplitude of magnetic quantum oscillations. To date, only a single study has focused on the magnetoresistance and SdH oscillations of this compound. Ohmichi et al. measured angle-dependent magnetoresistance oscillations (AMRO) [52] (Fig. 3.9(a)) and Shubnikov-de Haas (SdH) oscillations [104] (Fig. 3.9(b)) at a pressure of 0.76 GPa. They reported SdH oscillations with a frequency of approximately 3780 T, a value comparable to the MB β-orbit observed in other κ-salts. The measured effective cyclotron mass was about $4m_0$.

These findings, together with the higher calculated correlation strength and frustration ratios [96], underline the uniqueness of κ-CN and emphasize its potential for further in-depth exploration. However, the reported magnetoresistance was only on the order of milliohms, and the relative amplitude of the SdH oscillations was less than 0.2 % (Fig. 3.9(b), inset), placing the signal near the noise threshold. These limitations significantly hinder a detailed investigation. In this work, we aim to overcome these challenges and enable a more comprehensive study of the magnetic and electronic properties of κ-CN.

3.7 Thermal history and glasslike structural ordering

In addition to the above-mentioned correlation strength and spin frustration, another degree of freedom influences the formation of the ground state. It is related to the geometrical structure of the BEDT-TTF molecule. There are two possible orientations of the ethylene end groups (EEG) relative to each other (Fig. 3.10(a) inset). The conformation in which the C-C bonds of the EEG are parallel and lie in the same plane is referred to as the *eclipsed* (E) state. In contrast, the conformation in which these bonds are oriented at an angle with respect to each other is known as the *staggered* (S) state. The equilibrium occupation probability of each conformation depends on both temperature and the specific salt [126, 127, 146, 147]. In the case of κ-Cl and κ-Br, the E conformation is stable at low temperatures, whereas the S conformation is metastable. In contrast, for κ-CN, the S conformation is the energetically favored state at low temperatures [148].

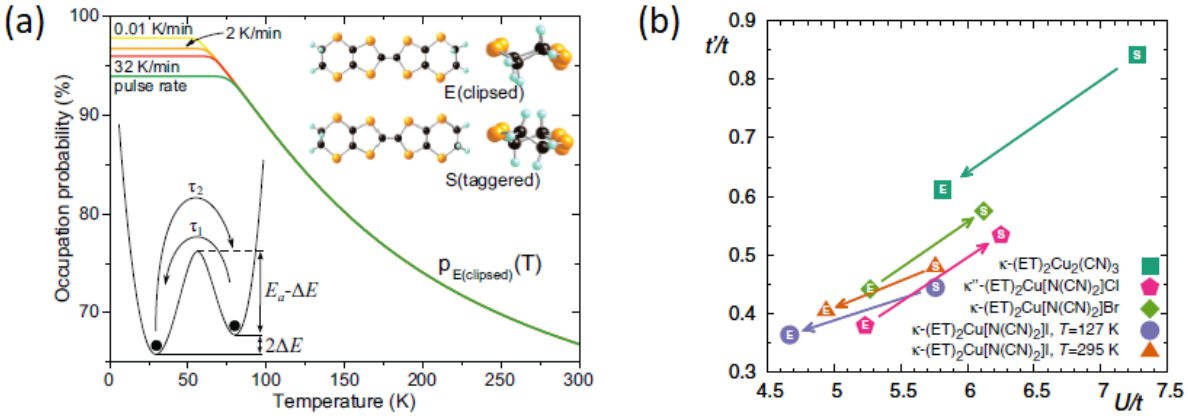

Figure 3.10: (a) Temperature-dependent occupation probability $p_E(T)$ of the favored eclipsed conformation of the ethylene end groups in BEDT-TTF molecules, calculated using the general model of Eq. (3.1) for different cooling rates [149]. Insets: Schematic double-well potential representing the staggered and eclipsed conformations, showing the energy difference ΔE and activation barrier E_a (left), and the molecular structures corresponding to E and S conformations (right). (b) Values of the model parameters t'/t and U/t in the effective dimer model for the E and S conformations, taken from [148]. The arrows indicate the direction of parameter changes when transitioning from the low-energy (E) to the high-energy (S) configuration of the EEG.

To describe this system, we can consider it as a two-level system, with an energy difference between the ground and excited states ($2\Delta E$) and a potential barrier (E_a) (Fig. 3.10(a) inset) [149]. The equilibrium occupation probability at different temperatures is given by the Boltzmann distribution as

$$p_E^{\infty}(T) = \frac{1}{1 + \exp\left(-2\Delta E / k_B T\right)}. \tag{3.1}$$

The occupation probability from this equation, calculated by [149], is shown in Fig. 3.10(a). We observe an increase in the equilibrium occupation probability of the

E conformation as temperature decreases. However, due to the energy barrier E_a between the conformations, the system requires time to relax into the new equilibrium state. This relaxation occurs with an effective relaxation time given by [149]

$$\tau_{\text{eff}}(T) = \nu_0^{-1} \exp\left(\frac{E_a}{k_B T}\right)\left(\exp\left(\frac{\Delta E}{k_B T}\right) + \exp\left(-\frac{\Delta E}{k_B T}\right)\right)^{-1}. \tag{3.2}$$

As the temperature decreases, the relaxation time increases exponentially, meaning that relaxation to the equilibrium conformation becomes significantly slower. Consequently, the system can be cooled down while maintaining a frozen nonequilibrium conformation, leading to the occurrence of the so-called glass transition [150–152]. For a moderate cooling rate (2 K/min), the glass transition temperature can be approximated as the temperature at which the effective relaxation time is ~ 100 s. Experimentally, a glass transition temperature T_g close to 75 K to 80 K has been observed for κ-Br and κ-Cl, while no effect of glass transition has been detected for κ-NCS and κ-CN [149, 153–156]. Therefore, further discussion will be focused on these two salts, with a greater emphasis on κ-Br, as the effect is more pronounced in this compound.

According to the band-structure calculations by Guterding [148], the ground state of the EEG depends on the anion. For κ-Cl and κ-Br, the eclipsed state is the ground state, with an energy difference between the staggered and eclipsed states of 72 meV for κ-Cl and 110 meV for κ-Br. Moreover, the EEG conformation is predicted to significantly influence the correlation strength and frustration. Fig. 3.10(b) shows the electronic parameters for salts in different EEG conformations from [148]. For κ-Br, the calculated correlation strength changes from approximately 5.25 in the pure eclipsed state to 6.15 in the pure staggered state, while the frustration ratio changes from 0.44 to 0.56. In a real state, with a mix of conformations, the electronic properties were suggested to be estimated by proportionally averaging over the conformations with different electronic states. Since the metastable S conformation has a higher correlation strength, increasing the occupation probability of this conformation was predicted to enhance the overall correlation strength of the system and shift it closer to the MIT. Based on the results of model calculations [148], we estimate that an increase of 1 % in p_S raises the correlation strength by $\Delta\,(U/t) \approx 0.009$, or by approximately 0.2 % from its initial value.

In [149], Hartmann et al. proposed a method for estimating the frozen nonequilibrium conformation during cooling at a constant rate q. The authors introduced a time-dependent occupation probability, $p_E(t)$, to describe the system's relaxation after quench-cooling from T_0 to T_1. If, instead of an abrupt change from T_0 to T_1, the temperature decreases continuously with a cooling rate $q = dT/dt$, the temperature-dependent relaxation can be expressed through a differential equation as

$$\frac{dp_E(t)}{dT} = \frac{p_E^{\infty}(T) - p_E(T)}{q\,\tau_{\text{eff}}(T)}. \tag{3.3}$$

The numerical evaluation of this equation for different cooling rates was performed using the following parameters: an energy barrier $E_a/k_B = 2650$ K [149, 157], an energy difference $\Delta E/k_B = 105 \pm 5$ K, and an attempt frequency $\nu_0 = 10^{16\pm3}$ [158]. The results are presented in Fig. 3.10(a). Curves with different colors correspond to different cooling rates. The frozen occupation probability of the nonequilibrium S conformation, $p_S = 1 - p_E$, remains relatively small across a wide range of cooling rates. The

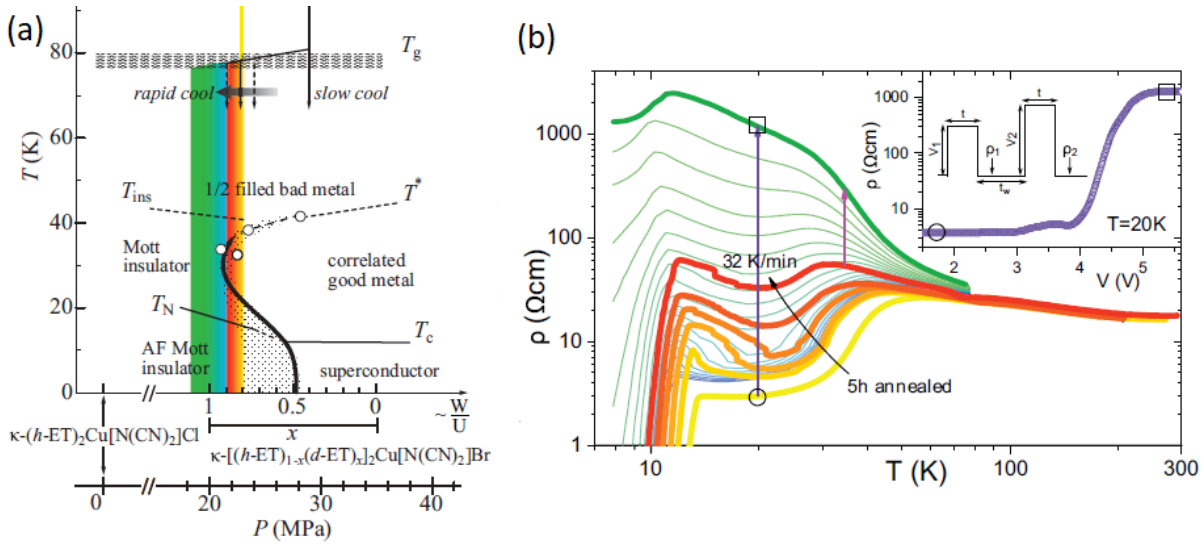

Figure 3.11: (a) Phase diagram of κ-(BEDT-TTF)$_2$X, from [149]. The horizontal axis represents the substitution ratio x for κ-[(h-BEDT-TTF)$_{1-x}$ (d-BEDT-TTF)$_x$]$_2$Cu[N(CN)$_2$]Br, and the corresponding hydrostatic pressure for κ-Cl. (b) Temperature dependence of the resistivity, ρ vs T , of κ-[(h-BEDT-TTF)$_{0.2}$(d-BEDT-TTF)$_{0.8}$]$_2$Cu[N(CN)$_2$]Br for cooling rates ranging from 5-h annealing at 75 K (yellow) to q = 1, 2, 5, 10, and 32 K/min (red). Vertical arrows indicate the possibility of reaching an insulating state (thick green line) after applying a voltage pulse.

occupation probabilities for the E and S conformations are shown in Table 3.3. Even at the highest pulse rate, p_S increases by only 4 % compared to the slow-cooled state (0.01 K/min) (see p_E at low temperatures in Fig. 3.10(b)). This increase in p_S significantly increases the resistance of the samples. Fig. 3.11(b) shows the resistance of partially deuterated κ-Br samples after different thermal treatments [149]. Differently colored curves correspond to different cooling rates. We observe that fast cooling shifts the system closer to the MIT and the insulating state. Fig. 3.11(a) presents the phase diagram of the compound. The curves in Fig. 3.11(b) are color-matched to the phase diagram. Green represents the insulating state, while yellow corresponds to the metallic/-coexistence state. Additionally, the phase diagram includes the corresponding deuteration rate and pressure to illustrate their relationship.

Although the resulting difference in the occupation probabilities of the nonequilibrium S conformation in states with different thermal histories is small (see Table 3.3), it can have a significant impact on the compound's ground state due to its essential influ-

q (K/min)	0.01	2	32	1000 (pulse rate)
p_E (%)	97.8	96.8	96.0	94.0
p_S (%)	2.2	3.2	4.0	6.0

Table 3.3: Occupation probabilities of the S and E conformations after cooling with different rates [149].

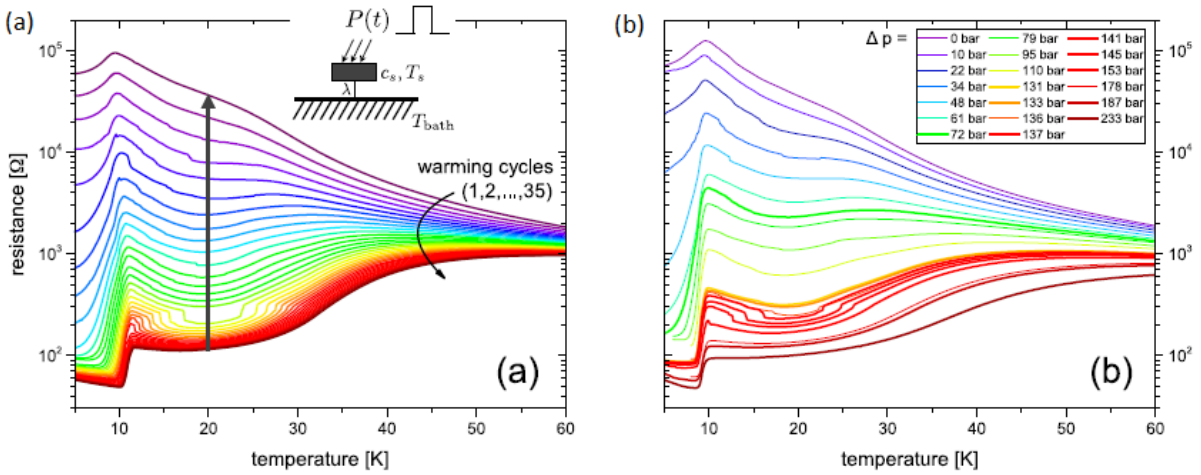

Figure 3.12: (a) Resistance (3-wire) as a function of temperature for different 'warming cycles' from [159]. The high-resistance state (vertical arrow) was prepared by applying a heat pulse. The lower-resistance curves have been created by relaxing the sample at $T = 70\,\mathrm{K}$ for $\Delta t = 120\,\mathrm{s}$. (b) R vs. T for different pressures for the same sample. The initial insulating state is prepared as in (a). Lower-resistance curves have been created by applying hydrostatic (He-gas) pressure.

ence on the correlation strength and the fact that κ-Br is located near the MIT at ambient pressure. In [159], a comparative study of the effects of the thermal treatment and pressure on the low-temperature state of κ-Br was reported. Fig. 3.12(a) shows $R(T)$ curves for different thermal histories. The high-resistance states were prepared by a heat pulse (quench), while the low-resistance curves were obtained after relaxation (annealing) near the glass transition temperature. The low-temperature resistance between different states varies by three orders of magnitude. Fig. 3.12(b) presents $R(T)$ curves under different applied pressures. The initial ambient pressure state is similar to the strongest-quenched state in Fig. 3.12(a). Hydrostatic pressure was then applied to compensate for the resistance increase caused by the heat pulse and to achieve a state similar to the annealed one. A comparison of the figures reveals that the difference between the annealed and quenched states is equivalent to an effective pressure difference of approximately $\Delta p \approx 20\,\mathrm{MPa}$. Therefore, this additional nonequilibrium conformation effect can be considered as a form of 'negative pressure'. Another possible scenario [160, 161] is that the nonequilibrium conformation acts as a source of disorder, increasing resistance by enhancing the scattering rate. However, it should be noted that resistance comparisons near the MIT may be imprecise, as the interplay between correlation strength and disorder is not yet fully understood.

3.8 Influence of X-ray irradiation

In the previous section, we discussed the influence of the EEG conformations on the electronic state. One possible mechanism for this influence is through acting as a disorder and increasing scattering. Another method of disorder enhancement can be

achieved through X-ray irradiation of samples. The impact of disorder on the ground state formation was discussed in Sec. 2.10. There, we introduced the disorder strength U_{dis}, which serves as a potential barrier and increases scattering. When U_{dis} is strong enough, it can lead to the clusterization of the bulk sample. The critical value of the disorder strength depends on the lattice type, dimensionality, and hopping parameters. However, various theoretical calculations yield a value on the order of $U^c_{\text{dis}} \sim 10t$, where t is the nearest-neighbor transfer integral [24, 87, 162]. Another method to induce clusterization is not by increasing U_{dis} itself, but by increasing the concentration of scattering centers. This scenario also results in a phase separation into conducting and localized regions.

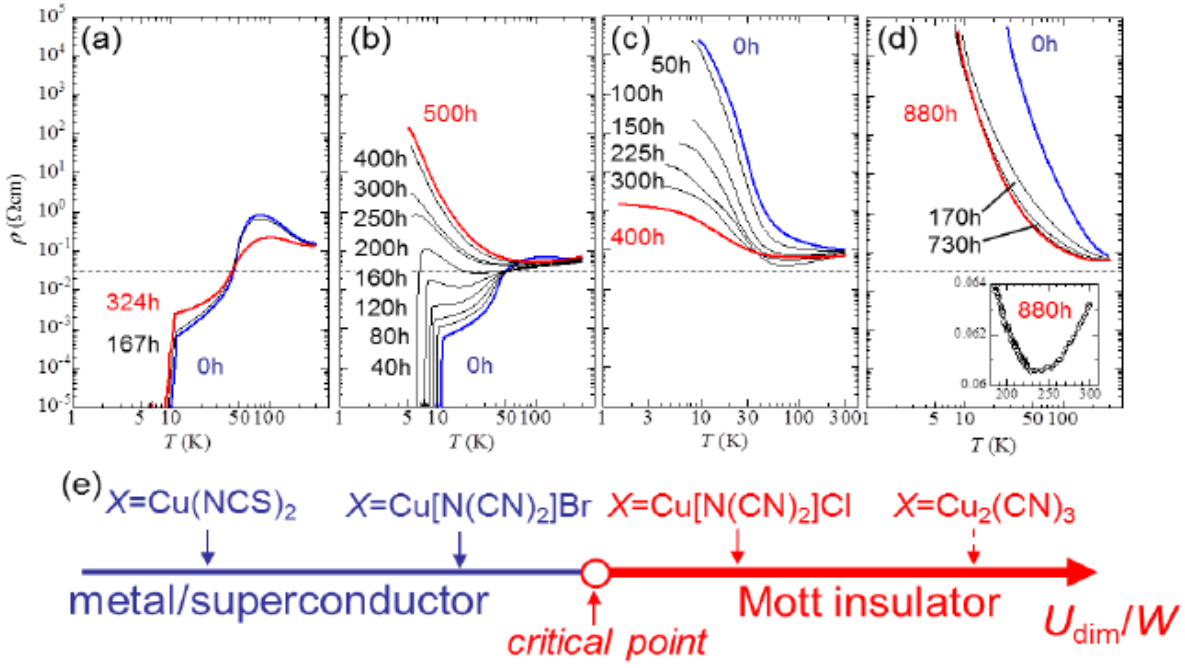

Figure 3.13: Temperature dependence of the resistivity of κ-(BEDT-TTF)$_2$X, (a) X = Cu(NCS)$_2$; (b) Cu[N(CN)$_2$]Br; (c) Cu[N(CN)$_2$]Cl and (d) Cu$_2$(CN)$_3$ irradiated by X-ray from [161]. The time indicated in each figure is the total X-ray exposure time at room temperature. (e) Schematic phase diagram in κ-(BEDT-TTF)$_2$X for $U_{\text{dim}}/W \sim U/t$.

As the concentration of disorder increases further, these localized regions expand, and conducting pathways become increasingly disrupted. Eventually, this percolative transition results in an insulating behavior as the localized clusters dominate, preventing electron transport across the sample. This scenario reflects a transition from a mixed metallic-insulating state to a fully insulating state driven by the concentration of disorder, rather than the disorder strength. This process was experimentally investigated in κ-salts in-plane resistivity using X-ray irradiation, which serves as a source of disorder without changing the bandwidth. Fig. 3.13 shows $\rho(T)$ curves for different κ-salts after various irradiation duration from [161].

The influence of irradiation differs depending on the compound. Initially, in κ-NCS and κ-Br (before irradiation), the resistivity exhibits distinct features: a broad resistivity hump around 100 K, a crossover at $T^* \sim 50$ K from a poorly metallic to a well-defined

metallic state at low temperatures (where resistivity follows $\rho(T) = \rho_0 + AT^2$), and a superconducting transition at $T_c \approx 10\,\mathrm{K}$.

However, X-ray irradiation drastically alters the resistive behavior. In the κ-NCS sample (Fig. 3.13(a)), irradiation suppresses the characteristic resistivity hump around 100 K, and the $\rho(T)$ curves intersect at a single point around $T \approx 50\,\mathrm{K}$. In the case of κ-Br (Fig. 3.13(b)), even a low irradiation dose significantly changes the temperature dependence of resistivity. The 100 K resistivity hump is completely suppressed, and the residual resistivity ρ_0 rapidly increases with irradiation time. When $t_{\mathrm{irr}} > 250\,\mathrm{h}$, the $\rho(T)$ curves exhibit insulating behavior at low temperatures. After extended irradiation ($t_{\mathrm{irr}} = 500\,\mathrm{h}$), the resistivity at 4 K is more than five orders of magnitude higher than ρ_0 before irradiation. This dramatic increase in resistivity clearly demonstrates that the observed metal-insulator transition is induced by disorder introduced through X-ray irradiation.

For κ-Cl and κ-CN, the effect was different. Before irradiation, both Mott insulators exhibit activation-type behavior in resistivity. With increasing irradiation dose, the resistivity decreases across the entire temperature range. Notably, in κ-Cl (Fig. 3.13(c)), a metal-like temperature dependence begins to appear at a relatively low irradiation dose. The resistivity decreases sub-linearly as the temperature drops to approximately 50 K, after which it reverses and rapidly increases. However, the temperature range exhibiting metal-like behavior does not extend below 50 K as the irradiation dose increases. Finally, after 400 h of irradiation, the sample's resistivity begins to increase at low temperatures, with the metal-like behavior gradually weakening.

In κ-CN (Fig. 3.13(d)), resistivity similarly decreases with irradiation time. However, a significantly larger irradiation dose is required to observe metal-like behavior in this sample, which is limited to a narrow temperature range above $\sim 230\,\mathrm{K}$, as shown in the inset of Fig. 3.13(d).

A possible explanation for the different influence of irradiation on the salts is related to their different ground states, as shown in Fig. 3.13(e). For κ-NCS, which is fully metallic, irradiation simply increases scattering and residual resistance, shifting the compound closer to the Anderson MIT. However, for κ-Br, which is near the Mott MIT, the increase in scattering, combined with high correlation strength, leads to the formation of the correlated Anderson MIT [88] and shifts the compound into an insulating state. For κ-Cl and κ-CN, which are already in the Mott insulating state, additional disorder competes with the correlation strength, effectively reducing its influence. This can shift compounds from the Mott insulating into the Anderson insulating or crossover regime [88]. For κ-Cl, a scenario in which disorder changes the fully-gapped Mott insulator to a Mott insulator with a soft Coulomb gap was proposed [163].

3.9 Disorder effects on T_c and residual resistivity

The change in the resistance in the organic salts with varying levels of disorder, induced by irradiation, suggests a shift of the system toward an Anderson insulating state. This transition may result from multiple factors, including modifications in bandwidth or enhanced scattering. In [164] and [165], the effects of various sources of dis-

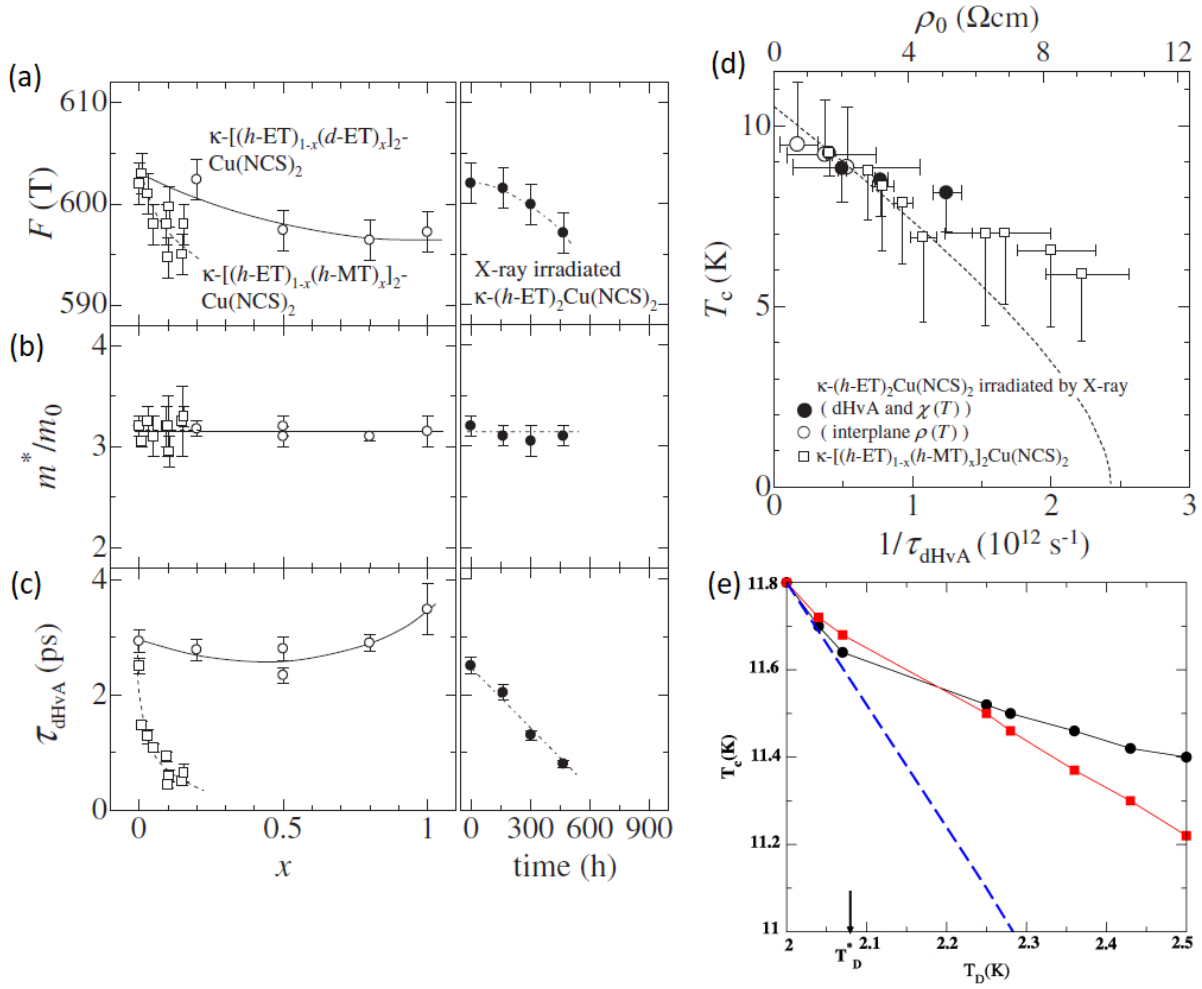

Figure 3.14: Molecule substitution (open circles), deuteration (open squares), and X-ray irradiation time (filled circles) dependencies of dHvA frequency F_α (a), effective mass ratio m^*/m_0 (b), and scattering time τ_{dHvA} (c), obtained from dHvA measurements [164] for κ-NCS. The curves serve as guides for the eye. (d) Relation between T_c and $1/\tau_{\mathrm{dHvA}}$ for κ-NCS from [164]. Symbol notation follows that of subfigures (a)-(c). The dashed curve represents the AG formula for $\tau_{\mathrm{AG}} = \tau_{\mathrm{dHvA}}$, with $T_c^{\mathrm{AG}} = 10.5\,\mathrm{K}$. The top scale bar corresponds to the residual resistivity. (e) Superconducting transition temperature as a function of the Dingle temperature for κ-Br from [166]. Red squares represent the results obtained from the proposed model, while black circles denote the experimental data [166]. The blue line corresponds to the AG law.

order, such as irradiation, deuteration, and organic molecule substitution, on κ-NCS were investigated. These studies examined both the impact of irradiation on disorder and its influence on electronic correlations, as determined through magnetic quantum oscillation measurements (de Haas-van Alphen effect).

They found that the Fermi surface and electronic correlation strength remained unaffected by irradiation, as indicated by the constant effective cyclotron mass and the unchanged frequency of α oscillations (Fig. 3.14(a) and Fig. 3.14(b)). However, irradiation significantly increased the scattering rate, as evidenced by the rise in the Dingle

temperature (Fig. 3.14(c)). Additionally, irradiation strongly suppressed the superconducting critical temperature T_c (Fig. 3.14(d)). According to Anderson's theorem on superconductivity, non-magnetic impurities should not affect the critical temperature of a conventional s-wave superconductor. Therefore, the authors proposed the presence of an unconventional *d*-wave order parameter. A similar effect was observed for κ-Br in [153, 167].

The influence of non-magnetic impurities on unconventional T_c is analogous to the effect of magnetic impurities on conventional T_c [168]. Consequently, the dependence of T_c on disorder can be analyzed using the Abrikosov-Gor'kov (AG) formula [156]:

$$\ln\left(\frac{T_{c0}}{T_c^{\mathrm{AG}}}\right) = \psi\left(\frac{1}{2} + \frac{\hbar}{4\pi k_{\mathrm{B}} T_c^{\mathrm{AG}}}\frac{1}{\tau_{\mathrm{AG}}}\right) - \psi\left(\frac{1}{2}\right). \tag{3.4}$$

Here, ψ represents the digamma function, and T_{c0} is the critical temperature in the ideally pure case. In the AG formula, scattering is assumed to be dominated by large-angle impurity scattering ($\tau_{\mathrm{AG}} \simeq \tau_{\mathrm{imp}}$). A similar scattering mechanism influences the residual resistivity in interlayer transport within a layered Fermi liquid model, as described by equation [156, 169]:

$$\rho_0 = \frac{\pi\hbar^4}{2e^2 m^* d t_\perp^2}\frac{1}{\tau_{\mathrm{imp}}}, \tag{3.5}$$

where d is the interlayer spacing, m^* is the effective quasiparticle mass, and $t_\perp$ is the interlayer hopping integral. Therefore, it is possible to convert the residual resistivity into an effective scattering rate. In contrast, the scattering time extracted from dHvA oscillations also includes contributions from small-angle scattering caused by dislocations, weak spatial potential modulations, and other factors, leading to the relation $\tau_{\mathrm{dHvA}}^{-1} = \tau_{\mathrm{imp}}^{-1} + \tau_{\mathrm{other}}^{-1}$.

Fig. 3.14(d) presents the dependence of T_c on the scattering rate in κ-NCS, as reported in [164]. The lower scale corresponds to the scattering rate directly obtained from dHvA measurements, while the upper scale represents the residual resistivity, ρ_0. The relationship between the residual resistivity and the scattering rate is given by Eq. (3.5). The dashed curve represents the AG equation for $\tau_{\mathrm{AG}} = \tau_{\mathrm{dHvA}}$. According to the authors, the dependence of T_c follows the AG formula at low disorder levels but deviates at higher disorder levels. One possible explanation for this deviation is the presence of a mixed order parameter with both s-wave and non-s-wave components. Another possibility is the involvement of multiple scattering mechanisms, where the contribution from τ_{other} increases as disorder strengthens. This additional contribution, τ_{other}, may originate from weak impurity potential modulations in bulk samples, which dampen dHvA oscillations without significantly affecting the suppression of T_c.

Similar deviations from the AG formula were also observed in κ-Br. However, an alternative explanation for T_c suppression was proposed in [166]. Instead of considering the system within the AG law, they modeled the bulk sample as a network of superconducting clusters embedded in a non-superconducting matrix, with Josephson coupling between the clusters. As disorder increases, the size of the non-superconducting domains grows, leading to a reduction in Josephson tunneling and, consequently, a suppression of T_c. Based on this model, the estimated dependence of T_c suppression on the

scattering rate is shown as red points in Fig. 3.14(e). This approximation aligns with the AG prediction (blue line) at low disorder but better fits the experimental data (black points) at higher disorder levels. However, the total investigated scattering range is relatively narrow, with $T_D \simeq 2.0\,K$ to 2.5 K, corresponding to only a 20 % increase in the scattering rate. If the system is considered to be in a low-disorder regime at $T_D \simeq 2.0\,K$ and follows the AG formula, then a mere 20 % increase in disorder is unlikely to shift it into a high-disorder regime. Conversely, if the system is already in a high-disorder regime, then the AG law should not be expected to hold from the outset. Anyway, both approaches do not perfectly fit experimental data or provide legit explanation of their deviations.

As observed in the previous sections, irradiation introduces disorder, shifting the electronic system of κ-NCS and κ-Br on the phase diagram toward the Mott-Anderson MIT. This disorder increases scattering, leading to higher residual resistance and the suppression of the superconducting critical temperature. Similar effects have been observed in κ-Br and κ-Cl following rapid cooling, which increases the concentration of nonequilibrium EEG conformations [149, 170, 171]. However, theoretical calculations on the influence of EEG conformations suggest that they alter the conduction bandwidth. Consequently, thermal history is expected to modify correlation strength, shifting the system on the phase diagram in a similar way as pressure. As previously discussed, these calculations may not be entirely precise and need experimental verification. This raises a critical question: does thermal history and the presence of nonequilibrium EEG conformations affect the system in a way analogous to irradiation, merely introducing disorder, or do they genuinely alter the electronic correlations of the material? Resolving this question is one of the objectives of this thesis.

4 Experimental setup

This chapter outlines the experimental methods employed in this study, focusing on the techniques used to apply and monitor high hydrostatic pressure, achieve low temperatures, and generate high magnetic fields. A brief discussion will highlight the advantages of different experimental setups, along with the challenges and limitations of each method. Additionally, the preparation of samples for the measurements will be addressed, with particular emphasis on establishing electrical contacts and configuring the equipment for resistive measurements.

4.1 Synthesis

Single crystals of κ-(BEDT-TTF)$_2$X [X=Cu(NCS)$_2$ (abbreviated as κ-NCS), Cu[N(CN$_2$)]Cl (abbreviated as κ-Cl), Cu[N(CN$_2$)]Br (abbreviated as κ-Br), and Cu$_2$(CN)$_3$ (abbreviated as κ-CN)] - where BEDT-TTF stands for bis(ethylenedithio)-tetrathiafulvalene - are synthesized via electrochemical methods [34, 172, 173]. The BEDT-TTF molecules are dissolved in a mixture of electrolytes essential for forming the anion layer. A constant current is applied using two platinum electrodes, inducing the electrochemical oxidation of BEDT-TTF, while the dissolved salts function as electrolytes. The electrochemical cell is maintained at a constant temperature of approximately 20 °C and subjected to a low current density of about 8 µA/cm^2 to 200 µA/cm^2 (total current 0.2 µA to 5 µA) over several weeks. During this period, small crystals, typically with an in-plane size of 0.5×0.5 mm^2, gradually form on the platinum anode (Fig. 4.1(a)). The thickness of our κ-Br and κ-Cl crystals was approximately 0.2 mm to 0.4 mm, resulting in a block- or cube-like shape, whereas the thickness of κ-CN was less than 0.1 mm, giving them a plate-like appearance.

The κ-Br samples examined in this thesis were provided by H. Müller[1] and N. Kushch[2]. The κ-Cl crystals were grown by N. Kushch, while the κ-CN samples were synthesized by A. Kawamoto[3] and tested and supplied by A. Pustogow[4].

4.2 Resistance measurement

As our focus is on the high-field magnetoresistance and magnetic quantum oscillations, the primary characterization technique employed in this work is interlayer resistance measurement. This method is more reliable than in-plane resistance measurements for

[1] European Synchrotron Radiation Facility, 38043 Grenoble, France
[2] Institute of Problems of Chemical Physics, 142432 Chernogolovka, Russian Federation
[3] Department of Physics, Graduate School of Science, Hokkaido University, Sapporo, Japan
[4] Institute of Solid State Physics, TU Wien, 1040 Vienna, Austria

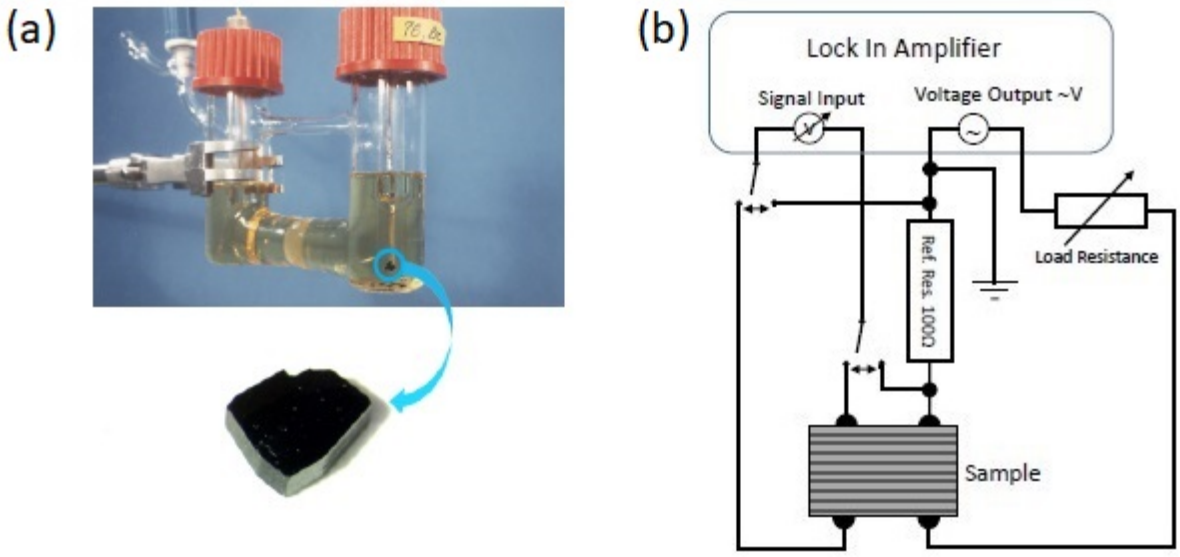

Figure 4.1: (a) Picture of organic metal single crystals growing in an electrocrystallization process. (b) Circuit of the four-point resistance measurement [175].

our highly anisotropic materials, where the resistivity anisotropy $\rho_\perp/\rho_\parallel \sim 10^3 - 10^5$. Interlayer resistance is significantly higher in magnitude and is less affected by crystal imperfections or inhomogeneous current distribution [7, 174]. Resistive measurements were performed using the conventional four-probe technique. This approach utilizes one pair of electrical leads to apply the current and another to measure the voltage. This method effectively eliminates the influence of extraneous resistances introduced by the wires or electrical contacts, ensuring accurate determination of the sample's intrinsic resistance. This distinction is crucial, as the resistance of the leads and contacts can be significantly higher than that of the sample, potentially distorting the measurements if a two-probe method were used.

To create mechanically stable and highly conductive contacts, commercial conductive graphite paste (Dotite) thinned with DuPont thinner was used to attach the electrical leads. The leads consisted of 20 µm thick annealed platinum wires, manually affixed to both sides of the sample surface. These carefully prepared contacts exhibited resistances below 30 Ω per contact, ensuring stability throughout the experimental process. For comparison, the typical resistance of the samples at room temperature ranged from 50 Ω to 1000 Ω, while at low temperatures, it varied between 0.01 Ω to 1000 Ω, depending on the compound. The sample resistance was measured by applying a low-frequency AC current (10 Hz to 300 Hz). The AC voltage was supplied by the oscillator output of a lock-in amplifier (SR830 and ZI MFLI). The measurement circuit, schematically illustrated in Fig. 4.1(b), included a large in-series load resistor to ensure a stable current flow and minimize variations in the current during measurements.

The oscillator was typically configured to an output of 1 V, with R_{load} values ranging from 1 kΩ to 10 MΩ (significantly higher than the sample and contact resistances), allowing measurement currents in the range of 100 nA to 1 mA. To fine-tune the current, the differential inputs of the lock-in amplifier were temporarily connected to the reference resistor ($R_{\text{ref}} = 10\,\Omega$ or 100 Ω), and U_{osc} was adjusted until the measured voltage

matched the desired I_{meas}. Once the current was set, the lock-in amplifier's differential inputs were switched to the sample. The measurement current, I_{meas}, was calculated using the relation

$$I_{\text{meas}} = \frac{U_{\text{ref}}}{R_{\text{ref}}} = \frac{U_{\text{osc}}}{(R_{\text{load}} + R_{\text{ref}} + R_{\text{sample}} + R_{\text{contacts}} + R_{\text{leads}}} \approx \frac{U_{\text{osc}}}{R_{\text{load}}}$$

The sample resistance, R_{sample}, was then determined using the relationship: $R_{\text{sample}} = V_{\text{sample}} / I_{\text{meas}}$.

During the magnetoresistance measurements, the typical change in sample resistance was approximately 10^4 times smaller than the load resistance. Consequently, the error in current determination was less than 0.01 %. However, during $R(T)$ measurements, at the peak of the resistance, the sample resistance could reach up to 5 % of the load resistance, increasing the error in current determination to 5 %. In the cases where an absolutely precise value of the sample resistance was required, it could be recalculated by adjusting the current determination accordingly.

4.3 Low temperature setup

Temperature control is a crucial factor when conducting measurements in a cryogenic environment. Essential considerations include the lowest reachable temperature, the cooling capacity, and the precision of temperature monitoring and regulation. The choice of the cooling system was determined based on the specific temperature requirements of each experiment to ensure optimal performance.

4.3.1 Temperature control

To measure the temperature, resistive Cernox1030 and RuO_x thermometers were primarily used, with their resistance monitored using a LakeShore Model 350 temperature controller. Each insert was equipped with one or more heaters to enable precise temperature control. Temperature regulation was managed using the LakeShore 350 PID controller, ensuring stable and accurate adjustments.

The primary thermometer used during $R(T)$ measurements was the Cernox sensor, as it provides good sensitivity over a wide temperature range, from the room temperature (RT) to low temperatures, down to $\lesssim 0.4$ K. However, due to its significant low-T magnetoresistance, it is not very suitable for measurements in high magnetic fields. In such cases, two alternative temperature measurement methods were employed. During measurements in liquid ^{3}He (discussed below), the temperature was monitored via ^{3}He vapor pressure measurements. The analog output of the manometer was connected to a voltmeter for continuous monitoring. Calibration between voltage and temperature was performed in advance at zero magnetic field, as shown in Fig. 4.2(a). This method enables precise temperature monitoring within the range of 0.4 K to 1.0 K.

Another method for temperature monitoring in a magnetic field involves the use of a specialized RuO_x thermometer [176], which exhibits very low magnetoresistance. Figure 4.2(b) shows the $T(B)$ curves of RuO_x at various constant temperatures and magnetic fields up to 30 T. The constant temperatures were maintained by controlling

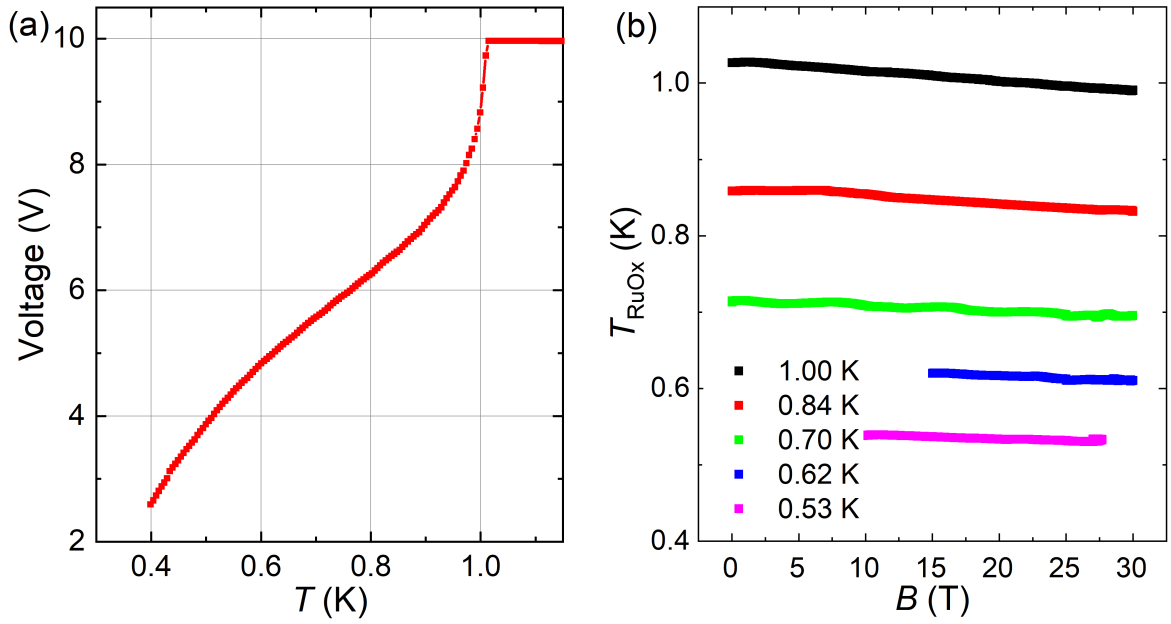

Figure 4.2: (a) Calibration curve between the temperature and the voltage analog output of the ^{3}He gas manometer. (b) Magnetic field dependence of RuO_x thermometer readings at various constant temperatures, stabilized by controlling the ^{3}He vapor pressure.

the ^{3}He vapor pressure. At higher temperatures (around 1 K), the temperature deviations from the initial setpoint were approximately 40 mK, while at lower temperatures, the deviations decreased to about 10 mK. These deviations must be taken into account during temperature monitoring. In [176], measurements with this type of thermometer in pulsed magnetic fields up to 50 T at 2 K reported temperature deviations of around 150 mK. Therefore, the RuO_x thermometer is particularly effective for temperature monitoring at $T < 1$ K.

4.3.2 ^{4}He VTI

To achieve temperatures down to 1.4 K, a ^{4}He variable-temperature insert (VTI) was used, placed in a bath of liquid ^{4}He at 4.2 K. As shown in Fig. 4.3(a), a thin capillary with high impedance to the gas flow connects the ^{4}He bath to the inner space of the VTI, which is otherwise isolated by a vacuum space. This capillary impedance allows small amounts of helium to enter the VTI's inner space. Additionally, a small amount of ^{4}He (0.5 mbar at RT) can be introduced into the vacuum space as a gas exchange medium to enhance the cooling rate at temperatures above 50 K.

Temperatures above 4.2 K can be regulated using a resistive heater. By pumping the inner space and thereby reducing the vapor pressure, the temperature can be varied from 4.2 K (no pumping) down to 1.4 K (full pumping). A manostat is used to stabilize the pressure in the sample space and control the temperature. The continuous flow of helium gas ensures a steady cooling power. The optimal method for temperature measurement across the entire range (1.4 K to 300 K) is a Cernox thermometer, which

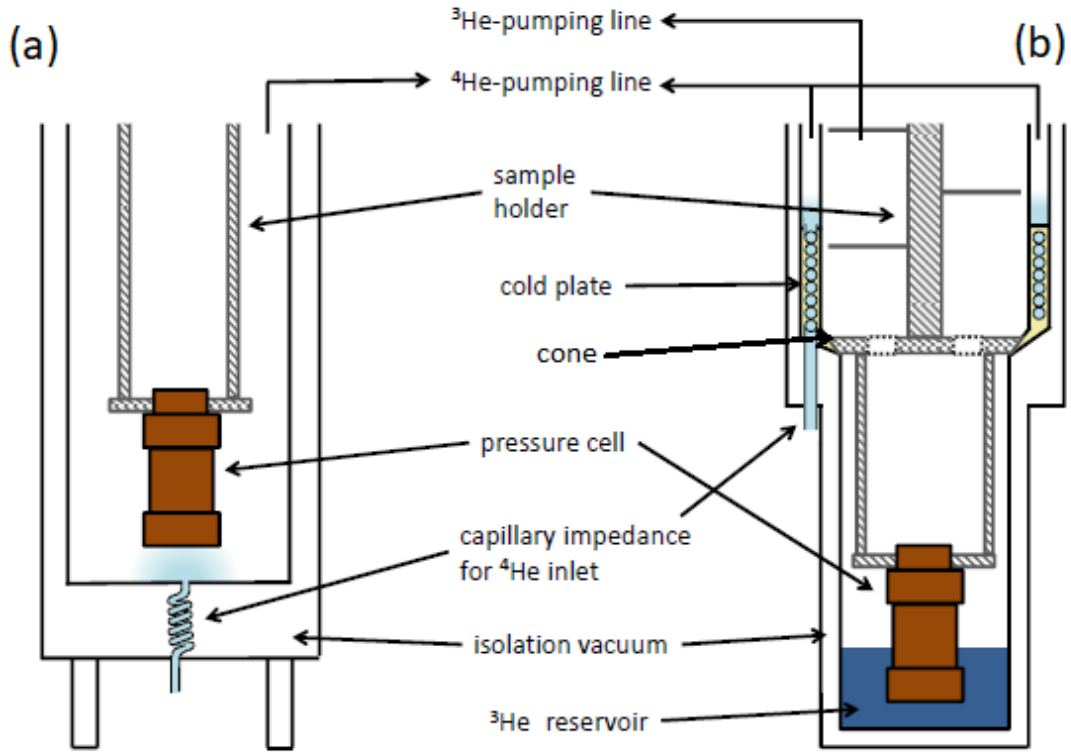

Figure 4.3: Schematic drawing of ^{4}He VTI (a) and ^{3}He VTI (b) from [42].

provides high sensitivity and reliability.

4.3.3 ^{3}He VTI

For experiments requiring temperatures below 1.4 K, a ^{3}He cryostat was used. A schematic diagram of the ^{3}He system is shown in Fig. 4.3(b). This setup allows for achieving temperatures as low as 0.4 K. The ^{3}He sample space is thermally isolated from the ^{4}He bath by a surrounding vacuum space and a 1 K pot connected to the ^{4}He bath through a capillary. During cooling, exchange He gas was introduced into the vacuum space to enhance the cooling rate. This gas was subsequently pumped out at low temperatures to improve thermal isolation of the sample space.

The 1 K pot terminates approximately 30 cm above the sample space at a copper cold plate with a conical surface. The sample holder stick, which also has a conical surface, makes direct thermal contact with this cold plate. Cooling is achieved by pumping the 1 K pot through the capillary, which lowers the temperature of the cold plate and subsequently cools the sample holder cone down to 1.3 K.

When ^{3}He gas is introduced into the sample space, it initially condenses as it is cooled by the sample holder cone at 1.3 K, until the equilibrium vapor pressure of approximately 50 mbar is reached. Further pumping of the ^{3}He gas progressively reduces the temperature, allowing the system to reach temperatures as low as 0.4 K. At low ^{3}He pressures, the thermal connection between the cone and the pressure cell con-

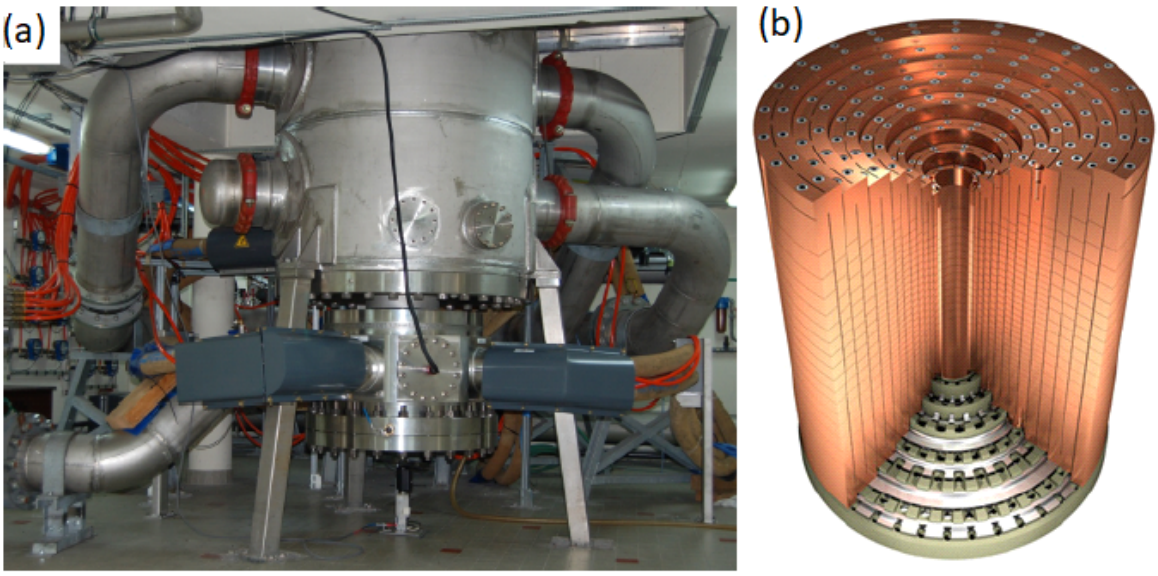

Figure 4.4: (a) Picture of the resistive magnet used at the LNCMI in Grenoble. The big pipes coming out of the core are for the supply and drain of cooling water [42]. (b) Profile of the polyhelix magnet core [42].

taining the samples becomes weak. To maintain stable temperatures in the range of 0.4 K to 1 K, the temperature is regulated by adjusting the valve at the entrance to the ^{3}He pump.

4.4 Magnetic field setup

4.4.1 Superconducting magnet 15 T

High magnetic fields are essential for observing magnetic quantum oscillations. One approach to achieving fields up to 15 T involves using a superconducting (SC) solenoid immersed in a liquid ^{4}He bath at 4.2 K. This method was employed for measurements on κ-Cl and κ-CN. By cooling the ^{4}He bath down to 2 K, the critical current of the solenoid increases, allowing the maximum field to be extended to 17 T.

4.4.2 Resistive magnet 30 T at the LNCMI Grenoble

For even higher fields, partially or fully resistive magnets are necessary, such as those available at the Laboratoire National des Champs Magnetiques Intenses (LNCMI) in Grenoble (Fig. 4.4). These magnets are operated at constant currents of up to 30 kA, making it crucial to minimize energy dissipation from Ohmic losses and ensure mechanical stability to withstand the substantial ponderomotive forces generated by the large currents in high magnetic fields. The magnet is a combination of two main parts: Bitter magnet (sequence of plates) and polyhelix magnet (concentric monolayer coils, Fig. 4.4(b)).

Since the magnet core generates up to 24 MW of heat, efficient cooling is required. Approximately 300 l/s of water flow is driven through the system to maintain the temperature below 100 °C. Using this setup, with a bore diameter of 52 mm, we achieved magnetic fields up to 30 T.

4.4.3 Pulse fields 70 T at the HLD

A pulsed magnet at the Hochfeld-Magnetlabor Dresden (HLD) was utilized to measure SdH oscillations at even higher magnetic fields. A 70 T magnet with a 24 mm bore diameter was used. The magnet was initially cooled to 77 K using a bucket filled with liquid nitrogen. To generate the magnetic pulse, several capacitor banks were charged to 21 kV, storing a total energy of 6.7 MJ. This stored energy was then discharged into the magnet, producing a magnetic field of up to 70 T. The typical pulse duration was approximately 100 ms. The discharge process heated the magnet above 200 K, requiring about three hours to cool down. The applied magnetic field was monitored using a pick-up coil, and its time dependence is illustrated in Fig. 4.5(b).

The resistance of the samples was measured using a procedure similar to the AC lock-in setup described previously. However, due to the short duration of the magnetic pulse, much higher measurement frequencies (33 kHz and 55 kHz) were employed with a measuring device 'Yokogawa DL850 scope recorder'. Additionally, the voltage drop across the reference resistor was recorded during the pulse to monitor the current through the samples. After the measurement, a digital lock-in procedure was applied to the raw data of the voltage signals from both the sample and the reference resistor to calculate the magnetoresistance during the pulse.

This method was used to measure κ-Br samples at ambient pressure and after different thermal histories. The samples were mounted on a holder made of PEK plastic (Fig. 4.5(a)). The use of a plastic holder prevented the generation of eddy currents due to the rapidly changing magnetic field, ensuring more stable and accurate mea-

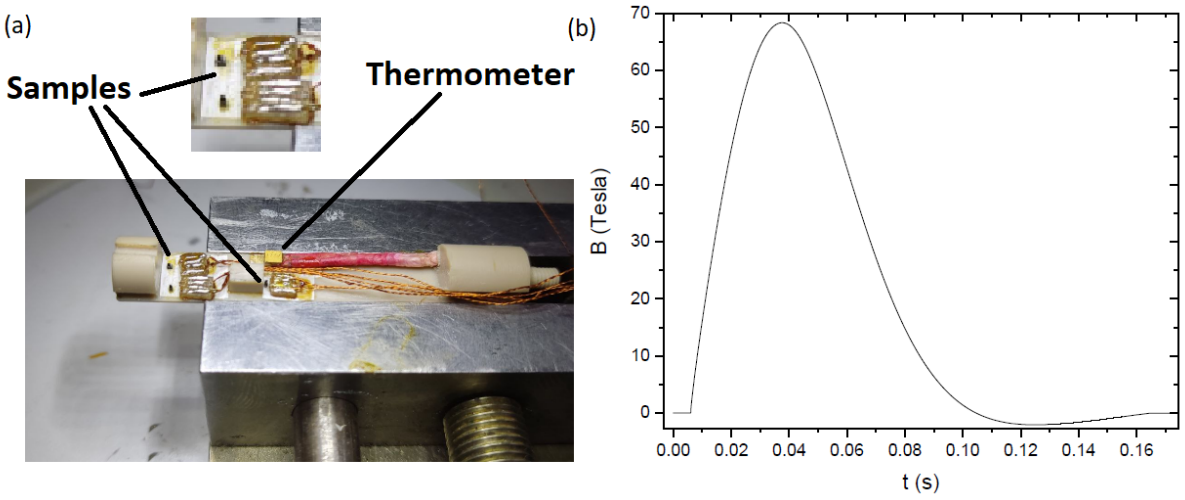

Figure 4.5: (a) Picture of the sample holder for the pulse fields facility in Dresden. (b) Magnetic field over time during the pulse in Dresden [175].

surements. A thermometer was placed near the samples to monitor and stabilize the temperature before the pulse.

4.5 Pressure Setup

4.5.1 Pressure clamp cell

Since we are particularly interested in the pressure-dependent phenomena, it is crucial to have a reliable method for both applying and measuring pressure. For this purpose, we primarily used the clamp cell technique (Fig. 4.6(a)). The pressure cells were constructed from a CuBe alloy. The feedthroughs for electrical leads were filled with Stycast 2850 epoxy with Catalyst 9, selected for their excellent low-temperature properties, including high hardness and a low thermal expansion coefficient.

There are two types of pressure cells: small and large, differing in size (Fig. 4.6(b)). The large cell is rated for pressures up to 1.5 GPa at low temperatures, while the small cell can sustain pressures up to 1 GPa at low temperatures and is compatible with the rotator setup (described in Sec. 4.6).

Samples were mounted inside the cells, which were then placed in a Teflon cup filled with PES, a silicone oil used as the pressure-transmitting medium. The assembly was subsequently inserted into the clamp cell, where force was applied using a hydraulic press until the desired pressure was reached. Once the target pressure was achieved, the nut of the clamp cell was tightened to maintain the applied force.

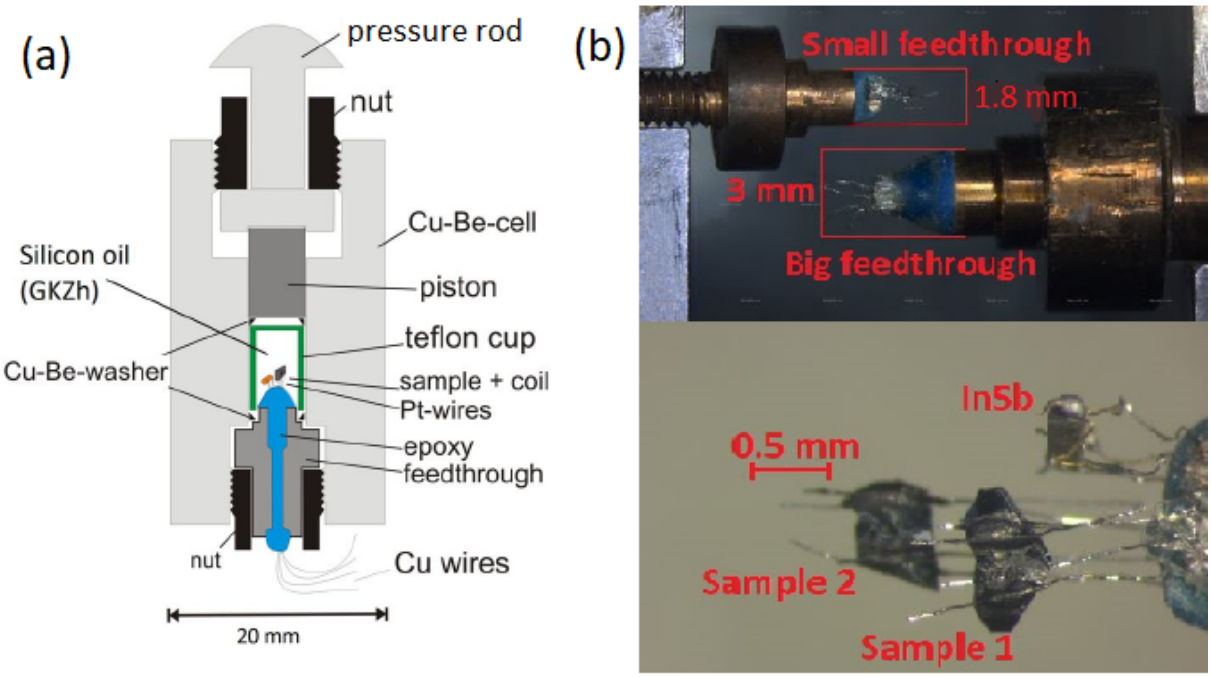

Figure 4.6: (a) Schematic drawing of the CuBe clamp pressure cell [177]. (b) Photograph of the small and large pressure cells. (c) κ-CN samples and InSb pressure sensor mounted inside the small pressure cell.

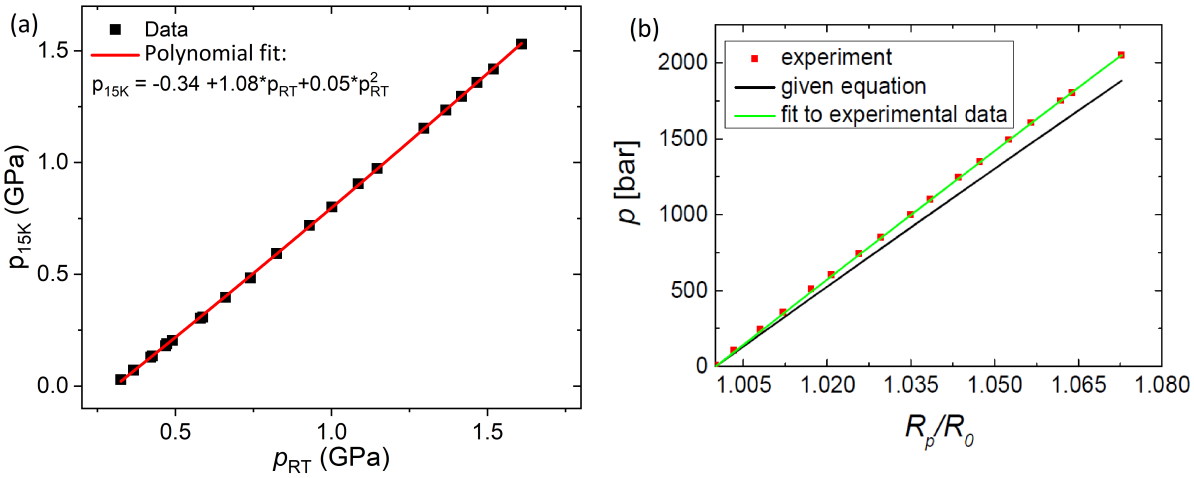

Figure 4.7: (a) Pressure inside the clamp cell at 15 K vs. the RT pressure after cooling from RT to 15 K. (b) Pressure dependence of the resistance, normalized to the ambient pressure resistance of the sensor, at temperatures below 77 K (red points) from [178]. The black curve represents the original equation provided in the sensor manual to describe the pressure dependence. This formula was slightly modified to better fit the experimental data (green curve, see text).

As the pressure within the cell decreases upon cooling, it was necessary to apply approximately 0.3 GPa more at RT than the target pressure for low-temperature measurements. A more detailed relationship between high- and low-temperature pressures is shown in Fig. 4.7(a).

The pressure inside the cell was monitored using a heavily n-doped InSb sensor [179]. These sensors exhibit a linear resistance-pressure dependence $R(p)$ of approximately 36 %/GPa, providing a relative accuracy of < 5 %. The sensors are supplied

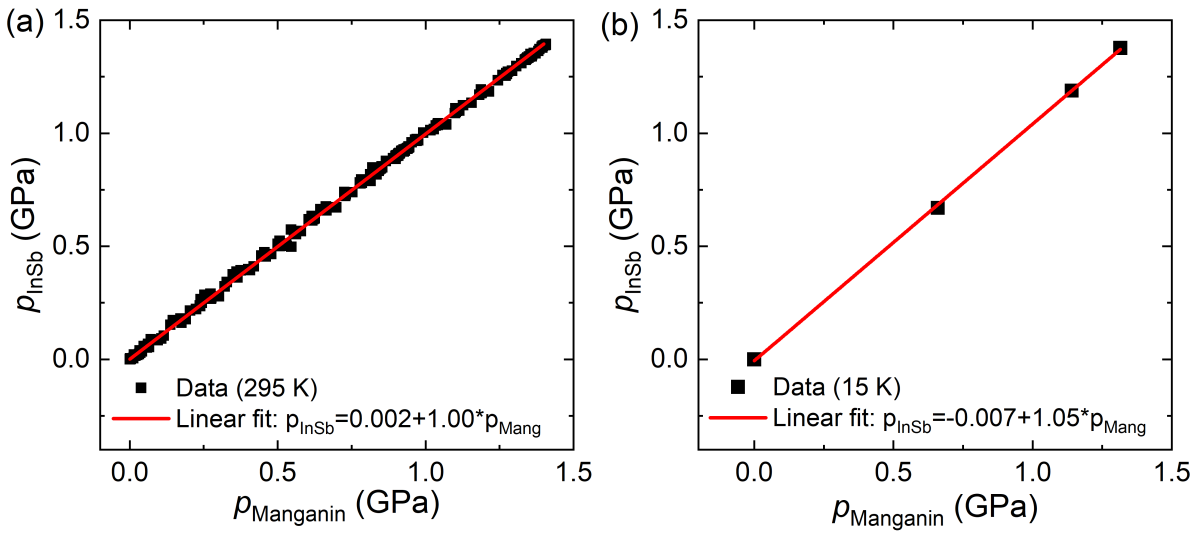

Figure 4.8: Pressure values calculated from the manganin resistance and InSb resistance at RT (a) and at 15 K, shown as black points. The red curves represent linear fits.

with a calibration at RT and at 77 K. [179]. Additionally, all sensors were calibrated in a gas pressure setup prior to use at both low (15 K and 77 K) and high (RT) temperatures and at pressures up to 0.2 GPa [178].

Fig. 4.7(b) shows the pressure dependence of the relative resistance, comparing the calibration data (blue line) [179] with the experimental calibration measurements (red points) [178]. The experimental data were further fitted using the standard calibration formula with an additional slope correction factor of 1.07 (green line) [178].

As the user's manual states that InSb exhibits a linear pressure dependence up to 2 GPa, we conducted comparative measurements of InSb sensors alongside a manganin coil, which is known for its linear pressure dependence [18, 180]. Fig. 4.8 presents the pressures recorded by the InSb sensor and the manganin coil at RT (a) and at 15 K (b). The red lines represent linear fits to the data. As shown by the fits, the InSb sensor maintains a linear dependence on pressure up to 1.5 GPa.

4.5.2 ^{4}He gas pressure

The pressure cell method described above allows the application of relatively high pressures. However, during temperature sweeps, the pressure inside the cell changes, making precise monitoring challenging. Additionally, adjusting the pressure requires a full thermal cycle, and it is difficult to accurately set pressures at low temperatures. These limitations can be overcome using a ^{4}He gas pressure setup, which enables more precise pressure control.

A schematic representation of the gas pressure setup [177] is shown in Fig. 4.9. In this system, helium is initially stored at room temperature in a high-pressure bottle at approximately 10 MPa to 15 MPa. Before entering the cryostat, the gas is purified using a liquid nitrogen cold trap, which removes impurities that could freeze inside the BeCu

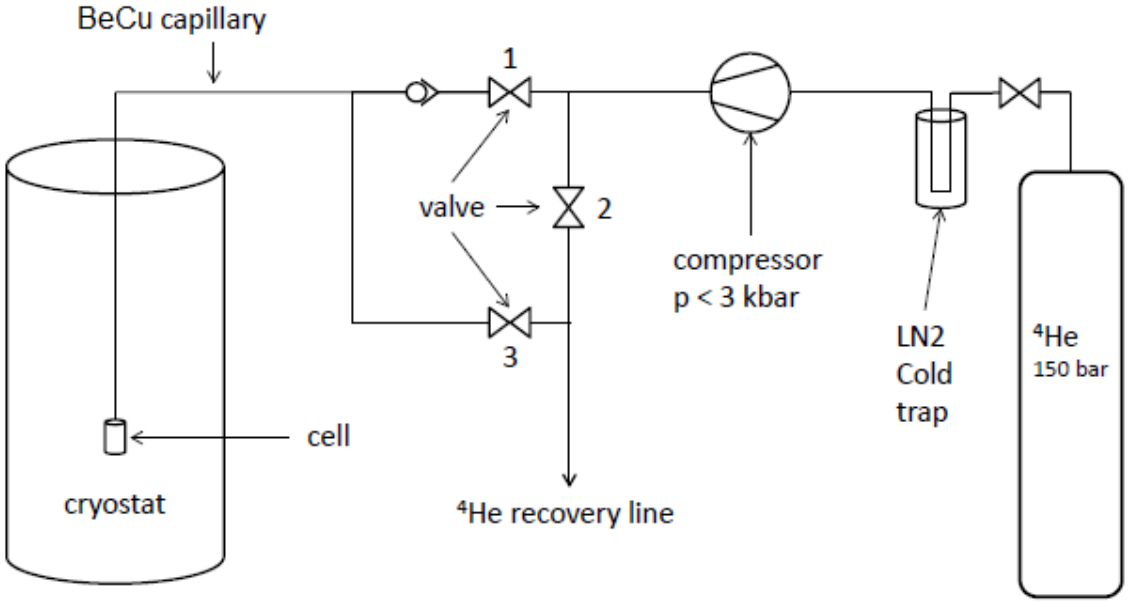

Figure 4.9: Schematic drawing of the gas pressure setup [42].

capillary (3 m long, diameter 3 mm, wall thickness 0.3 mm) and cause blockages. The capillary extends continuously from the output of the pressure system to the pressure cell, making the system robust up to 1 GPa.

To apply pressure above 15 MPa, a compressor with a maximum output of 300 MPa is used. Pressure adjustments can be made by operating valve 1, which connects the high-pressure reservoir to the capillary, or valve 3, which links the capillary to the helium recovery line. These valves enable smooth pressure control and sweeping. The pressure in the cell is monitored via a manometer with a precision ~ 0.2 MPa.

To ensure temperature stability and prevent uncontrolled helium freezing, four thermometers and heaters are positioned near the end of the capillary and on the pressure cell itself [177]. However, during our experiments at temperatures down to 10 K and pressures up to 0.1 GPa, the ^{4}He remained in the gaseous and liquid state.

This pressure setup was primarily used to calibrate InSb pressure sensors at both low and high temperatures. Additionally, it was utilized for $R(T)$ measurements of κ-Cl to investigate the influence of thermal history.

4.6 Two-axis rotator

The magnets described above are fixed solenoids, allowing only a single field direction. A two-axis rotator designed by D. Andres and M. Kartsovnik [177] was used to perform angle-dependent measurements. This insert enables adjustments of both the ϕ and θ angles, as shown in the photograph in Fig. 4.10(a). For better clarity, Fig. 4.10(b) shows a schematic of the sample in a tilted magnetic field B, illustrating the definitions of the azimuthal angle φ and the polar angle θ used during sample rotation. The rotation of θ corresponds to changing the angle between the magnetic field and the conducting layers of the sample. In contrast, the rotation of φ modifies the orientation of the field rotation plane with respect to the crystallographic axes of the sample.

The platform with pressure cell holder is rotated in situ using two worm-gear units. The ϕ angle is rotated manually by inserting a screwdriver into the screw in the sample holder platform. This requires the θ angle to be fixed, ensuring the screw on the platform aligns with the screwdriver position. The ϕ angle can be set with an resolution

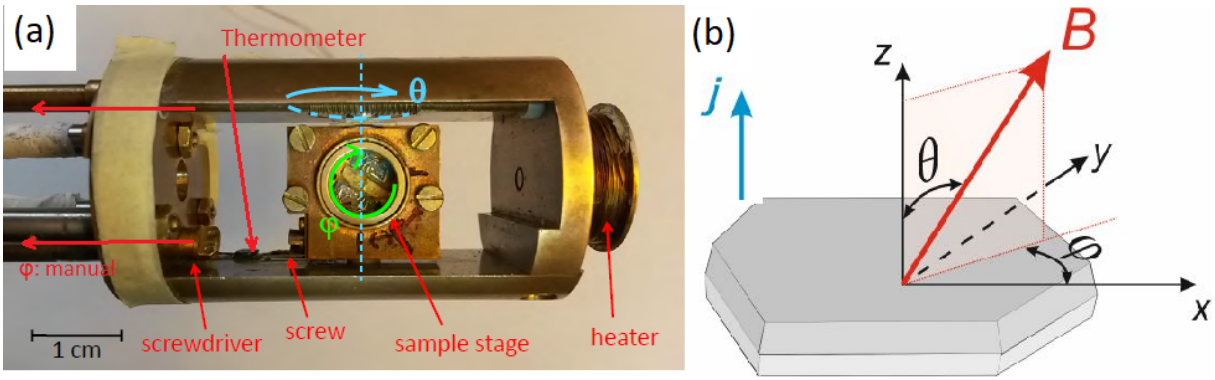

Figure 4.10: (a) Picture of the sample stage of the two-axis rotator [181] (b) Schematic representation of the sample unit cell axes and the φ and θ angles.

of approximately 0.2° due to play of the screw. Once the ϕ adjustment is complete, the screwdriver must be removed.

For continuous θ-angle rotation, a piezomotor is employed. The θ angle is determined by measuring the resistance of a 20-turn potentiometer coupled to the rotating rod at the top of the insert. During rotation, the angular accuracy is approximately 0.1°. The sweep rate for θ-angle rotation can be set between 0.1 °/min to 50 °/min.

4.7 Thermal treatment protocols

During experiments investigating the influence of thermal treatment, it was necessary to achieve different cooling rates near the glass transition temperature T_g, see Sec. 3.7. Using a conventional setup, cooling rates in the range of 0.1 K/min to 20 K/min could be achieved. To reach the maximum possible occupation probability of the stable E conformation, an annealing method was employed, where the sample temperature was stabilized using a heater at the desired temperature near T_g. For faster cooling, we utilized and further advanced the heat pulse method proposed in [149].

4.7.1 Annealing procedure

For annealing, the temperature was stabilized using a heater set and a proportional-integral-derivative (PID) temperature controller. The stabilization process typically requires several minutes, depending on the PID parameters as well as the heater and thermometer configuration. Consequently, we were unable to measure relaxation times comparable to the stabilization time. For complete annealing, the sample must be stabilized at the annealing temperature and maintained for a duration equivalent to $3-4$ relaxation times. However, this process can be optimized using a several-step annealing. In this approach, the sample is initially stabilized at a higher temperature and held for $1-2$ relaxation times before the temperature is decreased to the next annealing step. This process is repeated until the target annealing temperature is reached. Fig. 4.11(a) shows instances of step annealing performed at the HLD, where time constraints were a limiting factor, and we managed to complete low-temperature annealing in a shorter time.

4.7.2 Quenching procedure

For a rapid cooling of the samples, a heat pulse quenching method [149] was utilized. This method involves using the sample itself as a self-heater by applying a high-voltage pulse, which generates heat through Joule heating. The procedure for pulse application and sample resistance monitoring was developed together with F. Kollmannsberger during his Master's studies [175].

We utilized Zurich Instruments MFLI lock-in amplifiers to implement this method, which offer the significant advantage of simultaneously applying AC and DC voltages to the output. Fig. 4.11(b) shows the schematic circuit for pulse application. The sample and a reference resistor ($R_{\text{ref}} = 100\,\Omega$) were connected in series to the output of an MFLI, which provided a high-frequency ($\sim$ 2.5 kHz, 40 mV) voltage excitation. The

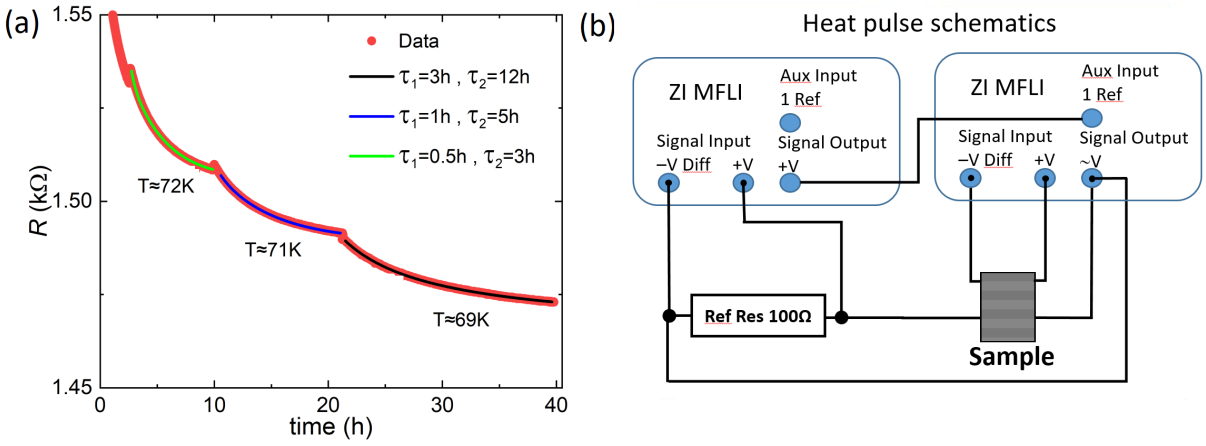

Figure 4.11: (a) Time dependence of the sample resistance during a several-step annealing process. Data at different temperatures was fit with two-exponential decay (black, blue, and green curves). (b) Circuit for the heat pulse application from [175].

sample was also connected to the input of this MFLI to monitor its voltage. The input of the second MFLI was connected to the reference resistor to monitor the current through the circuit. Both MFLIs were synchronized for simultaneous data acquisition. Without interrupting the AC signal, a DC voltage (5 V to 8 V) was applied by the first MFLI to the circuit for a short duration (approximately 2 seconds), serving as a heat pulse for the sample. During the heating and cooling phases, the resistance of the sample changed significantly. Therefore, the use of an AC voltage and two MFLIs was essential to continuously monitor the sample voltage and circuit current, allowing for a precise determination of the sample resistance throughout the process.

Before applying the heat pulse, the surrounding bath was stabilized at approximately 35 K to ensure a high temperature gradient and a rapid cooling rate near the glass transition temperature ($T_g \approx 80$ K). Fig. 4.12(a) shows the time-dependent sample resistance during the pulse, $R(t)$. During pulse application (Fig. 4.12(a), red curve), the sample was rapidly heated to a high temperature $T_{\max}$ within 1 seconds to 1.5 seconds (Fig. 4.12(c)). At this temperature, thermal equilibrium was reached, where the cooling rate balanced the heating power of the pulse. Once the pulse was turned off, the sample cooled down (Fig. 4.12(c)) to the bath temperature (Fig. 4.12(a), black curve).

Before and after the pulse, the temperature dependence of the sample resistance was measured. Fig. 4.12(b) shows the $R(T)$ curves recorded before (red curve) and after (black curve) the pulse. These curves were then matched with $R(t)$ during the pulse to determine the time-dependent sample temperature, $T(t)$. Fig. 4.12(c) shows the temperature evolution during the pulse. From these data, we estimated the maximum temperature reached during the pulse as well as the cooling rate following the pulse (Fig. 4.12(d)). To calculate the cooling rate, we performed a fourth-order polynomial fit to the time dependence of the temperature $T(t)$, and then computed the derivative of the fitted polynomial. The lower limit for the polynomial fit is approximately 75 K; therefore, the cooling rate estimation is considered reliable only above this temperature.

From these estimations, the maximum temperature achieved during the pulse was

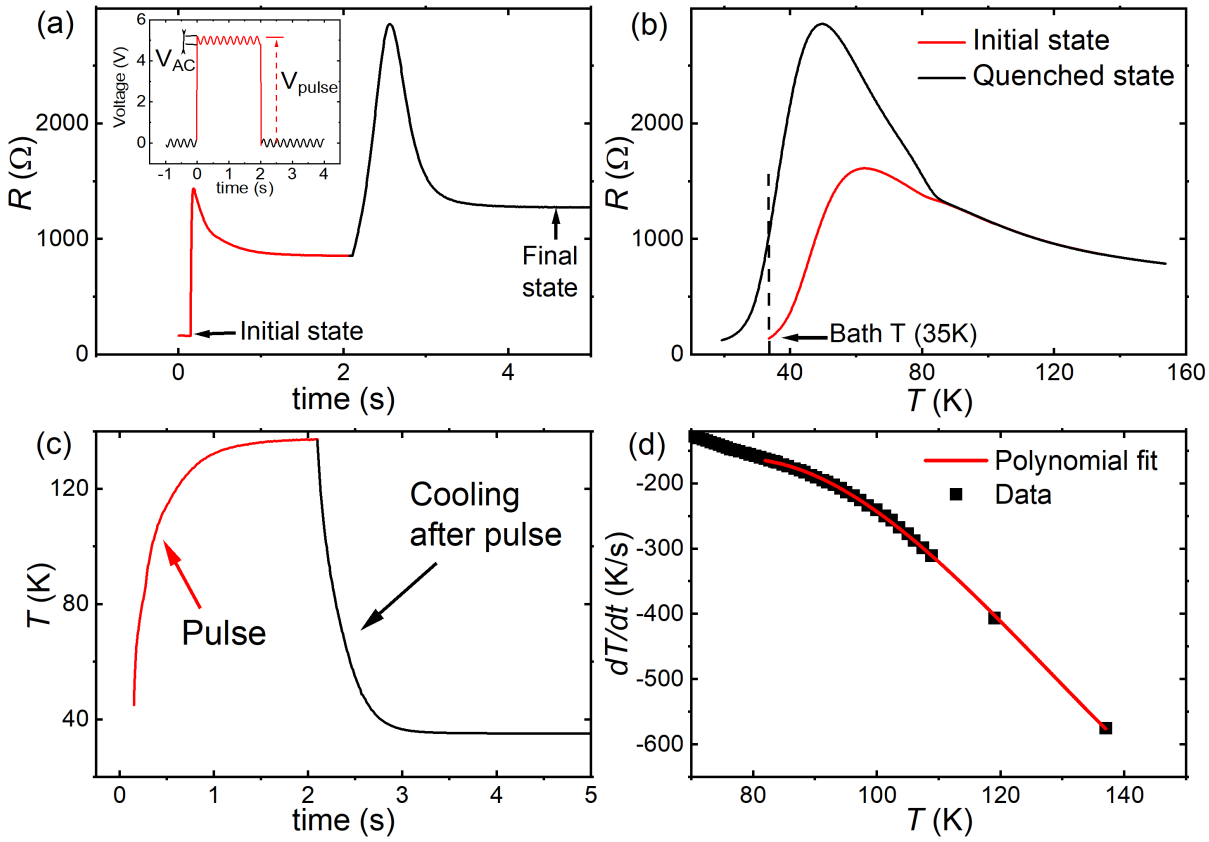

Figure 4.12: Sample measurements during a heat pulse. (a) Resistance before, during, and after the pulse. Inset: Application of AC and DC voltage to the sample. (b) Warming-up $R(T)$ curves of the initial (red) and quenched (black) states. (c) The temperature of the sample during and after the pulse is derived from the $R(t)$ and $R(T)$ curves. (d) Cooling rate after the pulse. Near the glass transition temperature (80 K), the cooling rate is approximately 200 K/s.

$T_{max} \approx 135$ K. The cooling rate after the pulse, near the glass transition temperature, reached up to 200 K/s. This rate is an order of magnitude higher than the estimated 1000 K/min reported in [149]. It should be noted that, in our method, the MFLIs cannot precisely measure the voltage during the first and last 0.05 s of the DC pulse. Therefore, the data in these regions were extrapolated based on the general trend.

To ensure that the samples do not suffer any damage, such as micro-cracks or resistance changes due to structural defects, the effect of the heat pulse was reversed by heating the sample to 100 K and then slowly cooling it again. The resistance curve obtained after this process was compared to the one recorded before the heat pulse, using the same cooling rate. In all cases, the curves coincided, confirming that the original state of the sample was fully restored.

5 Antiferromagnetic Mott insulator κ-Cl

This chapter presents the first set of experimental results. We provide a detailed description of the key analysis methods used throughout this work, including the determination of the cyclotron effective mass and Shubnikov-de Haas (SdH) frequencies, as well as the estimation of the spin frustration and electronic correlation strength ratios. Additionally, we outline the procedures for analyzing angle-dependent magnetoresistance oscillations (AMRO) and other relevant techniques. As these methods form the basis for the analysis in the subsequent chapters, we will frequently refer back to this chapter for reference. Regarding the different material systems, in this chapter we discuss the investigation of κ-Cl and compare it with κ-NCS. In Sec. 3.5, we already noted that, despite differences in their anion layers and ambient pressure ground states, these two salts exhibit a similar effective cyclotron mass in the metallic state near the metal-insulator transition (MIT). This observation suggests a similar correlation strength in both salts. This finding questions the conventional expectation of a 'chemical pressure' effect and strongly contradicts theoretical predictions. However, to unequivocally confirm this, it is necessary to demonstrate that the electron-electron renormalization factors are also similar. This can be achieved by measuring the effective cyclotron *band* mass deep in the metallic state, at high pressure. Consequently, we were motivated to extend our investigation of these salts over a broader pressure range.

In the first part, we present Shubnikov-de Haas measurements conducted in a ^{3}He cryostat at pressures up to 1.5 GPa. These measurements allow for a detailed analysis of the Fermi surface (FS) size, correlation strength, and frustration ratios. The results are compared with κ-NCS measurements performed by S. Fust as part of his Master's thesis [178].

In the second part, we discuss angle-dependent phenomena in κ-Cl, focusing on the angle-dependent magnetoresistance oscillations. These oscillations enable the determination of the FS. By measuring AMRO at both high and low pressures, we can trace the evolution of not only the size but also the shape of the FS as a function of pressure. The determined FS will also be compared with simulations based on the tight-binding effective dimer model.

During the SdH measurements, two κ-Cl samples were studied. In one set of measurements, one sample was oriented perpendicular to the magnetic field direction, while the second sample was tilted at an angle $\theta \approx 25°$. To enable a meaningful comparison with the first sample (perpendicular orientation), the SdH frequency and cyclotron mass for the tilted sample were normalized to those obtained for the perpendicular orientation. This normalization was achieved by multiplying the measured values by $\cos(\theta)$, accounting for the angular dependence of these parameters.

5.1 Temperature dependence of resistance

Initially, we measured the temperature dependence of the resistance at different pressures for κ-Cl. Fig. 5.1(a) shows the $R(T)$ curves with resistivity displayed on the right scale bar. In general, the resistance exhibiting a pronounced peak at $T \sim 130\,\mathrm{K}$, with further decreases upon cooling. The origin of this peak was discussed in Sec. 2.7 and is attributed to the quasiparticles' thermal destruction [65]. Increasing pressure reduces the peak resistivity, and the peak becomes suppressed for $p \gtrsim 0.3\,\mathrm{GPa}$.

According to the Fermi liquid theory, the resistivity is expected to show a quadratic temperature dependence at low temperatures, as described by Eq. (2.27). In the inset of Fig. 5.1(b) the resistivity is plotted versus the square of the temperature (black points) in the temperature range 10 K to 50 K, along with a linear fit (red line) used to extract the coefficient A. The temperature range over which the resistivity follows a quadratic dependence changes with pressure. Near the MIT, the system is only marginally metallic, resulting in a low coherence temperature (the temperature range for fitting is $T < 25\,\mathrm{K}$). With increasing pressure, the quasiparticles become better defined and the coherence temperature rises, reaching approximately 50 K to 60 K in the pressure range of 0.1 GPa to 0.5 GPa. Upon increasing pressure further, electron-electron interactions become weaker and electron-phonon scattering begins to dominate resistivity, leading to a subsequent decrease in the coherence temperature to around $T \sim 30\,\mathrm{K}$.

The coefficient A of the quadratic T-dependence of the resistivity is determined by the correlation strength and is related to the effective mass (see Sec. 2.7). Fig. 5.1(b) shows the pressure dependence of the coefficient A, obtained from separate sets of measurements at low and high pressures, which were merged to coincide at the overlap region near $p \approx 0.2\,\mathrm{GPa}$. This dependence was fitted using the relation $A \sim (p - p_c)^{-2\nu}$.

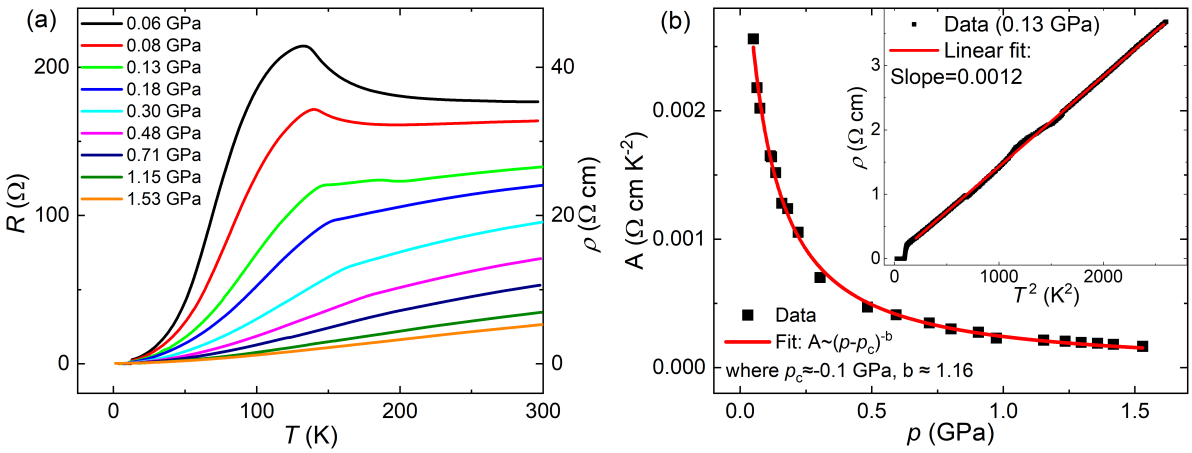

Figure 5.1: (a) Resistance vs. temperature curves, $R(T)$, of κ-Cl at different pressures. The right-hand scale shows the resistivity. (b) Pressure dependence of the coefficient A in the quadratic T-dependence of the resistivity, see Eq. (2.27). The red line represents a fit using the expression $A = a(p - p_c)^b$, see text. Inset: Resistivity as a function of the square of temperature (black points) at a pressure of 0.13 GPa in the temperature range 10 K to 50 K, with a linear fit (red line) yielding a slope of $A \approx 0.0012\,\Omega\mathrm{cmK}^{-2}$.

The fit yields the coefficients $p_c \approx 0.097 \pm 0.015\,\text{GPa}$ and exponent $2\nu \approx 1.16 \pm 0.07$. The obtained exponent is close to the theoretical prediction $\nu = 1.34$ [67] and is larger than the value reported for κ-CN, $\nu \approx 0.75$ [69, 182].

5.2 Shubnikov-de Haas oscillations at different pressures

The main results of the subsequent sections have already been published in [183]. Therefore, most of the figures were taken from that paper.

After cooling the samples, we performed measurements in an applied magnetic field. Fig. 5.2(a) shows an example of the SdH oscillations recorded for κ-Cl at a pressure of 0.48 GPa and at the base temperature of the ^{3}He cryostat $T \approx 0.4\,\text{K}$. Fig. 5.2(b) shows the fast Fourier transform (FFT) of the oscillations in the field window 9 T to 15 T. Consistent with the previous studies [102, 108, 110], two fundamental frequencies are observed, reflecting the Fermi surface topology characteristic of κ-type salts [6, 7], as illustrated in the inset in Fig. 5.2(b).

The lower frequency, F_α, is attributed to the classical orbit on the Fermi pocket located at the Brillouin zone boundary, as shown by the blue lines in the inset of Fig. 5.2(b). This frequency varies between about 530 T to 680 T as pressure increases from 75 MPa to 1.5 GPa. The dominant oscillations, which are clearly resolved across all pressures, exhibit a higher frequency, $F_\beta \sim 4\,\text{kT}$. As seen in Fig. 5.2(b) inset, the β orbit arises due to magnetic breakdown between the α-pocket (blue) and the pair of open sheets (red), effectively representing the entire Fermi surface. This frequency corresponds to a cyclotron orbit area equal to the first Brillouin zone (black rectangle in Fig. 5.2(b) inset). This mechanism has already been explained in detail in Sec. 2.3.

The β-oscillations exhibit a pronounced beating, indicating the presence of two closely spaced frequencies. This frequency splitting, $\Delta F_\beta / F_\beta \sim 0.01$, most likely originates from the maximal and minimal cross-sections of the quasi-2D Fermi surface cylinder, which is slightly warped along the interlayer direction. This phenomenon was described in Sec. 2.6 and will be further investigated in Sec. 5.12, where we examine SdH oscillations in a tilted magnetic field.

For instance, at 0.48 GPa, the two field values of the beating nodes are determined to 9.95 T and 12.63 T, respectively (Fig. 5.2). From these values, the warping of the Fermi surface can be roughly estimated using Eq. (2.25) to $\Delta k_\text{F}/k_\text{F} = \Delta F_\beta / 2F_\beta \approx 0.6 \times 10^{-2}$, where the experimental value $F_\beta(0.48\,\text{GPa}) \approx 3900\,\text{T}$ was used. This degree of warping is comparable to that observed in κ-Br [109, 184] and is approximately an order of magnitude stronger than in the related κ-NCS salt [185].

Fig. 5.3 illustrates examples of the SdH oscillations recorded at various pressures, normalized to the background resistance [$R_\text{osc} = R(B) - R_\text{bg}(B)$] [183]. The arrows mark the positions of the nodes in the beating pattern of the β-oscillations. As pressure increases up to 1.36 GPa, the beating nodes shift to higher magnetic fields in the range 11.7 T to 14.4 T (Fig. 5.3(a)), indicating an increase in the beating frequency by 25 %, while F_β increases by only 6 % (Fig. 5.8(a)). This implies an 18 % enhancement in Fermi surface warping.

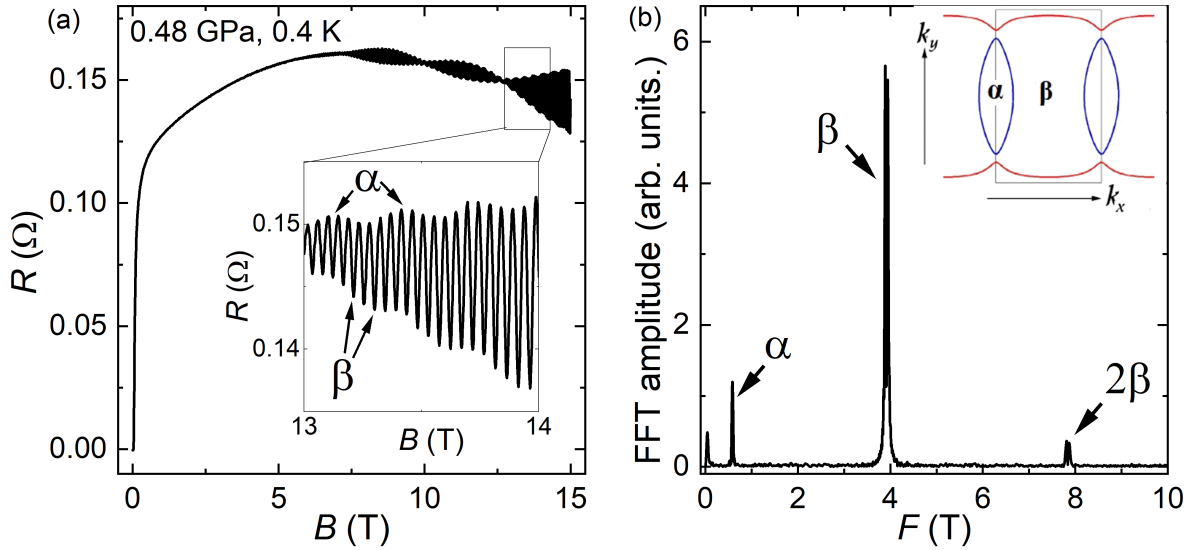

Figure 5.2: (a) Magnetoresistance of κ-Cl in the perpendicular to the layers magnetic field at a pressure of 0.48 GPa and a temperature of 0.4 K. Inset: enlarged view of the oscillations. (b) FFT of the oscillations in the magnetic field window 9 T to 15 T. Inset: 2D FS. Blue lines correspond to the classical α orbit, red lines represent open sheets, and the black rectangle denotes the first Brillouin zone [105].

Such a pressure-induced strengthening of the interlayer coupling is typical for layered organic conductors and is attributed to their relatively soft crystal structure. Interestingly, beyond 1.4 GPa, the node positions begin to shift to lower fields, suggesting a reduction in the beat frequency and an apparent weakening of the interlayer coupling at higher pressures. This unusual behavior at high pressures may warrant further investigation.

The amplitude of the SdH oscillations in Fig. 5.3(a) exhibits a non-monotonic variation with changing pressure. Fig. 5.3(b) shows the pressure dependence of the amplitudes of the main peaks in the FFT spectra, measured in the magnetic field range 12 T to 15 T. The magnitude of the β-oscillations displays pronounced minima at approximately 0.2 GPa and 0.9 GPa. Concurrently, the amplitude ratio between the second and first harmonics, $A_{2\beta}/A_{\beta}$ (Fig. 5.3(b), middle figure), exhibits sharp peaks at the same pressures. This distinct behavior strongly suggests the presence of the spin-zero effect (Sec. 2.2), which arises from the periodic modulation of the oscillation amplitude due to the spin-splitting factor (Eq. (2.12)). The Landé factor, g, in the spin-splitting factor is also renormalized and is expected to vary with pressure.

The pressure dependence of the α-oscillation amplitude is presented in Fig. 5.3(b) (bottom figure). Unlike the β-oscillations, no spin-zero dips are observed for the α-oscillations. This absence can likely be attributed to the significantly lower cyclotron mass, $m_{c,\alpha} \approx m_{c,\beta}/2$, which reduces the variation of the spin-reduction factor, R_S, under pressure. As shown in Fig. 5.9, $m_{\beta}(0.9\,\mathrm{GPa})$ is close to m_{α} at ambient pressure. Therefore, a spin-zero dip may be expected near ambient pressure, which would explain the low amplitude A_{α}.

The non-monotonic behavior of $A_{\alpha}(p)$, featuring a maximum near 0.5 GPa, might

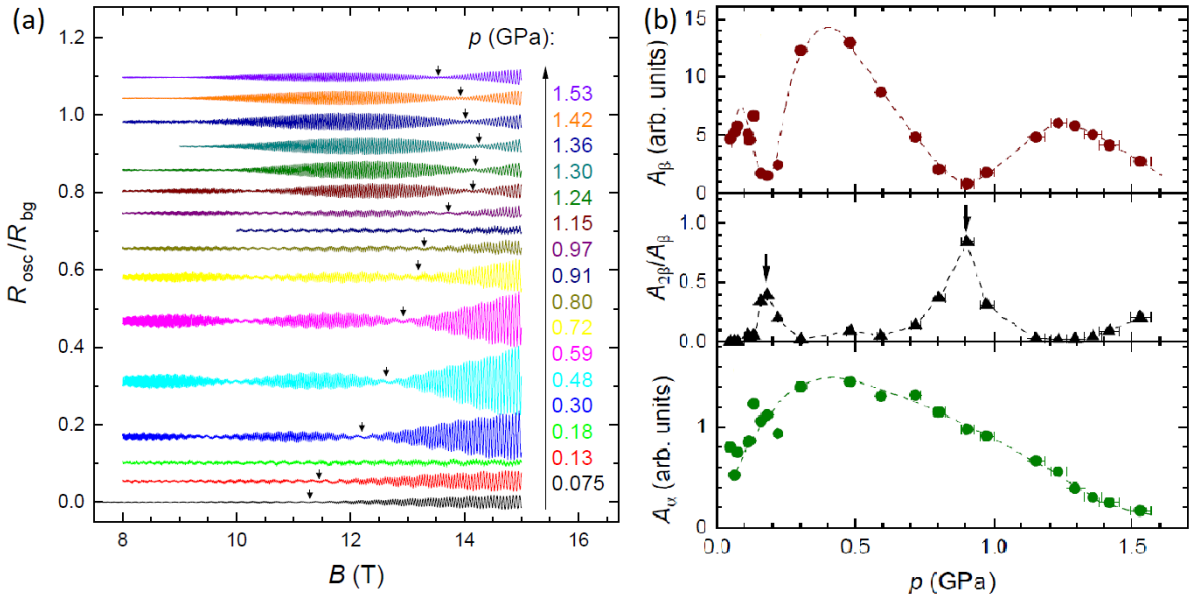

Figure 5.3: (a) SdH oscillations of the interlayer resistance of κ-Cl at different pressures, measured at $T \approx 0.38\,\mathrm{K}$. The magnetic field is applied perpendicular to the conducting layers. The curves are vertically shifted for clarity. Arrows indicate the pressure-dependent positions of the higher-field node in the beating pattern of the β-oscillations. (b) Pressure dependence of the FFT amplitudes of the SdH oscillations in κ-Cl, measured in the field window 12 T to 15 T at $T \approx 0.38\,\mathrm{K}$. Top: Amplitude of the β-oscillations. Middle: Ratio of the second to first harmonic of the β-oscillations. Bottom: Amplitude of the α-oscillations. Lines serve as guides to the eye. Graphs are taken from [183].

result from a gradual pressure-induced change in the spin-splitting factor $R_S(p)$. On the other hand, we note that $A_\alpha(p)$ dependence resembles the general trend observed in $A_\beta(p)$, excluding the modulation of A_β by the oscillating spin-splitting factor. Both amplitudes exhibit a global maximum near 0.5 GPa and tend to decrease at higher pressures. The mechanisms driving this behavior may be common for both the α- and β-oscillations. For instance, the initial increase in amplitude at low pressures might be linked to the rapid reduction of the cyclotron masses, which would reduce the temperature and scattering damping effects on the quantum oscillations, according to Eqs. (2.9) and (2.11). The gradual decline in the amplitude above 0.5 GPa could stem from a pressure-induced enhancement of Fermi surface warping, reflecting a stronger interlayer coupling. This enhancement likely reduces the number of charge carriers contributing coherently to the quantum oscillations, thereby suppressing the overall amplitude. Quantitatively, the FS-curvature factor appears in the denominator of the LK formula (Eq. (2.8)) [32]. Consequently, an increase in the interlayer transfer integral enhances the FS curvature, thereby reducing the amplitude of the SdH oscillations.

5.3 Effective dimer model

In this section, we briefly discuss the effective dimer model [186–188], which is commonly applied to the κ-salts. This model relates the ratio between the α- and β-oscillation frequencies to the electronic anisotropy of the conducting layers, in terms of the shape of the 2D Fermi surface. We follow the approach outlined by Pratt [188], which employs a tight-binding model for an anisotropic triangular lattice of BEDT-TTF dimers, characterized by the nearest-neighbor and next-nearest-neighbor transfer integrals, t and t', respectively (see Fig. 5.5(a)). The dispersion relation is given by:

$$E_{\pm} = 2t' \cos(k_y) \pm 4t \cos\left(\frac{k_x}{2}\right) \cos\left(\frac{k_y}{2}\right), \tag{5.1}$$

where k_x and k_y represent the wave vectors in the x- and y-directions within the plane of the conducting layers, normalized by the crystallographic parameters (a, c) and (b, c), respectively, as applicable to κ-Cl [90] and κ-NCS [92]. Fig. 5.4 shows the energy dispersion from Eq. (5.1) in energy units of $2t$.

The slice of E_- (Fig. 5.4(b)) at the Fermi energy level defines the closed pockets of the Fermi surface, which correspond to the α-orbit (S_α) and determine the associated SdH frequency, F_α. In contrast, the slice of E_+ (Fig. 5.4(a)) at the Fermi energy level forms the open sheets of the FS, which, in conjunction with the closed pockets, define the β-orbit (S_β) and its frequency, F_β (Fig. 5.5 inset). The SdH frequency and the corresponding FS area are connected through the Onsager relation (Eq. (2.5)). Thus, Eq. (5.1) provides a parametric description of the 2D Fermi surface. The primary parameter governing the FS shape is the spin frustration ratio t'/t, which reflects the anisotropy of the triangular lattice formed by the molecular dimers.

The inset in Fig. 5.5(b) shows the FS determined from Eq. (5.1) for $t'/t = 0.74$. It can be converted into nm^{-1} units using unit cell sizes. This FS can be used to determine the ratio between the α- and β-orbit areas. The same calculation was performed

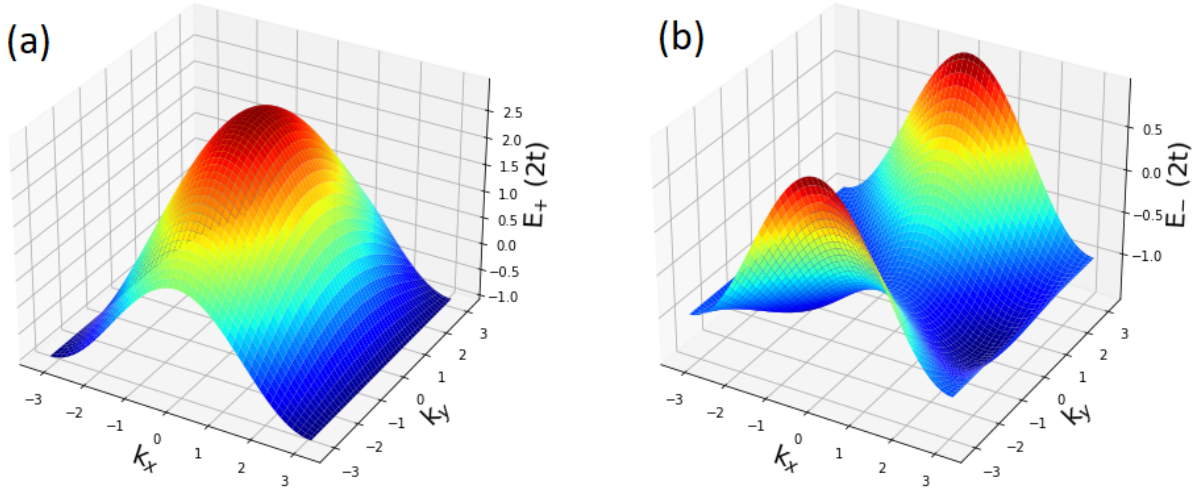

Figure 5.4: Energy dispersion from Eq. (5.1) for E_+ (a) and E_- (b), calculated for the frustration ratio $t'/t = 1.0$. The Fermi energy corresponds to $E_F \approx -0.42$, in units of $2t$.

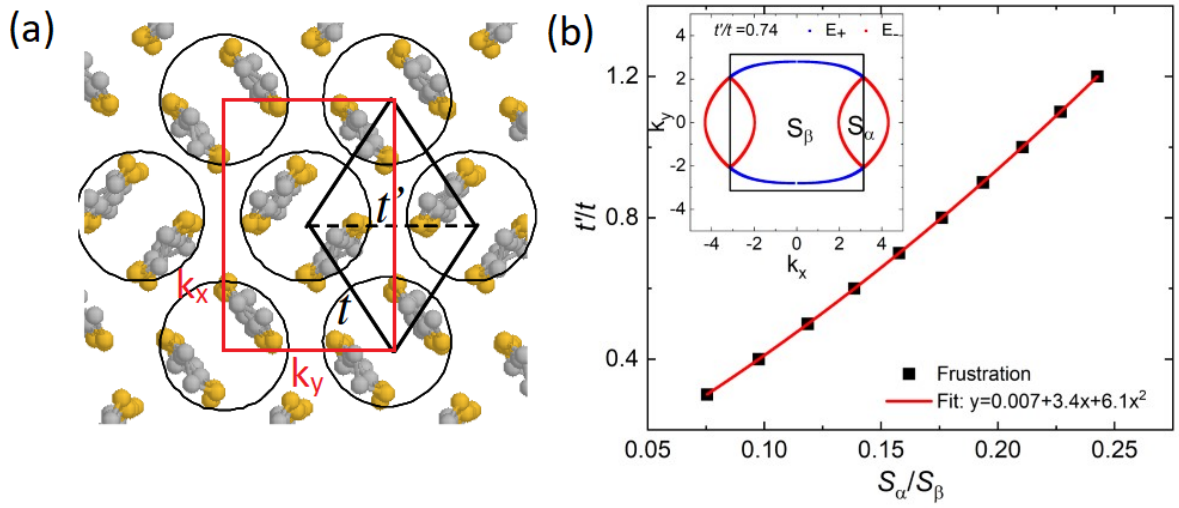

Figure 5.5: (a) Schematic representation of the dimer arrangement, showing the nearest-neighbor transfer integral t, the next-nearest-neighbor transfer integral t', and the directions of the axes k_x and k_y. (b) Dependence of the frustration ratio on the ratio of the α- and β-orbit areas. Inset: FS calculated for $t'/t = 0.74$ (blue and red curves), with the first Brillouin zone boundaries shown by black lines.

for different values of t'/t. Fig. 5.5(b) presents the dependence of the frustration ratio on the ratio between S_α and S_β, or equivalently, the frequencies ratio F_α/F_β. This plot serves as a direct reference for determining t'/t from the experiment. For easier interpolation, the frustration ratio points (black) are fitted with a second-order polynomial curve, represented by the red line in Fig. 5.5(b). The relationship is given by: $(t'/t)(x) = 0.0067 + 3.43x + 6.13x^2$, where $x = S_\alpha/S_\beta = F_\alpha/F_\beta$.

5.4 Frequency and cyclotron mass determination

To analyze the SdH data, several methods were implemented. The most conventional approach is through a FFT analysis. Fig. 5.6(a) shows the SdH oscillations at a pressure of $p \approx 0.11$ GPa and different temperatures. The oscillatory resistance component is normalized to the background resistance. Fig. 5.6(b) presents the FFT analysis of these oscillations in the field window 14 T to 15 T, using the Welch FFT windowing function. The field range was chosen to include approximately 10-15 oscillations, which is sufficient to ensure reliable averaging. At the same time, the variation of the oscillation amplitude over this field range remains negligible. According to [189], this approach allows the oscillation amplitude to be determined with an accuracy of 2 % to 3 %. The choice of the windowing function affects the absolute values of the FFT peaks; however, the ratio between peaks at different temperatures remains consistent. Therefore, the FFT windowing function has a negligible impact on the determination of the effective cyclotron mass [183]. Fig. 5.6(c) displays the temperature dependence of the FFT β-oscillation peak amplitudes, along with a fit using the LK formula with the temperature damping factor (Eq. (2.9)). The fit yields an effective cyclotron mass of

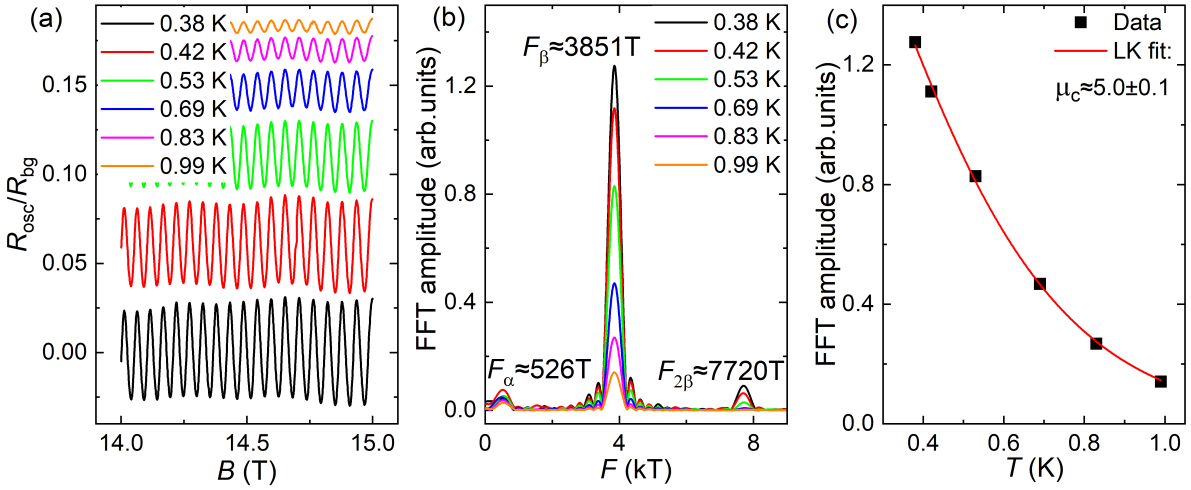

Figure 5.6: (a) Examples of the SdH oscillations in κ-Cl at $p = 0.11$ GPa and different temperatures. The curves are vertically shifted for clarity. (b) FFT spectra of the obtained oscillations using a 'Welch' window in the field range 14 T to 15 T. (c) LK plots of the β-oscillation amplitudes from the FFT panel (b).

$m_{c,\beta} \approx (5.01 \pm 0.08)m_0$. The β-oscillation frequency determined from FFT peak position is $F_\beta \approx 3851 \pm 10$ T.

Another method to determine the effective cyclotron mass and frequency is through a direct global fitting of the oscillations using the LK formula in Eq. (2.8) with the temperature and Dingle damping factors as fitting parameters. Fig. 5.7(a) shows the same oscillations from Fig. 5.6(a) in the field range 14.4 T to 14.8 T for better visibility (black points). These oscillations were fitted with the LK formula for β-oscillations (red lines) in the field range 14 T to 15 T. The fit reveals an effective mass of $m_{c,\beta} \approx (5.04 \pm 0.02)m_0$ and a frequency of $F_\beta \approx 3859 \pm 1$ T. Due to the large number of fitting points, the error bars in this method are significantly smaller and may be underestimated. Unfortunately, this method is not suitable for fitting oscillations with multiple frequencies and harmonics, as it would require additional terms in the fitting formula. This limitation is evident in the discrepancy between the fitting curve and the data at a temperature of 0.99 K in Fig. 5.7(a), where the α-frequency contribution becomes significant.

The values of the effective cyclotron mass and frequency obtained from both methods are consistent within the error margin, confirming the reliability of both approaches for our analysis. For further data analysis in this chapter, we used the method based on FFT analysis, as it allows to disentangle the contributions from the α- and β-oscillations and their harmonics. To calculate the β-frequency, we employed a method based on the period of oscillations. Fig. 5.7(b) shows the SdH oscillations in the field range 12 T to 15 T (black line) and their upper envelope (red line). The positions of the oscillation maxima from Fig. 5.7(b) are shown in Fig. 5.7(c) (black points), along with a linear fit (red line). The fit yields a frequency of 3854 ± 1 T. This value is also consistent with those obtained from the previous two methods, further validating the accuracy of our frequency determination. The high accuracy of the frequency determination is crucial for the evaluation of the spin frustration ratio t'/t. Therefore, this method was used for further determinations of the β-frequency.

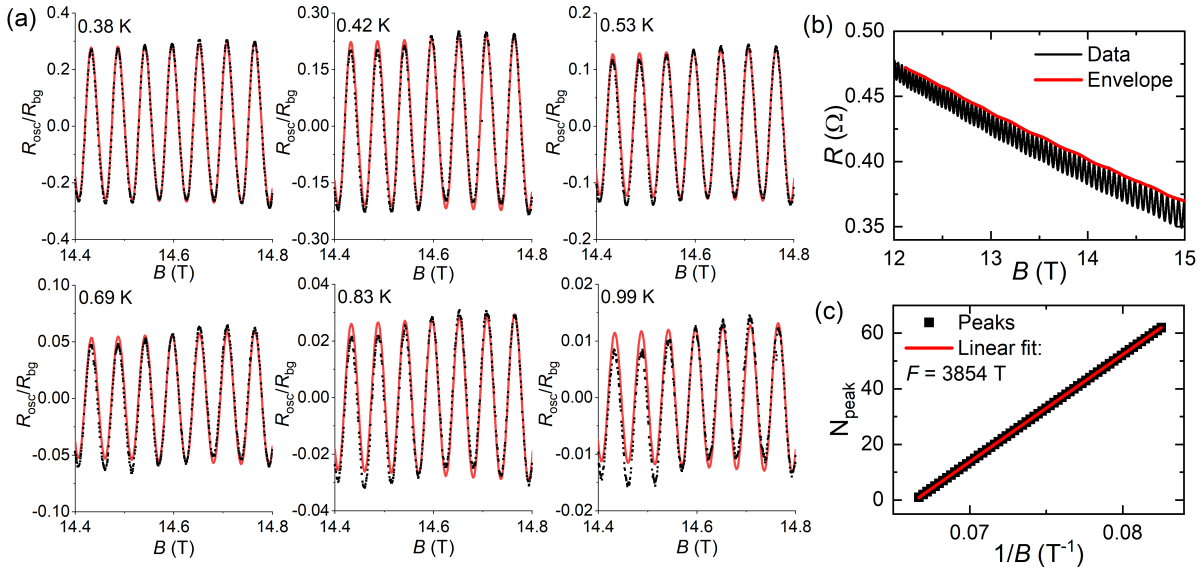

Figure 5.7: (a) Magnetoresistance oscillations in κ-Cl at $p = 0.11$ GPa at different temperatures (black points) and their global fit with the standard LK formula (red lines), using the frequency, phase, cyclotron mass, and Dingle temperature as common free parameters. The fit yields $m_{c,\beta} = 5.01\, m_0$ and $F_\beta = 3859$ T. (b) Magnetoresistance oscillations in κ-Cl at $p = 0.11$ GPa and $T = 0.38$ K (black line). The red line represents the upper envelope. (c) Positions of the maxima in the oscillations from panel (b). The red line shows a linear fit, yielding $F_\beta \approx 3854 \pm 1$ T.

5.5 Oscillation frequency and frustration ratio

In this section, we present a detailed analysis of the SdH frequencies, which are determined by the areas of the corresponding Fermi surface cross-sections. Fig. 5.8(a) illustrates the pressure dependence of the β-oscillation frequencies for κ-Cl (red symbols) and κ-NCS (blue symbols). The data points marked with stars represent measurements conducted by S. Oberbauer in a previous experiment on κ-Cl and κ-NCS at pressures up to 0.1 GPa [42] [110].

As discussed above, the β-oscillations are associated with the magnetic-breakdown orbit, whose area corresponds to the Brillouin zone area. This is confirmed by the zero-pressure frequency values: $F_\beta^{Cl}(0) = 3836 \pm 5$ T and $F_\beta^{NCS}(0) = 3867 \pm 7$ T, which correspond to Fermi surface areas of $36.62 \pm 0.05\,\mathrm{nm}^{-2}$ and $36.91 \pm 0.05\,\mathrm{nm}^{-2}$, respectively. Indeed, these values align precisely with the low-temperature Brillouin zone areas determined for these salts in the previous studies ($36.8\,\mathrm{nm}^{-2}$ for κ-NCS [190] and $36.6\,\mathrm{nm}^{-2}$ for κ-Cl [93]). The unit cell dimensions are provided in Sec. 3.1. This agreement provides strong evidence that the observed β-oscillations indeed correspond to the full Brillouin zone area, thereby confirming that one electron per dimer is effectively transferred to the anion layer.

The pressure dependence of the β-oscillation frequency, shown in Fig. 5.8(a) appears slightly different for the two salts, κ-Cl and κ-NCS. However, when the relative change in frequency with pressure is plotted (see Fig. 5.8(b)), it becomes evident that the dif-

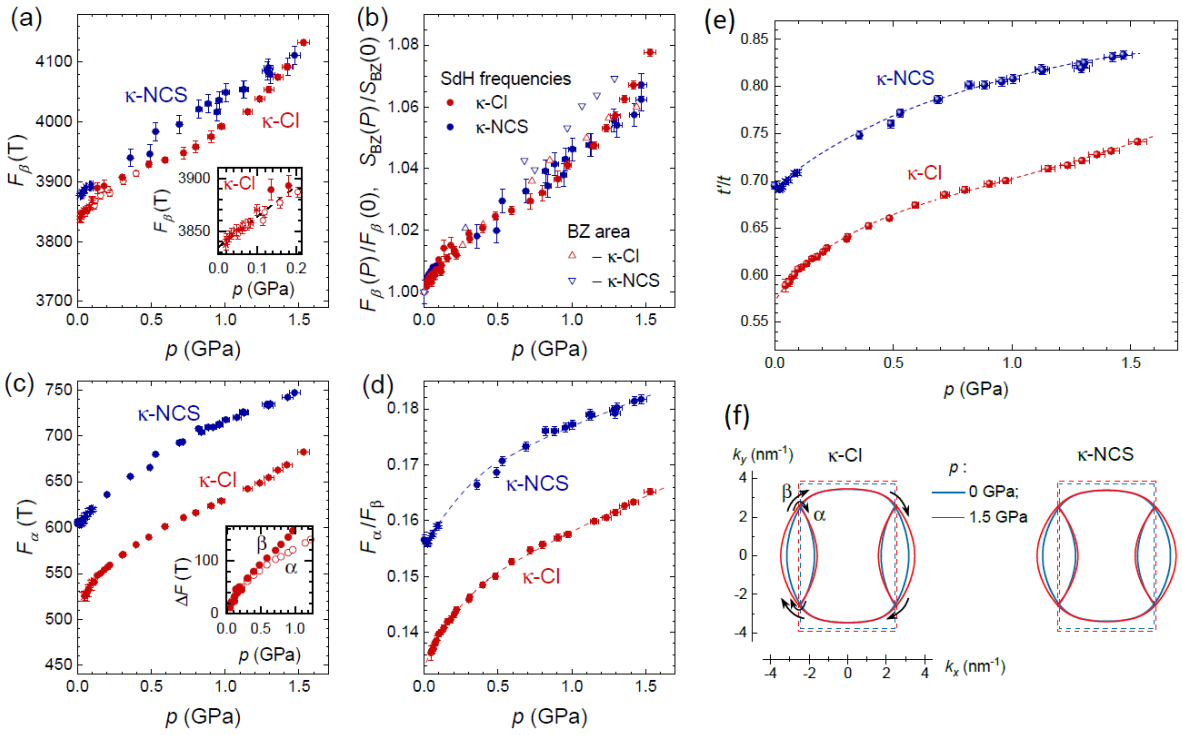

Figure 5.8: Pressure-dependent SdH frequencies in κ-Cl (red) and κ-NCS (blue). Different symbols represent different samples. (a) β-oscillations. Inset: close-up of the lower-pressure range for κ-Cl. The dashed line is a linear fit to the data, yielding the zero-pressure extrapolation $F_\beta(0) \approx 3840\,\mathrm{T}$. (b) The data from panel (a) normalized to the respective zero-pressure frequency (circles). For simplicity, no distinction between different samples is made. For comparison, the relative change of the pressure-dependent Brillouin zone area $S_{BZ}(p)/S_{BZ}(0)$ is shown by triangles. (c) α-oscillations. Inset: absolute changes of the α (open circles) and β (filled circles) frequencies in κ-Cl under pressure: $\Delta F = F(p) - F(0)$. (d) Pressure dependence of the ratio F_α/F_β. (e) Spin frustration ratio t'/t in κ-Cl (red) and κ-NCS (blue), calculated from the data in panel (d) using Eq. (5.1). (f) Solid lines: Fermi surfaces of κ-Cl and κ-NCS, calculated within the effective dimer model for ambient pressure and for $p = 1.5\,\mathrm{GPa}$. Dashed lines: respective Brillouin zone boundaries. The linear scales were calculated based on the low-T crystallographic parameters [90], [92] and room-temperature compressibilities [93], [190]. The arrows schematically indicate Bragg reflections and tunneling at the magnetic-breakdown junctions, leading respectively to the α and β orbits in strong magnetic fields. Taken from [183].

ferences between the two salts fall within the experimental error bars.

Additionally, our data align well with the quasi-linear pressure dependence of the Brillouin zone areas (represented by triangles in Fig. 5.8(b)) derived from previous X-ray studies [93]. It is worth noting that the X-ray measurements were conducted at room temperature. The excellent agreement between these room-temperature results and our low-temperature SdH data suggests that the compressibility of the salts does not vary significantly upon cooling.

Fig. 5.8(c) shows the pressure dependence of the α-frequency obtained in our experiment. For κ-NCS, our dataset agrees well with the earlier study by Caulfield et al. [186]. As noted by those authors, the relative increase of F_α with pressure is significantly stronger than that of F_β. At a pressure of 1.5 GPa, F_β increases by approximately 8 %, while F_α increases by nearly 24 %. A similar but even more pronounced trend is observed for κ-Cl, where F_β and F_α increase by 7 % and 29 %, respectively.

At lower pressures, $p < 0.3$ GPa, the relative rate of increase for the α-frequency, dF/Fdp, is approximately 0.25 GPa^{-1} for κ-NCS and 0.4 GPa^{-1} for κ-Cl. In comparison, the relative increase rate for the β-frequencies, shown in Fig. 5.8(b), is much smaller, around 0.04 GPa^{-1}. Interestingly, for κ-Cl, the absolute changes in $F_\alpha(p)$ and $F_\beta(p)$ within this pressure range are nearly identical, as shown in the inset of Fig. 5.8(c). This suggests that, despite the rapid expansion of the α-pocket, the rest of the Fermi surface remains largely unchanged at lower pressures.

At higher pressures, the increase of F_α becomes more moderate, with the slope saturating around 0.15 GPa^{-1}. For κ-NCS, due to the weaker β-oscillations at $p < 0.3$ GPa, an accurate comparison of $\Delta F_\alpha(p)$ and $\Delta F_\beta(p)$ is challenging. However, qualitatively, the behavior of κ-NCS at higher pressures appears similar to that observed for κ-Cl.

The difference in the pressure-dependent behaviors of the α- and β-frequencies is summarized in Fig. 5.8(d) as the ratio $F_\alpha/F_\beta(p)$. Using this data along with the fitting polynomial for $t'/t(S_\alpha/S_\beta)$ (Fig. 5.5(b)), we evaluate the frustration ratio t'/t and its pressure dependence for both salts, as shown in Fig. 5.8(e).

The first notable observation is that t'/t is closer to unity in κ-NCS, indicating significantly stronger spin frustration in the metallic κ-NCS salt compared to the ambient-pressure Mott insulator κ-Cl. The ambient-pressure values of the frustration ratio for κ-NCS and κ-Cl are 0.69 and 0.58, respectively. While this difference in frustration ratio has been predicted by some band structure calculations (0.58 for κ-NCS and 0.44 for κ-Cl [96]), our experimental results show a considerable quantitative difference from the calculated values.

Another notable observation is that, even under our quasi-hydrostatic pressure conditions, the electronic anisotropy within the conducting layers is significantly affected, leading to an enhancement of spin frustration. This result also apparently disagrees with the calculations [96], which predict no significant change in the frustration ratio under pressure. Over a broad pressure range, the t'/t ratio increases at an approximately constant rate of 0.07 GPa^{-1}. This rate further increases below 0.3 GPa, as the system approaches the MIT. The overall increase in the frustration ratio across the studied pressure range exceeds 20 %. Notably, at 1 GPa, the frustration in κ-Cl surpasses the ambient-pressure value observed for κ-NCS.

In Fig. 5.8(f), we present the Fermi surfaces of κ-Cl and κ-NCS, calculated using Eq. (5.1) and the experimental SdH frequencies at both the lowest and highest pressures. Although the compressibility of the crystal lattice is assumed to be isotropic within the plane of the layers - based on the room temperature studies [93, 190] - the observed changes in the Fermi surfaces of both salts are clearly anisotropic. The α-pocket in Fig. 5.8(f) undergoes significant expansion along its short axis (k_x), while the rest of the Fermi surface remains essentially unchanged. This behavior is consistent with the same absolute changes of frequencies $\Delta F_\beta(p)$ and $\Delta F_\alpha(p)$ at pressures up to 0.3 GPa as discussed above (see the inset of Fig. 5.8(c)). At higher pressures, however, $\Delta F_\beta(p)$ and

$\Delta F_\alpha(p)$ start to diverge (see the inset of Fig. 5.8(c)), indicating that the Fermi surface also begins to expand in the k_y-direction. The apparent absence of this k_y-expansion in the calculated FS in Fig. 5.8(f) is likely due to the limited precision of the simple effective dimer model used for these calculations. A more refined analysis, incorporating 'ab initio' band structure calculations that explicitly account for electronic correlations, would provide a more realistic FS. However, such a calculation would be highly challenging, requiring detailed low-temperature structural data under high pressures.

5.6 Effective mass renormalization and correlation strength

The results for the cyclotron mass (in units of the free electron mass m_0) associated with the β-orbit [183] are presented in Fig. 5.9(a). For κ-Cl, the mass values were averaged across the two samples. The green symbols represent the cyclotron mass for the κ-NCS salt, with data obtained by S. Fust [178] (filled triangles) and S. Oberbauer [42, 110] (empty triangles). In κ-NCS, the β-oscillations are relatively weak due to a larger magnetic breakdown gap, leading to larger error bars and an increased scatter of the data.

Within the experimental error, the κ-Cl and κ-NCS salts exhibit a similar behavior. At low pressure, the cyclotron mass ($m_{c,\beta}$) decreases rapidly as the system moves away from the MIT. This decrease slows down with increasing pressure and saturates above 1 GPa at approximately $m_{c,\beta} \approx 2.5 m_0$. Notably, this saturated value is close to the band cyclotron mass, $m_{c,\beta,\mathrm{band}} = 2.6 m_0$ [191], calculated for κ-NCS from the band structure without considering many-body interactions. This suggests that, at pressures above 1 GPa, the system effectively behaves as a non-interacting electron system.

Given that the primary change within the pressure range $0 < p < 1$ GPa is the electronically driven MIT, the effective mass renormalization is naturally attributed to electronic correlations. Other potential renormalization mechanisms, such as electron-phonon interactions, are not expected to vary significantly in this pressure range and thus likely play a negligible role. This argument is further supported by analyzing the pressure-dependent effective mass in terms of the electronic correlation strength ratio U/t. In particular, the observation that the cyclotron masses $m_{c,\beta}$ for κ-Cl and κ-NCS are very similar across the whole pressure range and converge to the same high-pressure limit, $m_{c,\beta,\mathrm{band}}$, confirms the earlier conclusion [110], drawn from lower-pressure data, that the correlation strength is essentially the same in both salts.

Turning to a more quantitative analysis, the previous low-pressure experiment [110] revealed an inverse-linear pressure dependence of the mass, which was interpreted using a Brinkman-Rice-like (BR-like) renormalization formula. However, the present data, covering a broader pressure range, indicate a deviation from this behavior starting at approximately $p = 0.25$ GPa. This deviation is clearly illustrated in the inset of Fig. 5.9(a), where the inverse mass (m_c^{-1}) for κ-Cl is plotted. The dashed line represents a linear fit to the low-pressure data from [110].

The linear relationship, $m_c^{-1} \propto (p - p_0)$, inferred from BR theory [77], assumes a linear pressure dependence of the correlation strength ratio U/t. This approximation is valid within a narrow pressure interval near the MIT, where the change in U/t is

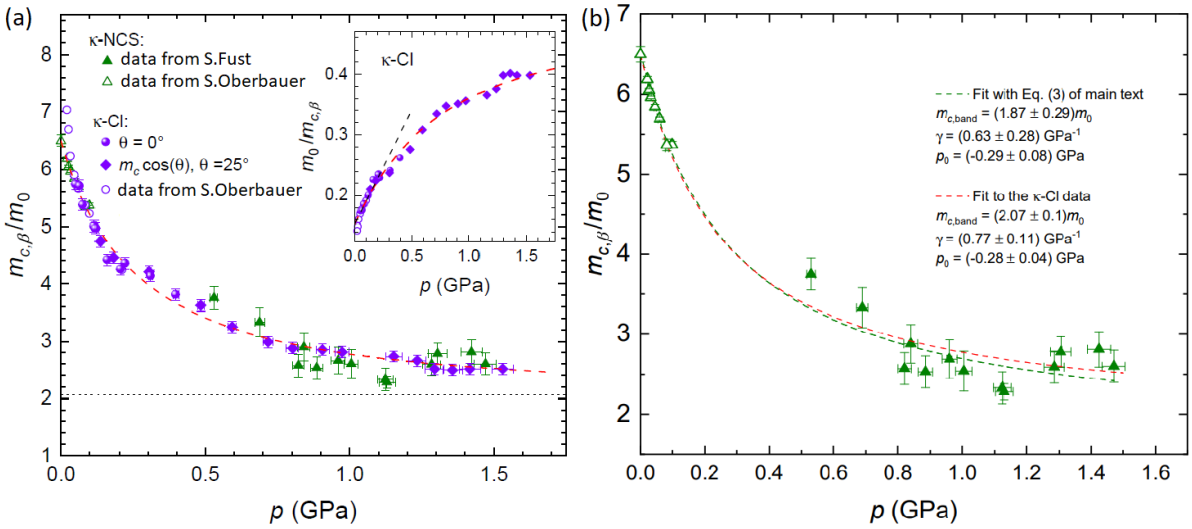

Figure 5.9: (a) Pressure dependence of the effective cyclotron mass on the β-orbit for κ-Cl (purple) and κ-NCS (green). The data is normalized by the free electron mass m_0. Results from the present experiment and the lower-pressure study [110] are shown by filled and empty points, respectively. The red dashed line represents a fit to the κ-Cl data using Eq. (5.2). The horizontal dotted line indicates the level of the non-interacting band cyclotron mass $m_{c,\beta,\text{band}}$ obtained from the fit. Inset: The inverse mass of κ-Cl versus pressure. The red line represents the same fit as in the main panel, while the black straight line corresponds to the linear fit from [110]. (b) Pressure dependence of the effective cyclotron mass on the β-orbit for κ-NCS. The solid triangles represent masses obtained in the present experiment, while the hollow triangles correspond to data from [42, 110]. The green dashed line represents the best fit to the data using Eq. (5.2). For comparison, the red dashed line shows the best fit to the κ-Cl data from panel (a). Taken from [183].

relatively small (1 % to 2 %) [110]. However, over a broader pressure range, this approximation becomes inaccurate.

In reality, the inter-dimer transfer integral t is significantly more sensitive to pressure than the on-site (intra-dimer) Coulomb repulsion U [96]. Thus, a more accurate approach is to assume $U = \text{const}$ and expand t, rather than U/t, linearly with pressure: $t(p) \approx t_0[1+\gamma(p-p_0)]$, where p_0 is the critical pressure at which the mass diverges in the BR model, $t_0 = t(p_0)$, and γ is a proportionality factor. Further, following [123], we set the correlation strength as: $\left(\frac{U}{t}\right)(p) = \frac{U}{t(p)} \approx \frac{U}{t_0[1+\gamma(p-p_0)]} = \left(\frac{U}{t}\right)_0 [1+\gamma(p-p_0)]^{-1}$. Then, the BR renormalization of the effective mass [77],

$$m_c = m_{c,\text{band}} \left[1 - \left(\frac{(U/t)}{(U/t)_0}\right)^2\right]^{-1},$$

can be expressed as

$$\frac{m_c}{m_{c,\text{band}}} = \left(1 - \frac{1}{[1+\gamma(p-p_0)]^2}\right)^{-1}. \tag{5.2}$$

Salt	κ-Cl	κ-NCS
$m_{c,\beta,\text{band}}$ (m_0)	2.07 ± 0.1	1.9 ± 0.3
p_0(GPa)	-0.28 ± 0.04	-0.29 ± 0.08
γ(GPa^{-1})	0.77 ± 0.11	0.63 ± 0.28

Table 5.1: Parameters used for fitting the pressure dependence of the effective cyclotron mass, $m_{c,\beta,\text{band}}(p)$, for κ-Cl and κ-NCS with the BR-like Eq. (5.2).

Here, we substituted the usual quasiparticle effective mass m^* and band mass m_{band} used in the original BR theory [77] with the respective cyclotron masses considered in the Lifshitz-Kosevich theory of magnetic quantum oscillations. This substitution is justified because the many-body renormalization effects are equivalent in both cases [32]. Despite its relatively simple form, Eq. (5.2) provides an excellent fit to the experimental data across the entire pressure range, as illustrated by the red dashed line in Fig. 5.9(a), which represents the fit to the κ-Cl data. This fit yields realistic estimates for the key parameters characterizing the electronic system, as shown in Table 5.1.

The fit to the κ-NCS dataset (Fig. 5.9(b)) results in very similar parameters, though with considerably larger error bars (see Table 5.1). The evaluated band mass is smaller than the previously calculated value of $2.6m_0$ [191], but this difference falls within the uncertainty of the band structure calculations [192, 193]. The relatively large error bars in the $m_{c,\beta}(p)$ dependence for κ-NCS are primarily due to the low amplitude of the magnetic-breakdown β-oscillations. To draw more definitive conclusions, additional measurements at higher magnetic fields ($B > 30$ T) would be highly beneficial.

The BR critical pressure p_0 obtained in this study is comparable to the value derived from the simpler low-pressure fit [110], as shown by the dashed straight line in the inset of Fig. 5.9(a). The sensitivity of the electronic correlation strength to pressure is described by the coefficient γ ($\gamma dp = dt/t_0$). The experimentally determined γ is approximately an order of magnitude larger than the value inferred from band structure calculations [96]. These calculations suggested that the U/t ratio in κ-NCS decreases by only 5 % as pressure increases from 0 to 0.75 GPa, corresponding to $\gamma \approx 0.07\,\text{GPa}^{-1}$. In contrast, the present analysis yields $\gamma \approx 0.77\,\text{GPa}^{-1}$, indicating a significant discrepancy between experimental and theoretical results.

A similar disagreement between theory and experiment was previously noted in data taken within a narrow pressure range near the MIT [110]. This study now confirms that the discrepancy persists across a much broader pressure range, extending even to conditions where the effective mass no longer follows an inverse-linear dependence on p and approaches the non-interacting band mass. This suggests that current theoretical models may underestimate the impact of pressure on electronic correlation strength, necessitating a re-evaluation of the assumptions underlying these calculations.

Thus far, we have focused on the cyclotron mass associated with the magnetic-breakdown β-orbit, which encircles the entire 2D Fermi surface. It is interesting to compare this with the mass on the classical α-orbit, which involves only one-half of the charge carriers. Such a comparison may provide insights into the momentum de-

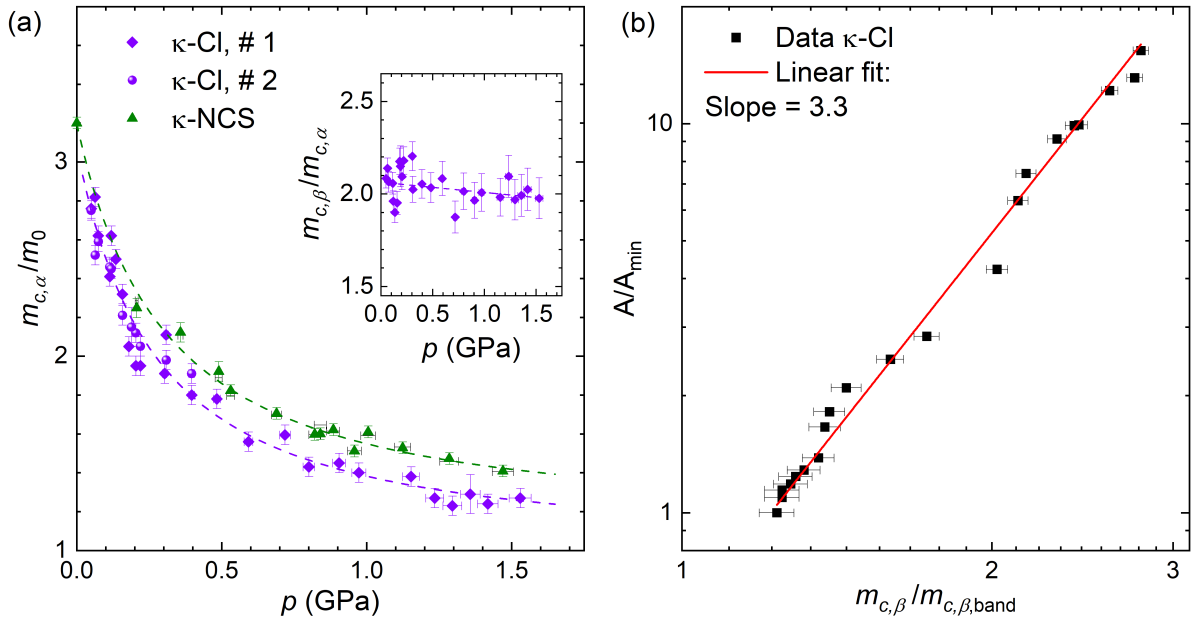

Figure 5.10: (a) Pressure dependence of the effective cyclotron mass on the α orbit for κ-Cl (purple) and κ-NCS (green). The dashed lines are fits with Eq. (5.2). Inset: the ratio of the β- and α-masses for κ-Cl. (b) Interdependence of the effective cyclotron mass of the β orbit, $m_{c,\beta}$, and the Fermi liquid coefficient A (from Fig. 5.1(b)) plotted on a double logarithmic scale (black dots). The effective mass is normalized to the band mass $m_{c,\beta,\mathrm{band}}$, while the coefficient A is normalized to its minimum value $A_{\mathrm{min}} = 8.3 \times 10^{-4}\,\Omega\,\mathrm{cm\,K^{-2}}$. The red line represents a linear fit with a slope of 3.3 ± 0.1.

pendence of electronic interactions. Fig. 5.10(a) presents our results for the pressure dependence of $m_{c,\alpha}(p)$ in κ-Cl and κ-NCS.

For κ-Cl, the α-mass is nearly exactly one-half of the β-mass, a relationship that remains virtually independent of pressure. To illustrate this, the ratio $m_{c,\beta}/m_{c,\alpha}$ is plotted in the inset of Fig. 5.10(a). A linear fit to the data (dashed line in the inset) shows a very slight slope of $-0.055 \pm 0.004\,\mathrm{GPa}^{-1}$, which lies within the experimental error bars. This weak variation, if it exists at all, may be attributed to the weak pressure dependence of the band masses. The blue dashed line in the main panel of Fig. 5.10(a) represents a BR fit based on Eq. (5.2), yielding the fit parameters shown in Table 5.2.

As expected, the band mass $m_{c,\alpha,\mathrm{band}}$ is approximately one-half of the β-band mass derived above. The other two parameters, p_0 and γ, closely match those obtained for the β-orbit. Overall, there is no evidence of any significant difference in mass renormalization between the α- and β-orbits [194]. Within the experimental accuracy, the electronic correlations in κ-Cl appear to be momentum-independent. For the κ-NCS salt (green triangles in Fig. 5.10(a)), the α-mass is about 10 % higher than that of κ-Cl. This difference is likely due to the larger size of the α-orbit in κ-NCS, resulting in a higher band cyclotron mass.

The pressure sensitivity γ is nearly identical for κ-Cl and κ-NCS and is close to the value obtained from the β-mass fit. The lower p_0 value for the α-orbit might indicate weaker electronic correlations on this part of the Fermi surface. If so, this would

Salt	κ-Cl	κ-NCS
$m_{c,\alpha,\text{band}}$ (m_0)	1.05 ± 0.07	1.18 ± 0.06
p_0(GPa)	-0.29 ± 0.04	-0.33 ± 0.03
γ(GPa^{-1})	0.81 ± 0.16	0.78 ± 0.13

Table 5.2: Parameters used for fitting $m_{c,\alpha}(p)$ for κ-Cl and κ-NCS with the BR-like Eq. (5.2).

suggest that correlation effects in κ-NCS slightly vary across the Fermi surface, being weaker on the α-pocket and stronger on the open sheets. However, it is important to note that the differences in p_0 are small and comparable with the evaluation error bars.

Knowing the pressure dependence of the effective mass, we can compare it with the Fermi liquid coefficient A (see Eq. (2.27)) and test the validity of the Kadowaki-Woods relation ($A \propto (m^*)^2$, see Sec. 2.7). Fig. 5.10(b) presents the dependence of the coefficient A on the effective cyclotron mass $m_{c,\beta}$ for the β-orbit, plotted on a double logarithmic scale (black dots). The effective mass is normalized to the band mass $m_{c,\beta,\text{band}} = 2.07\, m_0$, and the coefficient A is normalized to its minimum value, $A_{\text{min}} = 8.3 \times 10^{-4}\,\Omega\,\text{cm}\,\text{K}^{-2}$, at a pressure of 1.5 GPa. The red line represents a linear fit in the logarithmic scale, yielding a slope of 3.3 ± 0.1. This result corresponds to a cubic dependence of A on $m_{c,\beta}$, which significantly deviates from the quadratic dependence predicted by the Kadowaki-Woods law. This observation is very interesting and calls for further experimental investigation and theoretical clarification.

5.7 Angle-dependent magnetoresistance oscillations

The data on the SdH oscillations, presented above, provide information about the size of the FS and its evolution under pressure. Another important aspect that needs investigation is the precise shape of the FS within the plane of the conducting layers and its corrugation in the perpendicular direction.

To gather further information about the FS, we investigated the angle-dependent magnetoresistance oscillations (AMRO) (see Sec. 2.4). Fig. 5.11 displays the interlayer resistance as a function of the polar angle θ at a magnetic field strength of $B = 15\,\text{T}$ and a temperature of $T = 1.4\,\text{K}$. The AMRO data are presented for two pressure values: 0.3 GPa (Fig. 5.11(a)) and 1 GPa (Fig. 5.11(b)). For each pressure, measurements were performed at three distinct azimuthal angles φ, listed below. A visual representation of the φ and θ angles with respect to the sample unit cell axes is shown in the inset of Fig. 5.12(b).

- $\varphi = 0°$ (black curves): Corresponding to the field rotation in the ab-plane, where b represents the interlayer axis and a is the longer in-plane lattice period.
- $\varphi = 90°$ (green curves): Corresponding to the field rotation in the bc-plane, where c represents the shorter in-plane lattice period.

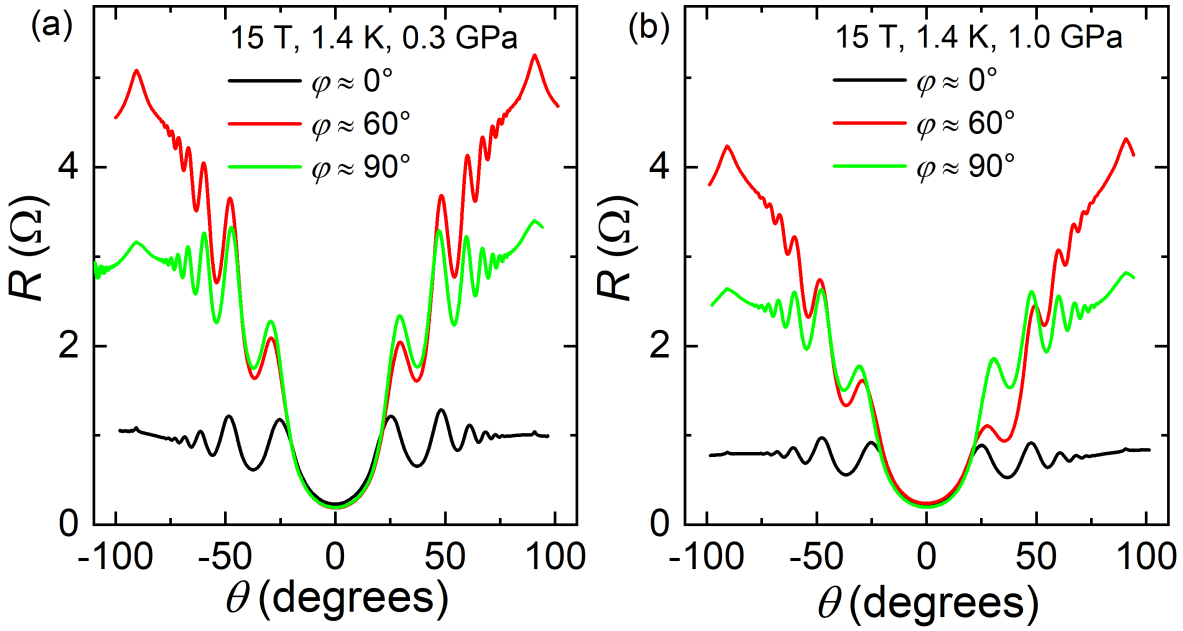

Figure 5.11: Interlayer resistance as a function of the polar angle (θ) at $B = 15\,\mathrm{T}$ and $T = 1.4\,\mathrm{K}$, measured at pressures of 0.3 GPa (a) and 1 GPa (b). Different curves represent measurements at various azimuthal angles: $\varphi = 0°$ (black), $\varphi = 60°$ (red), and $\varphi = 90°$ (green). The zero azimuthal angle ($\varphi = 0°$) corresponds to rotation in the plane with the longer in-plane lattice period a.

- $\varphi = 60°$ (red curves): Representing an intermediate orientation, which exhibits the highest in-plane magnetoresistance.

At both pressures, the AMRO data exhibit similar characteristics. Magnetoresistance peaks are observed at Yamaji angles (see Sec. 2.4) and are accompanied by a weak coherence peak around $\theta = 90°$. The AMRO amplitudes observed in our measurements are significantly stronger than those reported in [108], indicating a higher quality of the samples. The enhanced amplitude also enables a more accurate determination of the peak positions. Moreover, the data from [108] show almost no discernible coherence peak, whereas in our measurements a well-defined peak structure is clearly observed.

5.8 Determination of the Fermi surface

The positions of the AMRO peaks can be fitted using Eq. (2.19) (see Fig. 5.12(a)). The slope of the resulting linear fit (inset of Fig. 5.12(a)) yields the coefficient used to calculate $k_B^{\max}$, which corresponds to the maximum projection of the in-plane Fermi wave vector onto the plane of magnetic field rotation.

In case the Fermi surface is not highly anisotropic or does not exhibit pronounced bending, $k_B^{\max}$ serves as a reasonable approximation for the in-plane Fermi wave vector k_F. Therefore, in the following consideration, we will treat them as equivalent and neglect any difference between them. A more accurate determination of the Fermi

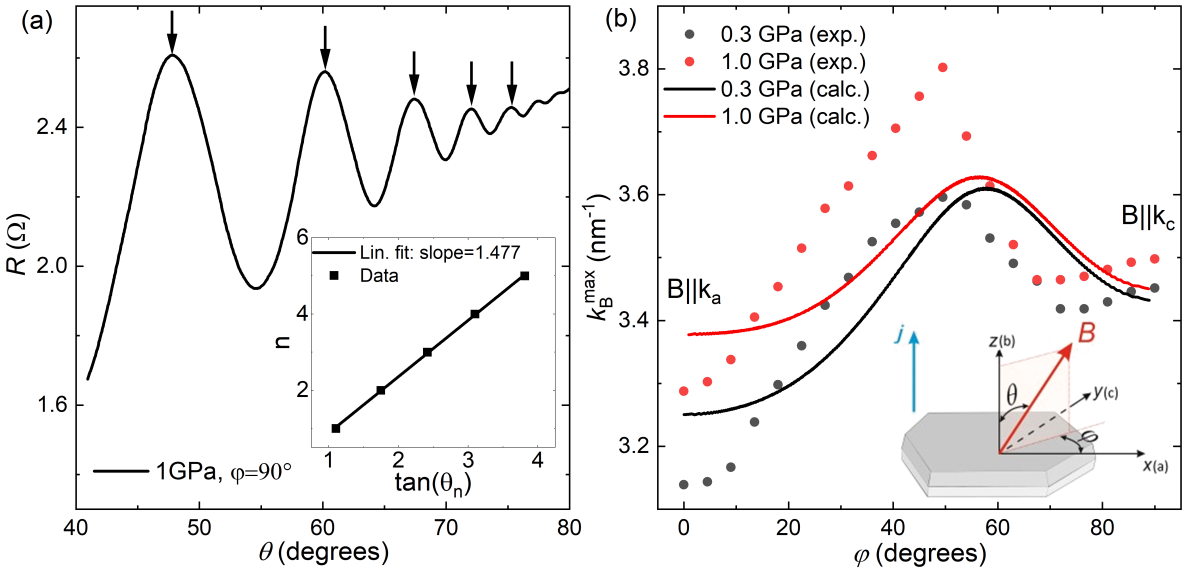

Figure 5.12: (a) AMRO curve at 1.0 GPa and $\varphi \approx 90°$. Arrows indicate the positions of the peaks used for fitting. Inset: Peak index as a function of the tangent of the θ angle (dots) with a linear fit (black line). (b) The wave vector $k_B^{\max}$ (see Eq. (2.19)) at different azimuthal angles φ at pressures of 0.3 GPa (black) and 1 GPa (red), calculated from experimental AMRO measurements (dots) and from a effective dimer model with a corresponding frustration ratio (black and red lines), see Sect. 5.3. Inset: Schematic representation of the sample unit cell axes and the φ and θ angles.

surface geometry is provided in Appendix 9. Fig. 5.12(b) shows the values of $k_B^{\max}$ obtained from the AMRO data at two different pressures: 0.3 GPa (black dots) and 1 GPa (red dots).

It is evident that an applied pressure compresses the sample, leading to an increase in the transfer integral and, hence, the bandwidth and the Fermi wave vector. Consequently, at all angles φ, k_F at 1 GPa is expected to be larger than that at 0.3 GPa. However, the change in k_F is not isotropic: pressure enhances k_F more significantly along the longer in-plane lattice period a compared to the shorter lattice period c (Fig. 5.12(b) inset).

This means that the area of the FS corresponding to the α-orbit, which is determined by k_F at low φ angles, grows more significantly than the rest of the FS. As a result, F_α exhibits a more pronounced increase compared to F_β. The increase in the frequency ratio also indicates an increase in the frustration ratio, leading to a more isotropic FS. This finding is fully consistent with the results from SdH measurements discussed in previous sections, where the relative increase of F_α with pressure was stronger than that of F_β.

Using $k_F(\varphi)$ from our AMRO measurements, we can construct the FS shape. Fig. 5.13 displays the FS (black dots) at pressures of 0.3 GPa (left) and 1 GPa (right). The FS is closer to a rectangular shape rather than an elliptical one. Additionally, the shape becomes more square-like with increasing pressure, and the sharp bending near the intersection with the Brillouin zone becomes more pronounced. Meanwhile, the arcs along k_x and k_y axes become flatter and exhibit an increased tendency for FS nesting.

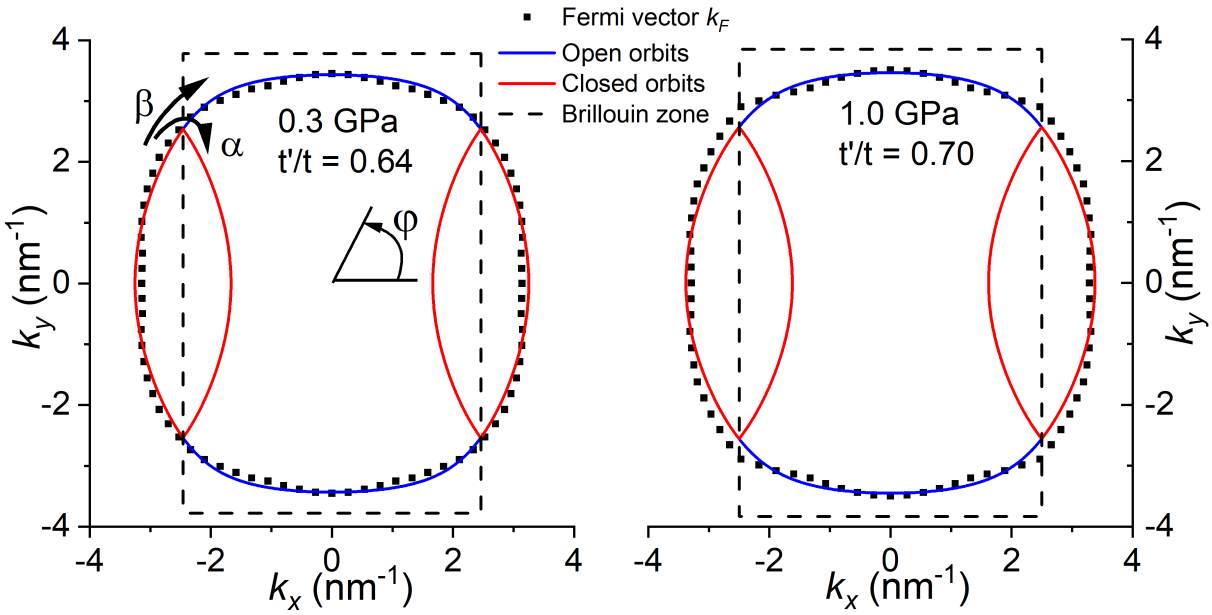

Figure 5.13: Black dots represent the in-plane Fermi surface at pressures of 0.3 GPa (left) and 1 GPa (right), calculated from the AMRO positions. The red and blue lines correspond to closed (red) and open (blue) Fermi sheets, respectively, calculated from the SdH frequencies using the effective dimer model in Sec. 5.3. The black dashed line indicates the first Brillouin zone.

Furthermore, the FS derived from the AMRO can be compared with that calculated using an effective dimer model and the SdH frequencies, as discussed in Sec. 5.5. In Fig. 5.12(b), the black and red lines represent k_F values derived from the effective dimer model. A comparison between the experimental k_F values from AMRO measurements and the model calculations reveals a generally consistent overall picture, with closely matching areas for the α- and β-orbits. Fig. 5.13 also shows the FS based on the SdH frequencies. Red lines correspond to the closed pocket, while blue lines represent the open sheets (in the effective dimer model Eq. (5.1), the gap between the sheets is absent). The difference between the FS calculated using the effective dimer model and the FS measured via AMRO is small.

For our calculations, unit cell dimensions from [90] at 15 K and ambient pressure were used. Adjustments for higher pressures were made by accounting for changes in SdH frequencies (see Sec. 5.5), under the assumption of isotropic lattice compression.

Pressure	$a(x)$[nm]	$b(z)$[nm]	$c(y)$[nm]	t'/t
0.3 GPa	1.278	2.922	0.832	0.64
1.0 GPa	1.257	2.874	0.819	0.70

Table 5.3: Unit cell dimensions and frustration ratio of κ-Cl. The dimensions of the unit cell at ambient pressure are taken from [90] and adjusted for higher pressures (see text).

All the relevant values are summarized in Table 5.3.

5.9 AMRO simulations

As observed in the AMRO curves (Fig. 5.11), the resistance value in a parallel magnetic field ($\theta = 90°$) varies significantly for different φ orientations, indicating a strong anisotropy in the resistance. In the following, we refer to this strong phi-dependence of magnetoresistance in an in-plane magnetic field as an 'in-plane magnetoresistance anisotropy'. One possible reason for this anisotropy is the anisotropic shape of the FS and interlayer transfer integral. Another important factor influencing the resistance is the scattering rate. It is possible that the scattering rate in our compound is also anisotropic and may contribute to the observed resistance anisotropy. To disentangle the contributions of the Fermi wave vector and the scattering rate to the resistance anisotropy, we perform numerical calculations.

Following the methods outlined in [49, 195, 196], the θ- and φ-dependent interlayer magnetoresistance can be computed using the FS shape and energy dispersion. To achieve this, we calculate the interlayer conductivity by solving Eq. (2.14) within the relaxation time approximation, which leads to the Chambers expression

$$\sigma_{zz} = 2e^2 \int \frac{d^3k(0)}{(2\pi)^3} \left(-\frac{\partial f}{\partial \epsilon}\right) v_z[\boldsymbol{k}(0)] \int_0^\infty dt\, v_z[\boldsymbol{k}(t)] e^{-t/\tau}, \tag{5.3}$$

where f represents the Fermi distribution function, τ denotes the electron scattering time, and the first integral is taken over the electron wave vector $\boldsymbol{k}(t=0)$, which serves as the initial condition for determining $\boldsymbol{k}(t)$. The electrons circle around the Fermi surface along closed orbits obtained by intersecting the Fermi surface with planes perpendicular to the magnetic field. These planes are labeled by the component $k_{b\parallel}$ of the electron wave vector parallel to the magnetic field. Consequently, the integral can be evaluated over the period of the motion on the orbit, T [195]:

$$\sigma_{zz} = \frac{e^3 H}{4\pi^3 \hbar^2 c} \frac{1}{1-\exp(-T/\tau)} \int dk_{b\parallel} \int_0^T dt\, v_z[\boldsymbol{k}(t)] \int_0^T dt'\, v_z[\boldsymbol{k}(t-t')] e^{-t'/\tau}.$$

We can switch from integration over time to integration over the position on the orbit. The integration time is related to the angle ϕ of the position on the FS as $d\phi = \omega_c \cos(\theta)\, dt$, with $2\pi = \omega_c \cos(\theta) T$. Fig. 2.3 illustrates the electron orbit, shifted by k_z^0 from $k_z = 0$, where k_z^0 is related to the Fermi wave vector component parallel to the field, given by $k_{b\parallel} = k_z^0 \cos(\theta)$. Then, we can rewrite the equation as

$$\begin{aligned}\sigma_{zz} = \frac{e^2 m_c}{4\pi^3 \hbar^2 \omega_c \cos(\theta)} \frac{1}{1-\exp(-2\pi/\omega_c \cos(\theta)\tau)} \int_{-\frac{\pi}{d}}^{\frac{\pi}{d}} dk_{b\parallel} \int_0^{2\pi} d\phi\, v_z[\boldsymbol{k}(\phi)] \\ \times \int_0^{2\pi} d\phi'\, v_z[\boldsymbol{k}(\phi-\phi')] \exp\left(\frac{-\phi'}{\omega_c \cos(\theta)\tau}\right).\end{aligned} \tag{5.4}$$

We can derive the velocity component $v_z[\boldsymbol{k}(t)]$ from the Lorentz equation of motion: $\hbar d\boldsymbol{k}/dt = e[\boldsymbol{v} \times \boldsymbol{B}]$, where the velocity is given by $\boldsymbol{v} = \partial\epsilon/\hbar\partial\boldsymbol{k}$, and the energy dispersion is $\epsilon(k_x, k_y, k_z) = \epsilon_\parallel(k_x, k_y) + \epsilon_\perp(k_z)$. Assuming the interlayer dispersion is isotropic $\epsilon_\perp(k_z) = -2t_\perp \cos(k_z d)$, where d is the interlayer distance, we

obtain $v_z(k_z) = \partial\epsilon_\perp/\hbar\partial k_z = 2t_\perp d\sin(k_z d)/\hbar$. The value of k_z can be determined from the geometrical relationship given by Eq. (2.17). In these equations, φ represents the angle between the magnetic field rotation plane and the x-axis ($\boldsymbol{B} = B(\sin(\theta)\cos(\varphi), \sin(\theta)\sin(\varphi), \cos(\theta))$), while ϕ and ϕ' are dimensionless variables used to integrate electron motion over the FS. The term $k_F(\phi - \varphi)\cos(\phi)$ corresponds to the projection of the in-plane electron wave vector onto the in-plane component of the magnetic field. Note that this geometrical relationship neglects the FS warping in the z-direction, which is justified as long as $t_\perp \ll \epsilon_\parallel$. Eq. (2.17), along with the expression for $v_z(k_z)$, can be inserted into Eq. (5.4) for the integration over k_z^0. Using the trigonometric identity $2\sin(a)\sin(b) = \cos(a-b) - \cos(a+b)$, the Chambers equation simplifies to its final form:

$$\sigma_{zz}(\theta,\varphi) = \frac{e^2 m_c t_\perp^2 d}{\pi^2\hbar^4\omega_c\cos(\theta)} \frac{1}{1-\exp(-2\pi/\omega_c\cos(\theta)\tau)} \int_0^{2\pi} d\phi \int_0^{2\pi} d\phi' \times$$
$$\cos(d\tan(\theta)[k_F(\phi-\varphi)\cos(\phi) - k_F(\phi-\phi'-\varphi)\cos(\phi-\phi')]) \exp\left(\frac{-\phi'}{\omega_c\cos(\theta)\tau}\right) \quad (5.5)$$

It is possible to numerically integrate Eq. (5.5) for different angles θ and φ, with the cyclotron frequency and scattering parameter $\omega_c\tau$ serving as variable parameters. The calculations were performed using the in-plane Fermi wave vectors $k_F(\varphi)$ obtained from the AMRO measurements and unit cell sizes corresponding to a pressure of 0.3 GPa. The resultant resistivity, calculated as the inverse conductivity Eq. (5.5), and normalized to its value at a polar angle close to $\theta = 0$, is shown in Fig. 5.14. Calculations were carried out up to angles of $\theta = 75°$. At higher angles, the integration orbit becomes a highly elongated "ellipse," which prevents an accurate numerical integration with our resolution (1°).

For a fixed azimuthal angle $\varphi = 0°$, Fig. 5.14(a) displays the calculated AMRO curves (solid lines) at different values of $\omega_c\tau$, normalized to the value at the perpendicular orientation, $R(\theta = 0°)$. The amplitude of the oscillations increases with the parameter $\omega_c\tau$ [195]. A comparison with the experimentally measured AMRO (dashed line) at $\varphi = 0°$ allows us to roughly estimate the parameter $\omega_c\tau$. The ratio of the amplitudes of the angular oscillations to the background results in a value of $\omega_c\tau = 2.4 \pm 0.2$. On the other hand, $\omega_c\tau$ can also be estimated from the Dingle temperature measurements in these samples [110], where $T_D = 0.7$ K was obtained. Using the relation: $\omega_c\tau = \frac{eB}{m} \cdot \frac{h}{2\pi k_B T_D}$, we estimate $\omega_c\tau \approx 1.2$. The estimate from the Dingle temperature is roughly one-half of that obtained from the AMRO simulations. The agreement between the two values is quite good, considering the various factors that could contribute to stronger deviations. The main possible reason for the discrepancy is that scattering in SdH oscillations is much more sensitive to small-angle scattering, whereas transport scattering is largely insensitive to these factors (this was also discussed in Sec. 3.9). Another possible reason is that we used $k_B^{\max}$ rather than the actual Fermi wave vector k_F. While $k_B^{\max}$ is close to k_F, they are not exactly the same, as mentioned earlier (comparison of k_F and k_B^{max} is given in Appendix 9).

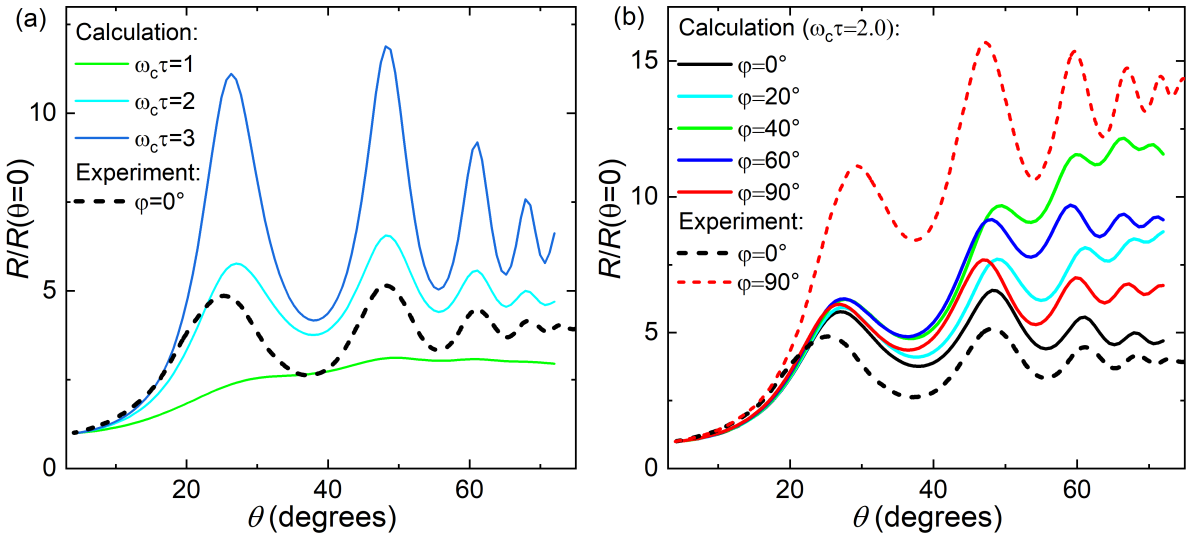

Figure 5.14: (a) Calculated angle-dependent magnetoresistance for different values of $\omega_c\tau$ (solid lines) compared to the experimentally measured $R(\theta)$ dependence at 15 T and 1.4 K (dashed line). Both the experimental and calculated curves correspond to an azimuthal angle of $\varphi = 0°$. (b) Calculated angle-dependent magnetoresistance curves for $\omega_c\tau = 2.0$ at different azimuthal angles φ (solid lines), compared to experimentally measured curves for $\varphi = 0°$ and $\varphi = 90°$ (dashed lines). In both graphs, the magnetoresistance is normalized to the resistance at $\theta = 0°$.

5.10 In-plane magnetoresistance anisotropy

For a fixed parameter $\omega_c\tau = 2.0$, we calculated AMRO for different azimuthal angles φ (Fig. 5.14(b), solid lines). The background resistance at $\theta \to 90°$ increases with φ, reaching a maximum at approximately $\varphi = 40°$, followed by a subsequent decrease. Notably, the calculated value at $\varphi = 90°$ is higher than that at $\varphi = 0°$, which is qualitatively consistent with the experimental observations. The dashed line in Fig. 5.14(b) show the measured AMRO curves for $\varphi = 0°$ (black) and $\varphi = 90°$ (red).

The calculations for $\varphi = 0°$ (Fig. 5.14(b), black solid line) yield values higher than the experimental results (black dashed line), whereas the calculations for $\varphi = 90°$ (red solid line) are significantly lower than the experimental results (red dashed line). This discrepancy cannot be explained by simply introducing an additional scaling coefficient or by increasing the parameter $\omega_c\tau$.

Overall, the dependence on φ in the calculations is weaker than in the experimental results. Fig. 5.15(a) shows the resistance at $\theta = 70°$ for various φ angles, normalized to the resistance at the same θ and $\varphi = 0°$ (global minimum). The peak resistance for $\omega_c\tau = 2.0$ (red dots) is smaller than that for $\omega_c\tau = 2.5$ (green dots), indicating that an increase in $\omega_c\tau$ leads to a higher peak resistance and greater anisotropy. However, for both sets of calculations, the resistance peaks are significantly smaller than those observed in the experimental measurements. This discrepancy may arise from approximations in the calculation model, such as neglecting the anisotropy of the FS warping or inaccuracies in the Fermi wave vectors used. Another plausible explanation is an anisotropic scattering rate, where different values of $\omega_c\tau$ are assumed on the open and

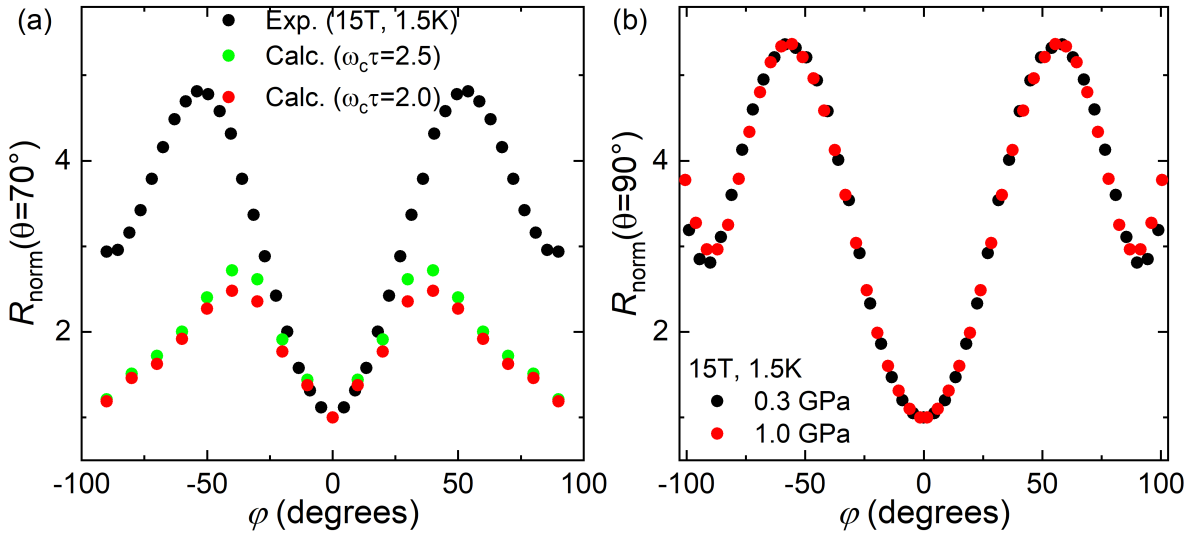

Figure 5.15: (a) Azimuthal angle φ-dependence of magnetoresistance at a polar angle $\theta = 70°$, measured at $B = 15\,\mathrm{T}$, $T = 1.4\,\mathrm{K}$, and pressure $p = 0.3\,\mathrm{GPa}$ (black points). Calculations are shown for scattering rates $\omega_c\tau = 2.5$ (green dots) and $\omega_c\tau = 2.0$ (red dots). (b) Azimuthal angle φ-dependence of magnetoresistance extrapolated to a polar angle $\theta = 90°$, measured at $B = 15\,\mathrm{T}$ and $T = 1.4\,\mathrm{K}$ for pressures 0.3 GPa (black dots) and 1.0 GPa (red dots). Resistances in both graphs are normalized to their minimum values at $\varphi = 0°$.

closed Fermi surface sheets. Additionally, Ref. [197] reports enhanced antiferromagnetic fluctuations in the regions where the FS intersects the Brillouin zone boundary, which may further increase scattering in those areas.

Despite changes in the FS and resistance caused by increasing pressure from 0.3 GPa to 1.0 GPa, the φ-dependent normalized resistance for in-plane magnetic field orientations remains practically the same (Fig. 5.15(b)). From the analysis in the previous section, only a small change in the anisotropy of the FS is observed. Consequently, the anisotropy of the scattering rate is also likely to exhibit minimal variation across different pressures.

The data in Fig. 5.15 show a maximum in the resistance at $\varphi \approx 60°$. This φ value is close to the maximum of the Fermi wave vector $k_F(\varphi)$, as measured from the AMRO and obtained from the effective dimer model calculations (Fig. 5.12(b)). According to the AMRO, this region of the FS clearly exhibits a stronger curvature. In [195, 198], it was shown that in a magnetic field parallel to the layers, regions of the FS where the tangent is perpendicular to the field dominate the conductivity. When this area has a small curvature, meaning it is relatively flat and large, the conductivity is large, leading to low magnetoresistance. Conversely, when the curvature is strong, the area with a tangent perpendicular to the field is narrow, resulting in a lower conductivity and a higher resistance.

This explanation is consistent with our FS shape and magnetoresistance anisotropy. When the field is aligned along the main crystallographic axes, the curvature in these regions is weak, leading to a minimum in resistance. At intermediate field orientations, the curvature increases, reaching a maximum at orientations close to $\varphi \approx 50°$,

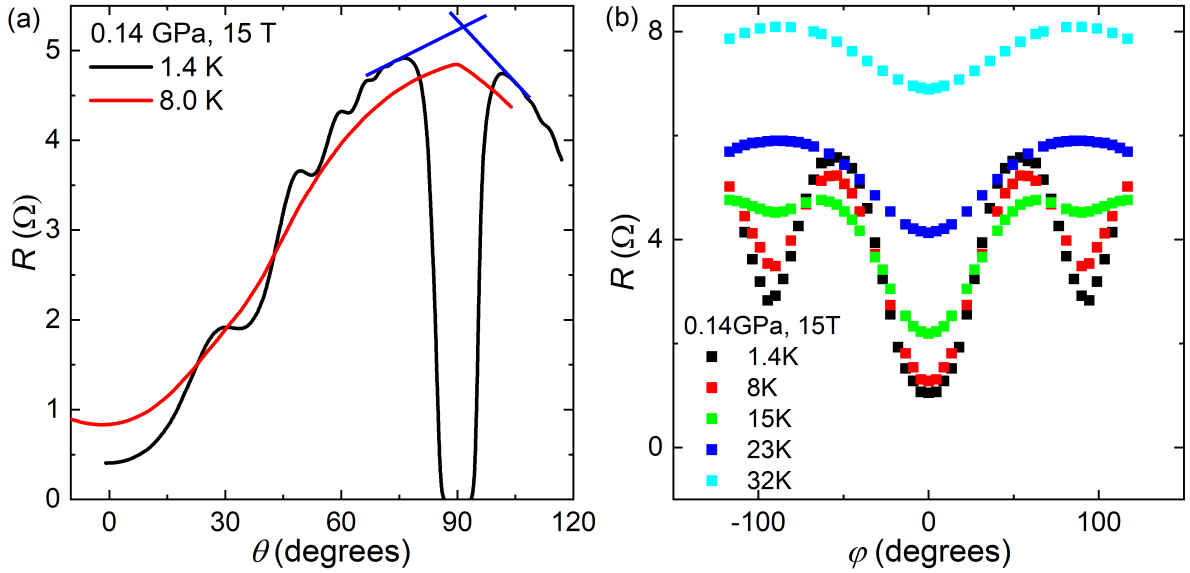

Figure 5.16: (a) AMRO curves at $p = 1.4\,\mathrm{GPa}$, $B = 15\,\mathrm{T}$, $\varphi = 45°$, and temperatures 1.4 K (black) and 8 K (red). Blue lines indicate the extrapolation of resistance to $\theta = 90°$ for 1.4 K. (b) Azimuthal angle φ-dependence of magnetoresistance at $\theta = 90°$, $p = 0.14\,\mathrm{GPa}$, and different temperatures. For 1.4 K, the value was extrapolated as shown in panel (a).

where the resistance also reaches a maximum. Meanwhile, the maximal curvature of the FS (close to $\varphi \approx 50°$) appears to increase with pressure (Fig. 5.13). However, the anisotropy at both pressures remains practically the same (Fig. 5.15(b)), suggesting either an imprecision in the FS determination or the influence of an additional dominant mechanism in the formation of magnetoresistance anisotropy.

Fig. 5.16(a) presents $R(\theta)$ curves measured at temperatures 1.4 K (black) and 8 K (red) and at a pressure of 0.14 GPa. At 1.4 K, a magnetic field of 15 T is not sufficient to fully suppress superconductivity when the field is oriented parallel to the layers, resulting in a superconducting transition. Therefore, we extrapolated the resistance linearly to estimate its value at $\theta = 90°$ (blue lines). This resistance can be estimated for different φ orientations. Similar to the observations in [108], the amplitude of AMRO decreases with decreasing pressure. This behavior may be attributed to a reduction in the interlayer transfer integral or to the system becoming less metallic as it shifts closer to the MIT.

Fig. 5.16(b) shows the φ-dependent magnetoresistance at $\theta = 90°$ for different temperatures. The magnetoresistance measured at 1.4 K and 8 K (black and red dots, respectively) are nearly identical. This behavior was previously reported for other organic salts and quasi-2D materials in [196, 198–200], where it was shown that the conductivity in a moderate magnetic field ($\omega_c\tau \gtrsim 1$), applied parallel to the conducting layers, becomes largely independent of the scattering rate. Specifically, the conductivity at $\theta = 90°$ is described by $\sigma(\theta = 90°) \propto \sigma_0/(\omega_c\tau)$, where the zero-field conductivity σ_0 is proportional to the scattering time τ. Consequently, in this regime, the magnetoresistance exhibits only weak temperature dependence. At elevated temperatures, however, the scattering time τ decreases, the condition $\omega_c\tau \gtrsim 1$ is no longer satisfied,

and the magnetoresistance becomes more strongly temperature dependent.

Starting from 15 K (green dots), the magnetoresistance anisotropy begins to decrease. The local minima at $\varphi = 0°$ and $\varphi = 90°$ increase, while the local maximum at $\varphi = 60°$ diminishes and shifts toward $\varphi = 90°$. At 23 K (blue dots), the local maximum fully shifts to $\varphi = 90°$, and the anisotropy decreases to approximately 40 %. By 32 K (light blue), the magnetoresistance anisotropy decreases further down to 18 %.

5.11 Coherence peak

For magnetic field orientations around parallel to the sample layers, we observed the coherence peak, as previously introduced in Sec. 2.5. Overall, the coherence peak shapes at both pressures, 0.3 GPa (Fig. 5.17(a)) and 1.0 GPa (Fig. 5.17(b)), were quite similar. However, the peak shape varied with the φ-angle. At angles close to $\varphi = 0°$ (Fig. 5.17(a) and Fig. 5.17(b), black curves), the coherence peak was well-defined, exhibiting a clear local minimum associated with self-crossing orbits, followed by a pronounced local maximum. As the φ-angle increased, the local minimum near the base of the peak disappeared. Additionally, the height of the coherence peak progressively decreased. These factors rendered the coherence peak nearly indistinguishable at orientations close to $\varphi = 45°$ (blue curves), where determining the peak width became impossible. Instead of the peak, we observed a pronounced triangular 'hill'. It is doubtful that the observed triangular-shaped feature represents a true coherence peak; it is more likely associated with self-crossing orbits.

The different coherence peak shapes may be attributed to the complex topology of the FS. In [185], two types of closed orbits were identified for κ-NCS: those occurring

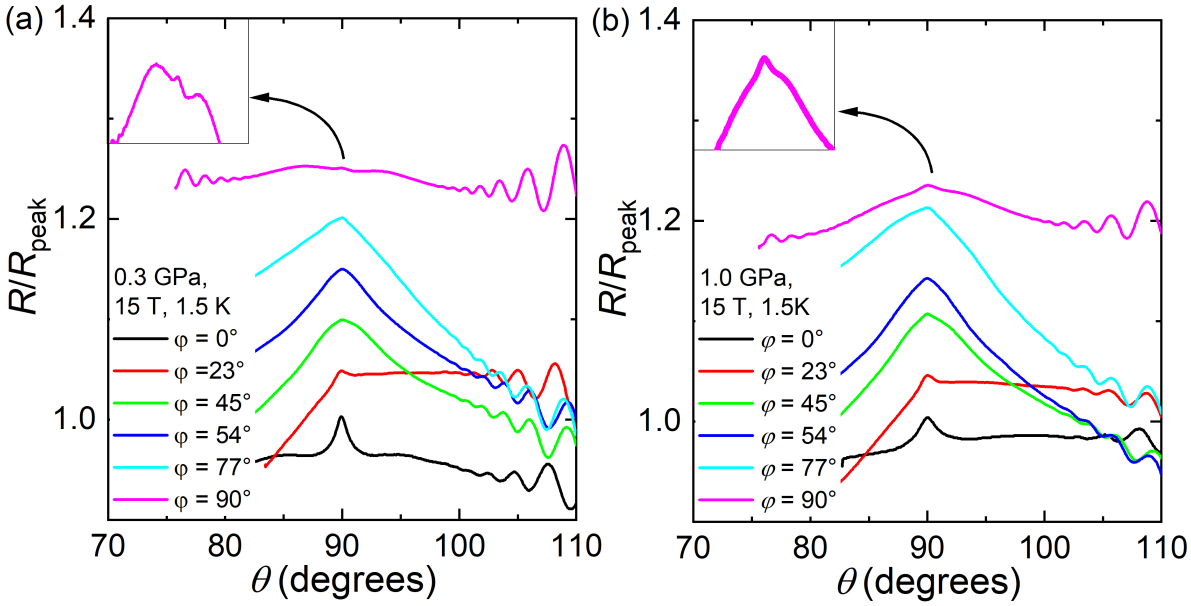

Figure 5.17: The θ-dependence of the resistance, normalized to the resistance at $\theta = 90°$ and vertically shifted for clarity, is shown for pressures of 0.3 GPa (a) and 1.0 GPa (b) at various azimuthal angles φ. Similar colors correspond to similar φ values.

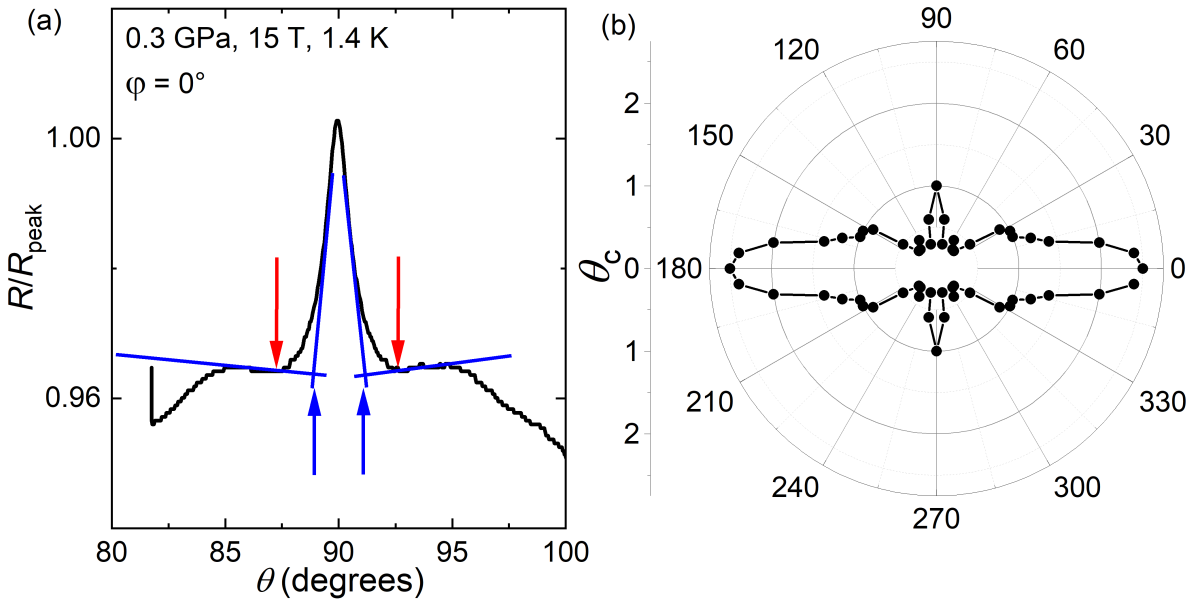

Figure 5.18: The θ-dependence of the resistance, normalized to the resistance at $\theta = 90°$, for $p = 0.3\,\mathrm{GPa}$ and $\varphi = 0°$. Arrows indicate two methods used for determining the peak width: (blue) through the intersection of tangents of the peak slope and base ($\theta_c \approx 1.2°$). (red) through the base of the slope ($\theta_c \approx 2.5°$). (b) Coherence peak width dependence on the azimuthal angle φ at a pressure of 0.3 GPa. The analysis was performed using the method corresponding to the base of the slope of the peak, as indicated by the red arrows in panel (a).

in the relatively flat regions and those in more highly curved regions of the FS. The authors associated the variation in coherence peak shapes in κ-NCS with the influence of these distinct orbit types.

At orientations near $\varphi = 90°$, the coherence peak reappeared (pink curves) but with a significantly reduced height and width. This made a precise determination of the peak width more complicated and increased its uncertainty. Fig. 5.18(a) shows two methods for estimating the coherence peak width. Blue arrows indicate the intersection of the tangents of the peak slope and base ($\theta_c \approx 1.2 \pm 0.2°$), while red arrows indicate the start of the peak slope ($\theta_c \approx 2.5 \pm 0.4°$). In this work, we employed the second method, determining the peak width from the base of the slope.

Fig. 5.18(b) shows the peak width at different φ orientations for $p = 0.3\,\mathrm{GPa}$. The strong anisotropy of the peak width suggests an anisotropy in the interlayer transfer energy $\epsilon_\perp$ and a more complex energy dispersion than what we used in the AMRO simulations. This anisotropy of interlayer energy could be one of the main reasons for the mismatch between the anisotropies in the calculated and experimentally measured magnetoresistance $R(\varphi)$.

As we can reliably determine the width of the coherence peak at $\varphi = 0°$, we can compare these values at different pressures. All utilized and calculated values are presented in Table 5.4. The peak widths for the two pressures, 0.3 GPa and 1.0 GPa, are approximately $\theta_c \approx 2.4 \pm 0.4°$ and $3.1 \pm 0.5°$, respectively. These values can be recalculated into the ratio of the interlayer transfer integral and Fermi energy using

p(GPa)	F(T)	d(nm)	k_F(nm^{-1})	$m_c(m_0)$	E_F(eV)	θ_c(°)	$t_\perp / E_F$	$t_\perp$ (meV)
0.3	3900	1.461	3.14	4	0.11	2.5 ± 0.4	0.0091	1.0 ± 0.2
1.0	3990	1.437	3.29	2.8	0.16	3.1 ± 0.5	0.0114	1.9 ± 0.3

Table 5.4: Calculated values of $t_\perp$ along with all parameters required for its evaluation. The SdH frequency F, effective cyclotron mass m_c, interlayer distance d, and Fermi wave vector k_F were taken from previous sections. For details on the calculation of the Fermi energy E_F and the interlayer transfer integral $t_\perp$, see the main text.

Eq. (2.21). The estimation gives ratios of 0.009 and 0.011 for pressures 0.3 GPa and 1.0 GPa, respectively. To calculate $t_\perp$, we estimated the Fermi energy using the SdH oscillation frequency, assuming a parabolic energy dispersion and an effective mass equal to the cyclotron mass. Thus, we obtain $t_\perp(0.3\,\text{GPa}) \approx 1.0$ meV and $t_\perp(1.0\,\text{GPa}) \approx 1.9$ meV. The values of the interlayer transfer integral increase with pressure, which is consistent with the squeezing of the layers and improved interlayer coupling.

The estimated $t_\perp$ values are an order of magnitude larger than those in κ-Br (0.1 meV) [103, 184] and κ-NCS (0.04 meV) [185], measured at ambient pressure. This difference may arise from either a real difference in $t_\perp$ or imprecision in the determination of E_F, where we assumed a simple parabolic dispersion. All the parameters used for the calculations are provided in Table 5.4.

The ratio of the interlayer transfer integrals can be used to estimate the ratio of the residual resistances using Eq. (3.5): $\frac{\rho(0.3\,\text{GPa})}{\rho(1.0\,\text{GPa})} = \frac{m_2}{m_1}\left(\frac{t_2}{t_1}\right)^2 \approx 2.7$. This value is close to the experimental result (Sec. 5.1) from $R(T)$ curves: $\frac{R(0.3\,\text{GPa})}{R(1.0\,\text{GPa})} \approx 2.0$.

5.12 Beating pattern in Shubnikov-de Haas oscillations

In the previous sections, we discussed SdH oscillations in magnetic field sweeps and angle-dependent magnetoresistance oscillations. Now, we can combine these two methods to investigate SdH oscillations in a tilted magnetic field. As shown in Fig. 5.3, beat nodes appear in the SdH oscillations, with their positions shifting under pressure. There are several possible causes for beats, including warping of the FS, a magnetic-field-dependent spin-zero effect, or a slightly misoriented bicrystal. We consider the most likely origin to be the warping of the FS, as also proposed in Sec. 2.6. In this case, the beat frequency depends on the difference between the extremal FS cross-sectional areas, which changes when measuring SdH in a field tilted by an angle θ. Fig. 5.19(a) shows SdH oscillations with beat nodes at various θ angles. As the magnetic field is tilted, the positions of the nodes shift toward lower fields. The angular dependence of the beat frequency is discussed in Sec. 2.6 and is given by Eq. (2.23), which is recalled here:

$$\Delta F \approx \frac{\Delta F_0}{\cos(\theta)} J_0(k_F d \tan(\theta)).$$

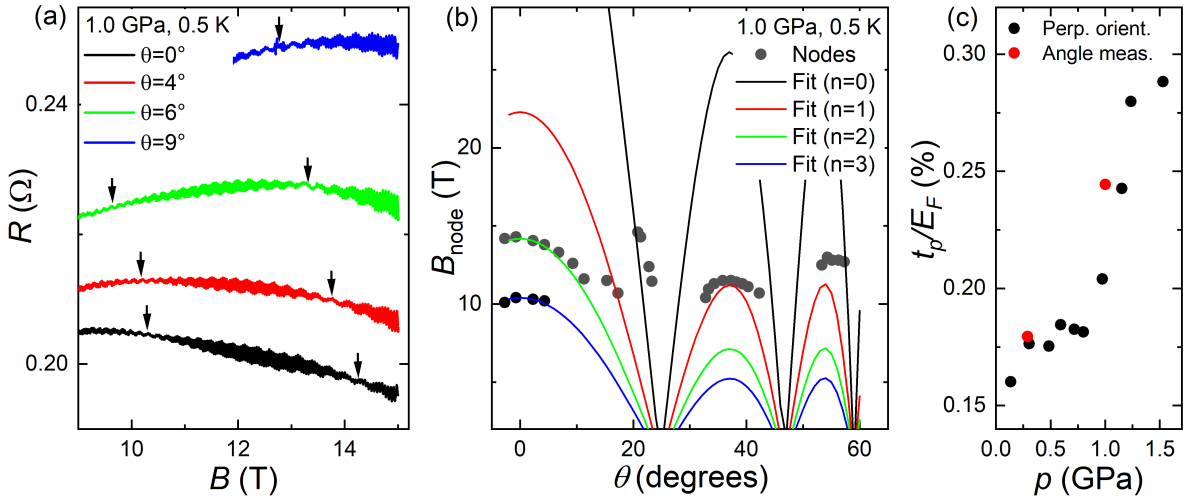

Figure 5.19: (a) Magnetoresistance field sweeps at different angles θ for a pressure of 1.0 GPa and a temperature of 0.5 K. Arrows indicate the positions of the nodes. (b) θ-angle dependence of the node positions (black dots) fitted using Eq. (2.24) for different node indices (lines). (c) Pressure dependence of the ratio between the interlayer transfer integral and the Fermi energy, $t_\perp/E_\mathrm{F}$, obtained from the angle-dependent measurements (red dots) and from the data presented in Fig. 5.3(a), obtained in a perpendicular field (black dots).

In this equation, d is the interlayer distance, J_0 is the zero-order Bessel function, and ΔF_0 is the beat frequency in a perpendicular field. Further, the beat frequency can be converted into the node position by inserting it into the beat oscillation condition: $\cos(\pi\Delta F/B - \pi/4) = 0$. The positions of the nodes at different polar angles are given according to Eq. (2.24) as

$$B_n \approx \frac{4\Delta F}{4n+3}.$$

We can fit the θ-dependence of the node positions using this equation, treating ΔF_0 as a fitting parameter.

Fig. 5.19(b) shows the positions of the nodes at different θ angles for a pressure of 1 GPa. Our fits reveal four possible nodes within the entire range of θ, and the nodes in the perpendicular orientation correspond to node indices $n = 2$ and $n = 3$. The fits yield beat frequencies of $\Delta F_0 = 28$ T and $\Delta F_0 = 39$ T for pressures of 0.3 GPa and 1 GPa, respectively. Knowing the SdH frequencies at these pressures, we can estimate the FS warping using the relation: $t_\perp/E_\mathrm{F} \approx \Delta F/4F$, which yields values of 0.18 % and 0.24 % for these pressures.

The node indices can also be used to analyze the data in a perpendicular field from Sec. 5.2 (Fig. 5.3). Using the positions of both nodes, we can estimate ΔF_0 from Eq. (2.24): $B_2(p) - B_3(p) \approx \frac{4\Delta F_0(p)}{4\cdot2+3} - \frac{4\Delta F_0(p)}{4\cdot3+3} \approx 0.097\Delta F_0(p)$. We can estimate the FS warping at different pressures from $\Delta F_0(p)$. Fig. 5.19(c) shows the dependence of $t_\perp/E_\mathrm{F}$ on pressure, extracted from both the pressure measurements (black dots) and the angle-dependent measurements (red dots). Both results are consistent. Due to the absence of low-field nodes at some pressures (because of a low SdH amplitude), some

points from Fig. 5.3 are missing in Fig. 5.19(c).

We can extrapolate Fig. 5.19(c) to ambient pressure, yielding a ratio of $t_\perp / E_F = 0.15\,\%$. This value is close to the previously measured $t_\perp / E_F = 0.2\,\%$ for κ-Br [103, 184]. Using the effective mass and frequency determined in Sec. 5.5 and Sec. 5.6 ($m_c \approx 6.5 m_0$ and $F = 3840\,\mathrm{T}$), we estimate the ambient pressure interlayer transfer integral as: $t_\perp = 0.1\,\mathrm{meV}$, with $E_F = 800\,\mathrm{K}$. This value is consistent with the estimate for κ-Br ($t_\perp = 0.1\,\mathrm{meV}$) [103, 184] and higher than in κ-NCS ($t_\perp = 0.04\,\mathrm{meV}$) [185], both measured at ambient pressure.

One can see that the $t_\perp / E_F$ ratio determined from the beat node positions is several times smaller than that derived from coherence peak width measurements in Sec. 5.11. This discrepancy could arise from the approximate character of both approaches. Additionally, the beat measurement method calculates $t_\perp$ based on the difference between the minimal and maximal Fermi surface cross-sectional areas, meaning it accounts for the warping averaged over the entire FS. In contrast, the coherence peak measurement method probes the local warping of the Fermi surface in the in-plane direction corresponding to a given azimuthal angle φ, and in Sec. 5.11, we considered the maximum values of $\theta_c(\varphi)$.

5.13 Scattering rate and Dingle temperature

From the SdH oscillation amplitude, we can analyze the scattering rate in the system. To achieve this, we fit the SdH amplitude dependence on magnetic field using the Dingle damping factor, given by Eq. (2.11). In the perpendicular magnetic field orientation, fitting the field-dependent amplitude is more complicated and less precise, as we must account for the amplitude modulation due to beating, described above. In this case, the fitting formula can be expressed by as

$$A(B) \propto \sqrt{B} \exp\left(\frac{-K\mu T_D}{B}\right) \cos\left(\pi \frac{\Delta F}{B} - \frac{\pi}{4}\right). \tag{5.6}$$

However, the beats disappear at field orientations near an AMRO maximum, making the fitting procedure more straightforward. Therefore, we can estimate the scattering rate at different orientations and compare the results.

Fig. 5.20(a) shows the amplitude of the oscillations for two samples at different orientations. Both samples exhibited almost the same dependence $R(\varphi)$ in a magnetic field parallel to the layers. Sample 1 was measured at $\varphi = 60^\circ$ under two orientations: the perpendicular orientation at $\theta = 0^\circ$ (black dots) and at the AMRO peak orientation at $\theta = 29^\circ$ (green dots). The corresponding Dingle temperatures were determined to be approximately $0.9 \pm 0.1\,\mathrm{K}$ and $0.72 \pm 0.02\,\mathrm{K}$, respectively. These values are close to our previously reported values at different pressures [110] (Fig. 5.20(b)).

Determining the Dingle temperature at $\theta = 0^\circ$ is more complicated due to the presence of nodes and an additional damping factor related to beats. Therefore, we believe that the 30 % difference in the Dingle temperature is a reasonable error bar for such estimations, and we consider the Dingle temperature to be essentially independent of the θ-angle. We adopt the value obtained at the AMRO peak for simplicity and accuracy, as its determination is more straightforward.

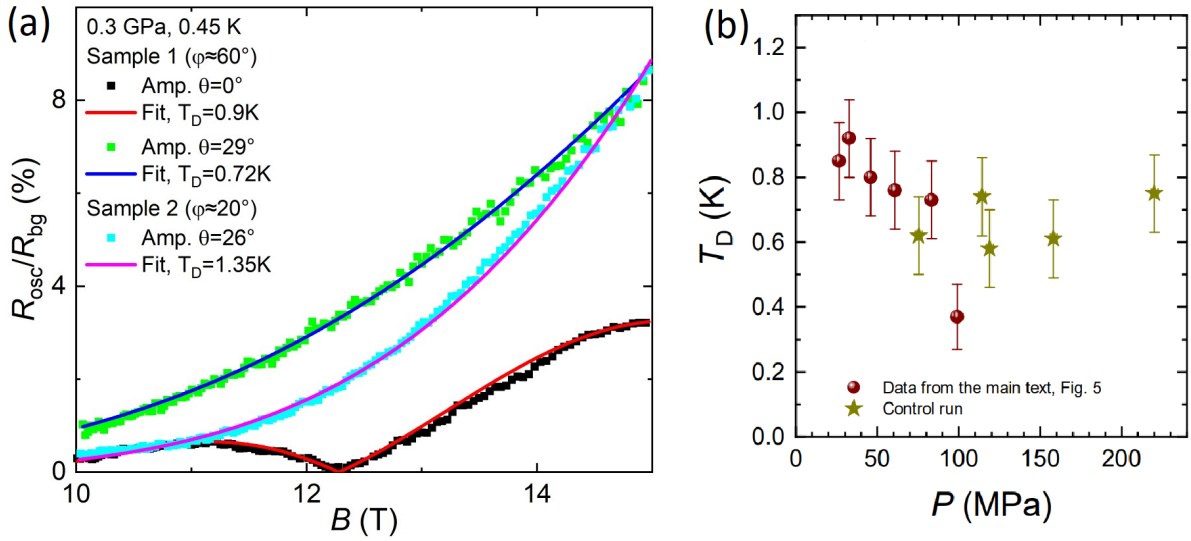

Figure 5.20: (a) Field dependence of the amplitude of SdH oscillations. Sample 1 was measured at $\varphi = 60°$ (close to the maximum of $R(\varphi)$, Fig. 5.15(b)) and at polar angles $\theta = 0°$ (black dots) and $\theta = 29°$ (green dots). The Dingle fit curves have parameters $T_D = 0.9\,K$ (red) and $T_D = 0.7\,K$ (blue), respectively. Sample 2 was measured at $\varphi = 20°$ (close to the minimum of $R(\varphi)$) and $\theta = 26°$, with a Dingle fitting curve using $T_D = 1.35\,K$ (pink). (b) Dingle temperature for Sample 1 obtained from SdH measurements in a perpendicular field, at different pressures, from [110].

Sample 2 was measured at $\varphi = 20°$, corresponding to the AMRO peak orientation (blue dots in Fig. 5.20(a)). The Dingle temperature in this case was approximately $1.35 \pm 0.05\,K$, nearly twice as high as that of Sample 1. This difference is unlikely to be attributed to variations in sample quality, as the resistance anisotropy was practically identical for both samples. Additionally, Sample 1 showed similar T_D at different θ orientations, indicating that the Dingle temperature depends only weakly on θ. Based on this observation, we suggest that this difference in the Dingle temperature is related to the φ-orientation. As discussed in Sec 5.9, when we increase the θ angle, the dominant contribution to the conductivity is given by the part of the FS with a tangent perpendicular to the field direction (or, for simplicity, the wave vectors on the FS with the same φ as the magnetic field direction). With this in mind, the azimuthal angles $\varphi = 20°$ (near the global minimum of $R(\varphi)$) and $\varphi = 60°$ (near the maximum of $R(\varphi)$) correspond to Dingle temperatures of $1.4\,K$ ($0.8 \times 10^{-12}\,s$) and $0.7\,K$ ($1.6 \times 10^{-12}\,s$), respectively. This suggests that the scattering time along the main axes is shorter than in intermediate orientations.

This observation appears counterintuitive, given the presence of a gap in the Fermi surface near $\varphi \sim 50°$. Furthermore, the suggested anisotropic scattering is at odds with the strong anisotropy observed in the magnetoresistance. At intermediate values of φ, we observe a higher parameter $\omega_c\tau$, which would typically result in a reduced magnetoresistance (Fig. 5.14(a)). However, this discrepancy may be reconciled by considering a strong anisotropy in the interlayer transfer integral, as discussed in Sec. 5.11, which could compensate the magnetoresistance anisotropy for the scattering rate.

5.14 Spin-splitting zeros and g-factor

As we saw in Sec. 5.2, the amplitude of SdH oscillations, $A_\beta(p)$, exhibits a non-monotonic dependence on pressure, with minima occurring at approximately 0.2 GPa and 0.9 GPa. The amplitude variations are primarily influenced by the decrease in the effective mass m_c with pressure and its impact on the different damping factors in Eq. (2.8). For the temperature and Dingle damping factors, the SdH amplitude exponentially increases as the effective mass decreases. Conversely, for the spin-splitting damping factor (see Eq. (2.12)), changes in the effective mass can either increase or decrease the amplitude. Therefore, it is reasonable to attribute the nonmonotonic behavior and the observed minima in the SdH amplitude to the influence of the spin-splitting factor, as discussed in Sec. 2.2. According to Eq. (2.12), the SdH amplitude can be strongly suppressed when the spin-splitting damping factor approaches zero, $R_S \approx 0$. This occurs when the condition $\frac{\pi r g \mu_c}{2 \cos\theta} \approx \frac{\pi}{2} + \pi n$ (with $n = 0, 1, 2, ...$) is satisfied. This condition can be achieved either by varying $g\mu_c$, as in the pressure-dependent experiments, or by changing the tilt angle θ. In the latter case, the SdH oscillation frequency will also change according to the geometric relation $F(\theta) = F_0/\cos(\theta)$, as illustrated in Fig. 5.21(a).

Fig. 5.21(b) and Fig. 5.21(c) show the θ-dependent FFT amplitude of the SdH β-oscillations (black dots) in the magnetic field range of 14 T to 15 T for pressures of 0.3 GPa and 1.0 GPa, respectively. The data reveal distinct angles where the amplitude is strongly suppressed. However, not all amplitude minima correspond to spin-splitting zeros; some result from a beat node entering the observed field range, as discussed in the previous section. For example, the minimum at 1 GPa and $\theta \approx 20^\circ$ is caused by a beat node, as identified from a wider field sweep.

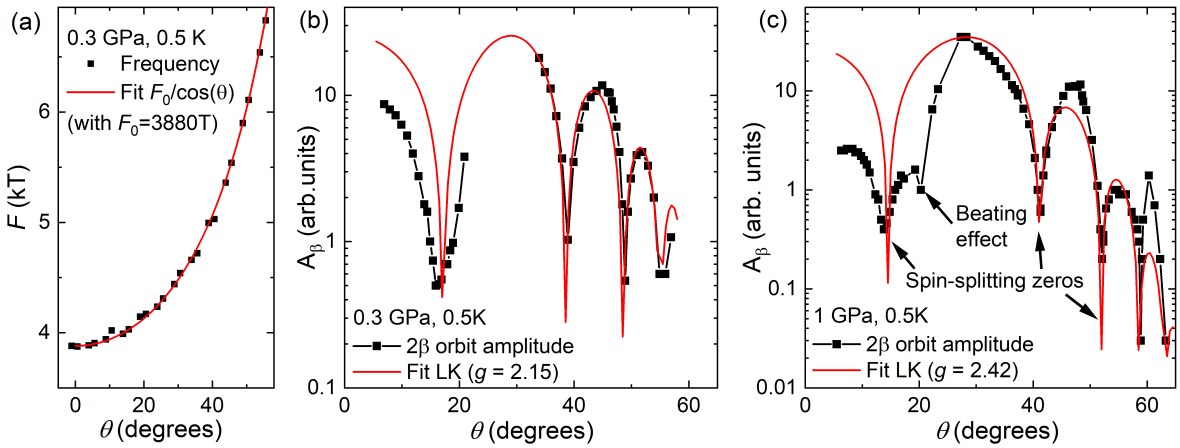

Figure 5.21: (a) Angular dependence of the frequency of the β-oscillations (black points) fitted with the equation $F(\theta) = F_0 \cos(\theta)$ (red line) at a pressure of 0.3 GPa and a temperature of 0.5 K. (b) Angular dependence of the FFT amplitude of the β-oscillations in the field range 14 T to 15 T at 0.5 K (black dots), fitted with the LK formula Eq. (2.8), incorporating the spin-splitting damping factor Eq. (2.12) (red line) for a pressure of 0.3 GPa. (c) The same dependence as in (b), but for a pressure of 1.0 GPa (black dots) with the corresponding fit using the same LK formula (red line).

The amplitude of the oscillations can be fitted using the LK formula, incorporating the spin-splitting damping factor R_S (Eq. (2.12)). In this fitting process, a higher priority is assigned to the positions of the zeros rather than the absolute amplitude values (Fig. 5.21(b) and Fig. 5.21(c), red curves). The fit yields g-factor values of $g \approx 2.15 \pm 0.02$ and $g \approx 2.42 \pm 0.02$ for pressures of 0.3 GPa and 1.0 GPa, respectively. These values are higher than those reported for κ-Br ($g \approx 1.5$ in [103, 184]) and κ-NCS ($g \approx 1.6$ in [39]).

Additionally, these g-factor values are higher than the free electron value ($g = 2$) and also exceed the values obtained from ESR measurements ($g_s \approx 2$) for κ-Br [201]. However, ESR measurements do not account for electron-electron interactions, which are significant in our case. Under pressure, the g-factor increases by 13 %, while electronic correlations and the effective cyclotron mass decrease by approximately 30 %. In a standard Fermi liquid regime, both m_c and g are expected to increase upon enhancing interactions. However, in our case, the effective mass decreases with pressure, whereas the g-factor increases. This phenomenon has also been observed in some organic conductors [202]. From m_c and g, we can estimate the interaction coefficients of the FL theory. The effective mass m_c is proportional to the FL interaction coefficient, following the relation: $m_c = m_{\text{band}}(1 + A_0)$. Under pressure, this coefficient changes from $A_0 = 0.93$ at $p = 0.3$ GPa to $A_0 = 0.35$ at $p = 1.0$ GPa. Meanwhile, the g-factor is inversely proportional to the coefficient B_0: $g = g_s/(1 + B_0)$, as given in [32], with B_0 changing from -0.07 to -0.17 within our pressure range. A possible reason for the increasing g-factor may be that, while pressure suppresses antiferromagnetic ordering, the system enters a metallic (paramagnetic) phase in which spin degrees of freedom are less constrained. As a result, ferromagnetic spin fluctuations may be enhanced, leading to an increase in the effective g-factor [61, 203].

To summarize this chapter, we have conducted a comprehensive investigation of pressurized κ-Cl, including both SdH oscillation and AMRO measurements. From the SdH oscillations, we determined the frequency and effective cyclotron mass of the α- and β-oscillations in κ-Cl and compared them with those of κ-NCS from [178]. The observed effective masses are similar for both salts in their metallic ground states, implying a similar correlation strength. The pressure dependence of the mass can be perfectly fitted using a BR-like formula. The fit reveals an effective band mass of $m_{c,\beta,\text{band}} \approx 2.1 m_0$, a sensitivity of the transfer integral to pressure of $\gamma = dt/t_0 dp \approx 0.8\,\text{GPa}^{-1}$, and a BR critical pressure of $p_c \approx -0.28$ GPa. The similar correlation strength values imply that chemical substitution in these two salts cannot be attributed solely to a 'chemical pressure' effect.

The determined SdH frequencies enabled us to estimate the frustration ratio in κ-Cl and κ-NCS. A comparison of the two salts revealed a significant difference in t'/t. At ambient pressure, the frustration values are 0.58 for κ-Cl and 0.69 for κ-NCS. Moreover, the application of 1.5 GPa of pressure increases the frustration ratio by more than 20 % for both salts. This finding implies that pressure strongly affects not only U/t but also t'/t. Therefore, these results highlight the dominant role of spin frustration in the 'chemical pressure' effect and in determining the ambient-pressure ground state for these two salts.

The AMRO measurements allowed us to determine the in-plane anisotropy of magnetoresistance and the FS of κ-Cl. According to our AMRO simulations, the curvature of the determined FS alone does not explain the strong magnetoresistance anisotropy, which can be caused by a strong anisotropy of the interlayer hopping or the presence of an anisotropic scattering rate. Near the field orientation parallel to the sample layers, we observed a coherence peak with a width $\lesssim 2.5^\circ$, and gave the corresponding $t_\perp / E_\mathrm{F} \approx 0.01$. The width of the coherence peak is also strongly anisotropic, revealing a significant dependence of the interlayer transfer integral on the in-plane Fermi wave vector. Additionally, $t_\perp / E_\mathrm{F}$ was determined from SdH oscillation beats at different field tilt angles. At ambient pressure, $t_\perp / E_\mathrm{F} \approx 0.15\,\%$ and increases with pressure with an absolute rate $0.1\,\%/\mathrm{GPa}$. Ambient pressure interlayer transfer integral is $t_\perp \approx 0.1\,\mathrm{meV}$. From the SdH amplitude at different field orientations, we determined the g-factor, which is 2.15 at $p = 0.3\,\mathrm{GPa}$ and increases with pressure, even though electronic correlations decrease.

From this systematic analysis of κ-Cl and its comparison with κ-NCS, we can draw a general perspective on electronic correlations in κ-salts. We observed the evolution of correlation strength and the frustration ratio under pressure and their roles in the ground-state formation. Additionally, we discussed the in-plane Fermi surface shape, the interlayer transfer integral, and their influence on the electronic transport. In the next chapters, we will examine two other κ-salts, compare them with κ-Cl, and attempt to identify similarities and differences. Therefore, this chapter, with its comprehensive investigation, will serve as a foundation for further discussions.

6 Influence of thermal history on κ-salts

In this chapter, we investigate κ-Br, κ-Cl, and their deuterated analogs κ-d_8-Br and κ-d_8-Cl with varying thermal histories. The results for the κ-h_8-Br and κ-d_8-Br salts will be presented side by side, allowing for a simultaneous comparison of their properties. The results on κ-Cl will be discussed at the end of the chapter. The chapter begins with an overview of the influence of different thermal treatments on the ground state (see Sec. 3.7 for a detailed introduction). This state is characterized by different conformations of the BEDT-TTF molecules with ethylene end groups (EEG). The change of EEG conformations and their occupational probabilities [Eclipsed (E) and Staggered (S) conformations] will be monitored through resistance measurements over time and temperature. This analysis, which includes evaluation of the residual resistance and superconducting critical temperature, will enable us to estimate the EEG conformation occupations and locate them on the phase diagram. Additionally, we will present measurements in a magnetic field to directly probe the electronic properties of different states and compare them with the resistive measurements.

6.1 Effect of thermal treatment

According to previous experimental reports and calculations, the EEG undergoes a glass-like transition at approximately $T_g \approx 75\,\mathrm{K}$, where the relaxation rate is around $t \approx 100\,\mathrm{s}$ [149, 167, 204, 205]. To achieve different occupational states, we either need to cool the samples rapidly through this temperature range (quenching) or hold them at temperatures slightly lower than T_g for an extended time period (annealing).

Figures 6.1(a) and 6.1(b) show $R(T)$ curves for fully hydrogenated κ-h_8-Br (h_8 stands for 8 hydrogen atoms in BEDT-TTF molecule) and fully deuterated κ-d_8-Br (d_8 stands for 8 deuterium atoms in BEDT-TTF molecule) salts for the states with different cooling histories. Since the two salts occupy slightly different initial positions on the phase diagram, they require different thermal treatments to alter their resistive behavior. For κ-h_8-Br, which is more metallic, a high cooling rate is necessary to shift it closer to the metal-insulator transition (MIT) region. In contrast, κ-d_8-Br, is already positioned in the phase-coexistence region of the MIT in the annealed state [126, 127, 146]. Therefore, it requires much slower cooling and prolonged annealing to move it toward a more metallic state. For both compounds, the resistance first increases as they are cooled from room temperature. Below T_g, the resistance curves diverge from each other depending on the cooling rate. In the temperature range of $40 - 60\mathrm{K}$, the resistance reaches a peak value before rapidly decreasing. Both compounds undergo a superconducting transition at temperatures between $10 - 13\mathrm{K}$.

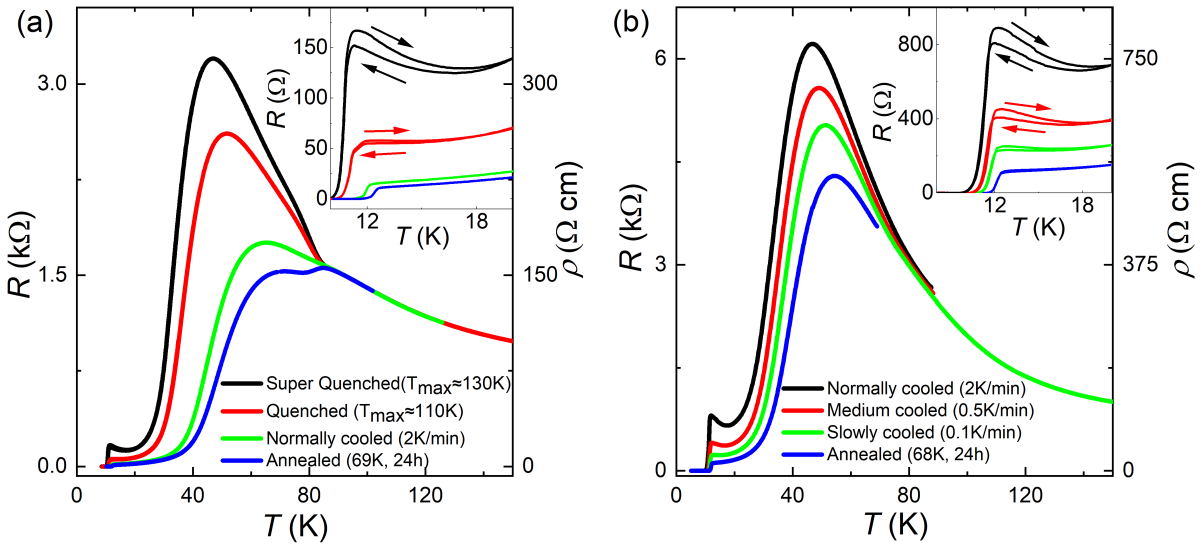

Figure 6.1: $R(T)$ curves of κ-h_8-Br (a) and κ-d_8-Br (b) with different cooling rates through the glass transition temperature $T_g \approx 75\,\mathrm{K}$. The left scale shows the resistance of samples, while the right scale shows resistivity. Insets display the resistance at low temperatures on an enlarged scale. Curves in different colors correspond to different cooling regimes through the glass transition temperature (see text).

The thermal history is readily reflected in the transport properties of the samples. For both compounds, annealing (blue curves) leads to the lowest residual resistance and a higher superconducting transition temperature. In contrast, quenching a higher fraction of the EEG in the metastable (S) conformation leads to an increased low-temperature resistance and a decreased T_c. For κ-d_8-Br, even the slow (0.1 K/min, green curve) and moderate (0.5 K/min, medium cooled, red curve) cooling rates noticeably increase the residual resistance and lower the superconducting transition temperature. The 'normal' cooling rate (2 K/min, black curve) further increases the residual resistance by almost an order of magnitude as compared to the annealed state. Meanwhile, for κ-h_8-Br, normal cooling (2 K/min, green curve) results in only a slight difference from the annealed state (cf. blue and green curves in Fig. 6.1(a)). To achieve a strong increase in residual resistance, a quenching process with heat pulses must be employed. Fig. 6.1(a) shows the resistance curves for quenched samples using voltage pulses of 7.3 V (red curve) and 8.5 V (black curve), corresponding to maximum heating temperatures of $\approx 110\,\mathrm{K}$ and 130 K, respectively.

The quenched state of κ-h_8-Br, as well as the normally and medium cooled states of κ-d_8-Br, exhibit a pronounced upturn in the $R(T)$ dependence at $T < 20\,\mathrm{K}$. The accompanying hysteresis (see inset in Fig. 6.1) clearly indicates a first-order MIT. This observation suggests that the applied thermal treatment effectively shifts the system within the phase diagram, enhancing the insulating instability. Notably, the implementation of the quenching technique in our experiments enabled the observation of a significantly larger suppression of the superconducting critical temperature, T_c ($\Delta T_c \approx -1.8\,\mathrm{K}$), compared to previously reported values for fully hydrogenated κ-h_8-Br ($\Delta T_c \approx -0.4\,\mathrm{K}$) [167].

Importantly, despite the seemingly harsh nature of the applied heat pulses, no irreversible damage was induced in our fragile crystals. The characteristics of the original normally cooled state were fully restored upon re-cooling the quenched samples. Fig. 6.3(a) displays the $R(T)$ curves for the quenched state and for the sample after being normally cooled post-quench, which perfectly coincides with the pre-quench normally cooled curve (not shown here due to complete overlap).

6.2 Annealing and quenching protocols

The annealing process, described in Sec. 4.7, involves temperature stabilization and waiting for the annealing. The relaxation process of the resistance (see Fig. 6.2(a)) can be fitted using a function with two independent exponential decays:

$$R(t) = R_0 + A_1 \exp(-t/\tau_1) + A_2 \exp(-t/\tau_2). \tag{6.1}$$

Both decays are characterized by different time constants and amplitudes (the fit with a single exponential decay is imprecise, as better seen in the inset of Fig. 6.2(a), which shows the relaxation at longer times on an enlarged scale).

This approach aligns with the earlier finding reported in [167]. We attribute the presence of two distinct time constants [175] to the following detail of the crystal structure (Fig. 6.2(a) inset). The EEGs of the BEDT-TTF molecules are exposed to two different local environments: on the one hand, they are surrounded by halogen atoms, while on the other, they are adjacent to Cu atoms and CN groups. These differing surroundings alter the energy barrier and energy difference between the staggered and eclipsed states of the EEG, resulting in two distinct ordering rates.

Considering Eq. (3.2) in the regime when $\Delta E \ll E_a$ and $T = T_0 + \Delta T$ ($k_B \Delta T \ll k_B T_0, \Delta E, E_a$ where $T_0 \approx 75\,\mathrm{K}$) we can simplify it to derive a linear dependence of the logarithm of the relaxation rate on temperature. We obtain

$$\begin{aligned} \tau_{\mathrm{eff}}(T) &= \nu_0^{-1} e^{\frac{E_a}{k_B T}} \left(e^{\frac{\Delta E}{k_B T}} + e^{\frac{-\Delta E}{k_B T}}\right)^{-1} \approx \nu_0^{-1} e^{\frac{E_a - \Delta E}{k_B T_0}} e^{\frac{-(E_a - \Delta E)}{k_B T_0^2}\Delta T} \\ &\approx \tau_{\mathrm{eff}}(T_0) e^{-\frac{E_a}{k_B T_0^2}\Delta T}, \end{aligned}$$

and finally

$$\ln\left(\frac{\tau_{\mathrm{eff}}(T)}{\tau_{\mathrm{eff}}(T_0)}\right) \approx -\frac{E_a}{k_B T_0^2}\Delta T. \tag{6.2}$$

Here, $\Delta T = T - T_0$ and the attempt frequency $\nu_0 \approx 10^{16(\pm 3)}\mathrm{Hz}$ [158]. Figure 6.2(b) shows the temperature dependence of the relaxation times on a logarithmic scale for both hydrogenated and deuterated κ-Br. Black and red curves are linear fits with Eq. (6.2) for the relaxation times τ_1 and τ_2 of hydrogenated κ-Br, respectively. Using relaxation times obtained from the experimental data at 75 K ($\tau_1 \approx 850\,\mathrm{s}$ and $\tau_2 \approx 2400\,\mathrm{s}$), we calculate the activation energy parameters as $E_a \approx 2615 \pm 97\,\mathrm{K}$ (for relaxation 1) and $E_a \approx 2773 \pm 75\,\mathrm{K}$ (for relaxation 2). These values are in good agreement with those of previous experimental reports [151, 157, 205] and with the results of high-resolution

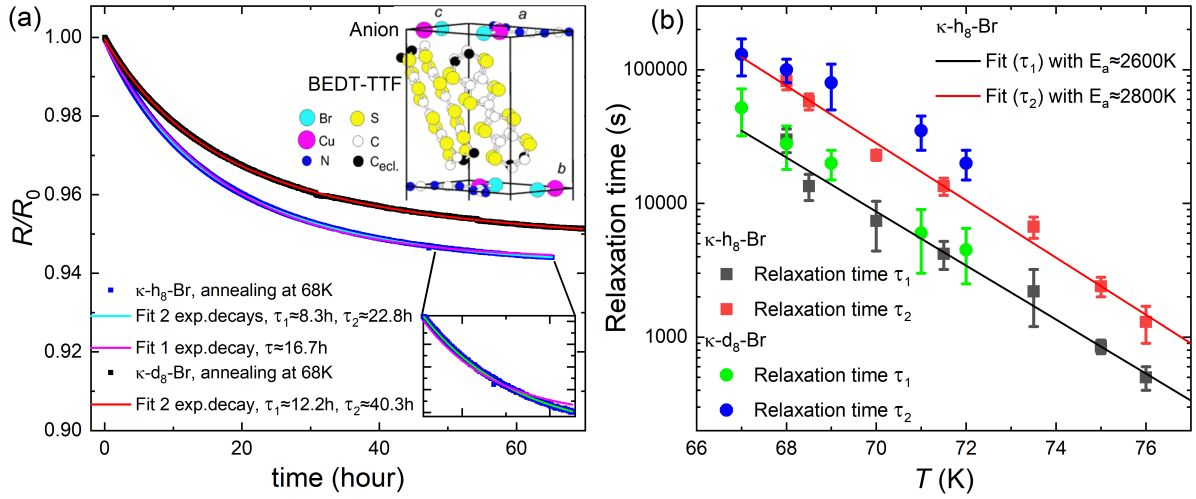

Figure 6.2: (a) Normalized resistance relaxation during annealing for κ-h_8-Br (blue dots) and κ-d_8-Br (black dots) and fit with 2 exp. decays (light blue and red lines) and 1 exp. decay for κ-h_8-Br (pink curve). Inset (top): The crystallographic structure of κ-Br from [158]. Inset (bottom): relaxation on an enlarged time scale. (b) Relaxation rates (τ_1 and τ_2) at different temperatures near the glass transition temperature for κ-h_8-Br (black and red) and for κ-d_8-Br (green and blue).

synchrotron X-ray diffraction studies [158]. We can extrapolate the obtained temperature dependence of τ_{eff} to higher temperatures to determine the glass transition temperature. The glass transition temperature T_g characterizes the range of temperatures over which the glassy freezing occurs. Typically, it is defined as the temperature at which the relaxation time reaches 100 seconds, as it matches with the common cooling rate $\sim 1\,\text{K/min}$ [149, 157]. The fit extrapolation yields $T_g \approx 79.6\,\text{K}$ and $T_g \approx 81.4\,\text{K}$ for relaxations 1 and 2, respectively. These values are consistent with previously reported results [149, 167] within the margin of error.

Measurements of κ-d_8-Br at the same temperature as κ-h_8-Br reveal slightly longer relaxation times: in Fig. 6.2(b), green and blue points for deuterated κ-Br are higher than black and red points for hydrogenated. Extrapolation to $T = 75\,\text{K}$ gives $\tau_1 \approx 1100\,\text{s}$ and $\tau_2 \approx 4000\,\text{s}$, compared to $\tau_1 \approx 850\,\text{s}$ and $\tau_2 \approx 2400\,\text{s}$ for hydrogenated samples at this temperature. This is expected given that deuterium atoms are heavier and exhibit lower mobility. This observation is in agreement with [157], where T_g in deuterated κ-Br was found to be 3 K higher than in hydrogenated samples.

For higher cooling rates, the glass transition temperature T_g for relaxation will be higher. We can set a rough correspondence between different cooling rates $q = dT/dt$ and glass transition temperatures T_g with several assumptions for the relaxation. We consider a system cooling with a constant rate q at a certain moment with temperature T and relaxation time $\tau_{\text{eff}}(T) = \tau_0$. If the system's temperature was kept stable for the time $\Delta t \approx \tau_{\text{eff}}(T) = \tau_0$ we would consider it like relaxed at this temperature. However, in our case with a constant cooling rate, the temperature during this time Δt changes by $\Delta T = q\Delta t = q\tau_0$, which leads to an increase in the relaxation time. If the relaxation time during this change increased significantly, we would have no relaxation. Therefore, we restrict the change in relaxation time to a factor of three from its initial value, i.e., we

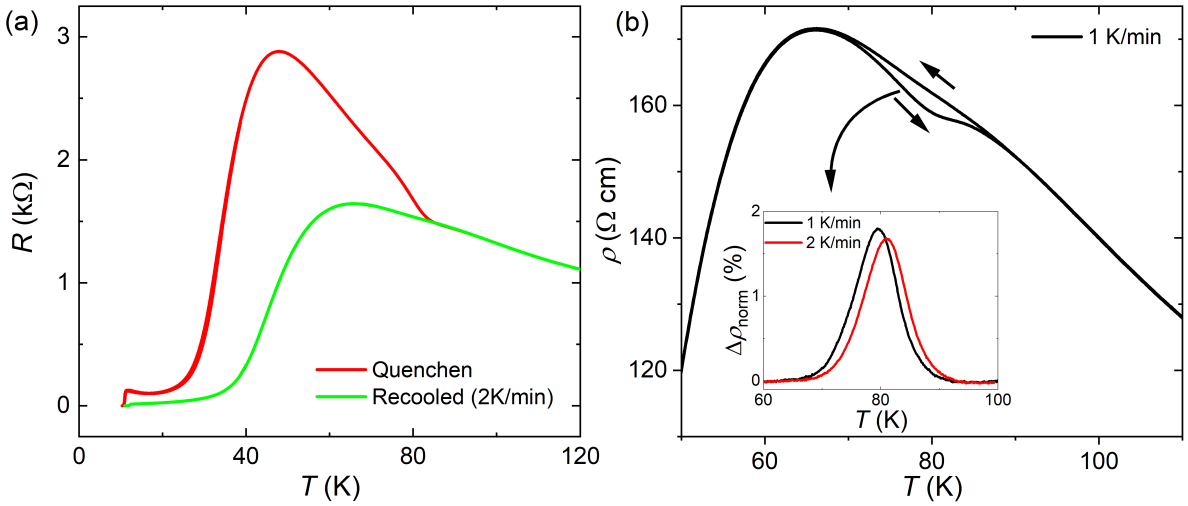

Figure 6.3: (a) $R(T)$ curves in the quenched state (red) and in the re-cooled state (2 K/min) after the quench (green). (b) Temperature dependence of the resistivity of κ-h_8-Br during cooling and warming at a constant rate of 1 K/min. Inset: Differences in resistivity during cooling and warming at rates of 1 K/min (black) and 2 K/min (red), normalized to the average resistivity value.

allow τ to increase up to $\tau_{\text{eff}}(T + \Delta T) = 3\tau_0$. Now, inserting the expressions for ΔT and τ_{eff} into Eq. (6.2) we can obtain the following relationship between the cooling rate and the corresponding temperature of relaxation:

$$\ln\left(\frac{\tau_{\text{eff}}(T+\Delta T)}{\tau_{\text{eff}}(T)}\right) = \frac{E_a}{k_B T^2}\Delta T \quad \Rightarrow \ln(3) = \frac{E_a}{k_B T^2} q \tau_0,$$

This leads to

$$q_{\text{equil}}(T) \approx \frac{k_B T^2}{E_a \tau_{\text{eff}}(T)}. \tag{6.3}$$

For a given temperature T, this equation yields the corresponding maximum cooling rate at which the EEG conformation occupations remain close to equilibrium. We refer to this rate as the *equilibrium cooling rate*, q_{equil}. The blue curve in Fig. 6.4(b) displays the temperature dependence of q_{equil}. To calculate this equilibrium cooling rate, we used $\tau_{\text{eff}}(T)$ obtained from a linear fit of the data in Fig. 6.2(b), averaged over the relaxation times τ_1 and τ_2 as follows: $\tau_{\text{eff}}^{-1} = (\tau_1^{-1} + \tau_2^{-1})/2$. Conversely, for a given constant cooling rate q_{equil}, the corresponding temperature can be interpreted as the glass transition temperature T_g. The green curve in Fig. 6.5(a) shows the dependence of T_g on the cooling rate.

We can compare this determination of the glass transition temperature with the criterion proposed in [147], given by $-|q|\, d\tau_{\text{eff}}/dT \simeq 1$. Taking the derivative of Eq. (3.2) with respect to temperature, we find:

$$\frac{d\tau_{\text{eff}}}{dT} = -\tau_{\text{eff}}\left(\frac{E_a}{k_B T^2} + \frac{\Delta E}{k_B T^2}\cdot\frac{e^{-\frac{\Delta E}{k_B T}} - e^{\frac{\Delta E}{k_B T}}}{e^{\frac{\Delta E}{k_B T}} + e^{-\frac{\Delta E}{k_B T}}}\right) \approx -\frac{E_a \tau_{\text{eff}}}{k_B T^2}.$$

This yields an expression for the cooling rate: $q(T) = (d\tau_{\text{eff}}/dT)^{-1} \approx k_B T^2/E_a\tau_{\text{eff}}(T)$. This expression is consistent with the earlier result from Eq. (6.3), thereby validating our determination of the glass temperature and estimated value of the equilibrium cooling rate.

We can compare the derived formulas for the equilibrium cooling rate $q_{\text{equil}}(T)$ with the experimental data taken at constant cooling rates. Fig. 6.3(b) shows resistivity vs. temperature curves obtained for $q = 1\,\text{K/min}$. A clear hysteresis is observed between the upward and downward temperature sweeps, caused by relaxation during cooling. The inset in Fig. 6.3(b) presents the resistivity difference between the upward and downward sweeps for cooling rates of 1 K/min (black) and 2 K/min (red), normalized to the average value. Increasing the cooling rate reduces the relaxation amplitude and, consequently, the resistance difference (the red peak is smaller than the black one). Additionally, the peak shifts to higher temperatures, indicating an increase in the glass transition temperature with increasing cooling rate. From the position of the hysteresis peak, we estimate the glass transition temperatures as: $T_g(q = 1\,\text{K/min}) \approx 79.5\,\text{K}$ and $T_g(q = 2\,\text{K/min}) \approx 81.1\,\text{K}$. On the other hand, using Eq. (6.3) and the temperature-dependent relaxation rates from Fig. 6.2(b), we can recalculate these T_g values into the corresponding optimal rates:

- For $q = 1\,\text{K/min}$: $q_{\text{equil}}(79.5\,\text{K}) \approx 1.5\,\text{K/min}$ and $0.5\,\text{K/min}$ for τ_1 and τ_2
- For $q = 2\,\text{K/min}$: $q_{\text{equil}}(81.1\,\text{K}) \approx 3.1\,\text{K/min}$ and $1.6\,\text{K/min}$ for τ_1 and τ_2

This comparison reveals good quantitative agreement between the estimated equilibrium cooling rate and the experimental results. The actual cooling rate lies precisely between the estimated equilibrium cooling rates corresponding to relaxations 1 and 2. Therefore, Eq. (6.3) can be reliably used for further estimations of the glass transition temperature for given cooling rates.

To achieve higher cooling rates, we utilized the heat pulse method described in Sec. 4.7. After applying a heat pulse, the sample rapidly cooled down to the bath temperature, well below T_g ($T_{\text{bath}} \approx 35\,\text{K}$), thereby effectively freezing a higher concentration of nonequilibrium S conformation. In Fig. 6.4(a), we show the traces of three subsequent pulses. The black curve corresponds to the first pulse (6 V). The initial temperature of the sample corresponds to T_{bath}. Once the pulse starts, the resistance increases until it reaches R_{peak}, after which it decreases, reaching the maximum temperature ($T_{\text{max}} \approx 107\,\text{K}$) - where the sample's self-heating and heat loss to the bath are balanced. When the pulse ends, the sample starts to cool down, and the resistance increases again, reaching a new R_{peak}, which corresponds to a new concentration of S and E conformations. Next, we applied a 6.4 V pulse (red curve). The initial state of this pulse corresponds to the final state of the previous one. The increase in the pulse voltage raised the maximum temperature ($T_{\text{max}} \approx 122\,\text{K}$) reached during heating and increased the concentration of S conformation, leading to a higher residual resistance. However, a further increase in the pulse voltage to 7 V, although increasing the maximum temperature ($T_{\text{max}} \approx 147\,\text{K}$) during the pulse, results in a decrease of the residual resistance. This implies a reduction of the nonequilibrium S conformation concentration, as compared to the previous pulse. The next paragraph will compare the cooling rates at different pulses with the previously described equilibrium cooling

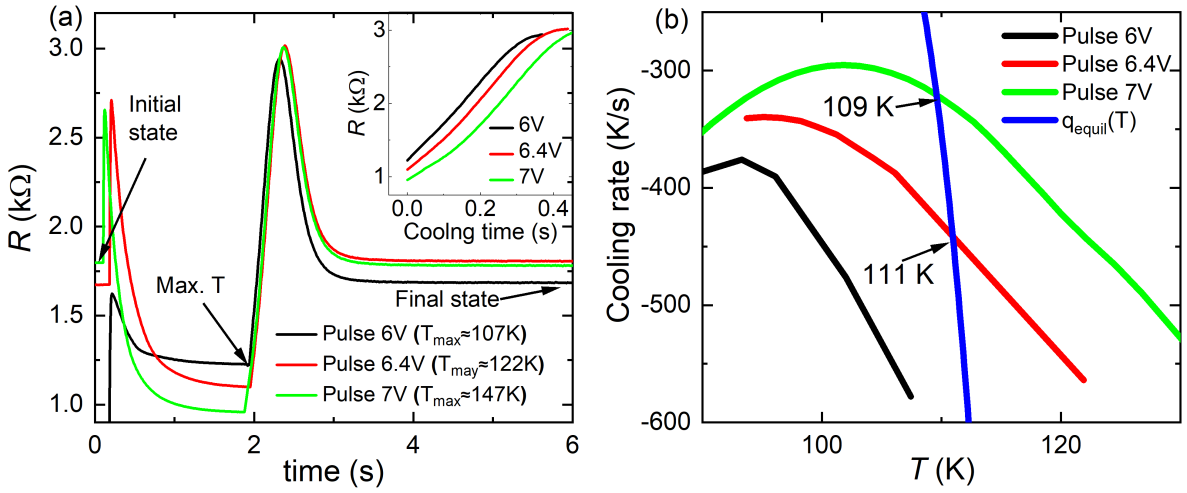

Figure 6.4: (a) Time dependence of the resistance of a κ-h_8-Br sample during heat pulses with different voltages and subsequent cooling. Inset: change of the resistance immediately after the pulse during cooling. (b) Temperature dependence of the cooling rate after the pulses with different voltage (black, red and green curves correspond to 6 V, 6.4 V and 7 V voltages) and equilibrium cooling rate, calculated with Eq. (6.3) (blue curve).

rates, explaining the observed changes in the residual resistance and S conformation concentration.

Fig. 6.4(b) shows the cooling rates during three pulses with voltages of 6 V (black), 6.4 V (red), and 7 V (green), along with the equilibrium rate curve, calculated with Eq. (6.3) (blue). Comparing the equilibrium curve with the cooling rate after the 7 V heat pulse, we observe that they areintersecting at $T_{7\,\mathrm{V}} \approx 109\,\mathrm{K}$ (intersection ofthe blue and green curve). At temperatures above this intersection point, the equilibrium cooling rate is higher (in absolute values) than the cooling rate after the heat pulse. This indicates that at these temperatures, the samples are in an equilibrium concentration of S and E conformations. At temperatures below the intersection, the pulse cooling rate exceeds the equilibrium rate, meaning that the samples cool faster than they relax towards the equilibrium state. Therefore, we can consider the concentration of E and S conformations after the pulse to be frozen at this intersection temperature. It can also be seen that the pulse at 6.4 V crosses the relaxation line at a temperature ($T_{6.4\,\mathrm{V}} \approx 111\,\mathrm{K}$), that is, at a higher than $T_{7\,\mathrm{V}}$ and thereby preserving a larger fraction of nonequilibrium S conformation. For the 6 V pulse (black curve), the analysis is more straightforward. Since it is located at a higher cooling rate than the equilibrium curve, we consider the concentration of conformations from $T_{\mathrm{max}} \approx 107\,\mathrm{K}$ to be preserved as the sample cools to lower temperatures. Because T_{max} for 6 V is lower than the intersection temperature for 6.4 V, the concentration of the nonequilibrium S conformation and the residual resistivity are also lower.

The pulse treatment was applied only to hydrogenated κ-Br samples, as the deuterated samples already exhibit high resistance, an upturn at low temperatures, and hysteresis, even after cooling at a rate of 2 K/min (as shown in Fig. 6.1), which can be achieved by the usual cooling process, controlled by the LakeShore 350 temperature

controller. For both compounds, we confirm that thermal treatments affect the low-temperature resistivity and the superconducting critical temperature through changes in the concentration of S and E conformations at low temperatures.

The occupational probability of the nonequilibrium S conformation (p_S) increases with temperature. Therefore, fast cooling preserves a higher p_S value at low temperature, which, in turn, is associated with a higher degree of disorder and also shifts the system closer to the MIT. However, we still did not answer the question of how different the actual concentrations of p_S are in the purely metallic state compared to those in the coexistence region of the MIT.

6.3 S-conformation occupation probability

In this section, we summarize our experiments on both the hydrogenated and deuterated κ-salts, which have been prepared by four different cooling processes. These four samples for both compounds were prepared and studied at the High Magnetic Field Laboratory (HLD) of the Helmholtz-Zentrum Dresden-Rossendorf. For κ-h_8-Br and κ-d_8-Br, the most ordered states were achieved through a multi-step annealing process at several temperatures. The lowest annealing temperatures were around 69 K ($\tau_{\text{eff}} = 5$ h, annealing time: 18 h) and 68 K ($\tau_{\text{eff}} = 12$ h, annealing time: 24 h) for κ-h_8-Br and κ-d_8-Br, respectively. The multi-step annealing process was used to reduce the annealing time and described in Sec. 4.7. The resulting annealed states were considered as fully relaxed at the respective lowest annealing temperatures. Unfortunately, in HLD, a significant temperature gradient existed between the samples and the thermometer when using a heater for annealing. Therefore, the annealing temperatures were estimated based on the temperature dependence of the relaxation times, which were measured beforehand in Garching, where the thermometer and samples had good thermal coupling. The occupation probability of S and E conformations for these states was estimated directly from Eq. (3.1) describing the equilibrium occupation probability [149], which is represented by green curve in Fig. 6.5(b).

For κ-d_8-Br, further three states were achieved with constant cooling rates: "slow cooling" (0.1 K/min), "medium cooling" (0.5 K/min) and "normal cooling" (2 K/min). For κ-d_8-Br, these cooling rates were sufficient to shift samples closer to the MIT region. This is evidenced by a prominent resistance upturn and hysteresis, as we saw at the beginning of this chapter (Fig. 6.1(b)). To calculate the occupation probability, we used the method proposed in [149] and described in detail in Sec. 3.7. We applied Eq. (3.3) for different constant cooling rates. The temperature dependence of the equilibrium occupation probability for E conformation is shown in Fig. 6.5(b).

There is also another method for the estimation of the occupation probability for cooling with a constant rate. The temperature dependence of the equilibrium cooling rate, previously introduced in Eq. (6.3), can be transferred into a dependence of the glass transition temperature on the (constant) cooling rate, $T_g(q)$. This $T_g(q)$ dependence is presented in Fig. 6.5(a) by the green curve. For a given T_g, it is possible to estimate the E- and S-conformation occupations by just taking the equilibrium occupation probability (Eq. (3.1), Fig. 6.5(b) green curve). Therefore, we can ascribe a certain occupation probability of S conformation to each constant cooling rate, as represented

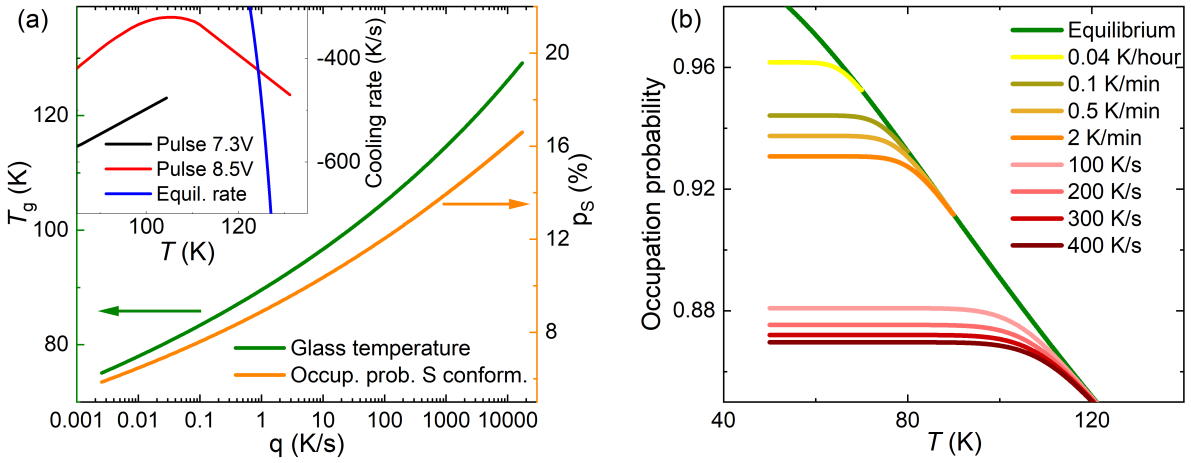

Figure 6.5: (a) Dependence of the glass temperature T_g (green curve, left scale) and of the occupation probability of the nonequilibrium S state on the cooling rate (orange curve, right scale). Inset: Temperature dependence of the cooling rate after applying heat pulses with different voltages (black and red curves correspond to 7.3 V and 8.5 V, respectively) and equilibrium cooling rate (blue curve). Blue curve shows equilibrium cooling rate from Eq. (6.3). (b) Temperature dependence of the occupation probability of the E conformation, calculated using Eq. (3.3) for different (constant) cooling rates.

by the orange curve in Fig. 6.5(a). This method gives 1 % to 2 % higher p_S values than the method based on the calculation via Eq. (3.3) (Fig. 6.5(b)). However, both methods provide only an approximate estimate for the occupation probability. Therefore, for further estimations we will take the method based on calculations with Eq. (3.3), as it takes into account both the cooling rate (q) and the initial temperature for cooling ($T_{\max}$).

For κ-h_8-Br, the second-most ordered state was the state obtained by normal cooling ($q \approx 2\,\mathrm{K/min}$). To achieve higher occupation probabilities of the nonequilibrium S conformation, two voltage pulses were applied (Fig. 6.5(a), inset): one with a voltage of 7.3 V, reaching a maximum temperature of approximately 105 K ("quenched" state), and another with a higher voltage of 8.5 V, reaching 130 K ("super-quenched" state).

To estimate the occupation probability in the quenched states, we used the same approach as for a constant cooling rate. For the 8.5 V pulse, we used the cooling rate at the temperature at which the cooling rate curve intersects with the equilibrium cooling rate curve (the red and blue curves in the inset of Fig. 6.5(a) intersect at $T_{\mathrm{inter}} \approx 124\,\mathrm{K}$). For the 7.3 V pulse, we used the initial cooling rate immediately after the pulse (black curve in the inset of Fig. 6.5(a)), as it does not intersect with the equilibrium cooling rate curve. Although this estimation may be imprecise due to variations in the cooling rate during fast cooling (as shown in the inset of Fig. 6.5(a), where the cooling rate varies by 100 K/s within the temperature range of interest), such fluctuations at very high cooling rates affect the occupation probability by less than 1 %, as evidenced in Fig. 6.5(b).

The states described above and their estimated occupation probabilities of S and E conformations are summarized in Table 6.1. The values reported in the table differ

Table 6.1: Occupation probabilities of the E and S conformations, calculated using Eq. (3.3) and the relaxation times extracted from Fig. 6.2(b).

κ-h_8-Br	Annealed	Normal cooling	Quenched	Super-quenched
p_E	0.955	0.931	0.882	0.867
p_S(%)	4.5	6.9	11.8	13.3
κ-d_8-Br	Annealed	Slow cooling	Medium cooling	Normal cooling
p_E	0.957	0.944	0.937	0.930
p_S(%)	4.3	5.6	6.3	7.0

slightly from those presented in [149], where this estimation method was originally introduced (see Sec. 3.7). In our case, the minimal value of p_S exceeds 4 %, whereas in [149], it was reported to be around 2 %. This discrepancy arises primarily because the calculation of p_E using Eq. (3.3) employed a different temperature dependence of the relaxation time $\tau_{\text{eff}}(T)$, which may vary slightly between compounds. In our experiments, we used fully hydrogenated and deuterated κ-Br, whereas in [149], partially deuterated κ-$h_{0.2}$-$d_{0.8}$-Br (with 80 % deuterated BEDT-TTF molecules) was used. Additionally, our estimation was based on an average $\tau_{\text{eff}}(T)$ obtained from the mean value of the two relaxation rates, $\tau_{\text{eff}}^{-1} = (\tau_1^{-1} + \tau_2^{-1})/2$. As a result, some difference in the absolute values of p_S is not surprising. Therefore, we suggest that more emphasis should be placed on the relative change in p_S rather than its absolute magnitude.

6.4 Thermal history and effective pressure

As observed from the resistance vs. temperature curves in Fig. 6.1, the occupation probabilities of the S and E conformations significantly influence the $R(T)$ behavior of the samples. The resistive peak increases in magnitude and shifts to the lower temperatures (Fig. 6.1) upon increasing the occupation probability of the nonequilibrium S state p_S. As discussed in Sec. 3.7, the effect of the EEG conformations on the electronic state of the κ-salts was suggested to be similar to the pressure effect [148, 159]. If so, one can set an approximate quantitative correspondence between the two effects. To this end, we make use of the shift of the resistive peak position in the $R(T)$ dependence as a criterion for the location of the material on the phase diagram.

In [62], the maximum in the $R(T)$ curves was explained by the destruction of heavy quasiparticles, which dominate electronic transport at low temperatures. These quasiparticles are characterized by a low coherence temperature, which can be identified as $T_{\text{peak}} \sim T_{\text{F}} m_{\text{band}}/m^*$. Since the effective mass m^*, renormalized by electron-electron interactions, is very sensitive to the applied pressure, one can correlate the EEG conformation occupation probability and pressure by comparing the shifts in T_{peak}.

According to [42], for κ-Cl under pressure in the vicinity of the MIT (40 MPa to 50 MPa), T_{peak} shifts by $dT_{\text{peak}}/dp \approx 20\,\text{K}/10\,\text{MPa}$. We assume that the pressure effects are similar in κ-Br and κ-Cl (this is indeed shown in the next chapter). Fig. 6.6(a) shows the peak temperature at different occupation probabilities of the S conformation for

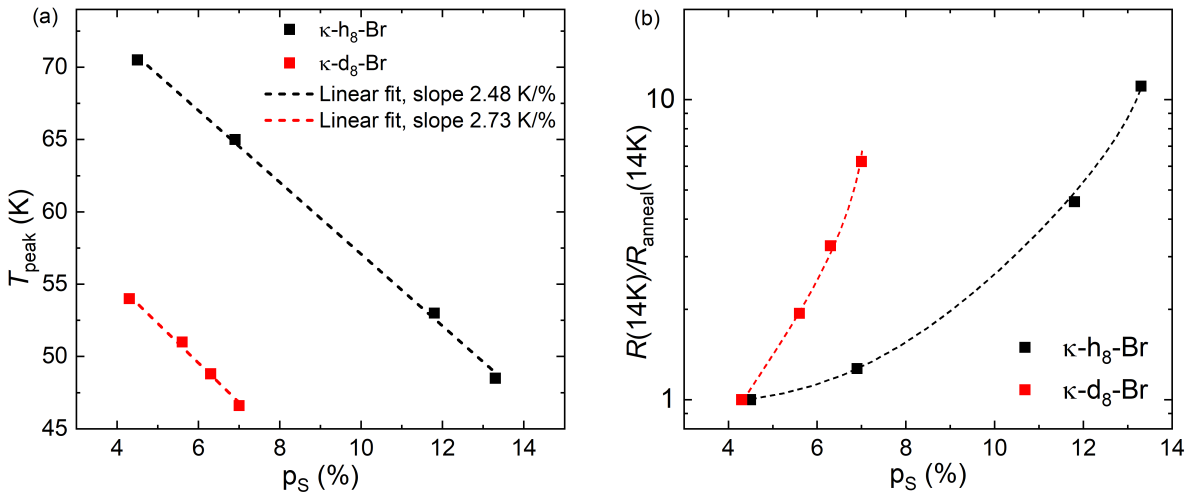

Figure 6.6: (a) Temperature dependence of the peak in the $R(T)$ curve for samples with different occupation probabilities of the S conformation for κ-h_8-Br (black) and κ-d_8-Br (red). (b) Resistance at $T = 14\,\mathrm{K}$ for the states with different occupation probabilities of the S conformation, normalized to the resistance of the annealed state for κ-h_8-Br (black) and κ-d_8-Br (red). The dashed lines are guides for the eye.

both hydrogenated (black points) and deuterated (red points) κ-Br. Both compounds show similar slopes of approximately $2.6\,\mathrm{K}/\%$. The shift in $\Delta T_{\mathrm{peak}} = 20\,\mathrm{K}$ corresponds to approximately 7 % difference in the occupation probability. Comparing the influence of the EEG conformations with the effect of pressure, one can conclude that a fraction of 1 % of nonequilibrium S conformation should act equivalently to 1.4 MPa of 'negative' pressure. Using these relationships, we can estimate that for the states with minimal and maximal occupation probabilities of the S conformation in κ-h_8-Br and κ-d_8-Br, the effective pressure differences correspond to approximately 12 MPa and 4 MPa, respectively.

Another method to correlate the pressure effect and influence of the EEG conformations, through comparison of the residual resistance, was proposed in [159] and discussed in Sec 3.7. The partially deuterated κ-$d_{0.8}$-Br compound was studied in two states with different occupation probabilities (annealed and quenched) at various applied pressures. The comparison of the $R(T)$ curves revealed an equivalent pressure difference between the states of approximately 20 MPa. The estimated difference in the occupation probability of the S conformation between the states is approximately 4 %. This value means that the relationship between pressure and occupation probability is approximately $5\,\mathrm{MPa}/\%$. That is, the estimated value is much higher than that derived in the previous paragraph. However, the coefficient between pressure and p_S obtained from this method may be overestimated, as the nonequilibrium S conformation also acts as an additional source of disorder, thereby increasing scattering and the low-temperature resistance. In contrast, pressure does not affect scattering and increases the residual resistance only through electronic correlations.

It is also possible to correlate the pressure with the occupation probability through theoretical calculations of the electronic correlation strength. According to [148], the correlation strength ratios in the pure E and S states are $U/t = 5.3$ and 6.1, respectively.

In a mixed state, a 1 % occupation probability of the nonequilibrium S conformation is estimated to increase the correlation strength by $\Delta(U/t)/(U/t) \approx 0.15\,\%$ (in absolute values $\Delta(U/t) \approx 0.008$). This change in the correlation strength ratio can be converted into a change in the effective mass using the Brinkman-Rice formula (Eq. (2.30)) and the coefficients obtained from the fitting of the experimental data [110]. While these coefficients were obtained for κ-Cl and κ-NCS, they can also be applied to κ-Br, as we will see that their effective mass behaviors are very similar. The change in the correlation strength $\Delta(U/t) \approx 0.008$ corresponds to the change in the inverse effective mass $m_{\text{band}}/m^* \approx 0.011$. This mass difference in the vicinity of the MIT can be achieved by application of 10 MPa of pressure. This value is also higher than our previous estimation. This discrepancy may be related to the inaccuracy of the correlation strength calculations [148].

All these estimations, based on different approaches, yield different predictions about the influence of the nonequilibrium EEG conformation occupation probability on electronic correlations. However, it is also possible that EEG conformations do not affect the correlation strength and instead act solely as additional disorder. Determining the actual mechanism requires direct measurements of the correlation strength. To address this, we measured SdH oscillations in the states with different occupation probabilities for the S and E conformations.

6.5 Shubnikov-de Haas oscillations in pulsed fields

To investigate the influence of the EEG conformations on the bandwidth and electronic correlations, we measured SdH oscillations. Since κ-Br requires a high B/T ratio [103, 109] to resolve distinct oscillations, we utilized pulsed magnetic fields in combination with a ^{3}He cryostat, as described in Sec. 4.4.3.

We measured the resistance of the samples in a magnetic field oriented perpendicular to the layer structure of the samples. The samples exhibited superconductivity with a transition occurring within the magnetic field range of 8 T to 20 T (Fig. 6.7(a) for hydrogenated and Fig. 6.7(b) for deuterated κ-Br). The notation for the states is the same as in Sec. 6.3. Beyond 20 T, superconductivity was completely suppressed, and the magnetoresistance became nearly flat, displaying a slight negative trend.

At the lowest temperatures of approximately 0.6 K, the relative amplitude of the SdH oscillations exceeded 5 % of the total resistance for all states in magnetic fields $B > 60$ T. A Fast Fourier Transform (FFT) analysis of the oscillations revealed a dominant β-frequency, which corresponds to orbitals enclosing an area about equal to the size of the first Brillouin zone. This frequency, as well as its second and third harmonics, were consistent across the different states (Fig. 6.7(c)). However, no evidence of the α-frequency was observed. Since our measurements were conducted in high magnetic fields, the magnetic breakdown orbit likely dominates the oscillations. Furthermore, the only reported observations of α-oscillations in κ-Br were made by [109], where the oscillations were detected within a field range of 20 T to 26 T for a magnetic field tilted relative to the direction perpendicular to the sample layers. In contrast, for a strictly perpendicular orientation, the α-oscillations amplitude was strongly suppressed.

The amplitude of the oscillations exhibited a clear trend, decreasing as the occupa-

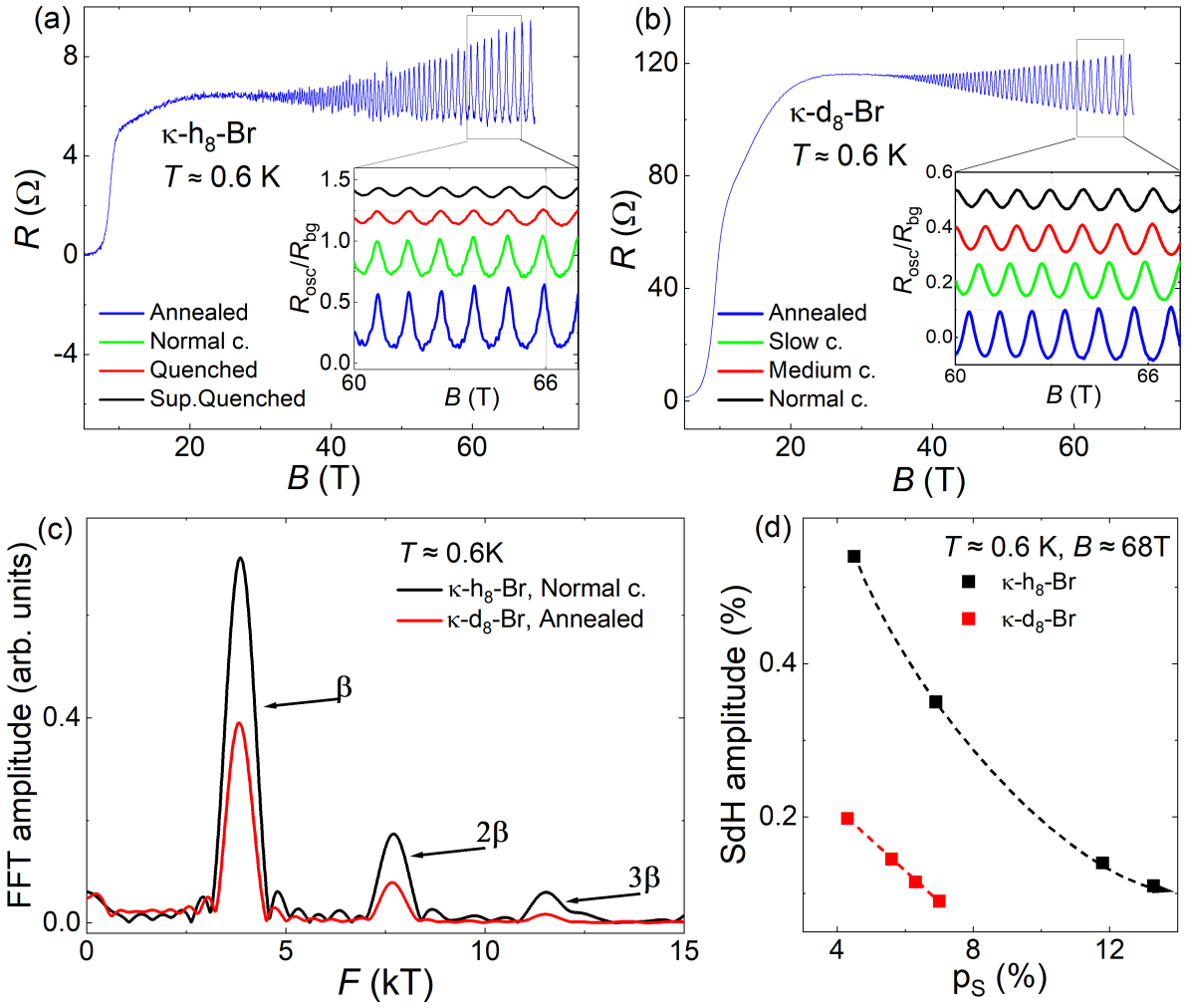

Figure 6.7: Magnetoresistance and SdH oscillations of κ-h_8-Br (a) and κ-d_8-Br (b) in the annealed state, measured at a temperature around 0.6 K. The insets display oscillations at states with different thermal histories, normalized to the background resistance and vertically shifted for clarity. (c) FFT of the SdH oscillations for κ-h_8-Br (black) in the normally cooled state and κ-d_8-Br (red) in the annealed state, measured at the temperature 0.6 K and analyzed in the field range 45 T to 65 T. (d) SdH β oscillations relative amplitude at a magnetic field of 68 T for the states with different occupation probabilities of the S conformation for κ-h_8-Br (black) and κ-d_8-Br (red). The dashed lines are guides for the eye.

tion probability of the nonequilibrium S conformation increases (Fig. 6.7(d)). This reduction may be due to enhanced scattering or an increased effective cyclotron mass. Despite this variation in amplitude, the oscillation frequency remained unchanged across different states within the error margins, which means that the Fermi surface is insensitive to the occupation probability of the EEG conformations. The measured frequencies were 3850 ± 10 T for κ-h_8-Br and 3860 ± 10 T for κ-d_8-Br. These values are slightly higher than the previously reported 3800 ± 30 T [103, 184], while the β-frequency calculated from the unit cell size [158] is around 3800 T. This discrepancy in

the frequencies may be attributed to a small misalignment of the samples.

6.6 Effective cyclotron mass

The primary aim of this section is to explore how electronic correlations evolve as the system approaches the MIT with the increasing occupation probability of the nonequilibrium conformation p_S. This investigation focuses on the evaluation of the effective cyclotron mass in different states, which serves as a key indicator of electronic correlations, as discussed in Sec. 2.8. The analysis was carried out by measuring the SdH

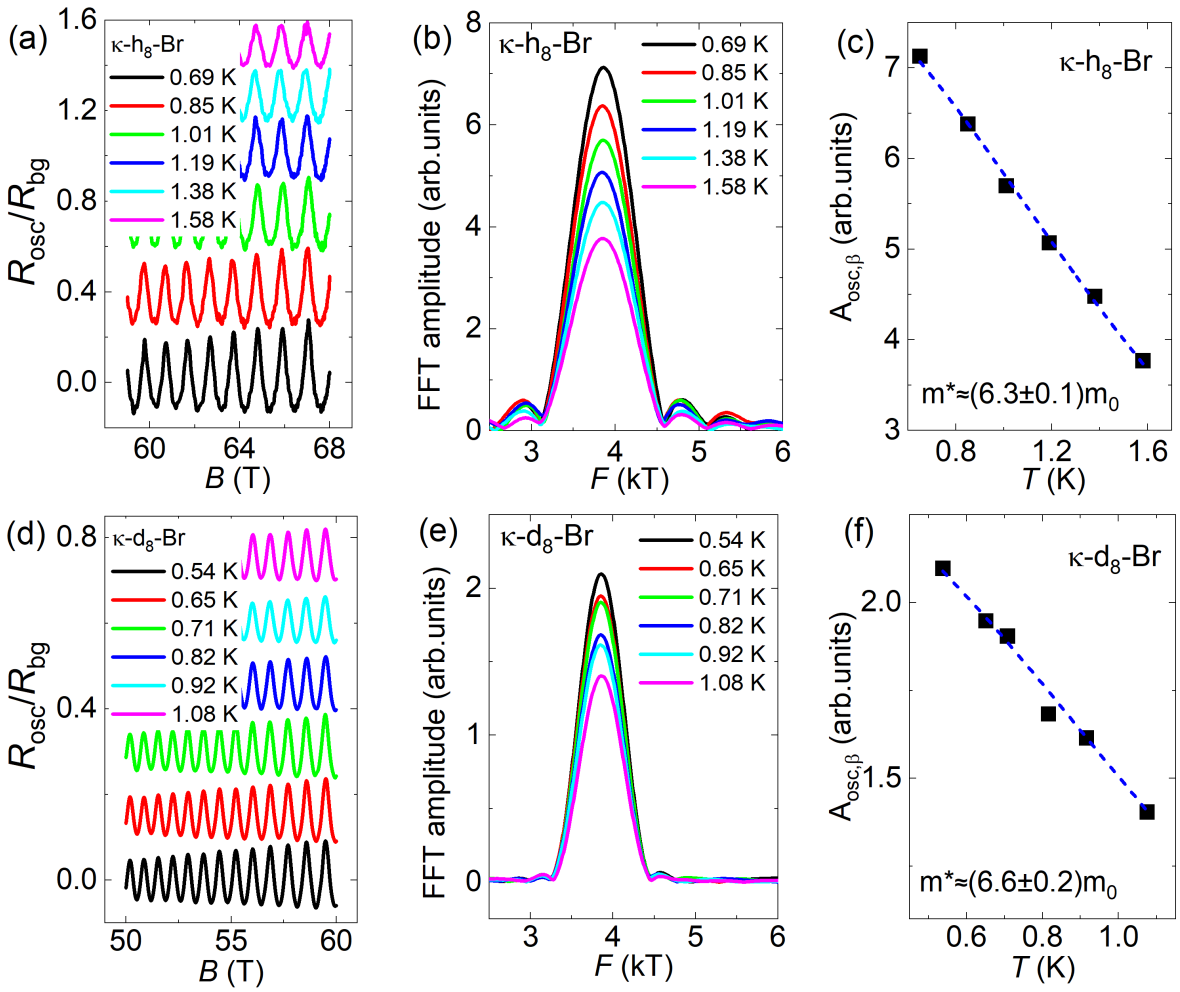

Figure 6.8: Steps in the evaluation process of the effective cyclotron mass for κ-h_8-Br (top row) prepared by normal cooling and for κ-d_8-Br (bottom row) prepared in the annealed state. SdH oscillations at different temperatures for κ-h_8-Br (a) and κ-d_8-Br (d). The curves are vertically shifted for clarity. First harmonic peak in the FFT of the oscillations at different temperatures for κ-h_8-Br (b) and κ-d_8-Br (e). Fit of the temperature dependence of the FFT amplitude of the β oscillations using the LK temperature damping factor (Eq. (2.9)) for κ-h_8-Br (c) and κ-d_8-Br (f).

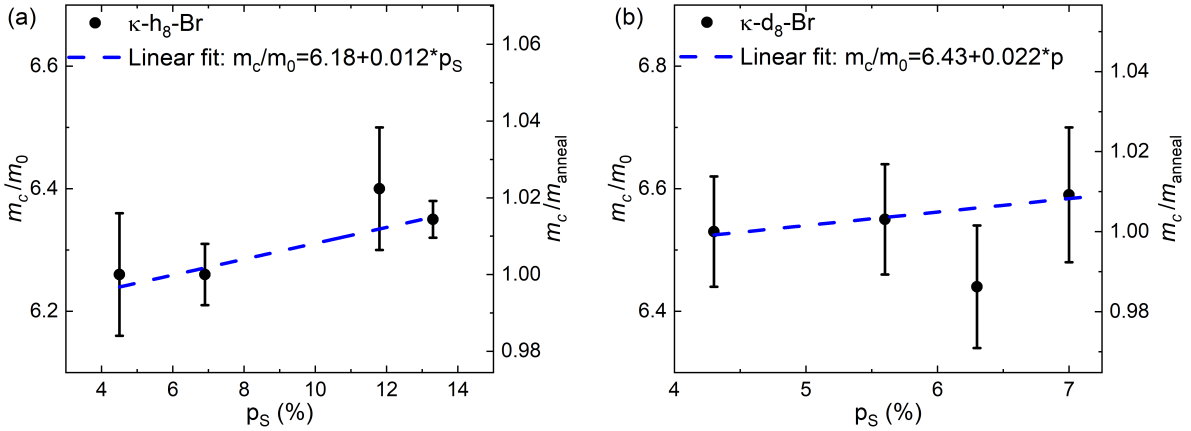

Figure 6.9: Effective cyclotron mass in the states with different occupation probability of the nonequilibrium S conformation for κ-h_8-Br (a) and κ-d_8-Br (b). Right scale normalized to the effective mass in the annealed state. The dashed blue lines are linear fits.

oscillations at different temperatures.

Fig. 6.8 shows the effective mass determination process for a κ-h_8-Br sample prepared by normal cooling and for a κ-d_8-Br sample prepared in the annealed state. To extract the effective cyclotron mass, the SdH amplitude was first normalized to the background (Fig. 6.8(a) for κ-h_8-Br and Fig. 6.8(d) for κ-d_8-Br) and analyzed within a magnetic field interval 50 T to 70 T using FFT (Fig. 6.8(b) for κ-h_8-Br and Fig. 6.8(e) for κ-d_8-Br). The temperature dependence of the FFT amplitude was then fitted using the temperature damping factor of the Lifshitz-Kosevich formula (Eq. (2.9)) (Fig. 6.8(c) for κ-h_8-Br and Fig. 6.8(f) for κ-d_8-Br). From this fitting, the effective cyclotron mass was determined.

The measured effective masses for both hydrogenated and deuterated κ-Br at different p_S are presented in Fig. 6.9. The averages over the different states masses for the compounds are $m_{h8} \approx 6.3 \pm 0.1\, m_0$ and $m_{d8} \approx 6.55 \pm 0.15\, m_0$. For κ-h_8-Br the relative mass differences between the lowest and highest p_S is less than 2 %, while for κ-d_8-Br its approximately 1 %. The slope of the relative mass dependence on the p_S is $dm/mdp_S \approx 0.002/\%$. These changes of the effective mass due to the increase of p_S lie well within the error margin of the mass determination. These masses can be converted into the corresponding effective pressures using the pressure dependence of the effective mass from further Chapter 7 with a coefficient between the relative mass change and pressure $dm/mdp \approx 0.0026\,\mathrm{MPa}^{-1}$. The mass differences correspond to the pressure differences of $\Delta p_{h8} \approx 6\,\mathrm{MPa}$ and $\Delta p_{d8} \approx 3\,\mathrm{MPa}$ and the coefficient between pressure and occupation probability $dp/dp_S \approx 0.6\,\mathrm{MPa}/\%$. These effective pressure differences are much smaller than the values suggested by the $R(T)$ measurements (for κ-h_8-Br $\Delta p_{h8} \approx 12\,\mathrm{MPa}$ and for κ-d_8-Br $\Delta p_{d8} \approx 4\,\mathrm{MPa}$ with a coefficient $dp/dp_S \approx 1.4\,\mathrm{MPa}/\%$) and theoretical calculations [148] (for κ-h_8-Br, $\Delta p_{h8} \approx 90\,\mathrm{MPa}$, and for κ-d_8-Br, $\Delta p_{d8} \approx 30\,\mathrm{MPa}$, with a coefficient $dp/dp_S \approx 10\,\mathrm{MPa}/\%$).

These small changes in the effective masses, which are below the error margins of mass determination, along with the discrepancy between the observed and predicted

effective pressures, suggest that the magnitude of this effect is much smaller than expected, although we can not completely rule out an influence of p_S on the strength of electronic correlations,. Therefore, p_S influences the electronic system through a mechanism other than correlation strength. Most likely, this mechanism is associated with enhanced scattering, which will be investigated in the next section.

6.7 Dingle temperature

Another important parameter, extracted from the SdH oscillations, is the Dingle temperature. It characterizes the quasiparticle lifetime and can be associated with the scattering rate through Eq. (2.10). To estimate the Dingle temperature T_D, one can fit the oscillation amplitude as a function of magnetic field with the LK formula including the Dingle damping factor, given by Eq. (2.11). An example of such a fit is shown in Fig. 6.10(a). For precise estimations, it is better to use a broader field range and purify the oscillatory signal by applying an appropriate FFT filter. The black line shows inverse FFT of the first harmonic of the normalized SdH oscillation in κ-h_8-Br in the annealed state at a temperature of 0.66 K. Blue lines are the Dingle fit of the peaks in the oscillations, with $T_D \approx 0.9$ K, which corresponds to a scattering rate of $\tau^{-1} \approx 0.8 \times 10^{12}\,\mathrm{s}^{-1}$.

The calculated T_D shows a significant increase with p_S as shown in Fig. 6.10(b), implying an increase in the scattering rate. This indicates that the nonequilibrium S con-

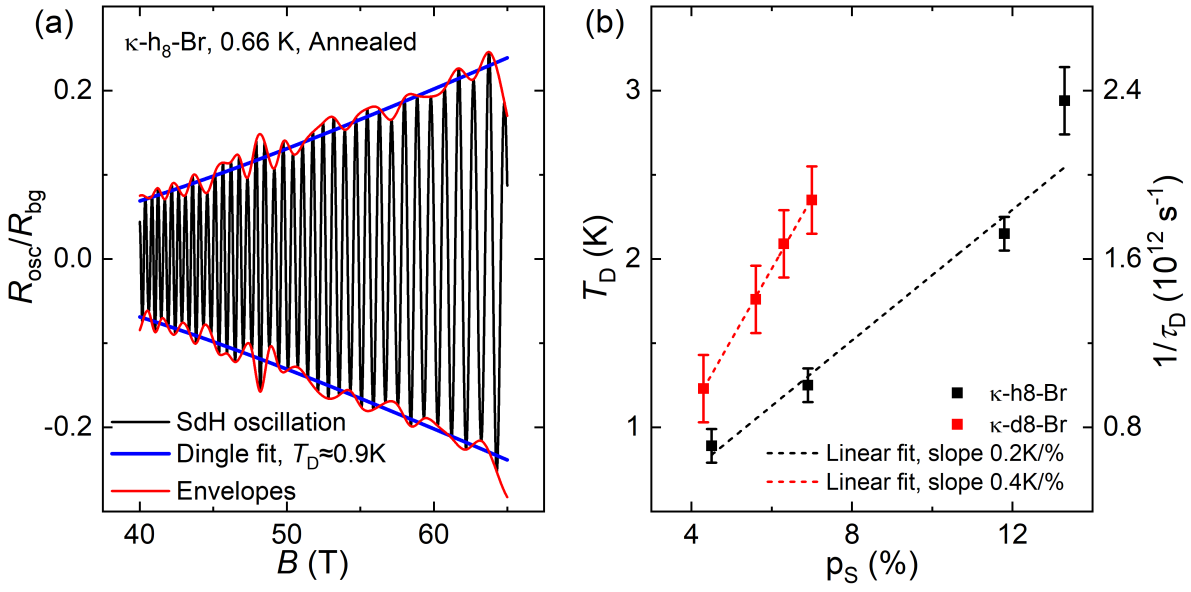

Figure 6.10: (a) Normalized SdH oscillations for κ-h_8-Br in the annealed state (black line), measured at 0.66 K, with the upper and lower Dingle fits (blue lines) derived from the Dingle damping factor R_D. The red lines represent the upper and lower envelopes. (b) Dependence of the Dingle temperature on occupation probability p_S for κ-h_8-Br (black) and κ-d_8-Br (red). Dashed lines are linear fits. The right scale shows rescaling of the Dingle temperature to the scattering rate.

formation acts as an additional source of disorder. However, the hydrogenated and deuterated salts exhibit different dependencies of the scattering rate on p_S. For κ-h_8-Br, an increase of p_S by 1 % of p_S increases the scattering rate by $\Delta(\tau^{-1})_{h8} \approx 0.2 \times 10^{12}\,\mathrm{s}^{-1}$, while for κ-d_8-Br it increases the scattering rate by $\Delta(\tau^{-1})_{d8} \approx 0.3 \times 10^{12}\,\mathrm{s}^{-1}$. This suggests that a single nonequilibrium S conformation in deuterated κ-Br induces a defect with either a stronger scattering potential or a larger effective size. One possible explanation is the influence of the heavier deuterium atoms in this compound, as these atoms are one of the main distinguishing attributes in the formation of EEG conformations. The linear extrapolation of the Dingle temperature dependence on p_S to zero S conformation occupation probability yields values that are either close to zero or slightly negative. This suggests that p_S is the primary source of disorder in these compounds and indicates the high quality and purity of the samples.

6.8 Scattering rate

Fig. 6.11(a) shows the dependence of the Dingle temperature on the residual resistivity ρ_{res}. The latter was determined by extrapolating the magnetoresistance curves (Fig. 6.7(a)) to zero magnetic field and presented in Fig. 6.11(a) on a logarithmic scale for better visibility. The right and top scales show the rescaling of the Dingle temperature and residual resistivity to the corresponding scattering rate. The scattering rate associated with the residual resistivity was calculated with Eq. (3.5) using $d = 1.47\,\mathrm{nm}$ [158], $t_\perp = 0.1\,\mathrm{meV}$ [103, 184] and the effective masses from the previous section. A comparison of the Dingle temperatures and residual resistance reveals a significant deviation from linearity. This linear dependence was initially proposed under the assumption that both the Dingle temperature (Eq. (2.10)) and residual resistance (Eq. (3.5)) depend linearly on the scattering rate, with the same source of scattering affecting both transport and magnetic properties.

A similar discrepancy was already observed in several works, including [156, 164, 165, 167, 170]. A possible explanation for this discrepancy was provided in [164]. They suggested that different components of the scattering rate affect the residual resistance and Dingle temperature in the distinct ways and scattering entering in the Dingle temperature has additional sources $\tau_{\mathrm{D}}^{-1} = \tau_{\mathrm{imp}}^{-1} + \tau_{\mathrm{other}}^{-1}$. Here, the residual resistivity is dominated mainly by the elastic large-angle scattering by impurities $\tau_{\mathrm{trans}} = \tau_{\mathrm{imp}}$. On the other hand, the scattering rate obtained from the Dingle temperature includes additional contributions from smaller-angle scattering by dislocations, weak potential modulation in space, and so on. This approach would imply that an enhanced scattering rate is entering the Dingle temperature with increasing p_S. However, we observe that the scattering rate associated with residual resistivity increases even stronger. Therefore, this explanation is not applicable.

Another parameter that may change with increasing p_S is the interlayer transfer integral $t_\perp$, which also strongly influences the residual resistivity according to Eq. (3.5). As the EEGs are located at the bonds of the layers, changes in their conformation may increase the potential barrier between the layers and, thereby, decrease the effective $t_\perp$ (in other words, S and E conformations have different local $t_\perp$). As a result, the interlayer resistivity will significantly increase. In [126], a detailed structural study found that

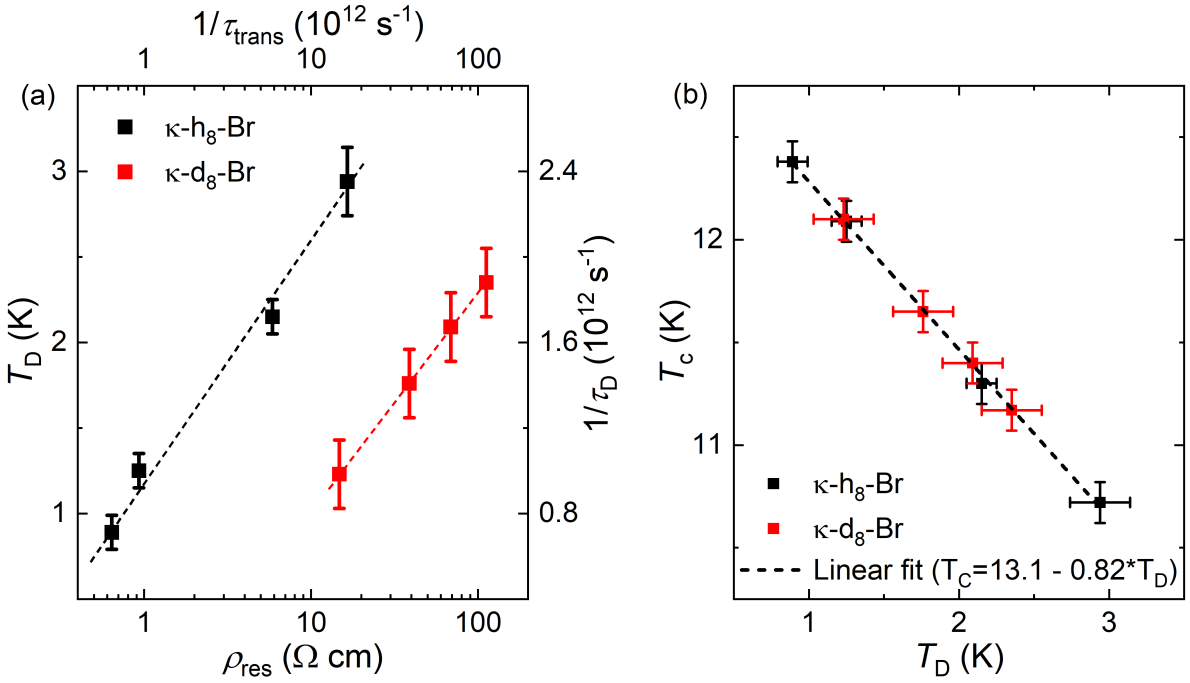

Figure 6.11: (a) Dingle temperatures for κ-h_8-Br (black) and κ-d_8-Br (red) as a function of the residual resistivity. The residual resistivity axis is given on a logarithmic scale for better visibility. The top and right scales show rescaling of the Dingle temperature and residual resistivity to the scattering rate. The dashed lines are guides for the eye. (b) Critical temperature of the superconducting transition for κ-h_8-Br (black) and κ-d_8-Br (red) as a function of the Dingle temperature, with a linear fit (black dashed line).

the rapid cooling process decreases the inter-dimer transfer integral compared to the intra-dimer one. However, to prove this scenario, one would need direct $t_\perp$ measurements in states with different p_S. This can be done through coherence peak (Sec. 2.5) measurements or by observing the beat effect (Sec. 2.6). Moreover, Eq. (3.5) is valid for the case of a homogeneous Fermi liquid. Therefore, its applicability in the vicinity of the MIT or in the coexistence area is questionable. In such cases, the resistivity strongly increases due to electronic interactions.

Another property affected by the scattering rate is the superconducting critical temperature T_c. From the $R(T)$ curves (Fig. 6.1), we observe a decrease in T_c with increasing p_S. This effect has already been observed in κ-NCS and κ-Br [156, 164, 165, 167, 170] as discussed in Sec. 3.9. In these publications the dependence of T_c on the scattering rate τ^{-1} was analyzed by calculating the scattering rate from residual resistivity. Then, the resulting dependence was fitted with the Abrikosov-Gor'kov equation (Eq. (3.4)). The obtained results are in good agreement with AG theory at small scattering rates but show significant deviations at high scattering rates. Therefore, it was suggested that the superconducting state has a mixed order parameter with both s-wave and unconventional components. However, as we saw from the previous paragraph, the straightforward recalculation of the residual resistivity into the scattering rate is invalid in the transient phase-coexistence region of the MIT.

To avoid the questionable recalculation of the residual resistivity into the scattering

rate, we analyzed the relation of T_c and the Dingle temperature. The results presented in Fig. 6.11(b) clearly show that the dependence of T_c on T_D is linear in the entire range studied. Interestingly, the dependencies for both hydrogenated and deuterated compounds coincide, implying that the isotope effect on T_c is solely due to scattering τ. The linear fit of this dependence gives an intercept of $T_{c0} \approx 13.1$ K, which corresponds to the state without disorder. The slope of the dependence is $dT_c/dT_D \approx -0.82 \pm 0.02$. We can estimate that 1 % of disorder decreases T_c by 0.16 K in κ-h_8-Br and by 0.33 K in κ-d_8-Br.

This dependence can be analyzed using the AG formula, given by Eq. (3.4). By considering this equation in the limit of a small amount of disorder, a small change in T_c, and assuming the same scattering time $\tau_{AG} = \tau_D = \hbar/2\pi k_B T_D$, it can be simplified to [156]

$$T_c = T_{c0} - \frac{\pi^2}{4} T_D \approx T_{c0} - 2.46 T_D. \tag{6.4}$$

At first glance, the observed experimental linear relationship between T_c and T_D appears to be consistent with Eq. (6.4) for non-s-wave pairing, suggesting that an unconventional superconducting mechanism is realized in our compounds. However, the experimentally determined slope, $dT_c/dT_D \approx -0.8$, is approximately three times smaller than the theoretical prediction. A similar result was previously reported in [164] for κ-NCS, where the coefficient was found to be $dT_c/dT_D \approx -1.0 \pm 0.3$.

A possible explanation for this discrepancy may lie in the different scattering mechanisms contributing to T_D. In the AG model, the relevant scattering time $\tau_{AG} \approx \tau_{imp}$ corresponds primarily to large-angle impurity scattering. In contrast, the Dingle temperature reflects the total scattering rate, including both large- and small-angle contributions: $\tau_D^{-1} = \tau_{AG}^{-1} + \tau_{other}^{-1}$. Based on the difference between experimental and theoretical coefficients in Eq. (6.4), one can estimate $\tau_{AG} \approx 3\tau_D$ and $\tau_{other} \approx 3\tau_D/2$, indicating that small-angle scattering contributes approximately twice as much as large-angle scattering to the total scattering rate. An alternative explanation could be that the AG formula is derived for 3D systems with scattering integrated over a spherical Fermi surface. In contrast, our system is quasi-2D, and the appropriate integration should be carried out over a cylindrical Fermi surface, which may alter the quantitative predictions of the model.

6.9 Disorder strength

We can try to roughly estimate the disorder strength from the scattering rate. For this, we use Fermi's golden rule [206]: $\tau^{-1} = 2\pi n_i \langle |V_{kk'}|^2 \rangle \rho(E_F)/\hbar$. Here, the impurity potential $\langle |V_{kk'}|^2 \rangle$, averaged over space, can be substituted with the disorder strength and in-plane unit cell area: $\langle |V_{kk'}|^2 \rangle \sim (U_{dis} A_{cell})^2$ [207, 208], where $A_{cell} = (2\pi)^2 S_{BZ}^{-1}$ (see Sec. 3.1). The impurity concentration n_i can be substituted with the concentration of S conformations, $p_S A_{cell}^{-1}$, and for the density of states $\rho(E_F)$ we use the expression from [191] with effective cyclotron mass, $m_c = \pi\hbar^2 \rho(E_F)$. This leads to the formula: $\tau^{-1} = 2 m_c \, p_S A_{cell} \, U_{dis}^2/\hbar^3$.

Further, using the effective dimer model with Eq. (5.1), we can roughly relate the effective mass to the intralayer transfer integral for a system with a frustration ratio

$t'/t \approx 0.6$: $t \approx \hbar^2/(A_{\mathrm{cell}} m_{\mathrm{band}})$, where the values for the frustration ratio and the effective band mass $m_{\mathrm{band}} \approx 2.2 m_0$ are given in Chapter 7. Using the Onsager relation Eq. (2.6), we can express the scattering rate as

$$\tau^{-1} = \frac{m_c e F_\beta}{\pi m_{\mathrm{band}}^2} p_S \left(\frac{U_{\mathrm{dis}}}{t}\right)^2. \tag{6.5}$$

Taking from the previous paragraph that the scattering rate corresponds to full scattering, i.e., $\tau \approx \tau_{\mathrm{D}} = \hbar/(2\pi k_{\mathrm{B}} T_{\mathrm{D}})$, we can rewrite Eq. (6.5) as

$$T_{\mathrm{D}} \approx \frac{m_c m_0}{m_{\mathrm{band}}^2} \frac{F_\beta}{K} \left(\frac{U_{\mathrm{dis}}}{t}\right)^2 p_S. \tag{6.6}$$

Disorder concentrations within the coexistence region of the MIT are approximately 10 % and 6 %, with corresponding Dingle temperatures of $T_{\mathrm{D}} \approx 2\,\mathrm{K}$ for κ-h_8-Br and $T_{\mathrm{D}} \approx 1.8\,\mathrm{K}$ for κ-d_8-Br, respectively (Fig. 6.10(b)). Based on these values, we estimate the disorder strength as $(U_{\mathrm{dis}}/t)_{h8} \approx 0.24$ and $(U_{\mathrm{dis}}/t)_{d8} \approx 0.30$. The slight difference in disorder strength between the two compounds may be attributed to variations in their correlation strength, which is known to be stronger in the deuterated compound. According to [88], the critical disorder strength increases with increasing correlation strength, which is consistent with our observations.

Another approach for estimating the disorder strength is based on the slope of the linear dependence of the Dingle temperature on disorder concentration, as shown in Fig. 6.10(b). The values of the slope are approximately $dT_{\mathrm{D}}/dp_S \approx 22\,\mathrm{K}$ for κ-h_8-Br and 38 K for κ-d_8-Br. From this, we can estimate the disorder strength as $(U_{\mathrm{dis}}/t)_{h8} \approx 0.26$ and $(U_{\mathrm{dis}}/t)_{d8} \approx 0.33$. Using the intralayer transfer integral of $t \approx 32\,\mathrm{meV}$ estimated from the effective dimer model, we obtain the absolute disorder strength $U_{\mathrm{dis}}^c \approx 10\,\mathrm{meV}$.

Both estimation methods yield comparable values for the disorder strength. Knowing the disorder concentration at which the systems lie within the coexistence region of the MIT (approximately 10 % for κ-h_8-Br and 6 % for κ-d_8-Br), we can estimate the effective critical disorder strength in these compounds as $(U_{\mathrm{dis}}/t)_{\mathrm{eff}} = \sqrt{p_S}(U_{\mathrm{dis}}/t) \approx 0.1$, corresponding to $U_{\mathrm{dis}}^{\mathrm{eff}} \approx 4\,\mathrm{meV}$.

This estimated effective disorder strength is significantly smaller than theoretical predictions. For 3D systems, theoretical models typically predict a critical disorder strength of $U_{\mathrm{dis}} \sim 10 - 20\,t$ [87, 209, 210], while other approaches yield values around $\sim 2 - 5\,t$ [162, 210, 211], depending on the computational method, assumed disorder distribution, and cluster size. In contrast, for quasi-1D and quasi-2D systems, the Anderson transition is expected to occur at much lower disorder strengths, with $U_{\mathrm{dis}}^c \sim 1 - 3\,t$ [88, 209].

Our experimentally estimated values remain significantly lower than theoretical expectations. This discrepancy may be attributed to the inaccuracy of our determination methods or theoretical calculations. Another possible reason is the nature of the disorder: while theoretical models commonly assume a uniform or Gaussian distribution of disorder, in our case, the disorder originates from two distinct molecular conformations. This suggests that the disorder potential associated with the nonequilibrium

conformation is a discrete constant, rather than a continuously distributed variable. Although not directly applicable to our system, it is noteworthy that, according to [212], in 2D systems with non-interacting electrons, any finite amount of disorder leads to the localization of all electronic states.

6.10 Thermal history effect in κ-Cl

To investigate further how the occupation probability of the EEG conformations affects systems nearing the Mott MIT, we studied κ-Cl salts with different thermal histories. Since κ-Cl exhibits an insulating ground state at ambient pressure, external pressure is required to induce a metallic ground state. For this purpose, we utilized a ^{4}He gas pressure system, which allows precise application of pressures up to 300 MPa. This setup enabled us to measure κ-Cl in both the coexistence region (20 MPa to 40 MPa) and the pure metallic state ($p > 40$ MPa).

The general behavior of κ-Cl in the metallic state is similar to that of κ-Br. In the coexistence region, κ-Cl exhibits a strong increase in resistivity at low temperatures due to the transition of some parts of the sample into the insulating phase. To investigate the glass transition in κ-Cl, we employed the same methods as those used for κ-Br. Fig. 6.12(a) shows resistance relaxation curves for hydrogenated and deuterated κ-Cl at ambient pressure and a temperature of 66.5 K. Time is presented on a logarithmic scale for better visibility. The relative amplitude of the relaxation (less than 2 %) is several times smaller than that observed in κ-Br. Similarly to κ-Br, the relaxation curves are better described by a fit with two independent exponential decays (green curves, Eq. (6.1)) rather than a single exponential decay (red curves).

Fig. 6.12(b) shows the relaxation times at different temperatures for κ-h_8-Cl (black and red symbols) and κ-d_8-Cl (green and blue symbols). Similarly to κ-Br, deuteration shifts the glass transition temperature by approximately 2 K to higher temperatures. Fitting the temperature dependence of the relaxation time yields activation energy barrier values of $E_a \approx 2550 \pm 100$ K for τ_1 of κ-h_8-Cl and τ_1 of κ-d_8-Cl (with the red and green points coinciding), and $E_a \approx 2750 \pm 150$ K for τ_2 of κ-d_8-Cl. Determining E_a for τ_2 of κ-h_8-Cl was too imprecise due to the significant spread of data points. The derived values are in good agreement with previous measurements (2650 ± 300 K) [157, 204, 205] and H-NMR results (2600 ± 100 K) [213]. Extrapolation of the relaxation times to higher temperatures gives a glass transition temperature of $T_g \approx 75$ K (corresponding to $\tau \approx 100$ s), which is about 5 K lower than that of κ-Br. This also matches well with the previous measurements [157].

We performed temperature sweeps at various constant pressures to investigate the influence of pressure on the properties of the EEG conformations. Fig. 6.12(c) shows the relative resistance difference between upward and downward temperature sweeps conducted at a constant rate of 1 K/min. This resistance difference arises due to relaxation processes occurring during the temperature sweeps, similar to the behavior observed in κ-Br (see Fig. 6.3(b)). Consequently, the position of the resistance peak corresponds to the glass transition temperature, T_g, for this specific sweep rate.

The relative amplitude of the peak is several times smaller than that observed for κ-Br. It decreases with increasing pressure, indicating reduced relaxation and fewer

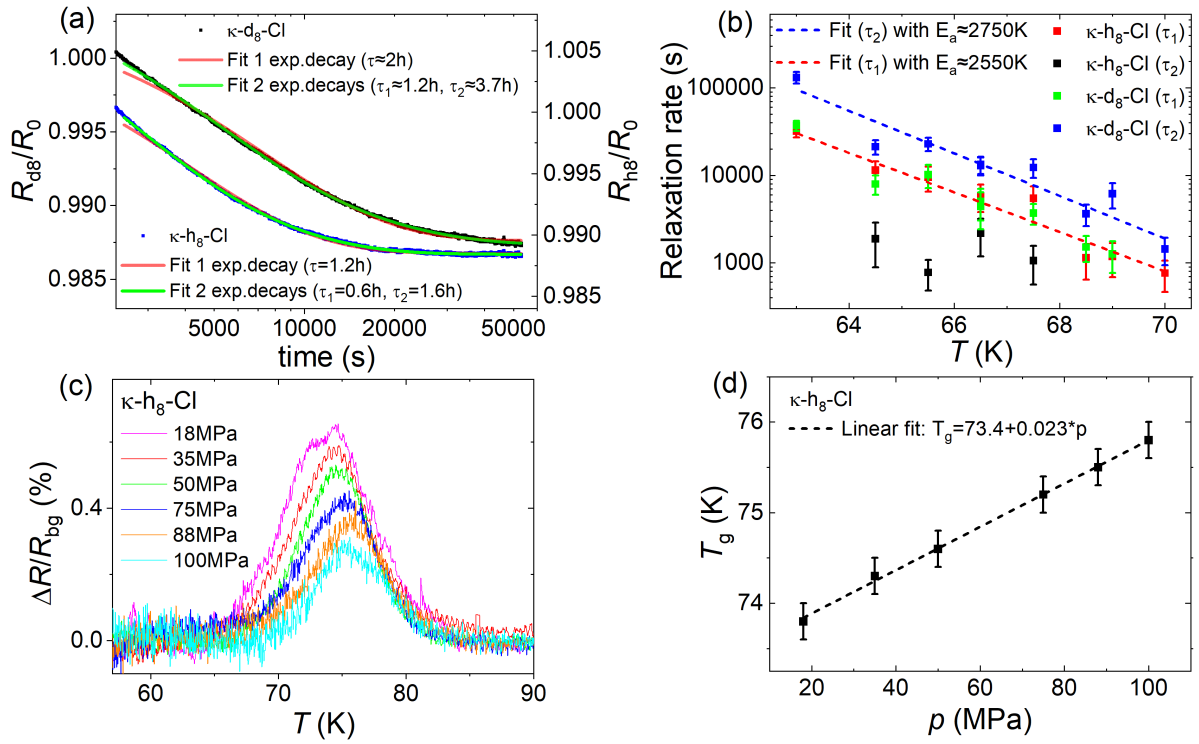

Figure 6.12: (a) Normalized resistance relaxation during annealing for κ-h_8-Cl (blue dots) and κ-d_8-Cl (black dots), fitted with two exponential decays (green curves) and a single exponential decay (red curves). The left axis corresponds to κ-d_8-Cl, while the right axis corresponds to κ-h_8-Cl. (b) Relaxation times (τ_1 and τ_2) as a function of temperature near the glass transition for κ-h_8-Cl (black and red points) and κ-d_8-Cl (green and blue points). Dashed lines represent linear fits. (c) Temperature dependence of the normalized resistance difference between cooling and warming cycles for κ-h_8-Cl near the glass transition temperature, measured at various pressures. The cooling rate was maintained at 1 K/min. (d) Pressure dependence of the glass transition temperature, derived from panel (c). The dashed line represents a linear fit.

transitions between the eclipsed (E) and staggered (S) conformations. One possible explanation for this reduction is a decrease in the energy difference between the conformational states ($\Delta E \rightarrow 0$), implying that both conformations become energetically equivalent. Alternatively, the reduction may result from an increase in the activation energy E_a, leading to longer relaxation times at a given temperature.

Furthermore, with increasing pressure, the peak position shifts to higher temperatures, and the peak width decreases slightly. Figure 6.12(d) shows the pressure dependence of the peak position, which represents the glass transition temperature T_g for this particular cooling rate. The glass transition temperature increases linearly with pressure at a rate of $dT_g/dp \approx 0.023\,\mathrm{K/MPa}$. Extrapolation to zero pressure yields $T_g \approx 73.4\,\mathrm{K}$, which corresponds to a relaxation time of approximately 140 s. By inserting this relaxation time into Eq. (6.3), we obtain a cooling rate of approximately 0.9 K/min, which is consistent with the experimental value.

The shift of T_g to higher values with increasing pressure implies an increase in the

relaxation time at the same temperature. In the previous paragraph, we suggested that ΔE decreases with pressure. Therefore, the increase in τ cannot be attributed to changes in ΔE. To analyze this further, let us consider Eq. (3.2), neglecting changes in ΔE for simplicity. Taking the pressure derivative of τ at a constant value, we can relate the pressure derivative of T_g to that of the activation energy E_a:

$$\frac{d\tau(T_g, E_a)}{dp} = \nu_0^{-1} \left(e^{\frac{E_a}{k_B T_g}} \frac{dE_a/dp}{k_B T_g} - e^{\frac{E_a}{k_B T_g}} \frac{E_a}{k_B} \frac{dT_g/dp}{T_g^2} \right) = 0.$$

This allows us to estimate how E_a changes with pressure:

$$\frac{dE_a}{dp} = \frac{E_a}{T_g} \frac{dT_g}{dp} \approx 0.8\,\mathrm{K/MPa}. \tag{6.7}$$

In the case where a change in ΔE is neglected, we observe a pressure dependence of the activation energy of approximately 0.8 K/MPa. This change is relatively small compared to the absolute value of E_a, and therefore, E_a can be considered effectively independent of pressure.

To investigate the correspondence between the EEG conformations and pressure, we measured the system in two distinct states - annealed and quenched - following a method similar to that in [159]. First, the samples were annealed at 65 K for 24 hours. Then, temperature sweeps were performed at various pressures (Fig. 6.13(a)). At the lowest pressure ($\sim$ 20 MPa), the samples exhibited high resistivity, while at higher pressures ($\sim$ 40 MPa), the samples transitioned to a fully metallic state. Subsequently, the same measurements were conducted for the quenched state (Fig. 6.13(b)), which was achieved by applying a heat pulse with an amplitude of 9.6 V and a duration of 3 s. The maximum temperature reached during the heat pulse was 115 K, while the bath temperature was maintained at 45 K. The general behavior in the quenched state was similar to that of the annealed state. However, a quantitative comparison of the resistances in these two states reveals slight differences. In particular, the resistance curve for the annealed state at 29 MPa closely matches that of the quenched state at 32 MPa, indicating an effective pressure offset of approximately 3 MPa between the two states. A similar offset is consistently observed at other pressures as well. Upward and downward temperature sweeps in the pressure range of 20 MPa to 40 MPa exhibit pronounced hysteresis at low temperatures, consistent with the presence of a Mott MIT coexistence region in κ-Cl at these pressures [34, 42].

This pressure difference is significantly smaller than that observed in κ-Br, where a shift of approximately 20 MPa was reported in [159], confirming that the impact of the EEG conformations in κ-Cl is substantially weaker compared to κ-Br. It is important to note, however, that comparing resistances near the Mott MIT may not yield entirely conclusive results, as the resistance in this regime is influenced by both disorder and electronic correlations, as previously discussed for κ-Br.

From this section, we conclude that the influence of the EEG conformations on κ-Br and κ-Cl is qualitatively similar. However, notable quantitative differences are observed, with κ-Cl exhibiting a much weaker effect than κ-Br. Additionally, the glass transition temperatures differ between the two compounds, being approximately 75 K for κ-Cl and 80 K for κ-Br.

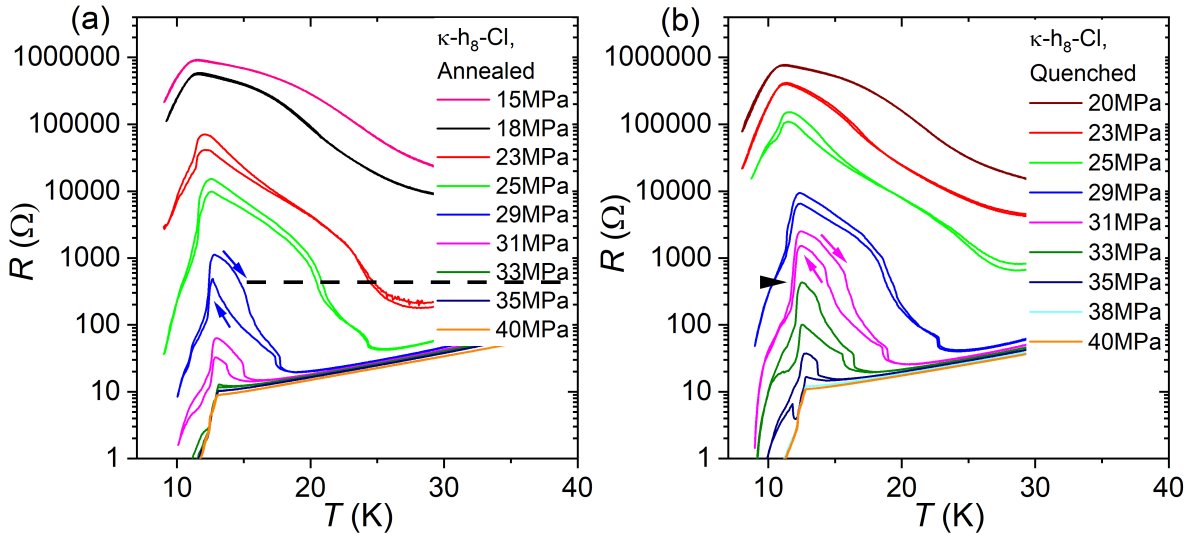

Figure 6.13: Resistance of κ-h_8-Cl at different pressures in the annealed state (a) and in the quenched state (b).

This behavior contrasts with the findings reported in [161] for κ-Cl, where irradiation was found to decrease the low-temperature resistance of the ambient-pressure insulating state. The discrepancy may stem from the differing effects of irradiation and thermal history. Another possible explanation is that the irradiation experiments were conducted at ambient pressure, where the correlation strength is higher, placing the compound at a different position in the phase diagram (see Fig. 2.9(c)).

Overall, in this chapter, we investigated the influence of thermal history on the electronic properties of κ-Br. We observed a glass-like transition between the eclipsed and staggered conformations of the ethylene end groups near 80 K, consistent with previous reports. By applying annealing and quenching procedures, we controlled the occupation probability of the nonequilibrium S conformation, p_S, achieving both low and high values.

An increase in p_S was found to enhance the low-temperature resistivity and shift the system closer to the metal-insulator transition. However, we observed no significant effect of p_S on correlation strength, as the effective cyclotron mass remained nearly unchanged within the experimental uncertainty. Meanwhile, S conformations introduce additional disorder, which increases the low-temperature resistance, suppresses the superconducting transition temperature T_c, and enhances the scattering rate. The observed linear decrease of T_c with increasing scattering rate is consistent with the Abrikosov-Gor'kov theory, though the experimental slope is approximately three times smaller than predicted. These findings suggest that the combined effect of increasing disorder and persistently strong electronic correlations drives the system toward a correlated Anderson (or Mott-Anderson) insulating state, consistent with the proposed phase diagram in Fig. 2.9(c).

This reduced sensitivity of the correlation strength to the thermal history allows for

a reliable investigation of the effective mass (and thus renormalization effects) without the need for strict control over the thermal treatment, except in experiments specifically targeting low scattering rate.

7 Anion substitution effect in κ-Br and κ-Cl

In the previous chapter (see Sec. 6.6) the comparison of the hydrogenated and deuterated κ-Br salts in their annealed states has revealed a systematic difference in their effective cyclotron masses: $(6.3 \pm 0.1)m_0$ for κ-h_8-Br and $(6.55 \pm 0.15)m_0$ for κ-d_8-Br. This mass difference indicates a variation in the strength of electronic correlations. It shifts the deuterated compound by ~ 14 MPa closer to the Mott metal-insulator transition (MIT), according to the pressure dependence of κ-Br, which will be discussed below in this chapter. This difference and shift are attributed to the so-called (negative) 'chemical pressure' effect, arising from the slight difference in C-H and C-D bond lengths [126]. In general, deuteration is expected to introduce an effective pressure shift of approximately -15 MPa [126], thereby pushing the system closer to the Mott MIT. This effective pressure difference is consistent with the value estimated from our experimentally observed difference in effective mass, as discussed above.

In the case of deuteration, structural differences are confined to the conducting layers. In contrast, the most common forms of chemical modification typically occur within the anion layer. In Chapter 5, we extensively investigated the κ-Cl salt and compared it with κ-NCS. Despite the difference in their anion layers and distinct ground states at ambient pressure (κ-Cl insulating and κ-NCS metallic), the comparison revealed almost no difference in their correlation strength. The primary influence of anion substitution manifests through variations in the frustration ratio, which differs significantly between these salts. Therefore, anion substitution in κ-Cl and κ-NCS does not mimic the effect of physical pressure on correlation strength and, consequently, cannot be referred to as 'chemical pressure'.

Another possible example of 'chemical pressure' might be sought in the comparison of κ-Cl and κ-Br, where the isoelectronic replacement of a single halogen atom in the complex anion leads to a significant change in the ambient-pressure electronic state. According to theoretical calculations [96, 100], the frustration ratios in both salts are pretty similar. Therefore, the primary influence on the ground state should arise from differences in the correlation strength. Moreover, a comparison of the mass renormalization factor in 'mixed' salts κ-Br_xCl_{1-x}, based on infrared conductivity measurements [214], suggests a dramatic, threefold increase upon reducing x from 0.85 to 0.73. This result would imply an unexpectedly high sensitivity of the correlation strength to Br-Cl substitution. However, it is important to note that optical studies, such as those using infrared conductivity, can be sensitive to spurious surface effects. In contrast, magnetic quantum oscillations provide a bulk-sensitive probe of the electronic properties.

To clarify this question, we performed a comparative study of κ-Br and κ-Cl using the Shubnikov-de Haas (SdH) oscillations method to probe the effective mass. The

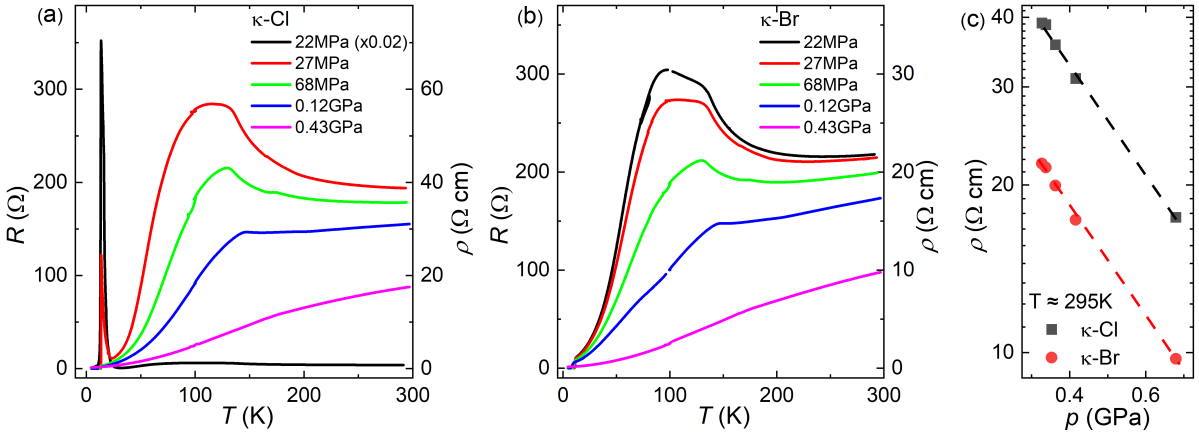

Figure 7.1: Temperature dependence of the resistance of κ-Cl (a) and κ-Br (b) at different pressures. The left scale shows the resistance of the samples, while the right scale shows the resistivity. (c) Pressure dependence of the resistivity of κ-Cl (black) and κ-Br (red) at room temperature (∼ 295 K). The dashed lines serve as a guide to the eye.

samples were mounted on the same feedthrough and positioned near each other inside the pressure cell, ensuring they experienced identical external conditions, including pressure, temperature, and magnetic field.

The resistivity of both samples in the metallic state exhibits similar behavior and comparable values (Fig. 7.1(a) and 7.1(b)), except in the phase coexistence region for κ-Cl ($p \simeq 20$ MPa to 40 MPa). In this region, the resistivity of κ-Cl increases significantly at low temperatures (Fig.7.1(a), black and red curves). This increase is associated with a first-order transition of part of the sample into the insulating state. However, at the superconducting transition temperature, the resistivity drops due to the superconducting short-circuiting of the bulk sample through the metallic (superconducting) region. Fig. 7.1(c) shows the pressure dependence of the resistivity of κ-Cl (red) and κ-Br (black) at room temperature. The resistivity of κ-Cl is approximately twice as high as that of κ-Br, but the slopes of their pressure-dependent decreases are similar.

We measured the SdH oscillations under pressure using a resistive solenoid for generating magnetic fields up to 30 T at the LNCMI in Grenoble. For all pressure values up to 0.6 GPa, distinct oscillations corresponding to the β-orbit were observed for both salts. Fig. 7.2(a) shows SdH oscillations for κ-Cl (black) and κ-Br (red) at several pressures. However, the oscillation amplitude in κ-Br was an order of magnitude lower than that in κ-Cl. We were restricted to this pressure range, as at pressures higher than 1 GPa, the amplitude of SdH oscillations for κ-Br significantly decreases [103], making an effective mass determination impossible.

The frequencies of β oscillations for the κ-Cl and κ-Br samples at 20 MPa were $F_{\mathrm{Cl}} = 3880 \pm 10$ T and $F_{\mathrm{Br}} = 3810 \pm 10$ T, respectively. These values are in good agreement with the previous measurements [103, 110] and coincide with the oscillation frequencies calculatedfrom the size of the first Brillouin zone of these salts ($36.62 \pm 0.05\,\mathrm{nm}^{-2}$) and ($36.21 \pm 0.05\,\mathrm{nm}^{-2}$) for κ-Cl and κ-Br, respectively [90] [158]. For both salts, the frequency increases by approximately 3.5 %/GPa, which is close

to the compressibility of κ-Cl at room temperature (2.7 %/GPa), as measured by X-ray diffraction [93]. This excellent agreement with our low-temperature SdH data suggests that the compressibility does not change significantly upon cooling.

Fig. 7.2(b) shows the pressure dependence of the effective cyclotron masses, $m_c(p)$, for κ-Cl and κ-Br. In the phase coexistence region of κ-Cl, the mass enhancement is strongly accelerated [110]. This explains the significant difference between m_c for κ-Cl and κ-Br in this region (Fig. 7.2(b) inset). In the homogeneous metallic state, at 68 MPa and 0.12 GPa, the masses of the two salts are similar, although m_c for κ-Br appears to be slightly smaller than that of κ-Cl by $\Delta m_c \approx 0.1\, m_0$. This observation aligns with expectations, as κ-Cl is closer to the MIT due to the 'chemical pressure' effect, which is equivalent to approximately 10 MPa of physical pressure and leads to stronger mass renormalization. However, in the actual phase diagram, the difference between the

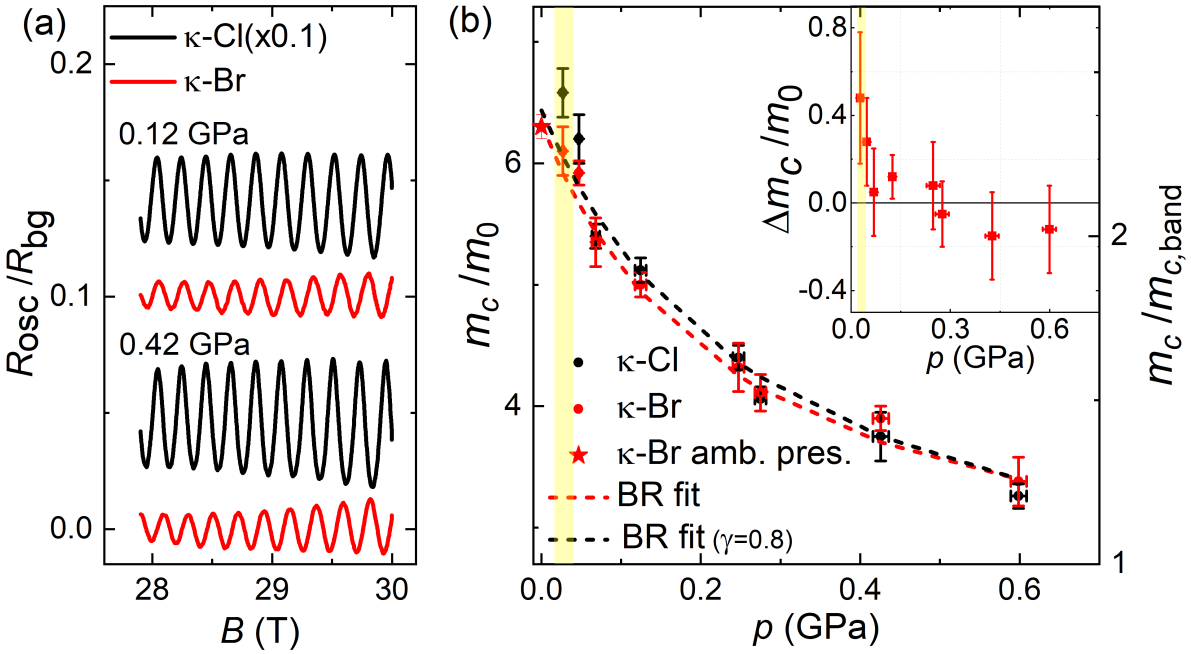

Figure 7.2: (a) Examples of the SdH oscillations in κ-Cl (black) and κ-Br (red) measured at pressures of 0.12 GPa and 0.42 GPa, respectively, and at a temperature of 0.7 K. The oscillation amplitude of κ-Cl is divided by a factor of 10 for better comparison, and the curves are vertically shifted. (b) Pressure dependence of the effective cyclotron mass for κ-Cl (black) and κ-Br (red). The red star indicates an ambient-pressure point obtained in the pulse-field measurements, see Sec. 6.6 (Fig. 6.9). The left scale shows the mass values in units of the free electron mass m_0, while the right scale shows these values in units of the calculated band cyclotron mass $m_{c,\mathrm{band}} = 2.7\, m_0$ [191]. The red dashed line represents a fit of the data for κ-Br (red) with the Brinkman-Rice formula (Eq. (2.30)). The black dashed line represents a similar fit of the same data with the Brinkman-Rice formula, but with a fixed parameter $\gamma = 0.8\,\mathrm{GPa}^{-1}$. Inset: Pressure dependence of the effective cyclotron mass difference between κ-Cl and κ-Br ($\Delta m_c = m_{\mathrm{Cl}} - m_{\mathrm{Br}}$).

compounds is $\Delta p_c \gtrsim 40\,\mathrm{MPa}$, which is significantly larger than this 'chemical pressure' effect.

At pressures of 0.3 GPa to 0.4 GPa, the masses of the two salts are practically the same. By 0.6 GPa, both masses approach the calculated band mass of approximately $2.7\,m_0$ [191]. However, the mass of κ-Br is about $0.2\,m_0$ higher. One possible explanation for this difference is that κ-Cl and κ-Br have slightly different compressibilities and different dependences of the correlation strength on pressure. In this case, κ-Cl would reach saturation faster than κ-Br and show a smaller effective mass. Another scenario is that κ-Br has a higher band mass, which would naturally lead to a larger difference in normalized masses. According to [191], the calculated band masses of the salts differ only slightly by $\Delta m_{\mathrm{band}} = 0.1\,m_0$. This possible difference in the band mass does not significantly affect the expected normalized mass difference in the metallic state. In any case, the mass difference is within the error bars ($\Delta m_c \approx 0.2\,m_0$). Therefore, in the metallic state, the possible effect of 'chemical pressure' is much smaller than the expected 40 MPa, and it is likely that this effect does not influence these compounds at all.

A more quantitative way of analyzing the pressure dependence of the effective mass is to fit with the Brinkman-Rice (BR) formula (Eq. (2.30)), as it was done for κ-Cl and κ-NCS in Sec. 5.6. The fitting reveals a critical pressure $p_0 \approx -0.26 \pm 0.03\,\mathrm{GPa}$, which is close to the critical pressures for κ-Cl and κ-NCS ($-0.28 \pm 0.02\,\mathrm{GPa}$) within the evaluation error bar. The observation of similar critical pressure values provides key evidence for the absence of a 'chemical pressure' effect in κ-Br. The band mass and the sensitivity of the correlation strength to pressure are $m_{\mathrm{band}} \approx 2.5 \pm 0.4\,m_0$ and $\gamma \approx 1.1 \pm 0.3\,\mathrm{GPa}^{-1}$, respectively. These values are slightly higher than those for κ-Cl and κ-NCS ($m_{\mathrm{band}} \approx 2.1 \pm 0.1\,m_0$ and $\gamma \approx 0.8 \pm 0.1\,\mathrm{GPa}^{-1}$). However, the differences remain within the error margins. A reason for the larger error bars for κ-Br is the relatively narrow pressure range used for fitting the data. Furthermore, we fitted the experimental data using a fixed compressibility parameter $\gamma = 0.8\,\mathrm{GPa}^{-1}$, consistent with the value used for κ-Cl and κ-NCS (Fig. 7.2(b), black dashed line). This fit yields a band mass of $m_{\mathrm{band}} \approx 2.2 \pm 0.1\,m_0$ and a critical pressure of $p_0 \approx -0.30 \pm 0.01\,\mathrm{GPa}$. These values are even closer to the corresponding parameters obtained for κ-Cl and κ-NCS. Therefore, we adopt them for further comparison and analysis throughout this work.

We can also analyze the $R(T)$ curves of κ-Br within the framework of the Fermi liquid model, analogous to the approach employed for κ-Cl in Sec. 5.1. Figure 7.3(a) shows the pressure dependence of the coefficient $A(p)$ in the quadratic temperature dependence of resistivity, as described by Eq. (2.27). The temperature range over which the quadratic dependence was fitted spans approximately 13 K to 25 K and varies slightly with pressure, as discussed in Sec. 5.1.

The pressure dependence of A was fitted using the relation $A(p) \sim (p - p_c)^{-2\nu}$ [67]. Two data points at higher pressures were excluded from the fit, as their inclusion significantly increased the uncertainty of the fitting parameters. The fit yields a critical pressure of $p_c \approx -0.16 \pm 0.05\,\mathrm{GPa}$, which is notably lower than the value obtained from the BR-like fit for effective mass ($p_0 \approx -0.3\,\mathrm{GPa}$). Furthermore, this critical pressure is approximately by $\Delta p_c \approx 60\,\mathrm{MPa}$ lower than that obtained for κ-Cl ($p_c \approx -0.10 \pm 0.02\,\mathrm{GPa}$). Although this difference falls within the margin of error, it is

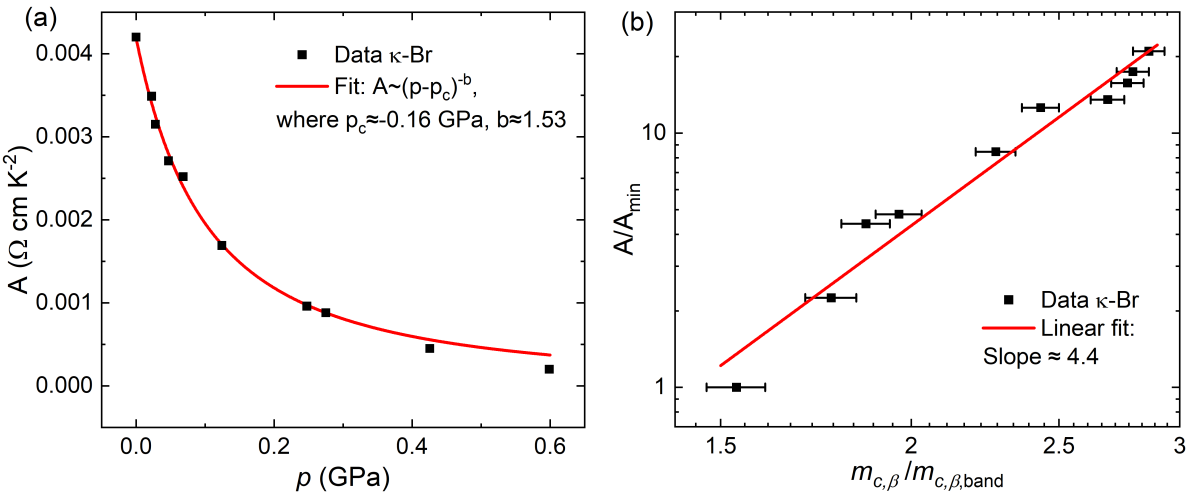

Figure 7.3: (a) Pressure dependence of the coefficient A in the quadratic T-dependence of the resistivity, see Eq. (2.27). The red line represents a fit using the formula $A = a(p - p_c)^b$, see text. (b) Fermi liquid coefficient A from panel (a) plotted versus the effective cyclotron mass on the β orbit, $m_{c,\beta}$, on a double logarithmic scale (black dots). The effective mass is normalized to the band mass $m_{c,\beta,\mathrm{band}} = 2.2\,m_0$, while the coefficient A is normalized to its minimum value $A_{\mathrm{min}} = 2 \times 10^{-4}\,\Omega\,\mathrm{cm\,K^{-2}}$. The red line represents a linear fit with a slope of 4.4 ± 0.4.

substantially greater than the pressure difference inferred from the effective mass comparison ($< 20\,\mathrm{MPa}$), and is consistent with the difference estimated from the phase diagram ($\sim 50\,\mathrm{MPa}$).

The fit also yields an exponent of $2\nu \approx 1.5 \pm 0.4$, which agrees within the error margins with the value obtained for κ-Cl ($2\nu \approx 1.16$), and is close to the theoretically predicted value of $2\nu = 1.34$ reported in [67].

The pressure dependence of the coefficient $A(p)$ can also be compared to the pressure dependence of the effective cyclotron mass, as was done for κ-Cl in Sec. 5.6. Figure 7.3(b) displays the dependence of the coefficient A on the effective cyclotron mass on a double logarithmic scale (black dots). The effective mass is normalized to the band mass ($m_{c,\mathrm{band}} = 2.2\,m_0$), obtained from the BR-like fit, and the coefficient A is normalized to its minimal value at the highest pressure.

This dependence was fitted linearly (red line). The fit yields a slope of 4.4 ± 0.4, indicating that the coefficient A scales with the effective mass to the power of approximately 4.4. This exponent is much higher than the result obtained for κ-Cl (3.3) and significantly deviates from the prediction of the Kadowaki-Woods law (see Sec. 2.7), which suggests a quadratic dependence.

All in all, the comparative analysis of the three salts with different anion layers (κ-Cl, κ-Br, and κ-NCS) reveals no significant difference in the strength of the electronic correlations. The observed difference in the critical pressure, $\Delta p_0 \approx 0.02 \pm 0.03\,\mathrm{GPa}$, is

within the error margin. It still allows for the presence of a very weak 'chemical pressure' effect, however, much weaker than inferred from the band structure calculations [96, 100] or from optical studies [214]. Therefore, it is more likely that the present chemical substitutions influence the ground state of these salts primarily through changes in the frustration ratio rather than through variations in the correlation strength.

Unfortunately, we could not observe the α oscillations in κ-Br to trace the evolution of the frustration ratio with pressure. The only work reporting measurable α oscillations [109] reveals a ratio between the α- and β-orbit areas at ambient pressure of approximately $S_\alpha/S_\beta \approx 14\,\%$, corresponding to a frustration ratio of $t'/t \approx 0.6$. This frustration ratio is lower than that observed for κ-NCS (0.69) and slightly higher than that of κ-Cl (0.57). The similarity of the frustration ratios for κ-Br and κ-Cl, along with their similar correlation strengths, confirms the closeness of κ-Br to the MIT. Moreover, even a slight increase in the correlation strength, such as through the deuteration of κ-Br, drives the compound into a phase coexistence state, as we have seen in the previous chapter (see Sec. 6.1).

8 Non-magnetic Mott insulator κ-CN

In the previous chapters, we conducted comparative investigations of the κ-Cl, κ-Br, and κ-NCS salts. We observed similar electronic correlation strength ratios for all three compounds in the metallic phase, with closely matching band masses. These results indicate that the salts do not exhibit a significant effect of 'chemical pressure'. Instead, the differences in their ground states at ambient pressure were attributed to variations in the spin frustration ratio.

Compounds with a lower frustration ratio are more susceptible to magnetic ordering instabilities. According to theoretical calculations, magnetic ordering drives the system into a Mott insulating state at lower correlation strengths and higher quasiparticle residue (as discussed in Sec. 2.9). To test the validity of these calculations, it is necessary to shift the Mott transition to lower quasiparticle residue values. This can be achieved by exploring compounds with higher correlation strengths and stronger frustration under ambient conditions.

A promising candidate for this purpose is the κ-(BEDT-TTF)$_2$Cu$_2$(CN)$_3$ salt (κ-CN). This compound is predicted to exhibit a stronger negative chemical pressure effect than the other three salts, resulting in a higher correlation strength at ambient pressure [96]. The frustration ratio is also expected to approach unity, making κ-CN a viable candidate for realizing a spin-liquid state [91, 96]. Increased frustration suppresses magnetic ordering, enabling the observation of the Mott metal-insulator transition (MIT) at higher correlation strengths. Therefore, this chapter is dedicated to the investigation and discussion of the κ-CN compound and its comparison with the salts described above. In particular, we studied κ-CN using isotope-enriched BEDT-TTF-^{13}C molecules. It has been established that such isotope substitution does not affect the electronic properties or alter the phase diagram of the material [215, 216]. The main measurement techniques employed in this work are angle-dependent magnetoresistance oscillations (AMRO) and Shubnikov-de Haas (SdH) oscillations.

8.1 Temperature dependence of resistance

We investigated κ-CN referring to the phase diagram presented in Sec. 3.6 [69]. It predicts a phase coexistence region in the pressure range 135 MPa to 155 MPa. However, our samples exhibited a fully metallic ground state down to 100 MPa, where a slight upturn in the resistance at low temperatures appeared, indicating the onset of the transient phase-coexistence region. This discrepancy in the phase diagram may be attributed to the sample quality or uncertainties in pressure determination.

Fig. 8.1(a) shows the temperature dependence of resistance over a wide pressure range. The general behavior of the resistance is similar to that observed in the other salts, featuring a resistance peak at temperatures around 20 K to 50 K, followed by a

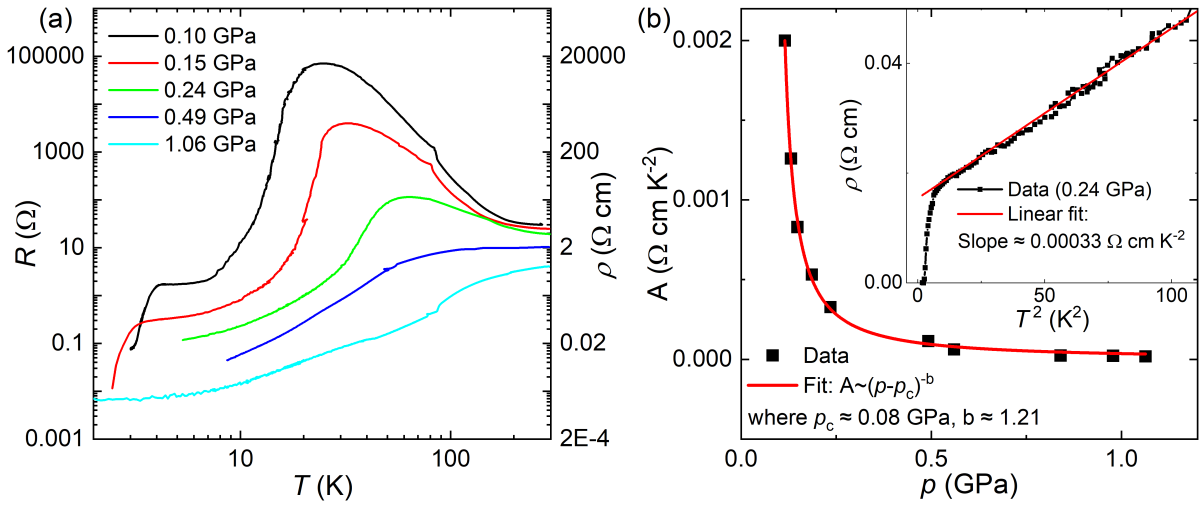

Figure 8.1: (a) $R(T)$ curves of κ-CN at various pressures. The right scale shows resistivity. (b) Pressure dependence of the coefficient A (the slope of the quadratic dependence of resistivity on temperature). The red line represents a fit using the $A = a(p - p_c)^{-b}$. The fit yields the parameters: $p_c = 0.08 \pm 0.01$ GPa and $b = 1.21 \pm 0.11$. Inset: Resistivity as a function of the square of temperature (black points) at a pressure of 0.24 GPa in the temperature range 0 K to 14 K, with a linear fit (red line) yielding a slope coefficient of $A \approx 0.000\,33\,\Omega\,\mathrm{cm\,K^{-2}}$.

dramatic decrease at lower temperatures. Notably, near the phase-coexistence region (0.1 GPa), the difference between the residual resistance and the peak resistance spans four orders of magnitude. The resistivity at low temperatures in the metallic state is significantly lower (below 0.1 Ω cm) than in the other three salts. A possible explanation for this could be a higher interlayer transfer integral or effective mass (see Eq. (3.5)) in κ-CN. The combination of lower resistivity and thinner crystals results in a substantially lower low-temperature resistance for κ-CN compared to the other salts.

We analyzed the $R(T)$ curves of κ-CN in the framework of the Fermi liquid (FL) model, predicting the quadratic temperature dependence of resistivity (Eq. (2.27)). Fig. 8.1(b) shows the pressure dependence of the coefficient A in the quadratic temperature dependence of the resistivity (see inset of Fig. 8.1(b)). This dependence was fitted with a power-law function $A \sim (p - p_c)^{-2\nu}$, yielding an exponent $2\nu = 1.21 \pm 0.09$, which closely matches the value obtained for κ-Cl (1.16) and κ-Cl (1.5), discussed in Sec. 5.1 and Chapter 7, respectively. These values are close to the theoretically predicted value of $2\nu \sim 1.34$ [67]. However, they differ from the experimentally determined value for κ-CN ($2\nu \approx 0.75$) reported in [69]. The method used to determine the actual pressure may be a possible reason for this discrepancy. In [69], two separate sets of measurements were conducted using ^{4}He and oil as pressure media, and the results were subsequently merged.

The critical pressure obtained from the fit is $p_c \approx 80$ MPa, which significantly differs from the values found for κ-Cl (−100 MPa) and κ-Br (−160 MPa). Since the coefficient A reflects the strength of electronic correlations, this difference in critical pressures may be attributed to a 'chemical pressure' effect of approximately 180 MPa between

the two salts. Notably, in κ-CN, the critical pressure nearly coincides with the MIT pressure, while in κ-Cl, it is about 120 MPa lower. This may indicate that the MIT is governed predominantly by electronic correlations in compounds with stronger frustration. However, definitive conclusions require direct measurements of the effective mass.

8.2 Angle-dependent magnetoresistance oscillations

Turning to magnetotransport measurements, we first investigated AMRO in κ-CN. Fig. 8.2(a) shows AMRO curves for several φ orientations. Hereafter, the azimuthal angle $\varphi = 0°$ corresponds to the longer crystallographic axis c, while $\varphi = 90°$ corresponds to the shorter axis b. All AMRO at different φ angles are quite similar, showing comparable amplitude, peak positions, and resistance in the field parallel to the layers. This suggests a nearly isotropic Fermi surface (FS).

Fig. 8.2(b) presents AMRO measurements at pressures of 0.1 GPa (green), 0.24 GPa (red), and 1.06 GPa (black). The absolute resistance decreases with increasing pressure, whereas the relative AMRO amplitude increases. The resistance at $\theta = 0°$ at the lowest pressure (0.1 GPa) is approximately 30 times higher than at the highest pressure (1.06 GPa). However, at the first AMRO peak, this ratio decreased to less than 10. This indicates that the pressure dependence of the magnetoresistance is significantly weaker

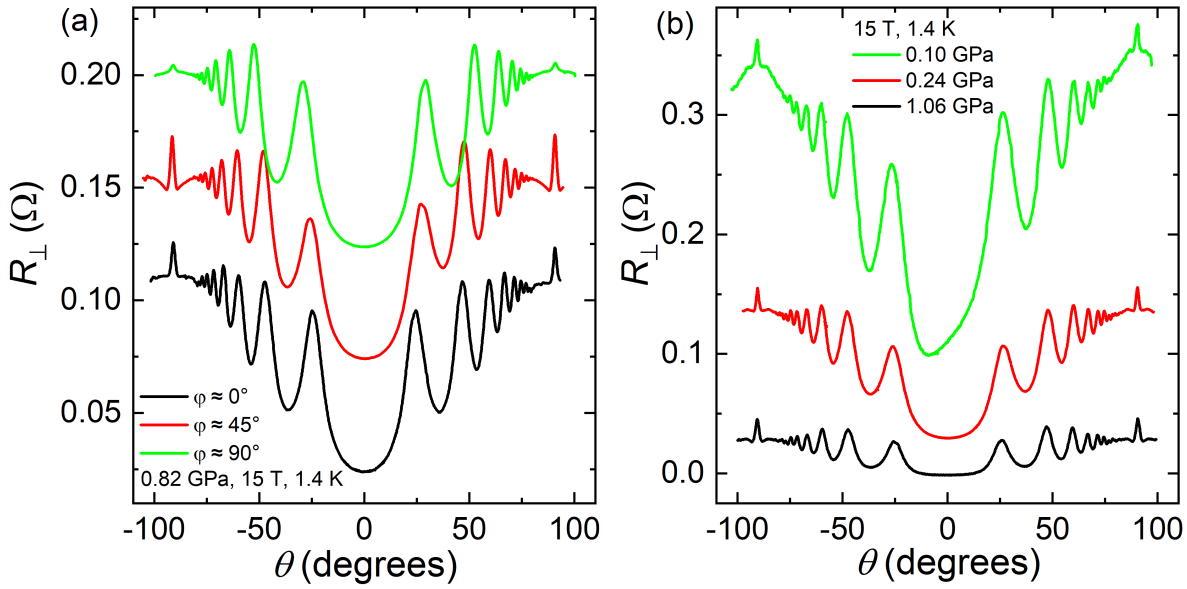

Figure 8.2: (a) Interlayer resistance of κ-CN as a function of the polar angle θ at $B = 15$ T and $T = 1.4$ K, measured at a pressure 0.82 GPa. Different curves represent measurements at various azimuthal angles. For clarity, the curves are vertically shifted by 0.05 Ω. The zero azimuthal angle ($\varphi = 0°$) corresponds to the longer crystallographic axis c. (b) AMRO curves at $B = 15$ T, $T = 1.4$ K, and at different pressures. The curves are not vertically shifted. The azimuthal orientation for all curves is the same ($\varphi \approx 30°$).

at AMRO peaks than at the perpendicular magnetic field orientation. This observation will be important for further investigations of magnetic quantum oscillations in κ-CN.

In addition to the increased resistance observed at low pressure near the Mott MIT region, the AMRO curve at 0.1 GPa exhibits a noticeable asymmetry, which may indicate a slight tilting of the effective interlayer hopping vector [7, 51]. In contrast, at higher pressures, the AMRO curves become more symmetric. The magnetoresistance at 0.24 GPa (red curve) lies roughly in the middle between the other two curves, despite its pressure being closer to the lower-pressure case. Remarkably, we could observe distinct AMROs even at pressures near the Mott transition. This contrasts with the experiments of Ohmichi et al. [52], in which AMROs were nearly absent at pressures around 0.2 GPa. This observation highlights the high quality of our samples.

8.3 Fermi surface determination

As described in Sec. 5.8 for κ-Cl, the positions of the AMRO peaks can be fitted using the formula for the Yamaji angles (Eq. (2.19)). This fitting allows the determination of the Fermi wave vector (k_F), based on the known interlayer distance, thus enabling the reconstruction of the in-plane FS. Figure 8.3(a) displays the k_F values (which we treat as equivalent to k_B^{max}, see Sec. 2.4; a more precise discussion of the distinction between k_F and k_B^{max} is provided in Appendix 9) calculated from the AMRO data at two different pressure values of 0.18 GPa (black dots) and 0.82 GPa (red dots). These results are consistent with those previously reported in [52] for a pressure around 0.7 GPa.

The effect of pressure is similar to what was observed in κ-Cl: it compresses the

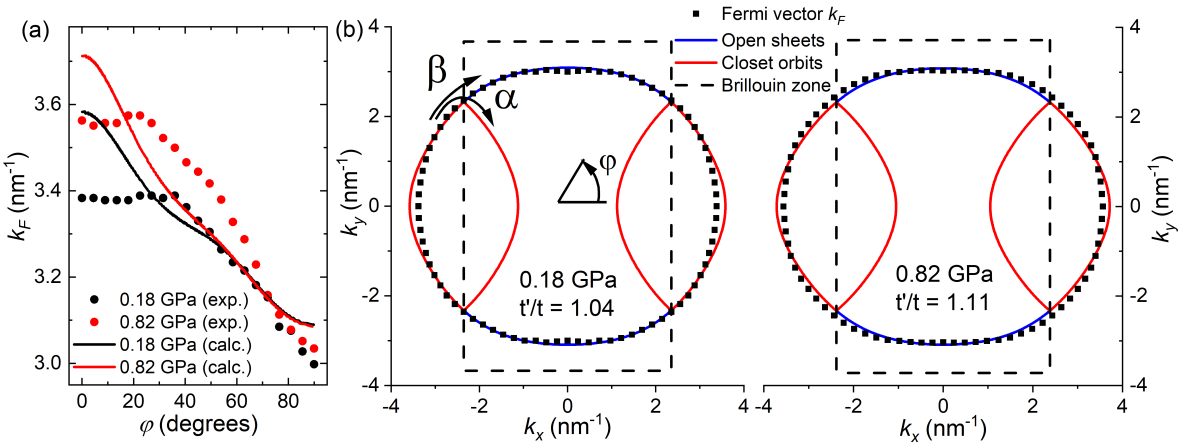

Figure 8.3: (a) Fermi wave vector as a function of azimuthal angle φ at pressures of 0.18 GPa (black dots) and 0.82 GPa (red dots), calculated from experimental AMRO data and the effective dimer model (black and red lines), using corresponding SdH frequencies (to be provided in Sec. 8.6). (b) Fermi surface at pressures of 0.18 GPa (left) and 0.82 GPa (right). Black dots represent the FS derived from the AMRO measurements. Red and blue lines correspond to open and closed Fermi sheets, respectively, obtained from the effective dimer model calculations. The black dashed line indicates the boundary of the first Brillouin zone.

Pressure	$a(z)$[nm]	$b(y)$[nm]	$c(x)$[nm]	t'/t
0.18 GPa	1.474	0.856	1.335	1.04
0.82 GPa	1.448	0.845	1.319	1.11

Table 8.1: Unit cell size and frustration ratio of κ-CN. The ambient-pressure unit cell parameters are taken from [91] and are listed in Sec. 3.1.

sample, resulting in larger Fermi wave vectors at all φ angles for 0.82 GPa as compared to 0.18 GPa. Similarly to κ-Cl (and κ-NCS), the change in k_F is anisotropic: pressure increases k_F more along the longer crystallographic axis c than along the shorter axis b. However, unlike in κ-Cl, for κ-CN the Fermi wave vector corresponding to the longer in-plane axis (c, $\varphi = 0°$) is already larger than that along the shorter axis (b, $\varphi = 90°$). This indicates that the FS is more extended in the direction of the longer axis c, as illustrated in Fig. 8.3(b), where it corresponds to k_x.

As shown in the previous chapter (Sec. 5.8) for κ-Cl, it is possible to determine the Fermi wave vector at different φ angles using an effective dimer model. Fig. 8.3(a) displays the calculated k_F values (solid lines) for two pressures: 0.18 GPa (black) and 0.82 GPa (red), using SdH data (to be shown below). The overall behavior of the calculated and experimental k_F values is consistent. At higher pressure, the k_F values are larger, with a more pronounced increase along the longer axis (c, $\varphi = 0°$). Additionally, the absolute value of the effective dimer model k_F decreases as φ increases. However, there is a notable discrepancy: the calculated k_F values exhibit a more monotonic decrease with φ, whereas the experimental values from AMRO measurements display a flat plateau for $\varphi < 30°$.

Fig. 8.3(b) shows the determined Fermi surface at pressures of 0.18 GPa (left) and 0.82 GPa (right). Black dots represent the experimental AMRO measurements, while red and blue curves correspond to values calculated using the effective dimer model. This comparison demonstrates that both the experimental and model-derived values agree at most angles, except in the region around the k_c-axis direction (along k_x). In this region, the effective dimer model overestimates k_F, resulting in a stronger convex curvature of the Fermi surface than according to the experimental data.

The low-temperature unit cell dimensions at ambient pressure from [91] were used for the calculations. Adjustments for higher pressures were made by accounting for pressure dependence in the SdH frequencies (see Sec. 8.6), under the assumption of isotropic compression [93]. The frustration ratio t'/t was taken from the SdH oscillations, which will be presented in Sec. 8.6. Table 8.1 summarizes all the relevant values.

8.4 AMRO simulations

As demonstrated in Sec. 5.9 for κ-Cl, it is possible to simulate AMRO behavior based on the known FS. This requires integrating Eq. (5.5) using the parameter $\omega_c\tau$ and the FS obtained from the experimental AMRO peak positions. The simulated curves for the pressure 0.18 GPa are shown in Fig. 8.4(a) as solid lines in different colors for various $\omega_c\tau$ values. Fig. 8.4(a) also presents the measured AMRO at a pressure of 0.18 GPa, for

two magnetic field strengths: $B = 15\,\mathrm{T}$ (black dashed line) and $B = 26\,\mathrm{T}$ (blue dashed line). These AMRO curves were obtained at an azimuthal angle of $\varphi \approx 20°$.

The experimental resistances were normalized to their value at $\theta = 0°$. In contrast, the calculated resistance values were scaled to match the experimental curves with AMRO amplitude and background resistance at high tilt angles. As a result, the initial resistance at $\theta = 0°$ differs between the calculated and experimental curves, whereas the AMRO amplitude and high-angle behavior show a good agreement.

To estimate the parameter $\omega_c\tau$, the experimental AMRO curves were compared with simulated curves for different $\omega_c\tau$ values. From this comparison, it was estimated that the magnetic fields $B_1 = 15\,\mathrm{T}$ and $B_2 = 26\,\mathrm{T}$ correspond to $\omega_c\tau \approx 2.5$ and $\omega_c\tau \approx 3.5$, respectively. The ratio of the magnetic fields ($B_2/B_1 = 26\,\mathrm{T}/15\,\mathrm{T}$) is approximately 1.7, while the ratio of the scattering parameters ($(\omega_c\tau)_2/(\omega_c\tau)_1 = 3.5/2.5$) is approximately 1.4. This difference between the two ratios (1.7 vs. 1.4) is relatively small, but it may also indicate either limitations of the AMRO simulation method or inaccuracies in the estimation of $\omega_c\tau$, which was inferred solely from the correspondence between the experimental and simulated AMRO amplitudes.

Fig. 8.4(b) illustrates the φ-dependence of the resistance at polar angles near $\theta = 75°$ for pressures of 0.18 GPa (black) and 0.82 GPa (red). These values are close to the

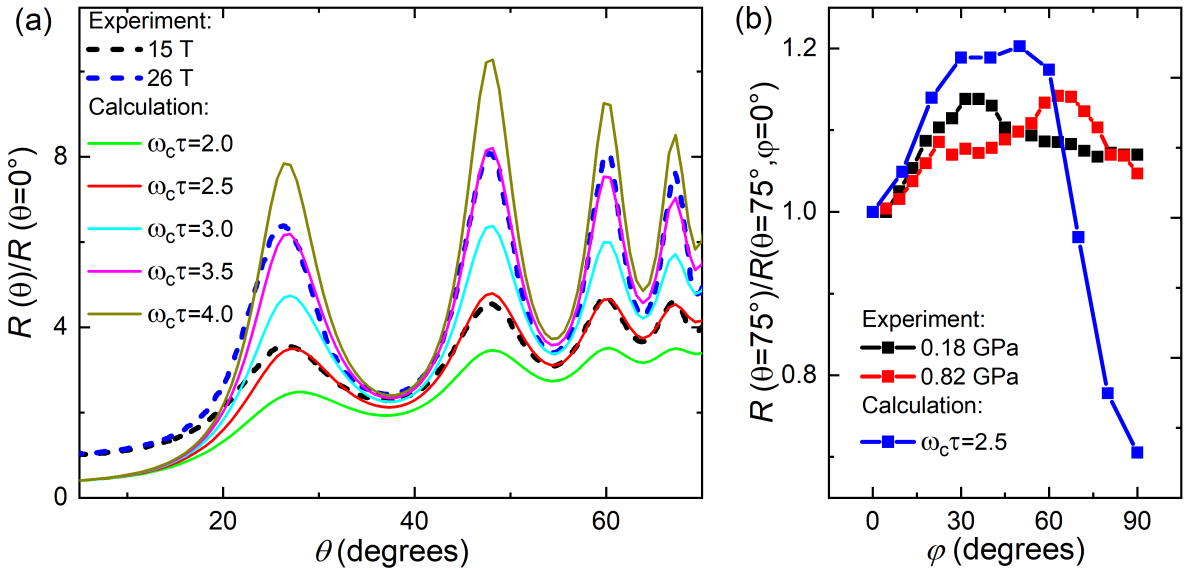

Figure 8.4: (a) Calculated AMRO curves for different values of the parameter $\omega_c\tau$ (solid lines) compared with experimentally obtained curves (dashed lines) at a pressure of 0.18 GPa and magnetic field strengths of 15 T and 26 T. Both experimental and calculated curves correspond to an azimuthal angle of $\varphi \approx 20°$. The resistances were normalized to their values at $\theta = 0°$, and the calculated values were further scaled by a factor of 0.4 to match the AMRO amplitudes and background resistance with the experimental data at high tilt angles. (b) Resistance values at $\theta = 75°$ from experimental measurements at 15 T and 1.4 K for pressures of 0.18 GPa (black) and 0.82 GPa (red), alongside calculated values for $\omega_c\tau = 2.5$ (blue). The resistance values are normalized to that at $\varphi = 0$.

resistance at $\theta = 90°$. They can be considered consistent with the φ-dependence of the resistance in a magnetic field parallel to the conducting layers (disregarding the coherence peak, which will be discussed separately). The absolute resistance values for both pressures are comparable, although the peak of the φ-dependence shifts to higher φ values with increasing pressure. The change in the absolute resistance is less than 15 %, which is significantly smaller than the variation observed in κ-Cl in Sec. 5.9, where the change was approximately fivefold. This difference suggests a more isotropic FS in κ-CN as compared to κ-Cl, which is consistent with the FS being more circular in κ-CN and more rectangular in κ-Cl.

The blue dots in Fig. 8.4(b) represent the calculated resistance at $\theta = 75°$ (calculation constraints restrict this upper limit) for the FS corresponding to 0.18 GPa. Like the experimental data, the calculations exhibit a maximum at intermediate φ angles. However, the calculated resistance shows a greater amplitude of variation (60 %) compared to the experimental data (15 %). Moreover, in the experiment, the resistance at $\varphi = 0°$ is lower than at $\varphi = 90°$. In contrast, the calculated resistance displays the opposite trend, with higher values at $\varphi = 0°$, corresponding to a higher k_F. This behavior in the calculations is also consistent with the FS curvature: the FS is flatter at $\varphi \approx 90°$, implying more conducting electrons and thus lower resistance (a similar reason was discussed for κ-Cl in Sec. 5.9).

The possible reason for these inconsistencies may lie in the difference between k_B^{max} and the actual k_F. As discussed earlier, AMRO curves reveal k_B^{max}, which approximates but does not exactly represent k_F. Estimating k_F by constructing perpendiculars to the k_B^{max} may flatten the FS and reduce curvature differences, thereby influencing the comparison between experimental and simulated results. Another possible reason may be related to inaccuracies in the calculations. Due to technical limitations, the simulations were performed at a polar angle of $\theta = 75°$. However, in a fully parallel magnetic field ($\theta = 90°$), the φ-dependence of the resistance may differ slightly.

8.5 Coherence peak

Similarly to κ-Cl, the shape of the coherence peak in κ-CN is also strongly dependent on the azimuthal angle φ. Fig. 8.5 shows coherence peaks at different φ orientations and at pressures of 0.18 GPa (a) and 0.82 GPa (b). Curves with the same color correspond to the same φ orientation, and the numbers $1-6$ label the curves in order of increasing φ for easier reference. The coherence peak region can be divided into three main parts:

- **The peak itself:** This corresponds to the range approximately 88° to 92°, where the magnetic field is nearly parallel to the layers. A steep increase in resistance characterizes this region.
- **The piedmont area:** This region, associated with self-crossing orbits, extends from approximately 80° to 88°. It exhibits increasing, decreasing, or nearly flat $R(\theta)$, depending on the φ orientation and pressure.
- **Saturation of base resistance:** Around $\theta = 80°$, the resistance value is influenced by the in-plane Fermi wave vector $k_F(\varphi)$ and the warping of the Fermi surface. It reflects the resistance at high polar angles.

To analyze the changes in each region of the coherence peak, we define several characteristic points (indicated by arrows in Fig. 8.5(a) and Fig. 8.5(b)):

- R_{max}: The maximum resistance value at the peak.
- R_{min}: The resistance value at the base of the peak.
- R_{base}: The resistance value at $\theta = 80°$, averaged over possible angular oscillations.

Using these definitions, the peak height is defined as $R_{peak} = R_{max} - R_{min}$, and the piedmont slope as $R_{slope} = R_{min} - R_{base}$.

The dependence of R_{peak} and R_{slope} on the azimuthal angle φ is shown in Fig. 8.5(c). The resistance values have been normalized to the minimum base resistance R_{base} at $\varphi = 0°$.

The peak height exhibits a pronounced maximum at $\varphi = 40°$, in contrast to κ-Cl, where the maximum occurs at $\varphi = 0°$. This difference can be attributed to the complex topology of the Fermi surface. As discussed before, two possible types of closed orbits were proposed in [185] for κ-NCS, each contributing differently to the formation of the coherence peak. Under applied pressure, the relative height of the coherence peak increases, reaching up to one-quarter of the base resistance at its maximum at 0.82 GPa.

The behavior of the slope resistance (R_{slope}) is more complex and non-monotonic. However, the overall φ-dependence remains similar across different pressures (Fig. 8.5(c) green and blue). Notably, the resistance drops sharply at azimuthal angles near $\varphi = 45°$, where the coherence peaks are most pronounced. This suggests that warping in this region enhances self-crossing and closed orbits that contribute to the slope and the coherence peak. At other φ angles, R_{slope} either shows a slight positive slope or remains nearly flat.

Despite differences in the shape and height, the width of the coherence peak only weakly depends on φ. Fig. 8.5(d) shows the φ-dependence of the coherence peak width in polar coordinates for a pressure of 0.18 GPa. The width remains nearly constant, with only minor variations across all φ ($1.8° < \theta_c < 2.3°$). It is possible that this variation is not due to actual changes in the peak width, but rather to difficulties in its determination, particularly in cases where the peak amplitude is small and the piedmont exhibits a positive slope at specific φ orientations. Therefore, the interlayer transfer integral in κ-CN can be considered isotropic. The most reliable determination of the peak width is possible at $\varphi = 45°$, where the peak is flanked by pronounced dips, providing clear boundaries for defining its extent [50].

For pressures of 0.18 GPa and 0.82 GPa, the coherence peak widths were measured as $\theta_c = 1.9 \pm 0.2°$ and $2.4 \pm 0.2°$, respectively. These widths correspond to the ratio of the interlayer transfer integral to Fermi energy, $t_\perp / E_F$, of 0.68 % and 0.84 %. A linear extrapolation to ambient pressure yields a ratio of approximately 0.62 %. This value is smaller than that for κ-Cl at ambient pressure (0.8 %) but significantly larger than the value reported for κ-NCS (0.05 %) [185].

We can convert these ratios into absolute values of the interlayer transfer integral by estimating the Fermi energy under the assumption of a quadratic dispersion, using the effective cyclotron mass (to be presented in the next section). This estimation yields

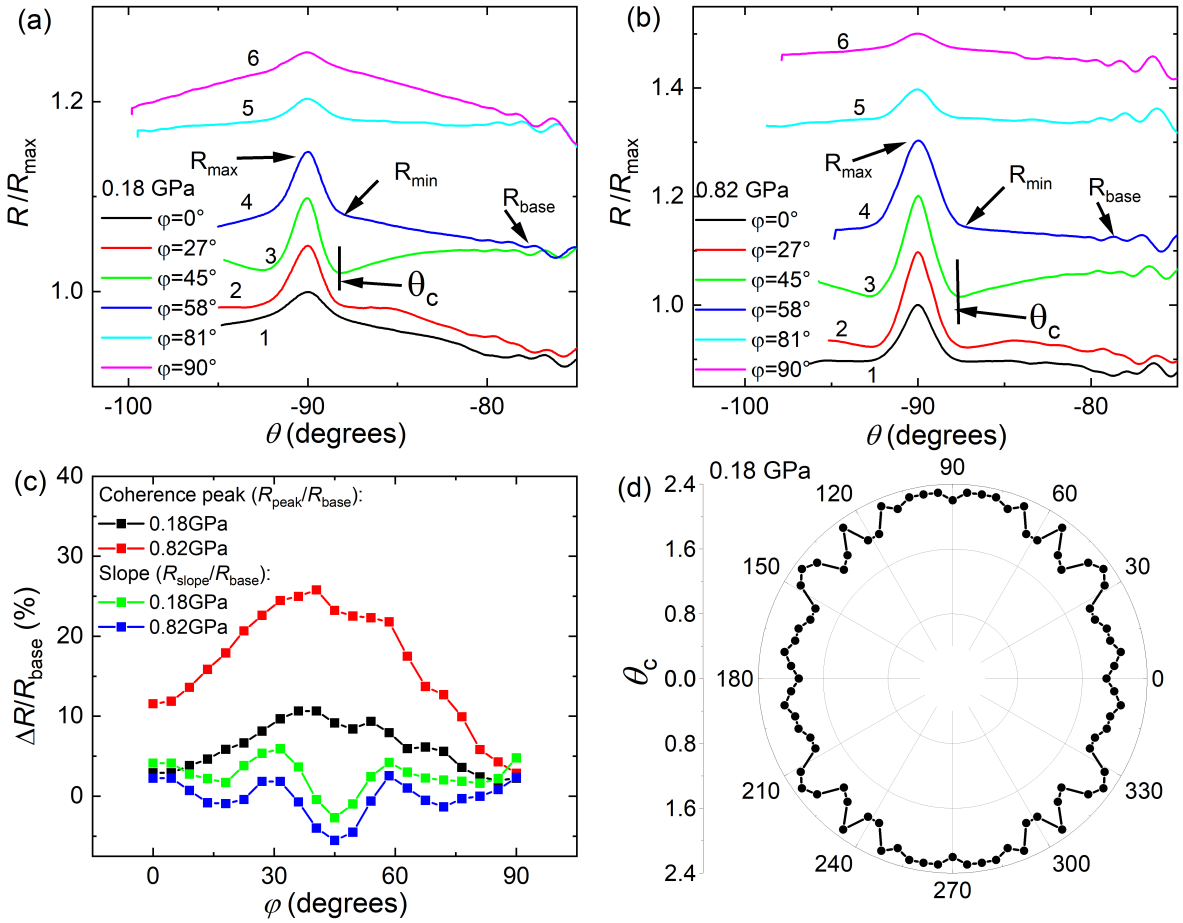

Figure 8.5: Resistance as a function of the azimuthal angle for a pressure of 0.18 GPa (a) and 0.82 GPa (b) at various azimuthal angles φ showing the coherence peak. The resistance is normalized to the maximum resistance, and the curves are vertically shifted for clarity. Curves with the same color correspond to the same azimuthal angle φ. Numbers $(1-6)$ label the curves in order of increasing φ. R_{max} denotes the resistance at the peak value, R_{min} corresponds to the resistance near the piedmont of the peak, and R_{base} represents the saturation resistance at high polar angles, close to $\theta = 80°$. θ_c denotes the polar angle at which the coherence peak width is determined. (c) φ-dependence of the coherence peak height ($R_{\mathrm{peak}} = R_{\mathrm{max}} - R_{\mathrm{min}}$), normalized to the minimum base resistance at $\varphi = 0°$, for pressures of 0.18 GPa (black) and 0.82 GPa (red), along with the φ-dependence of the change in resistance at the piedmont of the coherence peak (green and blue) ($R_{\mathrm{slope}} = R_{\mathrm{min}} - R_{\mathrm{base}}$), also normalized to the minimum base resistance at $\varphi = 0°$. (d) φ-dependence of the coherence peak width in polar coordinates for pressure 0.18 GPa.

values of 0.4 meV and 0.9 meV for the two measured pressures, respectively. Linear extrapolation to ambient pressure gives an estimated value of 0.2 meV. This is significantly higher than the interlayer transfer integral in κ-NCS (0.04 meV) and about three times lower than in κ-Cl (0.6 meV).

Although the $t_\perp / E_{\mathrm{F}}$ ratios are quite similar among these salts, the primary difference

p(GPa)	F(T)	d(nm)	k_F(nm^{-1})	$m_c(m_0)$	E_F(eV)	θ_c(°)	$t_\perp / E_F$	$t_\perp$(meV)
0.18	3680	1.474	3.33	7.2	0.059	1.9 ± 0.2	0.0068	0.40 ± 0.05
0.82	3780	1.448	3.44	4.0	0.109	2.4 ± 0.2	0.0084	0.9 ± 0.1

Table 8.2: Calculated values of $t_\perp$ along with all parameters required for its evaluation. The SdH frequency F and effective cyclotron mass m_c were taken from Sec. 8.6. For details regarding the calculation of the Fermi energy E_F and the interlayer transfer integral $t_\perp$, refer to the main text.

in the absolute values of $t_\perp$ originates from variations in the estimated Fermi energy, which arise due to differences in the effective masses. Furthermore, for κ-Cl, to calculate the value of $t_\perp$ we used the maximal width of the coherence peak (at $\varphi = 0°$), whereas $t_\perp(\varphi)$ exhibits strong anisotropy (see Fig. 5.18). The average effective $t_\perp$ may therefore be significantly smaller; in Sec. 5.12, we estimated it to be around 0.1 meV based on the analysis of SdH oscillation beats. This larger effective $t_\perp$ in κ-CN, combined with its larger effective cyclotron mass, likely accounts for the significantly lower low-temperature resistivity observed in κ-CN compared to the other three salts (as discussed in Sec. 8.1).

All parameters used in the calculations are summarized in Table 8.2. The interlayer transfer integral $t_\perp$ was calculated using Eq. (2.21), assuming a quadratic energy dispersion to estimate the Fermi energy. The values for the effective cyclotron mass and the SdH frequency were taken from Sec. 8.6, while the interlayer distances d are listed in Table 8.1.

8.6 Shubnikov-de Haas oscillations in tilted field

The primary challenges in measuring SdH oscillations in this compound are the small oscillation amplitude (less than 2 % in a perpendicular magnetic field up to 30 T), as compared to other κ-salts, and the low residual resistance in the metallic state ($\sim 10\,\mathrm{m\Omega}$). However, these challenges can be mitigated near the AMRO peaks, where the resistance increases by nearly an order of magnitude, and the relative amplitude of the oscillations rises significantly [7], as was also demonstrated for κ-Cl (Sec. 5.14). For this reason, the SdH oscillations were measured at orientations close to the first AMRO maximum. At these orientations, the absolute amplitude of the SdH oscillations increased by more than an order of magnitude.

Fig. 8.6(a) shows examplary oscillations at orientations $\theta = 0°$ (perpendicular) and $\theta \approx 25°$ (near the AMRO peak) at magnetic fields of 28 T to 29 T. The absolute oscillation amplitude is more than an order of magnitude larger at the AMRO peak orientation compared to the perpendicular one, with the relative amplitudes R_{osc}/R_{bg} being approximately 12 % and 2 %, respectively. In the perpendicular orientation, the oscillation amplitude is close to the noise level, making the oscillations barely distinguishable by the eye.

Fig. 8.6(b) presents the FFT of the SdH oscillations at the two orientations described

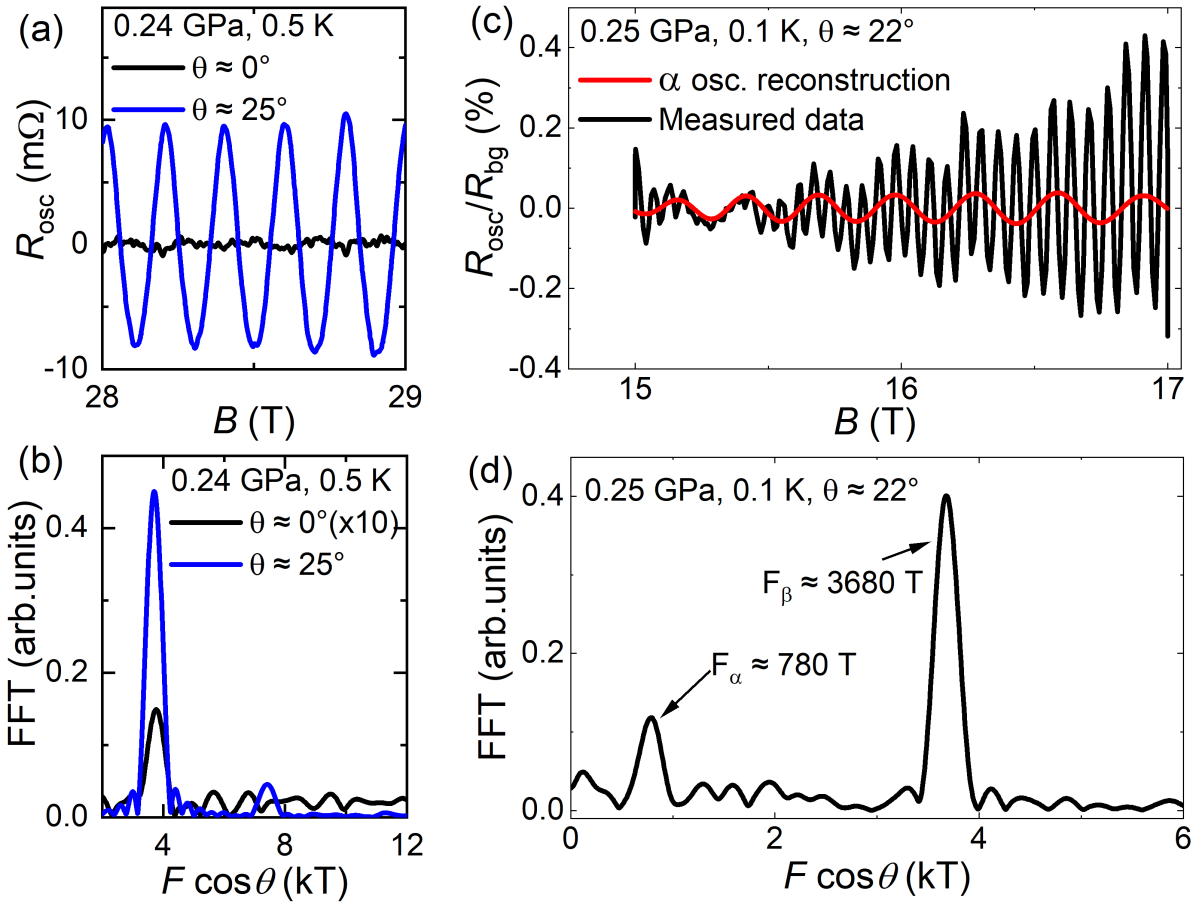

Figure 8.6: (a) SdH oscillations measured at polar orientations $\theta = 0°$ (black) and $\theta = 25°$ (blue) at a pressure of 0.24 GPa and temperature of 0.5 K. (b) FFT of the oscillations shown in panel (a) in the field window 28 30T, with frequencies normalized by multiplying by $\cos(\theta)$. The FFT of the oscillations in the perpendicular field was multiplied by 10 for better visibility. (c) SdH oscillations measured at 0.25 GPa, 0.1 K, and polar orientation $\theta = 22°$. The red line represents the α-oscillations, reconstructed via inverse FFT from the corresponding FFT peak. (d) FFT of the SdH oscillations from panel (c), with frequencies normalized by multiplying by $\cos(\theta)$.

above. For measurements on tilted samples, the frequency was multiplied by $\cos(\theta)$ to normalize it and facilitate comparison with measurements in the perpendicular orientation. As expected, the FFT amplitude of measurements in the tilted field is much higher than in the perpendicular field. Notably, as in κ-Cl, the Dingle temperatures for all orientations and pressures were within $T_D = 0.7 \pm 0.2$ K.

Interestingly, we also observed α-oscillations at certain pressures and orientations. Fig. 8.6(c) shows SdH oscillations measured at 0.25 GPa, 0.1 K, and $\theta \approx 22°$, with the α-oscillations highlighted by the red line. An FFT analysis reveals frequencies around $F_\alpha \approx 780$ T and $F_\beta \approx 3680$ T (Fig. 8.6(d)). The ratio between the α- and β-frequencies is approximately 21 %, which is significantly higher than that observed in κ-Cl (13 %) and κ-NCS (16 %), as presented in the previous chapter (Sec. 5.5). This higher ratio is consistent with the observation from the previous section that the Fermi surface is

more extended along the longer unit cell axis.

Additionally, Fig. 8.6(c) shows a beat node in the oscillations, attributed to Fermi surface warping, similar to the behavior discussed for κ-Cl. The FFT reveals a corresponding peak with two closely spaced maxima. The frequency splitting is estimated as $\Delta F_\beta / F_\beta \sim 0.02$, which is higher than in κ-Cl. However, the determination of ΔF_β is imprecise due to the short magnetic field range over which the oscillations were measured.

8.7 Frustration ratio and effective mass

The implementation of SdH measurements near the AMRO maximum allows us to significantly enhance the amplitude of oscillations across a wide pressure range (0.1 GPa to 1 GPa). Fig. 8.7(a) shows the pressure dependence of the β-frequency. It can be extrapolated to ambient pressure as $F_\beta(0) \approx 3670 \pm 20$ T and increases with pressure at a rate of approximately 4 %/GPa, which is similar to the behavior observed in κ-Cl.

Fig. 8.7(b) presents the pressure dependence of the α-frequency. Extrapolation to ambient pressure gives $F_\alpha(0) \approx 740 \pm 20$ T, and the frequency increases with pressure by approximately 20 %/GPa. Similarly to κ-Cl, the α-frequency shows a much stronger pressure dependence, indicating a more pronounced expansion of the Fermi surface along the longer unit cell axis, consistent with the k_F determination discussed in Sec. 8.3. The observed frequencies are consistent with the previous SdH measurements reported at $p \approx 0.8$ GPa [104].

As shown previously for κ-Cl, we can convert the ratio of frequencies into the

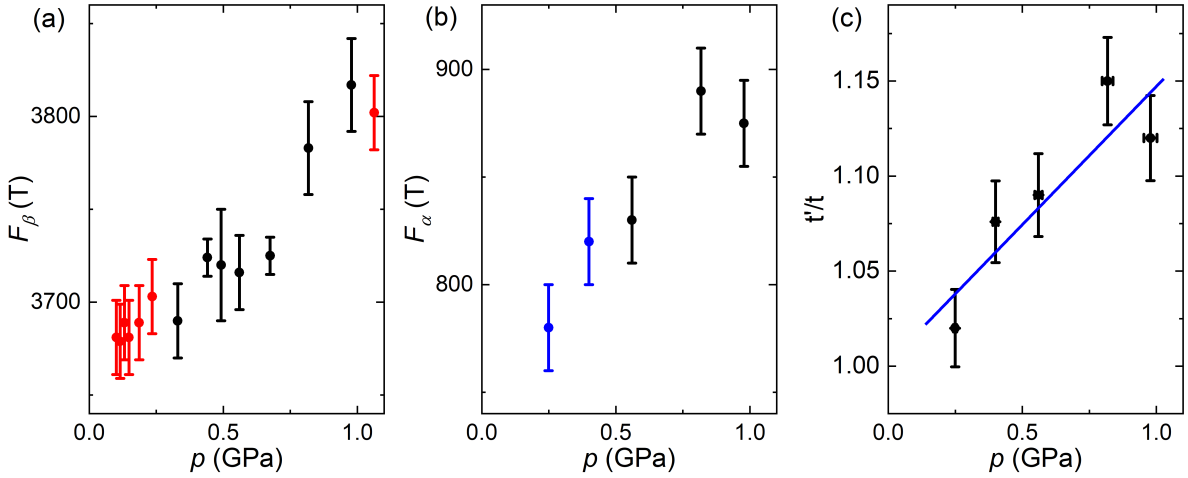

Figure 8.7: Pressure dependence of the SdH β-frequency (a) and α-frequency (b). Black points represent measurements taken in a 15 T magnet (Garching), blue points in an 18 T magnet (Dresden), and red points in a 30 T magnet (Grenoble). All the frequencies are reduced to the values corresponding to $\theta = 0$ by multiplying them by $\cos(\theta)$. (c) Spin frustration ratio t'/t in κ-CN (black dots), obtained from the ratio F_α / F_β, with a linear fit shown in blue. The fit yields an intercept of 1.00 ± 0.02 and a slope of 0.15 GPa^{-1}.

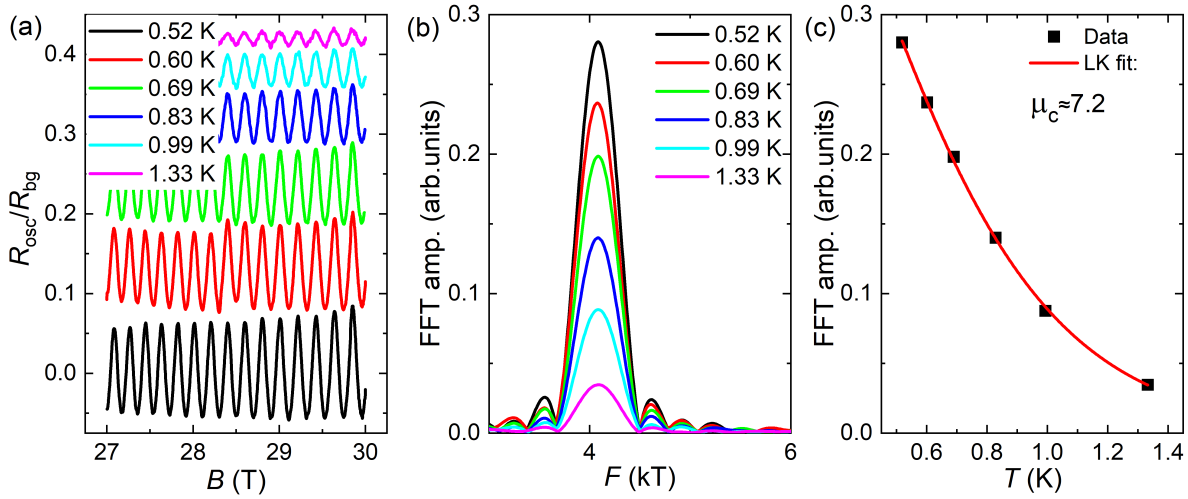

Figure 8.8: (a) SdH oscillations measured at 0.24 GPa, $\theta \approx 24°$ (at the first AMRO peak), at different temperatures. The oscillatory resistance is normalized to the background resistance. The curves are vertically shifted for better visibility. (b) FFT of the oscillations from panel (a) near the β-frequency. (c) Temperature dependence of the amplitude of the FFT peak at the β-frequency (black points), fitted using the LK temperature damping factor Eq. (2.9). The fit yields an effective cyclotron mass $\mu_c \approx 7.2 \pm 0.1$.

spin frustration ratio t'/t. Fig. 8.7(c) shows the pressure dependence of the frustration ratio. A linear extrapolation to ambient pressure yields a frustration ratio value $t'/t = 1.00 \pm 0.02$. This value is significantly closer to unity than the predictions from DMFT calculations ($t'/t = 0.83$) [96], the extended Hückel method ($t'/t = 1.06$) [91], and DFT calculations ($t'/t = 0.86$) [217]. A frustration ratio near unity suppresses antiferromagnetic ordering and favors the emergence of a valence bond solid (VBS) or a quantum spin-liquid (QSL) state [116, 117, 218, 219].

The frustration ratio in κ-CN is significantly higher than those presented in Sec. 5.5 for κ-Cl and κ-NCS. Nevertheless, the relative frustration values among these three salts are qualitatively consistent with the theoretical predictions [96].

At orientations near the AMRO peak, the amplitude of the SdH oscillations was sufficiently large to allow measurements at different temperatures and the extraction of the effective cyclotron mass. Fig. 8.8(a) shows SdH oscillations at a pressure of 0.24 GPa and $\theta \approx 24°$ in the magnetic field range 27 T to 30 T, measured at various temperatures.

Fig. 8.8(b) displays the FFT amplitude of the SdH oscillations near the β-frequency. Fig. 8.8(c) presents the temperature dependence of the β-oscillation amplitude (black points), along with a Lifshitz-Kosevich fit (red line) according to Eq. (2.9). Since the measurements were performed at a tilted field, the extracted effective cyclotron mass must be multiplied by $\cos(\theta)$ to obtain the value corresponding to the orbit in the layer plane.

A similar procedure was applied to determine the effective cyclotron mass over a broad pressure range (0.1 GPa to 1 GPa). Fig. 8.9(a) shows the pressure dependence of the effective mass, $m_c(p)$ (black points). To evaluate the electronic correlation strength,

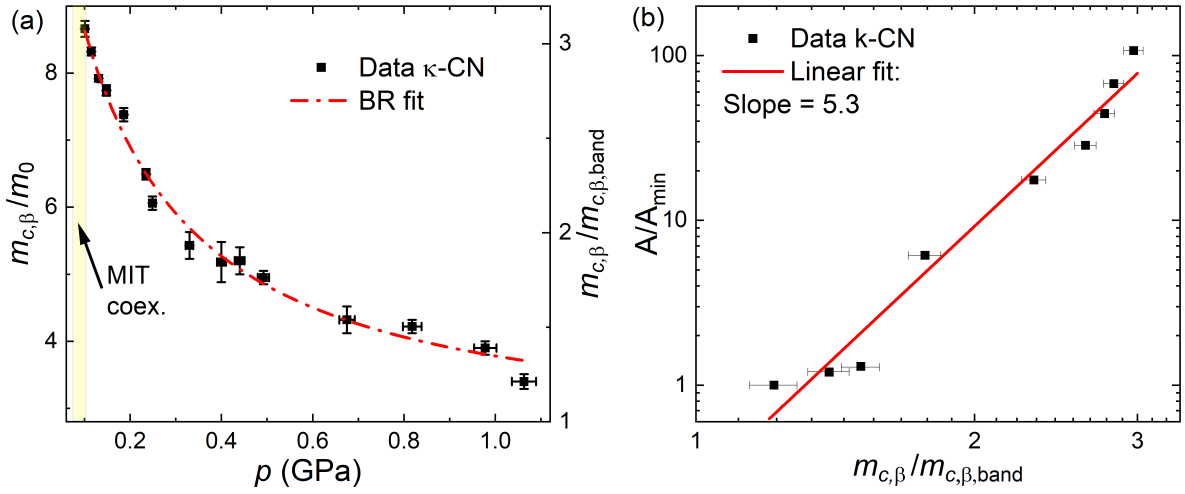

Figure 8.9: (a) Pressure dependence of the effective cyclotron mass $m_{c,\beta}$ (black dots). The left vertical axis shows values in units of the free electron mass (m_0), while the right axis shows the scale in units of the band cyclotron mass ($m_{c,\text{band}} = 2.8\,m_0$), extracted from the BR-like fit. The red dashed line represents a fit to the experimental data using Eq. (5.2). The yellow rectangle denotes the phase coexistence region for κ-CN. All the masses are reduced to the values corresponding to $\theta = 0$ by multiplying them by $\cos(\theta)$. (b) Effective cyclotron mass m_c dependence of the Fermi liquid coefficient A from the Fig. 8.1(b) in a double logarithmic scale (black dots). The effective mass is normalized to the band mass $m_{c,\text{band}} = 2.8\,m_0$, while the coefficient A is normalized to its minimum value $A_{\text{min}} = 1.9 \times 10^{-5}\,\Omega\,\text{cm}\,\text{K}^{-2}$. The red line represents a linear fit with a slope of 5.3 ± 0.4.

we fitted $m_c(p)$ using a BR-like expression Eq. (5.2). The fit is shown as the red line in Fig. 8.9(a). As described in Sec. 5.6, we assume a linear pressure dependence of the transfer integral, $t(p) = t_0 + \gamma(p - p_0)$, where γ is the pressure sensitivity of the transfer integral, and p_0 is the critical pressure corresponding to effective mass divergence in the BR model.

A fit to the experimental data yields the sensitivity coefficient of the transfer integral to pressure, $\gamma = 0.8 \pm 0.2\,\text{GPa}^{-1}$, which is very close to the values obtained for κ-Cl and κ-NCS (Sec. 5.6). This indicates a similar sensitivity of the electronic correlation strength to applied pressure, following the relation $\gamma\,dp = dt/t_0$.

On the other hand, the obtained value of γ is approximately three times higher than that predicted by the band structure calculations [96]. These calculations suggest that the U/t ratio in κ-CN decreases by roughly 18 % when pressure increases from 0 to 0.75 GPa, implying $\gamma \approx 0.23\,\text{GPa}^{-1}$. This discrepancy is smaller than that observed for κ-NCS (Sec. 5.6), which may indicate that the calculations for κ-CN are more accurate. Nonetheless, the experimentally determined sensitivity γ for both κ-CN and κ-NCS is similar within the error bars. At the same time, the calculated values differ significantly between the two salts and are consistently much smaller than the experimental results. This discrepancy should be taken into account in future theoretical models and may prompt a recalculation of the correlation strength for these salts.

The critical pressure obtained from the fit is $p_0 = -0.16 \pm 0.03$ GPa (we will call it BR critical pressure), which is approximately 0.12 GPa higher than the values found for κ-Cl and κ-NCS (Sec. 5.6). Since these salts exhibit similar p-sensitivity coefficients γ, we attribute the difference in critical pressures to the chemical substitution of the anion. Therefore, this difference can be considered an effect of 'chemical pressure'. Notably, in this case, the 'chemical pressure' modifies the ground state not only by altering the spin frustration (as seen in the comparison between κ-Cl and κ-NCS; see Sec. 5.6) but also by shifting the correlation strength.

The saturation value of the effective mass, $m_{c,\beta,\text{band}} \approx 2.8 \pm 0.3\, m_0$, is consistent with the calculated band mass $m_{\text{band}}^{\text{calc}} = 3.0\, m_0$ within the error margins of both experimental measurements and theoretical calculations. To estimate this band mass, we used the proportionality of the density of states calculated for κ-CN and κ-NCS ($1.04/0.9 \approx 1.16$) from [91], and multiplied it by the calculated band mass of κ-NCS ($m_{c,\text{band}} = 2.6\, m_0$) from [191]. The mass renormalization factor near the MIT in κ-CN, given by $m_c/m_{c,\text{band}} \approx 3.13$, is just slightly larger than that of κ-Cl (2.95) near the MIT and κ-NCS (3.09) at ambient pressure.

However, the measured saturation band mass might not be entirely precise due to the limited pressure range available for the κ-CN measurements (maximum pressure of 1 GPa), compared to the broader pressure range used for κ-Cl and κ-NCS (up to 1.5 GPa). Due to technical constraints (see Sec. 4.5), this limitation may have prevented the effective mass values from fully reaching saturation, potentially leading to a slight overestimation of the band mass and underestimation of the renormalization factor.

It is also worth mentioning that this BR critical pressure is significantly different from the critical pressure associated with the divergence of the Fermi liquid coefficient A, as observed in Sec. 8.1 ($p_c = 0.08$ GPa), which lies close to the actual Mott MIT. Figure 8.9(b) displays the dependence of the coefficient A on the effective mass in a double logarithmic scale. The effective mass is normalized to the band mass ($m_{c,\beta,\text{band}} \approx 2.8\, m_0$), while the coefficient A is normalized to its minimal value, $A_{\text{min}} = 1.87 \times 10^{-5}\,\Omega\,\text{cm}\,\text{K}^{-2}$. The fit yields an exponent value of 5.3 ± 0.4 for the scaling of A with the effective mass. This value is larger than those observed for κ-Cl (3.3) and κ-Br (4.5). The increase in exponent with frustration ratio suggests that the correlation between the Fermi liquid coefficient A and the effective mass m^* may not be universal, as often assumed in the literature [65, 70].

8.8 Comparison of κ-NCS, κ-Br, κ-Cl and κ-CN

In the previous section, we observed a difference in the BR critical pressures between κ-CN and κ-NCS. This difference, $\Delta p_0 = 0.12$ GPa, corresponds to approximately a 0.48 % change in the β-frequency. The ratio of the in-plane first Brillouin zones of κ-NCS and κ-CN at ambient pressure is $36.82\,\text{nm}^{-2}/34.27\,\text{nm}^{-2} \approx 1.074$ (unit cell parameters are provided in Sec. 3.1), which would correspond to an effective pressure difference of roughly 1.5 GPa. This value is significantly larger than the pressure difference attributed to the 'chemical pressure' effect. In contrast, the unit cell sizes of κ-Cl and κ-NCS are nearly identical, which explains the absence of a pronounced 'chemical pressure' effect between these two salts and their similar BR critical pressures. This

strong discrepancy indicates that, although a comparison of unit cell dimensions may offer a qualitative indication of 'chemical pressure', it does not provide a reliable quantitative measure without supporting band-structure calculations.

Taking into account the critical pressure and sensitivity ($\gamma\, dp = dt/t_0$) from the BR-like fit, along with the correlation strength from the theoretical calculations [96], we can position our salts on the 'correlation strength-frustration ratio' phase diagram. Fig. 8.10(a) shows the phase diagram (black lines) adapted from [220], with our experimentally evaluated parameters for κ-Cl (black points), κ-NCS (red points), κ-Br (green point), and κ-CN (blue points) overlaid. The parameters were estimated in the pressure range from 0 GPa to 1 GPa, with arrows indicating the direction of the parameter evolution under increasing pressure. To estimate the absolute value of the correlation strength, we used the ambient pressure values of $(U/t)(0)$ from [96] and the experimentally determined compressibility $\gamma \approx 0.8\,\mathrm{GPa}^{-1}$. In this framework, the pressure-dependent correlation strength can be expressed as: $(U/t)(p) = (U/t)(0) \cdot \frac{1-\gamma p_0}{1+\gamma(p-p_0)}$.

The overall qualitative trend appears consistent: all compounds lie near the phase boundaries, and both pressure and anion substitution shift the system in directions that

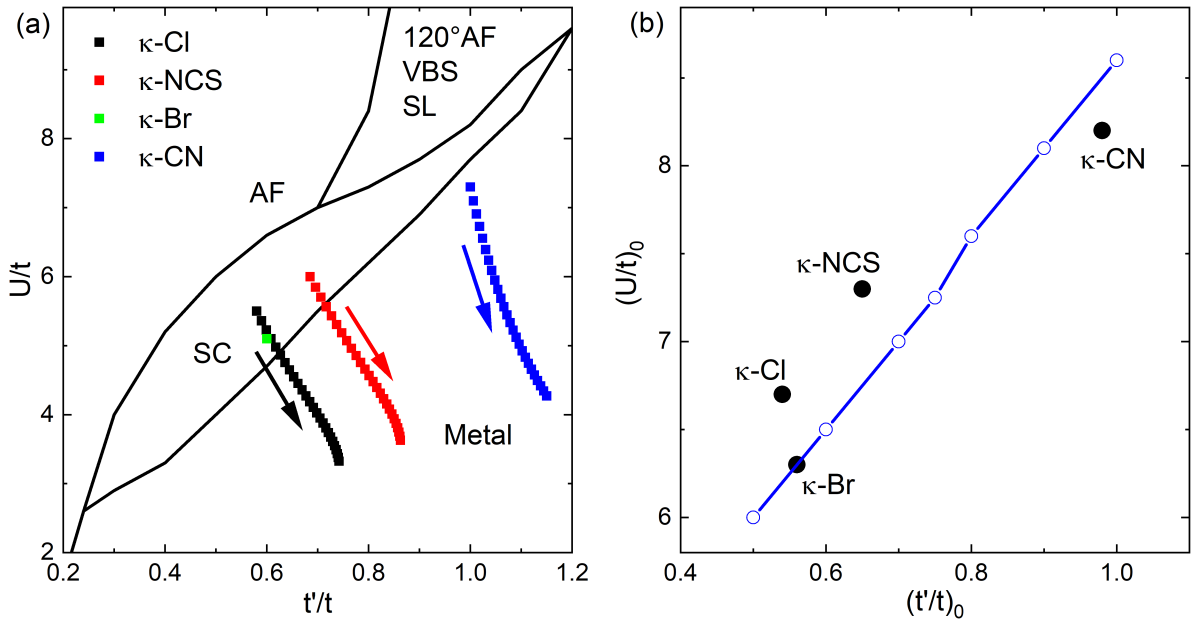

Figure 8.10: (a) Phase diagram for the frustrated triangular lattice Hubbard model. Solid lines represent the phase boundaries determined in [220]. Colored points indicate the ground states of κ-Cl (black), κ-NCS (red), and κ-CN (blue) over the pressure range from ambient pressure to 1 GPa. κ-Br (green) is shown only at ambient pressure. Arrows indicate the direction of parameter evolution with increasing pressure. All values were estimated from our SdH measurements. (b) Critical correlation strength versus critical frustration ratio at the BR critical pressure. The blue line is the superconductor-insulator phase boundary from panel (a), adapted from [220], while the black points represent an extrapolation of our experimental data to the BR critical pressure.

align with the theoretical phase diagram. For κ-NCS, its location on the phase diagram agrees with its experimentally observed metallic ground state. However, for κ-Cl and κ-CN, the phase diagram predicts a superconducting/metallic ground state at ambient pressure, whereas experimental measurements reveal an insulating ground state. In both cases, external pressure is required to drive the system into the metallic state. This discrepancy suggests that the calculated ambient pressure correlation strengths [96] may be underestimated, or that the phase boundaries in the diagram are not precise and the critical correlation strength required for the Mott transition may occur at lower values than predicted. Additionally, the boundaries of the MIT may be affected by disorder, as described in the Mott-Anderson scenario [88]. For κ-Br, the correlation strength also appears to be underestimated. According to our estimation, it lies very close to the MIT boundary, as even a slight increase in the correlation strength - such as that induced by deuteration ($\Delta p \approx 15\,\mathrm{MPa}$ or $\Delta(U/t) \approx 0.1$) - shifts the compound into the phase coexistence region of the transition.

Despite these quantitative discrepancies, the positioning of the materials on the phase diagram still provides valuable insight into the mechanisms governing ground-state formation in these compounds.

Using the experimentally determined BR critical pressure and the absolute value of the correlation strength from the calculations [96], we can estimate the correlation strength near the BR critical pressure, denoted as $(U/t)_0$. Additionally, by extrapolating the pressure dependence of the frustration ratio, we can estimate the frustration ratio near the BR critical pressure, $(t'/t)_0$. Fig. 8.10(b) shows the dependence of the correlation strength $(U/t)(p_0) = (U/t)_0$ on the frustration ratio $(t'/t)_0$ near the BR critical pressure for different salts (black points), along with the frustration ratio dependence of the critical correlation strength extracted from the phase diagram in Fig. 8.10(a) (blue line). The experimental estimates are in good agreement with the theoretical predictions. Therefore, we can conclude that the critical correlation strength $(U/t)_0$ indeed depends on the frustration ratio of the system.

Figure 8.11(a) shows the dependence of the quasiparticle residue on the correlation strength near the MIT for different κ-salts. The correlation strength was estimated using the method described in the previous paragraph, while the quasiparticle residue was calculated as the inverse mass renormalization, $Z = m_{c,\mathrm{band}}/m_c$. The values of Z near the MIT, obtained from our BR-like fits, were found to be comparable for κ-CN ($Z \approx 0.32 \pm 0.05$), κ-Cl ($Z \approx 0.35 \pm 0.02$), κ-d_8-Br ($Z \approx 0.34 \pm 0.02$), and κ-NCS at ambient pressure ($Z \approx 0.33 \pm 0.02$), within the uncertainty of the experimental measurements and fit evaluations. Notably, κ-NCS at ambient pressure exhibits a Z value comparable to that of κ-CN near the MIT. This suggests that, under 'negative' pressure (i.e., reduced pressure), κ-NCS may exhibit an even lower quasiparticle residue Z than κ-CN, despite its significantly smaller frustration ratio. However, the exact proximity of κ-NCS to the Mott insulating transition remains uncertain.

The inset of Fig. 8.11(a) displays the dependence of the quasiparticle residue on the frustration ratio near the MIT. The data suggest that the quasiparticle residue does not vary significantly with frustration. This observation implies that the critical value of Z at which the MIT occurs exhibits only a weak dependence on both the correlation strength and frustration. Although this finding aligns with theoretical studies predicting a lower Z near the MIT for systems with higher frustration ratios [80], the influence

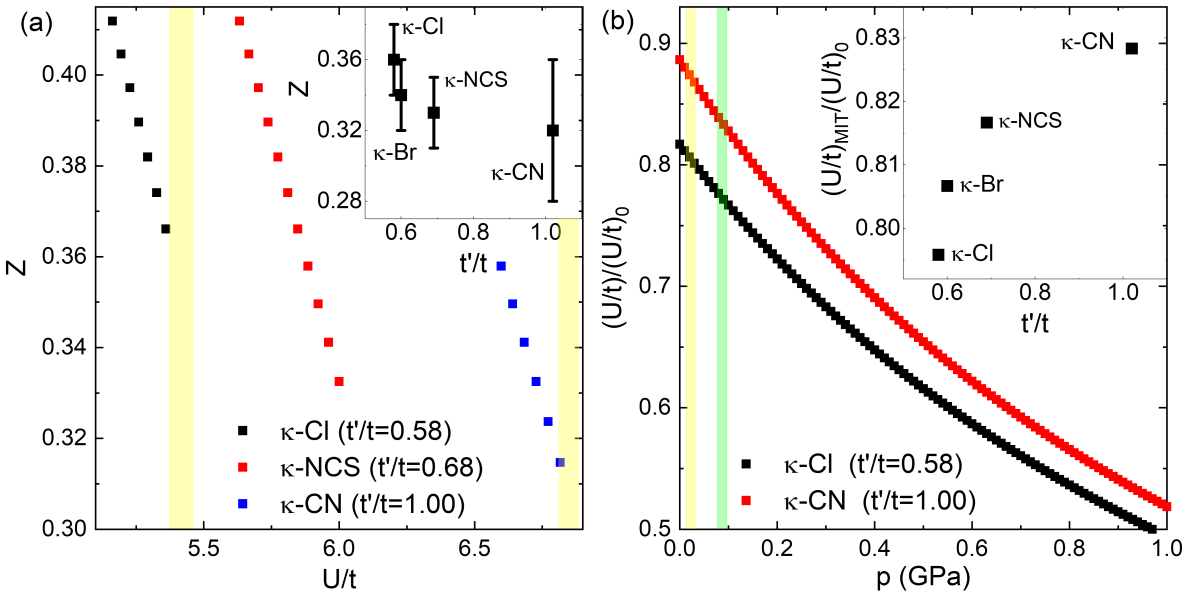

Figure 8.11: (a) The quasiparticle residue Z as a function of the correlation strength for κ-Cl (black), κ-NCS (red), and κ-CN (blue), measured at pressures near the MIT or at ambient pressure. Yellow rectangles indicate the MIT regions for κ-Cl and κ-CN. Inset: Frustration ratio dependence of the quasiparticle residue at the MIT. (b) Pressure dependence of the correlation strength (U/t), normalized to the BR critical correlation strength $(U/t)_0$, for κ-Cl (black) and κ-CN (red). The data were obtained from BR-like fits to experimental measurements. The hatched yellow and green rectangles show the phase coexistence regions for the κ-Cl and κ-CN, respectively. Inset: Frustration ratio dependence of the correlation strength at the MIT, normalized to $(U/t)_0$.

appears minimal. Consequently, the slope of the phase boundary in Fig. 8.10(a) is expected to be small, albeit likely always positive.

In discussing the weak dependence of the quasiparticle residue near the MIT on the correlation strength, we initially relied on the absolute ambient-pressure values of correlation strength obtained from calculations in [96]. However, these calculated values may not be sufficiently precise. To avoid the reliance on absolute values, we instead estimate the correlation strength in units of the BR critical correlation strength, $(U/t)_0$. Using the compressibility and the BR critical pressure extracted from experimental fits, the correlation strength at different pressures can be expressed as $(U/t)(p) = (U/t)_0/(1+\gamma(p-p_0))$. Figure 8.11(b) displays the pressure dependence of the normalized correlation strength $(U/t)/(U/t)_0$ for κ-Cl (black points) and κ-CN (red points). For κ-NCS and κ-Br, this dependence is expected to follow a similar trend to that of κ-Cl, given the close similarity of their BR-like fit parameters.

Using these data, we can estimate the correlation strength at which the MIT occurs, $(U/t)_{\mathrm{MIT}}$. The inset of Fig. 8.11(b) presents the dependence of $(U/t)_{\mathrm{MIT}}$ on the frustration ratio for various salts. In this representation, a trend emerges: the correlation strength required for the Mott transition increases with the frustration ratio. This behavior is consistent with theoretical predictions, although the relative variation is rather modest. A summary of the correlation strength and frustration parameters for

Salt	κ-NCS (M)	κ-Br (M)	κ-Cl (AFI)	κ-CN (NMI)
p_c^{MIT} (MPa)		-25	30	90
p_c^{FL} (MPa)		-160	−100	80
p_0 (MPa)	-280	-300	-280	-160
$(U/t)(0)$	6.0	5.1	5.5	7.3
$(U/t)(p_0)$	7.3	6.3	6.7	8.2
$(t'/t)(0)$	0.69	0.60	0.58	1.00
$(t'/t)(p_0)$	0.65	0.56	0.54	0.98
$(U/t)_{\mathrm{MIT}}/(U/t)_0$	0.817	0.807	0.796	0.828

Table 8.3: Correlation strength and frustration ratio at the Mott MIT for various κ-salts. The ambient-pressure ground states are indicated as metallic (M), antiferromagnetic insulating (AFI), and nonmagnetic insulating (NMI). The salts are arranged in order of decreasing metallic character. Here, p_c^{MIT} is the pressure corresponding to the MIT coexistence area on the phase diagram, p_c^{FL} is the critical pressure from the fit of FL coefficient A, p_0 is the BR critical pressure, $(U/t)(0)$ is the correlation strength at ambient pressure, $(U/t)(p_0)$ and $(t'/t)(p_0)$ are the values at the BR critical point, and $(U/t)_{\mathrm{MIT}}/(U/t)_0$ is the normalized correlation strength at the MIT.

the investigated salts is provided in Table 8.3.

However, an alternative explanation for the slight discrepancy with theory regarding the weak dependence of the quasiparticle residue on correlation strength may lie in the definition of Z. Our analysis assumed the quasiparticle residue to be equivalent to the inverse mass renormalization factor, $Z = m_{c,\mathrm{band}}/m_c$. However, cluster DMFT calculations reported in [221] suggest that the quasiparticle residue Z does not always coincide with the renormalization factor derived from the effective mass. The discrepancy between these two quantities increases with growing correlation strength and may become significant near the MIT. Under such conditions, the effective mass may not reliably reflect the strength of electronic correlations, and thus Z cannot be accurately estimated from mass renormalization.

Another parameter widely considered to be related to the correlation strength is the Fermi liquid coefficient A [65, 70]. The critical pressures p_c^{FL} for the divergence of this coefficient in different salts are listed in Table 8.3. The difference between this FL critical pressure and the Mott MIT pressure for κ-Cl and κ-Br is approximately $\Delta p_c = p_c^{\mathrm{MIT}} - p_c^{\mathrm{FL}} \approx 130\,\mathrm{MPa}$, while for κ-CN it is only around $\Delta p_c \approx 10\,\mathrm{MPa}$. This suggests that the MIT occurs closer to the critical pressure in more frustrated systems, consistent with theoretical predictions [80]. In this context, the difference in the ambient-pressure ground states between κ-NCS, κ-Cl, and κ-Br may be attributed primarily to differences in the frustration ratio. However, the direct relationship between the coefficient A and the correlation strength is not unambiguous and may deviate from the conventional Kadowaki-Woods ratio [72], as also observed in this thesis.

In summary, in this chapter, we used the AMRO technique to investigate the Fermi surface anisotropy in κ-CN and its evolution under pressure. The experimentally determined FS was compared with that calculated using an effective dimer model and SdH frequencies. Additionally, precise sample rotation enabled the observation of the coherence peak feature near the exact in-plane field orientation. This feature was used to extract the interlayer transfer integral, which was determined to be approximately 0.2 meV at ambient pressure. This value is consistent with those reported for the κ-Cl and κ-Br salts.

Furthermore, by measuring quantum oscillations near AMRO maximum orientation, we could observe sizeable SdH oscillations in κ-CN across a broad pressure range up to 1 GPa. We determined the frustration ratio from a systematic analysis of the SdH frequencies. The resulting ambient-pressure value of the frustration ratio is closer to unity ($t'/t \approx 1.0$) than the predictions of both the Extended Hückel method [91] and DFT-based calculations [96]. These findings suggest that it is desirable to revise the theoretical calculations, taking into account our experimental results from SdH analysis.

The analysis of the SdH oscillation amplitudes at various temperatures and pressures enabled us to determine the renormalized effective cyclotron mass. Across the entire studied pressure range, the behavior of the effective mass is remarkably well described by the Brinkman-Rice model, assuming a linear pressure dependence of the transfer integral $t(p)$ and a pressure-independent on-site Coulomb repulsion. The fit yields a band mass of $m_{\text{band}} = 2.8\, m_0$, which is significantly higher than the values observed in κ-Cl and κ-NCS (2.1 m_0). The sensitivity of the transfer integral to pressure was found to be approximately $\gamma = 0.8\,\text{GPa}^{-1}$. This value is similar to that obtained for other κ-salts in this work (Sec. 5.5), and about three times higher than the value predicted by the theoretical calculations [96].

The critical pressure for the effective mass divergence was determined to be $p_0 = -0.16$ GPa, differing from that of κ-Cl and κ-NCS ($p_0 \approx -0.28$ GPa), which highlights the effect of 'chemical pressure'. The inverse mass renormalization parameters (m_{band}/m^*) near the MIT are similar for κ-CN ($Z \approx 0.32$), κ-NCS ($Z \approx 0.33$ at ambient pressure), κ-d_8-Br ($Z \approx 0.34$) and κ-Cl ($Z \approx 0.36$), indicating comparable levels of electronic correlation strength near the MIT in these compounds.

This observation may suggest either that the quasiparticle residue near the MIT weakly depends on the frustration ratio or that a mismatch exists between the quasiparticle residue and the mass renormalization factor near the Mott transition.

9 Summary

In this PhD thesis, the organic charge-transfer salts κ-(BEDT-TTF)$_2X$, with various anions X, were systematically investigated. These salts are ideal model systems for studying the bandwidth-controlled quasi-2D Mott instability. The primary experimental method employed was the measurements of Shubnikov-de Haas (SdH) oscillations, which provide valuable insights into the Fermi surface (FS) and electronic correlations in the material. Many experiments were performed at low temperatures and high magnetic fields. The latter included static fields generated by superconducting and resistive solenoids, as well as transient fields generated by pulsed-field facilities. SdH oscillations were measured with differently prepared samples and under various experimental conditions. This includes sample preparation under varying thermal history, the application of hydrostatic pressure, and the use of different orientations of the applied magnetic field.

The main objective of this work was to investigate the evolution of the electronic ground state in proximity to the bandwidth-controlled Mott metal-insulator transition (MIT). The ground state is determined by several characteristic material parameters, including the electronic correlation strength, spin frustration ratio, and disorder. We could systematically manipulate these material parameters by varying the external conditions - such as the applied pressure, chemical composition, and structural modifications induced by thermal history. This approach allowed us to disentangle the influence of each external factor on the internal electronic properties and clarify their respective roles in shaping the ground state and driving the MIT. The schematic block diagram shown in Fig. 9.1 summarizes the key relationships: the external parameters (pressure, chemical substitution, structural modification via thermal history), their effects on the material parameters (correlation strength, frustration, and disorder), and the resulting formation of different types of insulating states.

One of the central objectives of this thesis was to elucidate the effect of anion substitution on the material parameters controling the MIT in the κ-salts. To this end, we have conducted a comparative study of the κ-Cl, κ-Br, and κ-CN under pressure. These results were also compared with previously published data for κ-NCS [178]. The first parameter examined was the spin frustration ratio t'/t, where t and t' are the nearest- and next-nearest-neighbor transfer integrals, respectively, within the effective dimer model. This ratio was extracted from the SdH oscillation frequencies. The FS estimated within the effective dimer model closely match the experimental data obtained from the AMRO measurements in κ-Cl and κ-CN. The estimated spin frustration ratios at ambient pressure are approximately 0.58 for κ-Cl, 0.69 for κ-NCS, and 1.00 for κ-CN. For κ-Br, based on the previous report [109], the frustration ratio is approximately 0.6, that is, slightly above that of κ-Cl. While these trends are consistent with the theoretical predictions [91, 96], the absolute values are closer to unity. This suggests that the spin frustration in our salts is significantly stronger than predicted by theory. More-

over, it was observed that applying a pressure of approximately 1 GPa increases the frustration ratio t'/t by 15 % to 25 %, depending on the compound. This indicates that both chemical substitution and physical pressure influence spin frustration similarly (Fig. 9.1).

The second parameter investigated was the effective mass renormalization and the associated electronic correlation strength ratio U/t, where U is the on-site Coulomb repulsion and t is the transfer integral. We found that the pressure dependence of the effective mass is remarkably well described by the Brinkman-Rice (BR) model throughout the whole pressure range, assuming a linear dependence of the transfer integral on pressure. The fits revealed a similar sensitivity of the transfer integral to pressure across all four salts. At the same time, the BR critical pressure, leading to a divergence of the effective mass, differs significantly for κ-CN compared to the other three salts. This difference can be attributed to the effect of 'chemical pressure'. In this context, chemical substitution acts analogously to physical pressure in modifying the correlation strength. For κ-Cl, κ-NCS, and κ-Br, our measurements in the metallic state revealed similar mass renormalization factors (m^*/m_{band}) and BR critical pressures. Therefore, in these three salts, chemical substitution does not mimic the effect of physical pressure in altering correlation strength. Instead, the differences in their ambient-pressure ground states are primarily governed by variations in the spin frustration ratio.

The quasiparticle residue Z, commonly assumed to be equal to the inverse mass renormalization factor, was found to have a similar value near the MIT for κ-CN ($Z \approx 0.32$), κ-NCS ($Z \approx 0.33$ at ambient pressure), κ-d$_8$-Br ($Z \approx 0.34$), and κ-Cl ($Z \approx 0.36$), all within the experimental error margin. This observation aligns with theoretical predictions suggesting that systems with higher spin frustration tend to undergo the MIT at lower values of Z. However, the dependence of the critical quasiparticle residue on the frustration ratio appears to be weak. It is also possible that a distinction exists between the quasiparticle residue and the mass renormalization factor, which may become increasingly pronounced in the vicinity of the MIT [221].

We also have measured angle-dependent magnetoresistance oscillations (AMRO) in κ-Cl and κ-CN. These measurements enabled us to determine in detail the shape and size of the FS of these salts and their evolution with pressure. We have observed that the FS of κ-Cl exhibits a more rectangular shape, whereas that of κ-CN is more elliptical. Furthermore, the magnetoresistance anisotropy for in-plane magnetic fields was found to be significantly stronger in κ-Cl than in κ-CN, showing a nearly isotropic magnetoresistance. We have also observed a coherence peak in the magnetoresistance and estimated the interlayer transfer integrals. They are comparable in magnitude for both salts, but are significantly more anisotropic in κ-Cl.

In another part of this study, we investigated the effects of structural modifications induced by temperature treatments. The thermal history strongly influences the occupation of different conformations [staggered (S) and eclipsed (E)] of the ethylene end groups in the organic BEDT-TTF molecules. The effect is most prominent in the κ-Br salt. Rapid cooling through the temperature ($T_g \sim 80$ K) of the glass-like structural transition increases the probability for the presence of the metastable S state. Using a heat pulse technique based on applying short voltage pulses, we achieved high cooling rates, enabling an unprecedentedly high occupation of the S state. A higher

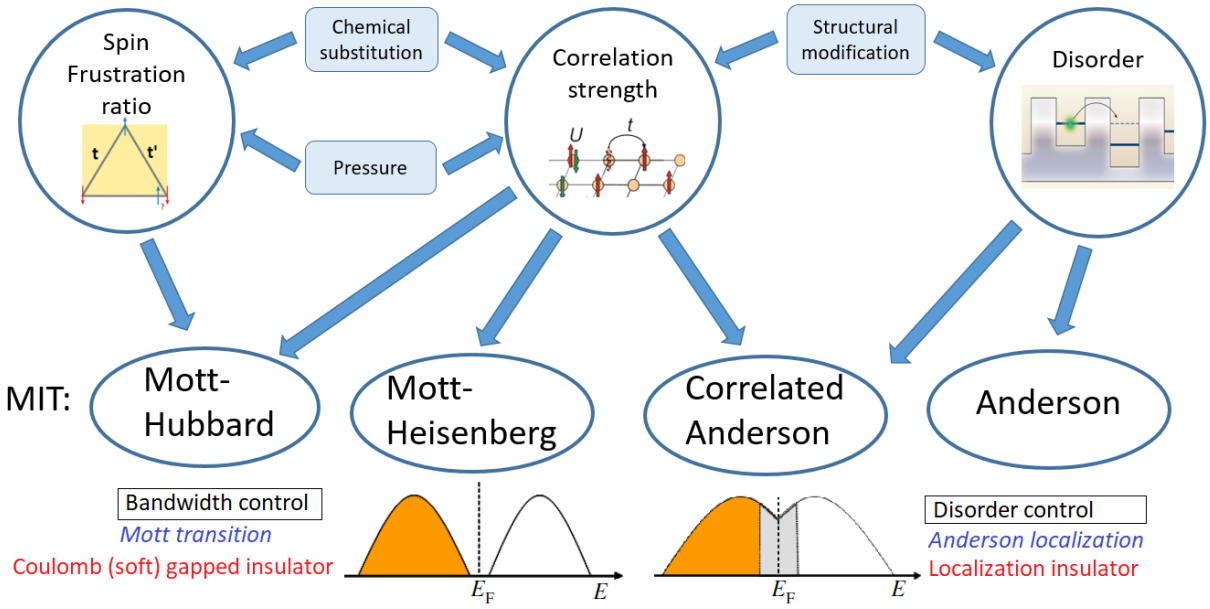

Figure 9.1: Schematic block diagram illustrating the influence of the various external experimental conditions and internal material parameters on the formation of different types of metal-insulator transitions. External tuning parameters such as physical pressure, chemical substitution, and structural modification (via thermal history) affect the internal electronic parameters, including correlation strength, spin frustration, and disorder. These internal material parameters, in turn, govern the nature of the resulting insulating state - either Mott, Anderson, or their variations. The diagram summarizes the conceptual framework underlying the experimental investigations in this work.

concentration of the S state acts as an additional disorder, significantly increasing the scattering rate and pushing the system closer to the MIT. However, in contrast to previous suggestions [148, 149], we found that the correlation strength remains nearly unchanged across states with different S concentrations, and that the shift toward the MIT is primarily driven by enhanced disorder. This observation supports a Mott-Anderson (correlated Anderson) scenario for the MIT rather than a Mott-Hubbard mechanism (Fig. 9.1).

To confirm our findings, we conducted similar experiments with deuterated κ-Br, which exhibits a stronger correlation strength and lies right on the metal-insulator phase boundary even in its most ordered state. The achieved results were consistent. We observed no visible influence of S-conformation occupation probability on the correlation strength. Meanwhile, the insulating behavior could be induced at significantly lower levels of disorder. Additionally, we investigated the effect of disorder on κ-Cl under pressure and observed a similar but less pronounced trend. Overall, this study demonstrated that thermal history does not significantly affect the correlation strength, allowing us to treat it as an independent parameter in subsequent measurements.

The results of our systematic study provide a thorough and detailed understanding of the physics underlying Mott metal-insulator transitions in the charge-transfer salts κ-(BEDT-TTF)$_2X$. In particular, we clarified the roles played by the electronic correlation

strength, spin frustration, and disorder. Moreover, our experimental findings are of key relevance for challenging theoretical model predictions, suggesting the presence of alternative mechanisms that may influence the formation of the MIT. The insights gained from our comprehensive study provide the basis for refining theoretical models and further advancing our understanding of strongly correlated electron systems.

Appendix

Fermi surface determination

In Secs. 5.8 and 8.3, the Fermi surfaces (FS) of κ-Cl and κ-CN were determined from angle-dependent magnetoresistance oscillations (AMRO) using Eq. (2.19). However, as noted in those sections, this equation does not provide the true Fermi wave vector k_F, but rather the maximum projection of the FS onto the magnetic field rotation plane, denoted k_B^{max}. To obtain an accurate representation of the Fermi surface, one must construct lines perpendicular to the k_B^{max} vectors. These lines serve as tangents to the true in-plane FS. The envelope formed by these lines outlines the actual shape of the Fermi surface.

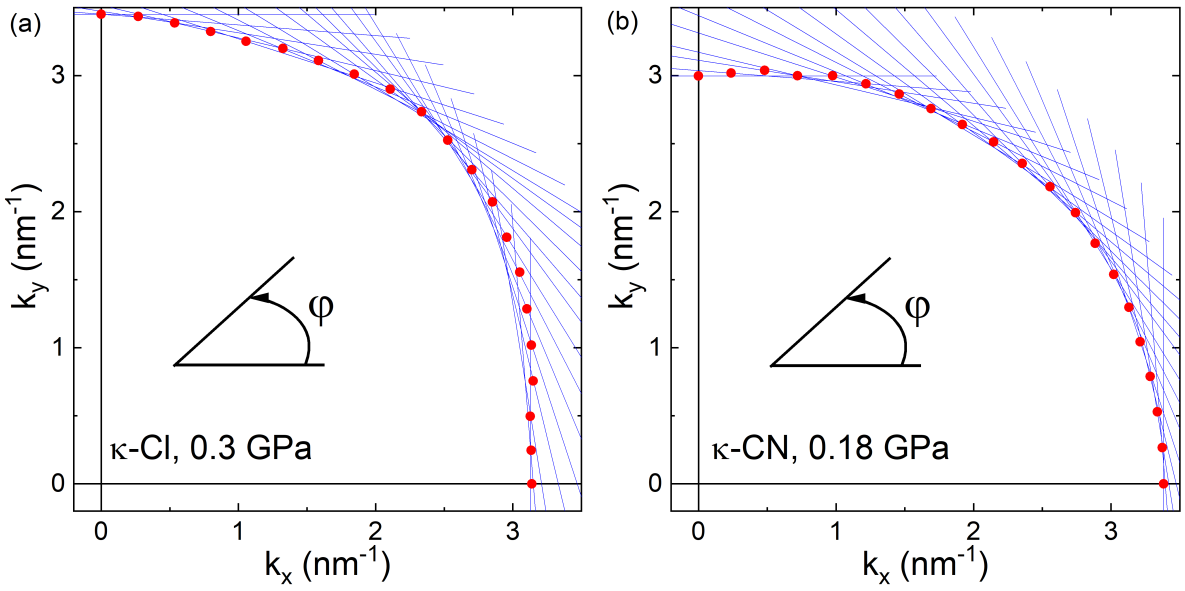

Figure 9.2: Dependence of the wave vector k_B^{max} (red points) on the in-plane angle φ for κ-Cl (a) and κ-CN (b). The blue lines represent perpendiculars on k_B^{max}.

In this section, we present the construction of the perpendiculars on the wave vector $k_B^{max}(\varphi)$ in order to evaluate the discrepancy between k_B^{max} and the true Fermi wave vector k_F. Figures 9.2(a) and 9.2(b) display $k_B^{max}(\varphi)$ (red points) along with the corresponding perpendiculars (blue lines) for κ-Cl and κ-CN, respectively. It is evident that k_B^{max} closely follows the direction of the tangents in most angular regions. In certain areas, the perpendiculars slightly underestimate the wave vector. For κ-Cl at 0.3 GPa, these deviations primarily occur at angular positions where $k_B^{max}(\varphi)$ exhibits relatively sharp features ($\sim 50°$). In these regions, the actual curvature of the FS is weaker and

should be taken into account in AMRO and $\rho(\varphi)$ simulations. For κ-CN at 0.18 GPa, the deviations are even smaller, and the overall curvature of the inferred and true contours remains nearly identical. Therefore, the discrepancy between $k_B^{\max}$ and k_F is minimal, validating the use of $k_B^{\max}$ as a good approximation for AMRO-based simulations.

Measurements of κ-^{12}C-CN

The primary results presented on κ-CN were obtained using a compound synthesized with the carbon isotope ^{13}C, grown by A. Kawamoto and provided by A. Pustogow. Additionally, we tested samples containing the ^{12}C isotope, synthesized by the group of M. Lang[1]. Figure 9.3(a) displays the angle-dependent magnetoresistance of κ-^{12}C-CN under a pressure of 0.9 GPa. Both the AMRO features and the coherence peak are markedly weaker in this sample compared to κ-^{13}C-CN, likely due to differences in crystal quality (see Sec. 8.2).

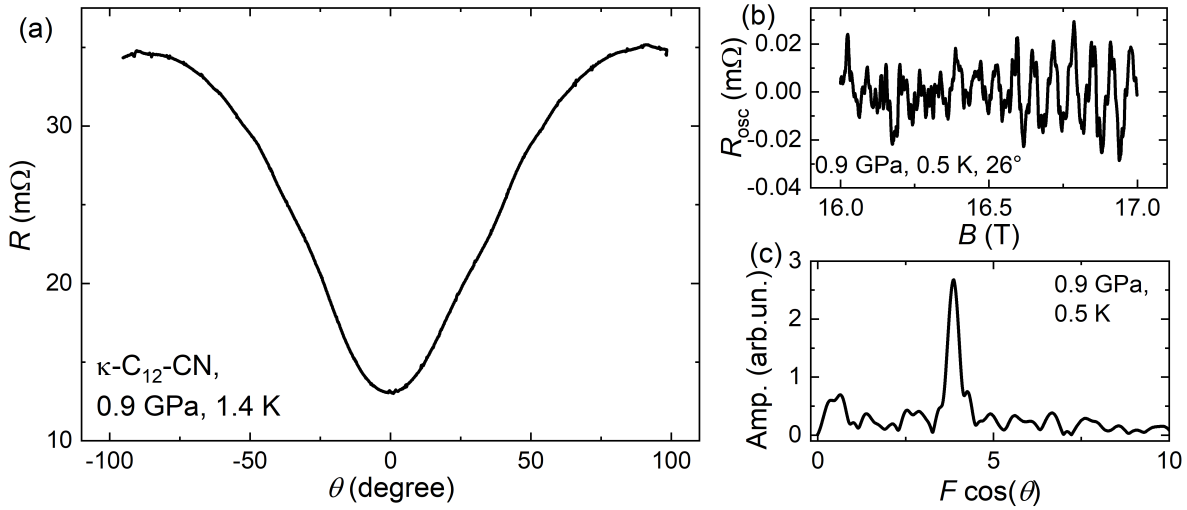

Figure 9.3: (a) Interlayer resistance of κ-^{12}C-CN as a function of the polar angle θ. (b) SdH oscillations measured at $\theta = 26°$ in the magnetic field range 16 T to 17 T. (c) FFT of the oscillations shown in the panel (b), with the frequency scaled by the polar angle $\theta = 26°$.

Figure 9.3(b) shows the SdH oscillations measured in the magnetic field range 16 T to 17 T, at an angle corresponding to the AMRO peak, and at a temperature of 0.5 K. The oscillation amplitude is approximately 0.02 mΩ, with a background resistance of around 20 mΩ, yielding a relative amplitude of only 0.2 %. This is more than an order of magnitude smaller than that observed in κ-^{13}C-CN under comparable conditions (approximately 3 %). The FFT spectrum of the oscillations, shown in Fig. 9.3(c), demonstrates that the SdH signal amplitude is only marginally above the noise level, making accurate SdH analysis highly challenging.

Consequently, for our core investigations involving the determination of the effective cyclotron mass and SdH frequency, we focused on the ^{13}C-enriched compound,

[1]Goethe University, 60323 Frankfurt, Germany

which exhibited significantly stronger AMRO and SdH responses.

Quality of κ-Br samples

In the chapters presenting results on κ-Br, we reported clear SdH oscillations at high magnetic fields. These measurements were carried out at the high-field facility in Dresden. However, not all samples exhibited strong oscillations. Therefore, prior to the main measurements, we performed extensive testing experiments on numerous samples from different batches to identify the most suitable ones.

The main criteria for sample selection were the visibility of SdH oscillations and the residual resistance ratio (RRR), defined as the ratio between the residual resistance and the resistance at the peak in $R(T)$ (Fig. 9.4(a)). Since the SdH amplitude in κ-Br at fields up to 17 T is very small, detecting any oscillations was challenging. Nevertheless, high-quality hydrogenated samples demonstrated weak but visible SdH oscillations, as shown in Fig. 9.4(b). The relative amplitude of these oscillations was around 0.01 %, only several times greater than the noise level (Fig. 9.4(c)). Despite their weakness, these oscillations served as a direct and effective method for identifying high-quality samples.

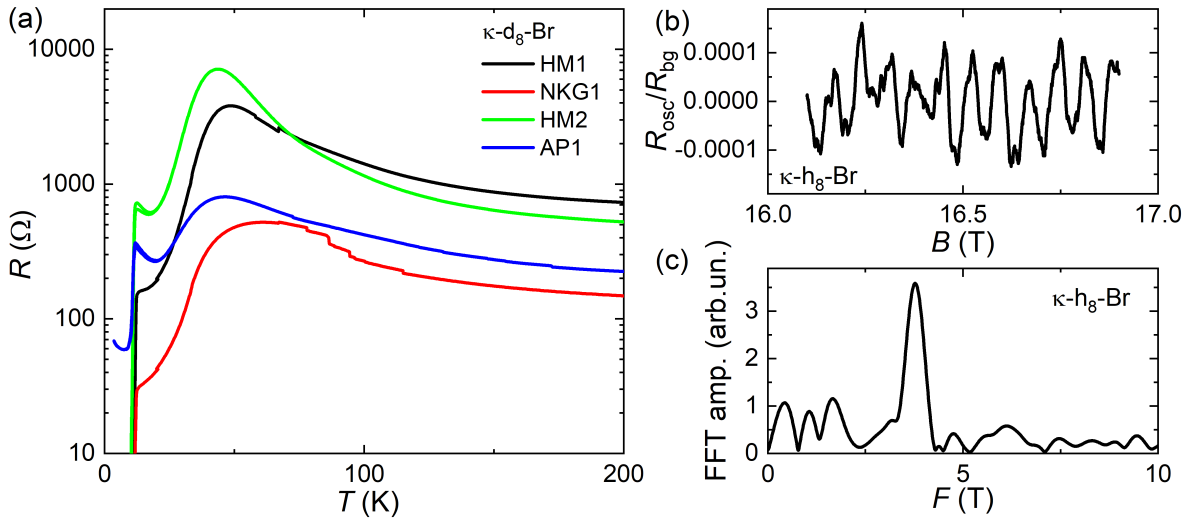

Figure 9.4: (a) $R(T)$ curves of deuterated κ-Br samples from different batches. (b) SdH oscillations measured in the hydrogenated κ-Br sample "Crumb" (see Table 9.1) in the magnetic field range 16 T to 17 T. (c) FFT of the oscillations shown in panel (b).

Table 9.1 summarizes the key parameters of all tested samples from different batches, including the information on observed SdH oscillations and RRR values measured in the normally cooled state (2 K/min). The samples selected for the Dresden measurements were *Crumb*, *NKG11*, and *Nizza*.

The situation with deuterated samples was even more challenging. As these compounds lie even closer to the Mott insulator transition, the amplitude of the SdH oscillations is smaller than in the hydrogenated analogues. So far, we have observed only a questionable SdH signal in one sample at a magnetic field around 17 T. Therefore, we

Sample	R_{RT} [Ω]	R_{peak} [Ω]	$R(15\,K)$ [Ω]	RRR	SdH amp.
S1	560	1080	13.8	80	3.2
Crumb	440	680	4.5	150	3.4
LB1	1590	1960	520	3	-
NKG11	5400	1350	19.5	70	3.6
NKG7	110	1710	8.7	190	0.8
NKG13	220	650	16.6	40	3.2
Nizza	730	1620	16.7	100	-

Table 9.1: Characteristic properties of the hydrogenated κ-Br samples. R_{RT} is the resistance at room temperature, R_{peak} is the maximum resistance in the temperature curve, and RRR is the residual resistance ratio. SdH amp. indicates the relative amplitude of SdH oscillations, R_{osc}/R_{bg} of the observed SdH oscillations in the annealed state.

used RRR as the primary selection criterion. Fig. 9.4(a) shows RT curves for deuterated κ-Br samples from different batches in the normally cooled state. Table 9.2 summarizes all tested samples with their respective characteristics, including RRR values measured in the annealed state at 68 K. The samples selected for the high-field measurements in Dresden were *HM2*, *HM3*, and *HM4*.

Sample	R_{RT} [Ω]	R_{peak} [Ω]	$R(15\,K)$ [Ω]	RRR	T_c [K]
HM1	690	3810	160	24	11.9
HM2	420	5200	180	29	11.7
HM3	700	4310	100	45	11.9
HM4	680	4020	160	25	11.9
HM5	250	880	70	13	12.0
HM6	300	480	20	19	12.7
NKG1	130	520	30	17	11.9
NKG2	70	210	15	14	11.7
AP1	210	640	100	7	11.6

Table 9.2: Characteristic properties of the deuterated κ-Br samples. The designation of the various quantities corresponds to that in Table 9.1

Python code for calculations of the frustration ratio

```
def Enp(tpt, kb, kc, const=0):  # Calculates E+, returns E/2t; tpt = t'/
                                t
    return tpt*np.cos(kb) + np.sqrt((1 + np.cos(kb)) * (1 + np.cos(kc)))
                                    + const
```

```
def Enm(tpt, kb, kc, const=0):  # Calculates E-, returns E/2t; tpt = t'/
                                t
    return tpt*np.cos(kb) - np.sqrt((1 + np.cos(kb)) * (1 + np.cos(kc)))
                                    + const
def sq_phase(k1, k2):  # Calculates the area enclosed by the Fermi
                       surface (k1, k2)
    return 2 * ((k1[1:-1] - k1[0:-2]) * (k2[1:-1] + k2[0:-2])).sum()
def fs3(Z, const=0):  # Finds k-points where energy Z equals the given
                      constant
    ind = np.where(np.abs(Z - const) < 0.001)
    return ind
kb = np.linspace(0, np.pi, 4000)
kc = np.linspace(0, np.pi, 4000)
X, Y = np.meshgrid(kb, kc)
Const = np.arange(-0.5, -0.2, 0.002)
Tpt = np.arange(0.5, 1.1, 0.1)  # List of t'/t values for calculation
Sa = []  # List to store alpha (E-) areas
Sb = []  # List to store beta (E+) areas
for tpt in Tpt:
    Zp = Enp(tpt, X, Y)
    Zm = Enm(tpt, X, Y)
    for const in Const:  # For each t'/t and energy level = const,
                             determine the k-points on the FS
        indp = fs3(Zp, const)
        indm = fs3(Zm, const)
        k1p1, k2p1 = kc[indp[0]], kb[indp[1]]
        k1m1, k2m1 = kc[indm[0]], kb[indm[1]]
        sa = sq_phase(k1m1, k2m1)  # Calculate E- (alpha) area for the
                                       slice
        sb = sq_phase(k1p1, k2p1)  # Calculate E+ (beta-alpha) area for
                                       the slice
        Sa.append(sa)
        Sb.append(sb)
Za = np.asarray(Sa).reshape(Tpt.size, Const.size)  # E- (alpha) areas
                                   for different slices
Zb = np.asarray(Sb).reshape(Tpt.size, Const.size)  # E+ (beta-alpha)
                                   areas for different slices
Zsquare = Za + Zb  # Total beta area
Zs = np.abs(Zsquare / (4 * np.pi**2) - 1.0)  # Difference from full
                                   Brillouin zone area (2pi)**2
Zt = Za / Zsquare  # Ratio of alpha to beta area
plt.figure(figsize=(15, 15))
# This plot shows the energy constant (const) and t'/t values where the
                                   total FS slice area equals (2$\pi$)^
                                   2
plot = plt.pcolormesh(Const, Tpt, Zs, cmap='RdBu', shading='flat')
plt.colorbar(plot)
```

```
tot = Zt[np.arange(0, Tpt.size), np.argmin(Zs, axis=1)]  # Ratio Sa/Sb
                                        at minimum deviation from (2$\pi$)^2
plt.scatter(Tpt, tot)
```

Python code for the AMRO simulations

```
# phi is a set of FS angles with a step of 1 degree from -360 to 360
# k is the Fermi surface wave vector as a function of angle phi
# Function to calculate AMRO. Theta is the polar angle.
# Integration is performed over the FS with a 1 degree step. phi_B is
                                        the azimuthal angle in degrees (must
                                         be integer).
def integr(wct, phi_B):
    Theta = np.linspace(np.pi/40, np.pi*0.4, 100)
    xp = np.linspace(0, 359, 360).astype(int)
    int_theta = []
    for theta in Theta:
        intS = 0
        for x in range(360):
            # For a given theta, calculate the conductivity over the FS
            kphi = k[phi_round[np.divmod(x - phi_B, 360)[1]]] * np.cos(
                                                phi_a[np.divmod(x, 360)[
                                                1]])
            kphip = k[phi_round[np.divmod(x - xp - phi_B, 360)[1]]] * np
                                                .cos(phi_a[np.divmod(x -
                                                 xp, 360)[1]])
            ds = 1 * 1/180 * np.pi * np.cos(d * (kphi - kphip) * np.tan(
                                                theta)) * np.exp(-xp * 1
                                                /180 * np.pi / wct / np.
                                                cos(theta))
            intS += ds.sum()
        int_theta.append(intS / wct / np.cos(theta) / (1 - np.exp(-2 *
                                            np.pi / wct / np.cos(theta))
                                            ))
    return Theta, int_theta
wct = 2
Int_phi = []
for i in range(10):  # 10*i is the azimuthal angle phi for calculation
    the, int_the = integr(wct, 10 * i)
    print(10 * i)
    Int_phi.append(int_the[0] / np.asarray(int_the))
    plt.plot(the / np.pi * 180, int_the[0] / np.asarray(int_the))
plt.show()
```

Bibliography

[1] L. D. Landau, "*The Theory of a Fermi Liquid*", JETP **3**, 920 (1957).

[2] W. J. de Haas and J. P. van Alphen, "*The dependence of the susceptibility of diamagnetic metals upon the field.*", Proc. KNAW **34**, 454 (1932).

[3] L. W. Schubnikow and W. J. de Haas, "*Magnetische Widerstandsvergrosserung in Einkristallen von Wismut bei tiefen Temperaturen*", Proc. KNAW **33**, 130 (1930).

[4] I. M. Lifshitz and A. Kosevich, "*Theory of Magnetic Susceptibility in Metals at Low Temperatures*", JETP **29**, 790 (1955).

[5] L. Onsager, "*Interpretation of the de Haas-van Alphen effect*", Philos. Mag. **43**, 1006 (1952).

[6] J. Wosnitza, "*Fermi Surfaces of Low-Dimensional Organic Metals and Superconductors*", Vol. 134, Springer Tracts in Modern Physics, Springer Verlag, Berlin Heidelberg, 1996.

[7] M. V. Kartsovnik, "*High magnetic fields: a tool for studying electronic properties of layered organic metals.*", Chem. Rev. **104**, 5737 (2004).

[8] S. E. Sebastian and C. Proust, "*Quantum Oscillations in Hole-Doped Cuprates*", Annu. Rev. Condens. Matter Phys. **6**, 411 (2015).

[9] T. Helm, M. V. Kartsovnik, C. Proust, B. Vignolle, C. Putzke, E. Kampert, I. Sheikin, E.-S. Choi, J. S. Brooks, N. Bittner, W. Biberacher, A. Erb, J. Wosnitza, and R. Gross, "*Correlation between Fermi surface transformations and superconductivity in the electron-doped high-T_c superconductor $Nd_{2-x}Ce_xCuO_4$*", Phys. Rev. B **92**, 094501 (2015).

[10] M. K. Chan, N. Harrison, R. D. McDonald, B. J. Ramshaw, K. A. Modic, N. Barišić, and M. Greven, "*Single reconstructed Fermi surface pocket in an underdoped single-layer cuprate superconductor*", Nat. Comm. **7**, 12244 (2016).

[11] A. Carrington, "*Quantum oscillation studies of the Fermi surface of iron-pnictide superconductors*", Rep. Prog. Phys. **74**, 124507 (2011).

[12] A. I. Coldea and M. D. Watson, "*The Key Ingredients of the Electronic Structure of FeSe*", Annu. Rev. Condens. Matter Phys. **9**, 125 (2018).

[13] T. Terashima, H. T. Hirose, D. Graf, Y. Ma, G. Mu, T. Hu, K. Suzuki, S. Uji, and H. Ikeda, "*Fermi Surface with Dirac Fermions in CaFeAsF Determined via Quantum Oscillation Measurements*", Phys. Rev. X **8**, 011014 (2018).

[14]P. J. W. Moll, N. L. Nair, T. Helm, A. C. Potter, I. Kimchi, A. Vishwanath, and J. G. Analytis, "*Transport evidence for Fermi-arc-mediated chirality transfer in the Dirac semimetal Cd_3As_2*", Nat. **535**, 266 (2016).

[15]S. Pezzini, M. R. van Delft, L. M. Schoop, B. V. Lotsch, A. Carrington, M. I. Katsnelson, N. E. Hussey, and S. Wiedmann, "*Unconventional mass enhancement around the Dirac nodal loop in ZrSiS*", Nat. Phys. **14**, 178 (2017).

[16]P. Wang, G. Yu, Y. Jia, M. Onyszczak, F. A. Cevallos, S. Lei, S. Klemenz, K. Watanabe, T. Taniguchi, R. J. Cava, L. M. Schoop, and S. Wu, "*Landau quantization and highly mobile fermions in an insulator*", Nat. **589**, 225 (2021).

[17]L. Jiao, Y. Chen, Y. Kohama, D. Graf, E. D. Bauer, J. Singleton, J.-X. Zhu, Z. Weng, G. Pang, T. Shang, J. Zhang, H.-O. Lee, T. Park, M. Jaime, J. D. Thompson, F. Steglich, Q. Si, and H. Q. Yuan, "*Fermi surface reconstruction and multiple quantum phase transitions in the antiferromagnet $CeRhIn_5$*", PNAS **112**, 673 (2015).

[18]L. Xiang, E. Gati, S. L. Bud'ko, R. A. Ribeiro, A. Ata, U. Tutsch, M. Lang, and P. C. Canfield, "*Characterization of the pressure coefficient of manganin and temperature evolution of pressure in piston-cylinder cells*", Rev. Sci. Instrum. **91**, 095103 (2020).

[19]G. Bastien, D. Aoki, G. Lapertot, J.-P. Brison, J. Flouquet, and G. Knebel, "*Fermi-surface selective determination of the g-factor anisotropy in* URu_2Si_2", Phys. Rev. B **99**, 165138 (2019).

[20]N. F. Mott and R. Peierls, "*Discussion of the paper by de Boer and Verwey.*", Proc. Phys. Soc. **49**, 72 (1937).

[21]J. Hubbard, "*Electron correlations in narrow energy bands*", Proc. R. Soc. Lond. A **276**, 238 (1963).

[22]A. Georges, G. Kotliar, W. Krauth, and M. J. Rozenberg, "*Dynamical mean-field theory of strongly correlated fermion systems and the limit of infinite dimensions*", Rev. Mod. Phys. **68**, 13 (1996).

[23]P. Anderson, "*Theory of dirty superconductors*", J. Phys. Chem. Solids **11**, 26 (1959).

[24]V. Dobrosavljevic and G. Kotliar, "*Mean Field Theory of the Mott-Anderson Transition*", Phys. Rev. Lett. **78**, 3943 (1997).

[25]W. A. Little, "*Possibility of Synthesizing an Organic Superconductor*", Phys. Rev. **134**, A1416 (1964).

[26]D. Jerome, A. Mazaud, M. Ribault, and K. Bechgaard, "*Superconductivity in a synthetic organic conductor $(TMTSF)_2PF_6$*", J. Phys. Lett. **41**, 95 (1980).

[27]M. Kano, M. Hedo, Y. Uwatoko, M. Miyashita, and H. Taniguchi., "*Pressure Induced Superconductivity of Organic Materials κ-$(BEDT\text{-}TTF)_2ICl_2$ and Development of Extremely High Pressure Cell*", Rev. High Press. Sci. Technol. **15**, 333 (2005).

[28]H. Kobayashi, H. Cui, and A. Kobayashi, "*Organic Metals and Superconductors Based on BETS*", Chem. Rev. **104**, 5265 (2004).

[29]A. Ardavan, S. Brown, S. Kagoshima, K. Kanoda, K. Kuroki, H. Mori, M. Ogata, S. Uji, and J. Wosnitza, "*Recent Topics of Organic Superconductors*", J. Phys. Soc. Jpn. **81**, 011004 (2012).

[30]K. Kanoda and R. Kato, "*Mott Physics in Organic Conductors with Triangular Lattices*", Annu. Rev. Condens. Matter Phys. **2**, 167 (2011).

[31]R. Gross and A. Marx, "*Festkörperphysik*", De Gruyter Oldenbourg, Berlin, Boston, 2022.

[32]D. Shoenberg, "*Magnetic Oscillations in Metals*", Cambridge University Press, Cambridge, 1984.

[33]A. A. Abrikosov, I. Dzyaloshinskii, and L. P. Gorkov, "*Methods of quantum field theory in statistical physics*", Dover, New York, NY, 1975.

[34]T. Ishiguro, K. Yamaji, and G. Saito, "*Organic Superconductors.*", 2st edn., Vol. 88, Springer Series in Solid-State Sciences, Springer Verlag, Berlin Heidelberg, 1998.

[35]N. Toyota, M. Lang, and J. Müller, "*Low-Dimensional Molecular Metals*", 1st, Vol. 154, Springer Series in Solid-State Sciences, Springer Verlag, Berlin Heidelberg, 2007.

[36]A. B. Pippard., "*The Dynamics of Conduction Electrons*", Gordon and Breach, 1965.

[37]R. B. Dingle and W. L. Bragg, "*Some magnetic properties of metals II. The influence of collisions on the magnetic behaviour of large systems*", Proc. R. Soc. A. **211**, 517 (1952).

[38]J. Wosnitza, G. W. Crabtree, H. H. Wang, U. Geiser, J. M. Williams, and K. D. Carlson, "*de Haas-van Alphen studies of the organic superconductors α-$(ET)_2(NH_4)Hg(SCN)_4$ and κ-$(ET)_2Cu(NCS)_2$*", Phys. Rev. B **45**, 3018 (1992).

[39]F. A. Meyer, E. Steep, W. Biberacher, P. Christ, A. Lerf, A. G. M. Jansen, W. Joss, P. Wyder, and K. Andres, "*High-Field de Haas-Van Alphen Studies of κ-(BEDT-$TTF)_2Cu(NCS)_2$*", EPL **32**, 681 (1995).

[40]T. Sasaki and T. Fukase, "*Spin splitting at the high-magnetic-field phase transition of the organic conductor α-$(BEDT\text{-}TTF)_2KHg(SCN)_4$*", Phys. Rev. B **59**, 13872 (1999).

[41]J. Wosnitza, V. M. Gvozdikov, J. Hagel, O. Ignatchik, B. Bergk, P. J. Meeson, J. A. Schlueter, H. Davis, R. W. Winter, and G. L. Gard, "*Spin-zero anomaly in the magnetic quantum oscillations of a two-dimensional metal*", New J. Phys. **10**, 083032 (2008).

[42]S. Oberbauer, "*Effective cyclotron mass and electronic properties of κ-phase organic superconductors in the vicinity of the Mott-insulator transition*", Diplomarbeit (Technische Universität München, 2017).

[43]M. V. Kartsovnik, P. A. Kononovich, V. N. Laukhin, and I. F. Shchegolev, "*Anisotropy of magnetoresistance and the Shubnikov-de Haas oscillations in the organic metal β-$(ET)_2IBr_2$*", JETP **48**, 498 (1988).

[44]K. Kajita, Y. Nishio, T. Takahashi, W. Sasaki, R. Kato, H. Kobayashi, A. Kobayashi, and Y. Iye, "*A new type oscillatory phenomenon in the magnetotransport of θ-(BEDT-TTF)$_2I_3$*", Solid State Commun. **70**, 1189 (1989).

[45]M. V. Kartsovnik, P. A. Kononovich, V. N. Laukhin, S. Pesotskii, and I. F. Shchegolev, "*Galvanomagnetic properties and the Fermi surface of the organic superconductor β-(ET)$_2IBr_2$*", JETP **70**, 735 (1990).

[46]J. Wosnitza, G. Crabtree, J. Williams, H. Wang, K. Carlson, and U. Geiser, "*De Haas - van Alphen studies and Fermi surface properties of organic superconductors (ET)$_2X$*", Synth. Met. **56**, 2891 (1993).

[47]V. G. Peschanskii, "*Galvanomagnetic phenomena in organic layered conductors*", JETP **94**, 1035 (2002).

[48]K. Yamaji, "*On the Angle Dependence of the Magnetoresistance in Quasi-Two-Dimensional Organic Superconductors*", J. Phys. Soc. Jpn **58**, 1520 (1989).

[49]T. Helm, "*Electronic Properties of Electron-Doped Cuprate Superconductors Probed by High-Field Magnetotransport*", PhD thesis (Technische Universität München, 2013).

[50]N. Hanasaki, S. Kagoshima, T. Hasegawa, T. Osada, and N. Miura, "*Contribution of small closed orbits to magnetoresistance in quasi-two-dimensional conductors*", Phys. Rev. B **57**, 1336 (1998).

[51]M.V. Kartsovnik, V.N. Laukhin, S.I. Pesotskii, I.F. Schegolev, and V.M. Yakovenko, "*Angular magnetoresistance oscillations and the shape of the Fermi surface in β(ET)$_2IBr_2$*", J. Phys. I France **2**, 89 (1992).

[52]E. Ohmichi, H. Ito, T. Ishiguro, T. Komatsu, and G. Saito, "*Angle-Dependent Magnetoresistance in the Organic Superconductor κ-(BEDT-TTF)$_2Cu_2(CN)_3$ under Pressure*", J. Phys. Soc. Jpn. **66**, 310 (1997).

[53]P. D. Grigoriev, M. V. Kartsovnik, W. Biberacher, N. D. Kushch, and P. Wyder, "*Anomaluos beating phase of the oscillating interlayer magnoresistance in layered metals*", Phys. Rev. B **65**, 060403 (2002).

[54]P. D. Grigoriev, "*Theory of the Shubnikov-de Haas effect in quasi-two-dimensional metals*", Phys. Rev. B **67**, 144401 (2003).

[55]I. F. Schegolev, P. A. Kononovich, V. N. Laukhin, and M. V. Kartsovnik, "*Electron Structure of Organic Metal β-(ET)$_2IBr_2$*", Phys. Scr. **1989**, 46 (1989).

[56]W. Kang, G. Montambaux, J. R. Cooper, D. Jérome, P. Batail, and C. Lenoir, "*Observation of giant magnetoresistance oscillations in the high-T_c phase of the two-dimensional organic conductor β-(BEDT-TTF)$_2$I$_3$*", Phys. Rev. Lett. **62**, 2559 (1989).

[57]M. Schiller, W. Schmidt, E. Balthes, D. Schweitzer, H.-J. Koo, M. H. Whangbo, I. Heinen, T. Klausa, P. Kircher, and W. Strunz, "*Investigations of the Fermi surface of a new organic metal: (BEDT-TTF)$_4$[Ni(dto)$_2$]*", EPL **51**, 82 (2000).

[58]C. Bergemann, S. R. Julian, A. P. Mackenzie, S. NishiZaki, and Y. Maeno, "*Detailed Topography of the Fermi Surface of* Sr_2RuO_4", Phys. Rev. Lett. **84**, 2662 (2000).

[59]P. Fulde, "*Correlated Electrons in Quantum Matter*", World Scientific, 2012.

[60]P. Nozieres and D. Pines, "*The Theory of Quantum Liquids*", Perseus Books, 1999.

[61]G. Baym and C. Pethick, "*Landau Fermi-Liquid Theory*", John Wiley and Sons, Ltd, 1991.

[62]M. M. Radonjic, D. Tanaskovic, V. Dobrosavljevic, K. Haule, and G. Kotliar, "*Wigner-Mott scaling of transport near the two-dimensional metal-insulator transition*", Phys. Rev. B **85**, 085133 (2012).

[63]H. Terletska, J. Vučičević, D. Tanasković, and V. Dobrosavljević, "*Quantum Critical Transport near the Mott Transition*", Phys. Rev. Lett. **107**, 026401 (2011).

[64]N. E. Hussey, K. Takenaka, and H. Takagi, "*Universality of the Mott-Ioffe-Regel limit in metals*", Phil. Mag. **84**, 2847 (2004).

[65]V. Dobrosavljevic and D. Tanaskovic, "*Chapter 1 Wigner-Mott Quantum Criticality: From 2D-MIT to 3He and Mott Organics*", in , May 2017, pp. 1–46.

[66]R. V. Mishmash, I. González, R. G. Melko, O. I. Motrunich, and M. P. A. Fisher, "*Continuous Mott transition between a metal and a quantum spin liquid*", Phys. Rev. B **91**, 235140 (2015).

[67]T. Senthil, "*Theory of a continuous Mott transition in two dimensions*", Phys. Rev. B **78**, 045109 (2008).

[68]W. Witczak-Krempa, P. Ghaemi, T. Senthil, and Y. B. Kim, "*Universal transport near a quantum critical Mott transition in two dimensions*", Phys. Rev. B **86**, 245102 (2012).

[69]T. Furukawa, K. Kobashi, Y. Kurosaki, K. Miyagawa, and K. Kanoda, "*Quasi-continuous transition from a Fermi liquid to a spin liquid in κ-(ET)$_2$Cu$_2$(CN)$_3$*", Nat. Commun. **9**, 307 (2018).

[70]K. Kadowaki and S. Woods, "*Universal relationship of the resistivity and specific heat in heavy-Fermion compounds*", Solid State Commun. **58**, 507 (1986).

[71]A. Hewson, "*The Kondo Problem to Heavy Fermions*", Cambridge University Press, 1993.

[72]A. Jacko, J. Fjarestad, and B. Powell, "*A unified explanation of the Kadowaki-Woods ratio in strongly correlated metals.*", Nat. Phys. **5**, 422 (2009).

[73]N. F. Mott, "*The Basis of the Electron Theory of Metals, with Special Reference to the Transition Metals*", Proc. Phys. Soc. A **62**, 416 (1949).

[74]P. W. Anderson, "*New Approach to the Theory of Superexchange Interactions*", Phys. Rev. **115**, 2 (1959).

[75]J. Kanamori, "*Electron Correlation and Ferromagnetism of Transition Metals*", Prog. Theor. Phys. **30**, 275 (1963).

[76]F. Gebhard, "*The Mott Metal-Insulator Transition*", Springer Tracts in Modern Physics, Springer Berlin Heidelberg, Berlin, Heidelberg, 2000.

[77]W. F. Brinkman and T. M. Rice, "*Application of Gutzwiller's Variational Method to the Metal-Insulator Transition*", Phys. Rev. B **2**, 4302 (1970).

[78]A. Georges, S. Florens, and T. Costi, "*The Mott transition: Unconventional transport, spectral weight transfers, and critical behaviour*", J. Phys. IV France **114**, 165 (2004).

[79]A. Georges and G. Kotliar, "*Hubbard model in infinite dimensions*", Phys. Rev. B **45**, 6479 (1992).

[80]H. Park, K. Haule, and G. Kotliar, "*Cluster Dynamical Mean Field Theory of the Mott Transition*", Phys. Rev. Lett. **101**, 186403 (2008).

[81]E. G. C. P. van Loon, M. I. Katsnelson, and H. Hafermann, "*Second-order dual fermion approach to the Mott transition in the two-dimensional Hubbard model*", Phys. Rev. B **98**, 155117 (2018).

[82]M. Balzer, B. Kyung, D. Sénéchal, A.-M. S. Tremblay, and M. Potthoff, "*First-order Mott transition at zero temperature in two dimensions: Variational plaquette study*", EPL **85**, 17002 (2009).

[83]T. Schäfer, F. Geles, D. Rost, G. Rohringer, E. Arrigoni, K. Held, N. Blümer, M. Aichhorn, and A. Toschi, "*Fate of the false Mott-Hubbard transition in two dimensions*", Phys. Rev. B **91**, 125109 (2015).

[84]G. Rohringer, H. Hafermann, A. Toschi, A. A. Katanin, A. E. Antipov, M. I. Katsnelson, A. I. Lichtenstein, A. N. Rubtsov, and K. Held, "*Diagrammatic routes to nonlocal correlations beyond dynamical mean field theory*", Rev. Mod. Phys. **90**, 025003 (2018).

[85]M. M. Wysoki ński and M. Fabrizio, "*Mott physics beyond the Brinkman-Rice scenario*", Phys. Rev. B **95**, 161106 (2017).

[86]P. W. Anderson, "*Absence of Diffusion in Certain Random Lattices*", Phys. Rev. **109**, 1492 (1958).

[87]H. Shinaoka and M. Imada, "*Single-Particle Excitations under Coexisting Electron Correlation and Disorder: A Numerical Study of the Anderson-Hubbard Model*", J. Phys. Soc. Jpn. **78**, 094708 (2009).

[88]K. Byczuk, W. Hofstetter, and D. Vollhardt, "*Mott-Hubbard Transition versus Anderson Localization in Correlated Electron Systems with Disorder*", Phys. Rev. Lett. **94**, 056404 (2005).

[89]U. Geiser, A. J. Schults, H. H. Wang, D. M. Watkins, D. L. Stupka, J. M. Williams, J. Schirber, D. Overmyer, D. Jung, J. Novoa, and M.-H. Whangbo, "*Strain index, lattice softness and superconductivity of organic donor-molecule salts: Crystal and electronic structures of three isostructural salts κ-(BEDT- TTF)$_2$Cu[N(CN)$_2$]X (X=Cl, Br, I)*", Phys. C **174**, 475 (1991).

[90]M. Watanabe, Y. Nogami, K. Oshima, H. Ito, T. Ishiguro, and G. Saito, "*Low temperature superstructure and transfer integrals in κ -(BEDT-TTF)$_2$Cu[N(CN)$_2$]X: X = Cl, Br*", Synth. Met. **103**, 1909 (1999).

[91]T. Komatsu, N. Matsukawa, T. Inoue, and G. Saito, "*Realization of Superconductivity at Ambient Pressure by Band-Filling Control in κ-(BEDT-TTF)$_2$Cu$_2$(CN)$_3$*", J. Phys. Soc. Jpn. **65**, 1340 (1996).

[92]A. J. Schultz, M. A. Beno, U. Geiser, H. Wang, A. M. Kini, J. M. Williams, and M.-H. Whangbo, "*Single-crystal X-ray and neutron diffraction investigations of the temperature dependence of the structure of the T_c = 10 K organic superconductor κ-(ET)$_2$Cu(NCS)$_2$*", J. Solid State Chem. **94**, 352 (1991).

[93]A. J. Schultz, H. H. Wang, J. M. Williams, L. W. Finger, R. M. Hazen, C. Rovira, and M.-H. Whangbo, "*X-ray diffraction and electronic band structure study of the organic superconductor κ-(ET)$_2$Cu[N(CN)$_2$]*", Phys. C **234**, 300 (1994).

[94]T. Mori, H. Mori, and S. Tanaka, "*Structural Genealogy of BEDT-TTF-Based Organic Conductors II. Inclined Molecules: θ, α, and κ Phases*", Bull. Chem. Soc. Jpn. **72**, 179 (2003).

[95]A. Fortunelli and A. Painelli, "*On the ab initio evaluation of Hubbard parameters. II. The κ-(BEDT-TTF)$_2$Cu[N(CN)$_2$]Br crystal*", J. Chem. Phys. **106**, 8051 (1997).

[96]H. C. Kandpal, I. Opahle, Y.-Z. Zhang, H. O. Jeschke, and R. Valentí, "*Revision of Model Parameters for κ-Type Charge Transfer Salts: An Ab Initio Study*", Phys. Rev. Lett. **103**, 067004 (2009).

[97]K. Nakamura, Y. Yoshimoto, T. Kosugi, R. Arita, and M. Imada, "*Ab initio Derivation of Low-Energy Model for κ-ET Type Organic Conductors*", J. Phys. Soc. Jpn. **78**, 083710 (2009).

[98]K. Nakamura, Y. Yoshimoto, and M. Imada, "*Ab initio two-dimensional multiband low-energy models of EtMe$_3$Sb[Pd(dmit)$_2$]$_2$ and κ-(BEDT-TTF)$_2$Cu(NCS)$_2$ with comparisons to single-band models*", Phys. Rev. B **86**, 205117 (2012).

[99]E. P. Scriven and B. J. Powell, "*Geometrical Frustration in the Spin Liquid β'-*$Me_3EtSb[Pd(dmit)_2]_2$ *and the Valence-Bond Solid* $Me_3EtP[Pd(dmit)_2]_2$", Phys. Rev. Lett. **109**, 097206 (2012).

[100]T. Koretsune and C. Hotta, "*Evaluating model parameters of the κ- and β'-type Mott insulating organic solids*", Phys. Rev. B **89**, 045102 (2014).

[101]K. Oshima, T. Mori, H. Inokuchi, H. Urayama, H. Yamochi, and G. Saito, "*Shubnikov-de Haas effect and the fermi surface in an ambient-pressure organic superconductor (BEDT-TTF)$_2$Cu(NCS)$_2$*", Phys. Rev. B **38**, 938 (1988).

[102]M. V. Kartsovnik, W. Biberacher, K. Andres, and N. D. Kushch, "*Shubnikov-de Haas effect in the organic superconductor κ-(BEDT-TTF)$_2$Cu[N(CN)$_2$]CI under pressure*", JETP Lett. **62**, 890 (1995).

[103]H. Weiss, M. V. Kartsovnik, W. Biberacher, E. Steep, E. Balthes, A. G. M. Jansen, K. Andres, and N. D. Kushch, "*Magnetotransport studies of the Fermi surface in the organic superconductor κ-(BEDT-TTF)$_2$Cu[N(CN)$_2$]Br*", Phys. Rev. B **59**, 12370 (1999).

[104]E. Ohmichi, H. Ito, T. Ishiguro, G. Saito, and T. Komatsu, "*Shubnikov-de Haas oscillation with unusual angle dependence in the organic superconductor* $\kappa-(\mathrm{BEDT-TTF})_2\mathrm{Cu}_2(\mathrm{CN})_3$", Phys. Rev. B **57**, 7481 (1998).

[105]P. A. Goddard, S. J. Blundell, J. Singleton, R. D. McDonald, A. Ardavan, A. Narduzzo, J. A. Schlueter, A. M. Kini, and T. Sasaki, "*Angle-dependent magnetoresistance of the layered organic superconductor* $\kappa-(\mathrm{ET})_2\mathrm{Cu}(\mathrm{NCS})_2$ *: Simulation and experiment*", Phys. Rev. B **69**, 174509 (2004).

[106]J. Singleton, "*Studies of quasi-two-dimensional organic conductors based on BEDT-TTF using high magnetic fields*", Rep. Prog. Phys. **63**, 1111 (2000).

[107]A. Audouard, J.-Y. Fortin, D. Vignolles, V. N. Laukhin, N. D. Kushch, and E. B. Yagubskii, "*New insights on frequency combinations and 'forbidden frequencies' in the de Haas-van Alphen spectrum of κ-(ET)$_2$Cu(SCN)$_2$*", J. Phys.: Condens. Matter **28**, 275702 (2016).

[108]Y. Yamauchi, M. V. Kartsovnik, T. Ishiguro, M. Kubota, and G. Saito, "*Angle-Dependent Magnetoresistance and Shubnikov-de Haas Oscillations in the Organic Superconductor κ-(BEDT-TTF)$_2$Cu[N(CN)$_2$]Cl under Pressure*", J. Phys. Soc. Jpn **65**, 354 (1996).

[109]H. Weiss, M. V. Kartsovnik, W. Biberacher, E. Balthes, A. G. M. Jansen, and N. D. Kushch, "*Angle-dependent magnetoquantum oscillations in κ-(BEDT-TTF)$_2$Cu[N(CN)$_2$]Br*", Phys. Rev. B **60**, R16259 (1999).

[110]S. Oberbauer, S. Erkenov, W. Biberacher, N. D. Kushch, R. Gross, and M. V. Kartsovnik, "*Coherent heavy charge carriers in an organic conductor near the bandwidth-controlled Mott transition*", Phys. Rev. B **107**, 075139 (2023).

[111]T. Sasaki, H. Sato, and N. Toyota, "*On the magnetic breakdown oscillations in organic superconductor κ-(BEDT-TTF)$_2$Cu(NCS)$_2$*", Phys. C **185**, 2687 (1991).

[112]S. Lefebvre, P. Wzietek, S. Brown, C. Bourbonnais, D. Jérome, C. Mézière, M. Fourmigué, and P. Batail, "*Mott Transition, Antiferromagnetism, and Unconventional Superconductivity in Layered Organic Superconductors*", Phys. Rev. Lett. **85**, 5420 (2000).

[113]F. Kagawa, T. Itou, K. Miyagawa, and K. Kanoda, "*Magnetic-Field-Induced Mott Transition in a Quasi-Two-Dimensional Organic Conductor*", Phys. Rev. Lett. **93**, 127001 (2004).

[114]B. J. Powell and R. H. McKenzie, "*Strong electronic correlations in superconducting organic charge transfer salts*", J. Phys.: Condens. Matter **18**, R827 (2006).

[115]K. Riedl, E. Gati, and R. Valenti, "*Ingredients for Generalized Models of κ-Phase Organic Charge-Transfer Salts: A Review*", Cryst. **12** (2022).

[116]Y. Shimizu, K. Miyagawa, K. Kanoda, M. Maesato, and G. Saito, "*Spin Liquid State in an Organic Mott Insulator with a Triangular Lattice*", Phys. Rev. Lett. **91**, 107001 (2003).

[117]A. Pustogow, "*Thirty-Year Anniversary of κ-(BEDT-TTF)$_2$Cu$_2$(CN)$_3$: Reconciling the Spin Gap in a Spin-Liquid Candidate*", Solids **3**, 93 (2022).

[118]Y. Shimizu, H. Akimoto, H. Tsujii, A. Tajima, and R. Kato, "*Mott Transition in a Valence-Bond Solid Insulator with a Triangular Lattice*", Phys. Rev. Lett. **99**, 256403 (2007).

[119]Y. Shimizu, T. Hiramatsu, M. Maesato, A. Otsuka, H. Yamochi, A. Ono, M. Itoh, M. Yoshida, M. Takigawa, Y. Yoshida, and G. Saito, "*Pressure-Tuned Exchange Coupling of a Quantum Spin Liquid in the Molecular Triangular Lattice κ-$(ET)_2Ag_2(CN)_3$*", Phys. Rev. Lett. **117**, 107203 (2016).

[120]M. Shimozawa, K. Hashimoto, A. Ueda, Y. Suzuki, K. Sugii, S. Yamada, Y. Imai, R. Kobayashi, K. Itoh, S. Iguchi, M. Naka, S. Ishihara, H. Mori, T. Sasaki, and M. Yamashita, "*Quantum-disordered state of magnetic and electric dipoles in an organic Mott system*", Nat. Comm. **8**, 1821 (2017).

[121]N. Hassan, S. Cunningham, M. Mourigal, E. I. Zhilyaeva, S. A. Torunova, R. N. Lyubovskaya, J. A. Schlueter, and N. Drichko, "*Evidence for a quantum dipole liquid state in an organic quasi-two-dimensional material*", Sci. **360**, 1101 (2018).

[122]M. Urai, K. Miyagawa, Y. Watanabe, E. I. Zhilyaeva, S. A. Torunova, R. N. Lyubovskaya, N. Drichko, and K. Kanoda, "*Anomalously field-susceptible spin clusters emerging in the electric-dipole liquid candidate κ-(ET)$_2$Hg(SCN)$_2$Br*", Sci. Adv. **8**, eabn1680 (2022).

[123]K. Semeniuk, H. Chang, J. Baglo, S. Friedemann, S. W. Tozer, W. A. Coniglio, M. B. Gamza, P. Reiss, P. Alireza, I. Leermakers, A. McCollam, A. D. Grockowiak, and F. M. Grosche, "*Truncated mass divergence in a Mott metal*", PNAS **120**, e2301456120 (2023).

[124]S. A. Carter, T. F. Rosenbaum, P. Metcalf, J. M. Honig, and J. Spalek, "*Mass enhancement and magnetic order at the Mott-Hubbard transition*", Phys. Rev. B **48**, 16841 (1993).

[125]B. J. Powell and R. H. McKenzie, "*Quantum frustration in organic Mott insulators: from spin liquids to unconventional superconductors*", Rep. Prog. Phys. **74**, 056501 (2011).

[126]T. Sasaki, N. Yoneyama, A. Suzuki, N. Kobayashi, Y. Ikemoto, and H. Kimura, "*Real Space Imaging of the Metal-Insulator Phase Separation in the Band Width Controlled Organic Mott System κ-(BEDT-TTF)$_2$Cu[N(CN)$_2$]Br*", J. Phys. Soc. Jpn. **74**, 2351 (2005).

[127]H. Taniguchi, K. Kanoda, and A. Kawamoto, "*Field switching of superconductor-insulator bistability in artificially tuned organics*", Phys. Rev. B **67**, 014510 (2003).

[128]T. Furukawa, K. Miyagawa, H. Taniguchi, R. Kato, and K. Kanoda, "*Quantum criticality of Mott transition in organic materials*", Nat. Phys. **11**, 221 (2015).

[129]M. Dressel and A. Pustogow, "*Electrodynamics of quantum spin liquids*", J. Phys.: Condens. Matter **30**, 203001 (2018).

[130]B. Lenz, S. R. Manmana, T. Pruschke, F. F. Assaad, and M. Raczkowski, "*Mott Quantum Criticality in the Anisotropic 2D Hubbard Model*", Phys. Rev. Lett. **116**, 086403 (2016).

[131]A. Wietek, R. Rossi, F. Šimkovic, M. Klett, P. Hansmann, M. Ferrero, E. M. Stoudenmire, T. Schäfer, and A. Georges, "*Mott Insulating States with Competing Orders in the Triangular Lattice Hubbard Model*", Phys. Rev. X **11**, 041013 (2021).

[132]K. Misumi, T. Kaneko, and Y. Ohta, "*Mott transition and magnetism of the triangular-lattice Hubbard model with next-nearest-neighbor hopping*", Phys. Rev. B **95**, 075124 (2017).

[133]T. Ohashi, T. Momoi, H. Tsunetsugu, and N. Kawakami, "*Finite Temperature Mott Transition in Hubbard Model on Anisotropic Triangular Lattice*", Phys. Rev. Lett. **100**, 076402 (2008).

[134]T. Watanabe, H. Yokoyama, Y. Tanaka, and J.-i. Inoue, "*Superconductivity and a Mott Transition in a Hubbard Model on an Anisotropic Triangular Lattice*", J. Phys. Soc. Jpn. **75**, 074707 (2006).

[135]B. J. Powell and R. H. McKenzie, "*Half-Filled Layered Organic Superconductors and the Resonating-Valence-Bond Theory of the Hubbard-Heisenberg Model*", Phys. Rev. Lett. **94**, 047004 (2005).

[136]H. Morita, S. Watanabe, and M. Imada, "*Nonmagnetic Insulating States near the Mott Transitions on Lattices with Geometrical Frustration and Implications for κ-(ET)$_2$Cu$_2$(CN)$_3$*", J. Phys. Soc. Jpn. **71**, 2109 (2002).

[137]K. Matan, T. Ono, Y. Fukumoto, T. J. Sato, J. Yamaura, M. Yano, K. Morita, and H. Tanaka, "*Pinwheel valence-bond solid and triplet excitations in the two-dimensional deformed kagome lattice*", Nat. Phys. **6**, 865 (2010).

[138]Y. Shimizu, K. Miyagawa, K. Kanoda, M. Maesato, and G. Saito, "*Emergence of inhomogeneous moments from spin liquid in the triangular-lattice Mott insulator* κ-$(\mathrm{ET})_2\mathrm{Cu}_2(\mathrm{CN})_3$", Phys. Rev. B **73**, 140407 (2006).

[139]R. S. Manna, M. de Souza, A. Brühl, J. A. Schlueter, and M. Lang, "*Lattice Effects and Entropy Release at the Low-Temperature Phase Transition in the Spin-Liquid Candidate κ-(BEDT-TTF)$_2$Cu$_2$(CN)$_3$*", Phys. Rev. Lett. **104**, 016403 (2010).

[140]S.-S. Lee and P. A. Lee, "*U(1) Gauge Theory of the Hubbard Model: Spin Liquid States and Possible Application to κ-(BEDT-TTF)$_2$Cu$_2$(CN)$_3$*", Phys. Rev. Lett. **95**, 036403 (2005).

[141]H. Ito, G. Saito, and T. Ishiguro, "*Antiferromagnetism and superconductivity of κ-(BEDT-TTF)$_2$Cu[N(CN)$_2$]X (X = Br, Cl)*", J. Phys. Chem. Solids **62**, 109 (2001).

[142]K. Miyagawa, K. Kanoda, and A. Kawamoto, "*NMR Studies on Two-Dimensional Molecular Conductors and Superconductors: Mott Transition in κ-(BEDT-TTF)$_2$X*", Chem. Rev. **104**, 5635 (2004).

[143]S. Yamashita, Y. Nakazawa, M. Oguni, Y. Oshima, H. Nojiri, Y. Shimizu, K. Miyagawa, and K. Kanoda, "*Thermodynamic properties of a spin-1/2 spin-liquid state in a κ-type organic salt*", Nat. Phys. **4**, 459 (2008).

[144]E. Yesil, S. Imajo, S. Yamashita, H. Akutsu, Y. Saito, A. Pustogow, A. Kawamoto, and Y. Nakazawa, "*Thermodynamic properties of the Mott insulator-metal transition in a triangular lattice system without magnetic order*", Phys. Rev. B **107**, 045133 (2023).

[145]B. Miksch, A. Pustogow, M. J. Rahim, A. A. Bardin, K. Kanoda, J. A. Schlueter, R. Hubner, M. Scheffler, and M. Dressel, "*Gapped magnetic ground state in quantum spin liquid candidate κ-(BEDT-TTF)$_2$Cu$_2$(CN)$_3$*", Sci. **372**, 276 (2021).

[146]A. Kawamoto, K. Miyagawa, and K. Kanoda, "*Deuterated κ-(BEDT-TTF)$_2$Cu[N(CN)$_2$]Br: A system on the borderof the superconductor-magnetic-insulator transition*", Phys. Rev. B **55**, 14140 (1997).

[147]J. Müller, B. Hartmann, R. Rommel, J. Brandenburg, S. M. Winter, and J. A. Schlueter, "*Origin of the glass-like dynamics in molecular metals κ-(BEDT-TTF)$_2$X: implications from fluctuation spectroscopy and ab initio calculations*", New J. Phys. **17**, 083057 (2015).

[148]D. Guterding, R. Valentí, and H. O. Jeschke, "*Influence of molecular conformations on the electronic structure of organic charge transfer salts*", Phys. Rev. B **92**, 081109 (2015).

[149]B. Hartmann, J. Müller, and T. Sasaki, "*Mott metal-insulator transition induced by utilizing a glasslike structural ordering in low-dimensional molecular conductors*", Phys. Rev. B **90**, 195150 (2014).

[150]K. Saito, H. Akutsu, and M. Sorai, "*Glass transition in the organic superconductor with the highest T_c under ambient pressure, κ-(ET)$_2$Cu[N(CN)$_2$]Br*", Solid State Commun. **111**, 471 (1999).

[151]H. Akutsu, K. Saito, and M. Sorai, "*Phase behavior of the organic superconductors κ-(BEDT-TTF)$_2$Cu[N(CN)$_2$]X (X=Br and Cl) studied by ac calorimetry*", Phys. Rev. B **61**, 4346 (2000).

[152]J. Müller, M. Lang, F. Steglich, and J. Schlueter, "*Glass-like transition in κ-(ET)$_2$Cu[N(CN)$_2$] Br at $T_g \sim 75$ K - implications for the superconducting ground-state properties*", J. Phys. IV France **114**, 341 (2004).

[153]X. Su, F. Zuo, J. A. Schlueter, M. E. Kelly, and J. M. Williams, "*Structural disorder and its effect on the superconducting transition temperature in organic superconductor κ-(BEDT-TTF)$_2$Cu[N(CN)$_2$]Br*", Phys. Rev. B **57**, R14056 (1998).

[154]J. Müller, J. Brandenburg, and J. A. Schlueter, "*$1/f$ noise in the quasi-two-dimensional organic conductor κ-(BEDT-TTF)$_2$Cu[N(CN)$_2$]Cl*", Phys. Rev. B **79**, 214521 (2009).

[155]J. Brandenburg, J. Müller, and J. A. Schlueter, "*Sudden slowing down of charge carrier dynamics at the Mott metal-insulator transition in κ-(D$_8$-BEDT-TTF)$_2$Cu[N(CN)$_2$]Br*", New J. Phys. **14**, 023033 (2012).

[156]B. J. Powell and R. H. McKenzie, "*Dependence of the superconducting transition temperature of organic molecular crystals on intrinsically nonmagnetic disorder: A signature of either unconventional superconductivity or the atypical formation of magnetic moments*", Phys. Rev. B **69**, 024519 (2004).

[157]J. Müller, M. Lang, F. Steglich, J. A. Schlueter, A. M. Kini, and T. Sasaki, "*Evidence for structural and electronic instabilities at intermediate temperatures in $\kappa-(\mathrm{BEDT-TTF})_2X$ for $X = \mathrm{Cu[N(CN)_2]Cl}$, $\mathrm{Cu[N(CN)_2]Br}$ and $\mathrm{Cu(NCS)_2}$: Implications for the phase diagram of these quasi-two-dimensional organic superconductors*", Phys. Rev. B **65**, 144521 (2002).

[158]A. U. B. Wolter, R. Feyerherm, E. Dudzik, S. Sullow, C. Strack, M. Lang, and D. Schweitzer, "*Determining ethylene group disorder levels in κ-(BEDT-TTF)$_2$Cu[N(CN)$_2$]Br*", Phys. Rev. B **75**, 104512 (2007).

[159]J. Müller, B. Hartmann, and T. Sasaki, "*Fine-tuning the Mott metal-insulator transition and critical charge carrier dynamics in molecular conductors*", Philos. Mag. **97**, 3477 (2017).

[160]K. Sano, T. Sasaki, N. Yoneyama, and N. Kobayashi, "*Electron Localization near the Mott Transition in the Organic Superconductor* κ-$(\mathrm{BEDT\text{-}TTF})_2\mathrm{Cu}[\mathbf{N}(\mathrm{CN})_2]\mathrm{Br}$", Phys. Rev. Lett. **104**, 217003 (2010).

[161]T. Sasaki, "*Mott-Anderson Transition in Molecular Conductors: Influence of Randomness on Strongly Correlated Electrons in the κ-(BEDT-TTF)$_2$X System*", Cryst. **2**, 374 (2012).

[162]V. Dobrosavljevic, A. A. Pastor, and B. K. Nikolic, "*Typical medium theory of Anderson localization: A local order parameter approach to strong-disorder effects*", EPL **62**, 76 (2003).

[163]E. Gati, U. Tutsch, A. Naji, M. Garst, S. Koehler, H. Schubert, T. Sasaki, and M. Lang, "*Effects of Disorder on the Pressure-Induced Mott Transition in κ-(BEDT-TTF)$_2$Cu[N(CN)$_2$]Cl*", Cryst. **8**, 38 (2018).

[164]T. Sasaki, H. Oizumi, Y. Honda, N. Yoneyama, and N. Kobayashi, "*Suppression of Superconductivity by Nonmagnetic Disorder in Organic Superconductor κ-(BEDT-TTF)$_2$Cu(NCS)$_2$*", J. Phys. Soc. Jpn. **80**, 104703 (2011).

[165]J. G. Analytis, A. Ardavan, S. J. Blundell, R. L. Owen, E. F. Garman, C. Jeynes, and B. J. Powell, "*Effect of Irradiation-Induced Disorder on the Conductivity and Critical Temperature of the Organic Superconductor κ-*(BEDT-TTF)$_2$Cu(SCN)$_2$", Phys. Rev. Lett. **96**, 177002 (2006).

[166]S. Haddad, S. Charfi-Kaddour, and J.-P. Pouget, "*Inhomogeneous superconductivity in organic conductors: the role of disorder and magnetic field*", J. Phys.: Condens. Matter **23**, 464205 (2011).

[167]T. F. Stalcup, J. S. Brooks, and R. C. Haddon, "*Temporal processes in a polymeric anion-based organic superconductor*", Phys. Rev. B **60**, 9309 (1999).

[168]P. J. Hirschfeld, P. Wölfle, and D. Einzel, "*Consequences of resonant impurity scattering in anisotropic superconductors: Thermal and spin relaxation properties*", Phys. Rev. B **37**, 83 (1988).

[169]R. H. McKenzie and P. Moses, "*Incoherent Interlayer Transport and Angular-Dependent Magnetoresistance Oscillations in Layered Metals*", Phys. Rev. Lett. **81**, 4492 (1998).

[170]O. J. Taylor, A. Carrington, and J. A. Schlueter, "*Superconductor-insulator phase separation induced by rapid cooling of κ-*(BEDT-TTF)$_2$Cu[N(CN)$_2$]Br", Phys. Rev. B **77**, 060503 (2008).

[171]N. Yoneyama, T. Sasaki, and N. Kobayashi, "*Substitution Effect by Deuterated Donors on Superconductivity in κ-(BEDT-TTF)$_2$Cu[N(CN)$_2$]Br*", J. Phys. Soc. Jpn **73**, 1434 (2004).

[172]J. M. Williams, A. M. Kini, H. H. Wang, K. D. Carlson, U. Geiser, L. K. Montgomery, G. J. Pyrka, D. M. Watkins, and J. M. Kommers, "*From semiconductor-semiconductor transition (42 K) to the highest-T_c organic superconductor, κ-(ET)$_2$Cu[N(CN)$_2$]Cl (T_c = 12.5 K)*", Inorg. Chem. **29**, 3272 (1990).

[173]H. Urayama, H. Yamochi, G. Saito, K. Nozawa, T. Sugano, M. Kinoshita, S. Sato, K. Oshima, A. Kawamoto, and J. Tanaka, "*A New Ambient Pressure Organic Superconductor Based on BEDT-TTF with T_c Higher than 10 K (T_c=10.4 K)*", Chem. Lett. **17**, 55 (2006).

[174]L. I. Buravov, N. D. Kushch, V. N. Laukhin, A. G. Khomenko, E. B. Yagubskii, M. V. Kartsovnik, A. E. Kovalev, L. P. Rozenberg, R. P. Shibaeva, M. A. Tanatar, V. S. Yefanov, V. V. Dyakin, and V. A. Bondarenko, "*The first ET salt with a metal complex anion containing a selenocyanate ligand, (ET)$_2$TlIHg(SeCN)$_4$: synthesis, structure and properties*", J. Phys. I France **4**, 441 (1994).

[175]F. Kollmannsberger, "*Thermal history dependent electronic properties of κ-(BEDT-TTF)$_2$Cu[N(CN)$_2$]X (X=Br,Cl) near the Mott-metal-insulator transition*", Diplomarbeit (Technische Universität München, 2023).

[176]Y. Kohama, C. Marcenat, T. Klein, and M. Jaime, "*AC measurement of heat capacity and magnetocaloric effect for pulsed magnetic fields*", Rev. Sci. Instrum. **81**, 104902 (2010).

[177]D. Andres, "*Effects of High Magnetic Fields and Hydrostatic Pressure on the Low-Temperature Density-Wave State of the Organic Metal κ-(BEDT-TTF)$_2$KHg(SCN)$_4$*", PhD thesis (Technische Universität München, 2004).

[178]S. Fust, "*Shubnikov-de Haas Effect and Magnetic Breakdown in the Layered Organic Superconductor κ-(BEDT-TTF)$_2$Cu(NCS)$_2$*", Diplomarbeit (Technische Universität München, 2016).

[179]I. of high pressure physics., *SPG10 Semiconductor Pressure Gauge*, Polish Academy of Scienses., 2009.

[180]L. H. Dmowski and E. Litwin-Staszewska, "*The variation of the pressure coefficient of manganin sensors at low temperatures*", Meas. Sci. Technol. **10**, 343 (1999).

[181]M. Kunz, "*Superconductivity and competing ordered states in layered organic metals*", PhD thesis (Technische Universität München, 2016).

[182]A. Pustogow, Y. Saito, A. Löhle, M. Sanz Alonso, A. Kawamoto, V. Dobrosavljevic, M. Dressel, and S. Fratini, "*Rise and fall of Landau's quasiparticles while approaching the Mott transition*", Nat. Comm. **12**, 1571 (2008).

[183]S. Erkenov, S. Fust, S. Oberbauer, W. Biberacher, N. D. Kushch, H. Müller, F. L. Pratt, R. Gross, and M. V. Kartsovnik, "*Electronic correlations and spin frustration in the molecular conductors κ-(BEDT-TTF)$_2$X probed by magnetic quantum oscillations*", Phys. Rev. B **110**, 205149 (2024).

[184]H. D. Weiss, "*Fermi surface studies on the organic superconductor κ-(BEDT-TTF)$_2$Cu[N(CN)$_2$]Br and on the Alkaline earth subnitride NaBa$_3$B by means of magneto-quantum oscillations*", PhD thesis (Hartung-Gorre Verlag Konstanz, 2001).

[185]J. Singleton, P. A. Goddard, A. Ardavan, N. Harrison, S. J. Blundell, J. A. Schlueter, and A. M. Kini, "*Test for Interlayer Coherence in a Quasi-Two-Dimensional Superconductor*", Phys. Rev. Lett. **88**, 037001 (2002).

[186]J. Caulfield, W. Lubczynski, F. L. Pratt, J. Singleton, D. Y. K. Ko, W. Hayes, M. Kurmoo, and P. Day, "*Magnetotransport studies of the organic superconductor κ -(BEDT-TTF)$_2$Cu(NCS)$_2$ under pressure: the relationship between carrier effective mass and critical temperature*", J. Phys.: Condens. Matter **6**, 2911 (1994).

[187]G. Visentini, A. Painelli, A. Girlando, and A. Fortunelli, "*The dimer model for κ-phase organic superconductors*", EPL **42**, 467 (1998).

[188]F. Pratt, "*Using Shubnikov-de Haas data to estimate the magnetic frustration parameter t'/t in the spin-liquid system κ-$ET_2Cu_2(CN)_3$*", Physica B Condens. Matter **405**, 205 (2010).

[189]A. Audouard and J. Fortin, "*Does Fourier analysis yield reliable amplitudes of quantum oscillations?*", EPJ AP **83**, 30201 (2018).

[190]M. Rahal, D. Chasseau, J. Gaultier, L. Ducasse, M. Kurmoo, and P. Day, "*Isothermal Compressibility and Pressure Dependence of the Crystal Structures of the Superconducting Charge-Transfer Salt κ-(BEDT-TTF)$_2$Cu(NCS)$_2$*", Acta Crystallogr. B **53**, 159 (1997).

[191]J. Merino and R. H. McKenzie, "*Cyclotron effective masses in layered metals*", Phys. Rev. B **62**, 2416 (2000).

[192]Y.-N. Xu, W. Y. Ching, Y. C. Jean, and Y. Lou, "*First-principles calculation of the electronic and optical properties of the organic superconductor κ-(BEDT-TTF)$_2$Cu(NCS)$_2$*", Phys. Rev. B **52**, 12946 (1995).

[193]J. Ferber, K. Foyevtsova, H. O. Jeschke, and R. Valentí, "*Unveiling the microscopic nature of correlated organic conductors: The case of κ-$(ET)_2Cu[N(CN)_2]Br_xCl_{1-x}$*", Phys. Rev. B **89**, 205106 (2014).

[194]V. N. Zverev, W. Biberacher, S. Oberbauer, I. Sheikin, P. Alemany, E. Canadell, and M. V. Kartsovnik, "*Fermi surface properties of the bifunctional organic metal κ-$(BETS)_2Mn[N(CN)_2]_3$ near the metal-insulator transition*", Phys. Rev. B **99**, 125136 (2019).

[195]A. Dragulescu, V. M. Yakovenko, and D. J. Singh, "*Theory of angular magnetoresistance oscillations in $Tl_2Ba_2CuO_6$*", Phys. Rev. B **60**, 6312 (1999).

[196]P. Moses and R. H. McKenzie, "*Comparison of coherent and weakly incoherent transport models for the interlayer magnetoresistance of layered Fermi liquids*", Phys. Rev. B **60**, 7998 (1999).

[197]T. Furukawa, K. Miyagawa, M. Matsumoto, T. Sasaki, and K. Kanoda, "*Microscopic evidence for preformed Cooper pairs in pressure-tuned organic superconductors near the Mott transition*", Phys. Rev. Res. **5**, 023165 (2023).

[198]A. G. Lebed and N. N. Bagmet, "*Nonanalytical magnetoresistance, the third angular effect, and a method to investigate Fermi surfaces in quasi-two-dimensional conductors*", Phys. Rev. B **55**, R8654 (1997).

[199]A. J. Schofield and J. R. Cooper, "*Quasilinear magnetoresistance in an almost two-dimensional band structure*", Phys. Rev. B **62**, 10779 (2000).

[200]N. E. Hussey, A. P. Mackenzie, J. R. Cooper, Y. Maeno, S. Nishizaki, and T. Fujita, "*Normal-state magnetoresistance of Sr_2RuO_4*", Phys. Rev. B **57**, 5505 (1998).

[201]V. Kataev, G. Winkel, N. Knauf, A. Gruetz, D. Khomskii, D. Wohlleben, W. Crump, J. Hahn, and K. Tebbe, "*ESR study of the electronic properties of the new organic conductors κ-(BEDT-TTF)$_2$Cu[N(CN)$_2$]X, X = Br; I*", Physica B: Condens. Matter **179**, 24 (1992).

[202]J. Hagel, J. Wosnitza, C. Pfleiderer, J. A. Schlueter, J. Mohtasham, and G. L. Gard, "*Pressure-induced insulating state in an organic superconductor*", Phys. Rev. B **68**, 104504 (2003).

[203]Z. Li, D.-H. Xu, X. Li, H.-J. Liao, X. Xi, Y.-C. Yu, and W. Wang, "*Anomalous spin dynamics in a two-dimensional magnet induced by anisotropic critical fluctuations*", Phys. Rev. B **106**, 054427 (2022).

[204]M. A. Tanatar, T. Ishiguro, T. Kondo, and G. Saito, "*Nonmetal to metal crossover and ethylene ordering in the organic superconductor κ-(BEDT-TTF)$_2$Cu[N(CN)$_2$]Br*", Phys. Rev. B **59**, 3841 (1999).

[205]X. Su, F. Zuo, J. Schlueter, M. Kelly, and J. M. Williams, "*Dynamic disorders and its relaxation in organic superconductor κ-(BEDT-TTF)$_2$Cu[N(CN)$_2$]Br*", Solid State Commun. **107**, 734 (1998).

[206]J. M. Ziman, "*Principles of the Theory of Solids*", Cambridge University Press, 1972.

[207]N. Ashcroft and N. Mermin, "*Solid State Physics*", HRW international editions, Holt, Rinehart and Winston, 1976.

[208]G. D. Mahan, "*Many-Particle Physics*", Springer New York, 2000.

[209]G. Schubert, A. Weisse, G. Wellein, and H. Fehske, "*Comparative numerical study of Anderson localisation in disordered electron systems*", in *High Performance Computing in Science and Engineering*, Springer-Verlag, 2006, p. 237.

[210]B. Bulka, M. Schreiber, and B. Kramer, "*Localization, quantum interference, and the metal-insulator transition*", Zeitschrift für Physik B Condensed Matter **66**, 21 (1987).

[211]J. T. Edwards and D. J. Thouless, "*Numerical studies of localization in disordered systems*", J. Phys. C: Solid State Phys. **5**, 807 (1972).

[212]E. Abrahams, P. W. Anderson, D. C. Licciardello, and T. V. Ramakrishnan, "*Scaling Theory of Localization: Absence of Quantum Diffusion in Two Dimensions*", Phys. Rev. Lett. **42**, 673 (1979).

[213]Wzietek, P., Mayaffre, H., Jérome, D., and Brazovskii, S., "*NMR in the 2D Organic Superconductors*", J. Phys. I France **6**, 2011 (1996).

[214]J. Merino, M. Dumm, N. Drichko, M. Dressel, and R. H. McKenzie, "*Quasiparticles at the Verge of Localization near the Mott Metal-Insulator Transition in a Two-Dimensional Material*", Phys. Rev. Lett. **100**, 086404 (2008).

[215]A. Kawamoto, Y. Honma, and K.-i. Kumagai, "*Electron localization in the strongly correlated organic system κ-(BEDT-TTF)$_2$X probed with nuclear magnetic resonance ^{13}C-NMR*", Phys. Rev. B **70**, 060510 (2004).

[216]Y. Shimizu, K. Miyagawa, K. Kanoda, M. Maesato, and G. Saito, "*Inhomogeneous Spin State in a Spin Liquid on a Triangular Lattice under a Magnetic Field*", AIP Conf. Proc. **850**, 1087 (2006).

[217]H. O. Jeschke, M. de Souza, R. Valentí, R. S. Manna, M. Lang, and J. A. Schlueter, "*Temperature dependence of structural and electronic properties of the spin-liquid candidate κ-(BEDT-TTF)$_2$Cu$_2$(CN)$_3$*", Phys. Rev. B **85**, 035125 (2012).

[218]Y. Zhou, K. Kanoda, and T.-K. Ng, "*Quantum spin liquid states*", Rev. Mod. Phys. **89**, 025003 (2017).

[219]Y. Kawasugi, S. Yamazaki, A. Pustogow, and N. Tajima, "*Negative Magnetoresistance near the Mott Metal-Insulator Transition in the Quantum Spin Liquid Candidate κ-(BEDT-TTF)$_2$Cu$_2$(CN)$_3$*", J. Phys. Soc. Jpn **92**, 065001 (2023).

[220]B. Kyung and A.-M. S. Tremblay, "*Mott Transition, Antiferromagnetism, and d-Wave Superconductivity in Two-Dimensional Organic Conductors*", Phys. Rev. Lett. **97**, 046402 (2006).

[221]O. Parcollet, G. Biroli, and G. Kotliar, "*Cluster Dynamical Mean Field Analysis of the Mott Transition*", Phys. Rev. Lett. **92**, 226402 (2004).

List of Publications

- S. Oberbauer, S. Erkenov, W. Biberacher, N. D. Kushch, R. Gross, M. V. Kartsovnik, "Coherent heavy charge carriers in an organic conductor near the bandwidth-controlled Mott transition", Phys. Rev. B, **107**, 075139 (2023).
- S. Erkenov, S. Fust, S. Oberbauer, W. Biberacher, N. D. Kushch, H. Müller, F. L. Pratt, R. Gross, M. V. Kartsovnik, "Electronic correlations and spin frustration in the molecular conductors κ-(BEDT-TTF)$_2X$ probed by magnetic quantum oscillations", Phys. Rev. B, **110**, 205149 (2024).

Acknowledgments

Over the past several years, the Walther-Meißner-Institut has felt like a second home to me. Most of my time and activities have been closely connected to it. I would therefore like to express my sincere gratitude to all my colleagues, including:

- Prof. Dr. Rudolf Gross, for giving me the opportunity to conduct my thesis work at the Walther-Meißner-Institut.
- Dr. Mark Kartsovnik, my mentor and supervisor, for his continuous guidance and support throughout this work, and for sharing with me his deep knowledge and experience during our many hours of joint measurements.
- Dr. W. Biberacher, for his help with experimental techniques and for reading this thesis, even after his retirement.
- My Master's student F. Kollmannsberger, for conducting a successful experiment on the influence of thermal treatment and for adapting the software accordingly.
- Our collaborators - T. Helm, I. Sheikin, J. Sourd, and F. Husstedt - for their assistance during experiments in their respective facilities.
- N. Kushch, H. Müller, M. Lang, A. Pustogow and A. Kawamoto for providing the crystals used in this work.
- The workshop, electronics, and chemistry teams, for their help in overcoming technical challenges and for their precise manufacturing of experimental equipment.
- The helium liquefier operators, for their patience during numerous helium alarms and their assistance in finding helium leaks.
- The institute administration, for their quick and efficient handling of bureaucratic matters.
- The cleaning team, for always keeping the institute in excellent condition.
- To all the PhD students, for sharing this time together - for our shared lunches and visits to Honghong, for our shared improvement in ping-pong skills and competitive games, and for the joyful celebration of the Fests and many other activities.

And finally, all praise is due to God, Lord of all the worlds.